Coggon, R.M., Teagle, D.A.H., Sylvan, J.B., Reece, J., Estes, E.R., Williams, T.J., Christeson, G.L., and the Expedition 390/393 Scientists
Proceedings of the International Ocean Discovery Program Volume 390/393
publications.iodp.org

Site U1583[1]

D.A.H. Teagle, J. Reece, T.J. Williams, R.M. Coggon, J.B. Sylvan, E.R. Estes, G.L. Christeson, E. Albers, C. Amadori, T.M. Belgrano, T. D'Angelo, N. Doi, A. Evans, G.M. Guérin, M. Harris, V.M. Hojnacki, G. Hong, X. Jin, M. Jonnalagadda, D. Kuwano, J.M. Labonte, A.R. Lam, M. Latas, W. Lu, P. Moal-Darrigade, S.F. Pekar, C. Robustelli Test, J.G. Ryan, D. Santiago Ramos, A. Shchepetkina, A. Villa, S.Y. Wee, S.J. Widlansky, M. Aizawa, C. Borrelli, J.D. Bridges, E.J. Carter, J. Dinarès-Turell, J.D. Estep, W.P. Gilhooly III, L.J.C. Grant, M.R. Kaplan, P.D. Kempton, C.M. Lowery, A. McIntyre, C.M. Routledge, A.L. Slagle, M. Takada, L. Tamborrino, Y. Wang, K. Yang, W. Kurz, M. Prakasam, L. Tian, T. Yu, and G. Zhang[2]

[1] Teagle, D.A.H., Reece, J., Williams, T.J., Coggon, R.M., Sylvan, J.B., Estes, E.R., Christeson, G.L., Albers, E., Amadori, C., Belgrano, T.M., D'Angelo, T., Doi, N., Evans, A., Guérin, G.M., Harris, M., Hojnacki, V.M., Hong, G., Jin, X., Jonnalagadda, M., Kuwano, D., Labonte, J.M., Lam, A.R., Latas, M., Lu, W., Moal-Darrigade, P., Pekar, S.F., Robustelli Test, C., Ryan, J.G., Santiago Ramos, D., Shchepetkina, A., Villa, A., Wee, S.Y., Widlansky, S.J., Aizawa, M., Borrelli, C., Bridges, J.D., Carter, E.J., Dinarès-Turell, J., Estep, J.D., Gilhooly, W.P., III, Grant, L.J.C., Kaplan, M.R., Kempton, P.D., Lowery, C.M., McIntyre, A., Routledge, C.M., Slagle, A.L., Takada, M., Tamborrino, L., Wang, Y., Yang, K., Kurz, W., Prakasam, M., Tian, L., Yu, T., and Zhang, G., 2024. Site U1583. In Coggon, R.M., Teagle, D.A.H., Sylvan, J.B., Reece, J., Estes, E.R., Williams, T.J., Christeson, G.L., and the Expedition 390/393 Scientists, South Atlantic Transect. Proceedings of the International Ocean Discovery Program, 390/393: College Station, TX (International Ocean Discovery Program). https://doi.org/10.14379/iodp.proc.390393.107.2024

[2] **Expedition 390/393 Scientists' affiliations.**

Contents

Keywords
International Ocean Discovery Program, IODP, *JOIDES Resolution*, Expedition 390, Expedition 393, South Atlantic Transect, Biosphere Frontiers, Earth Connections, Mid-Atlantic Ridge, Site U1583

Core descriptions

Supplementary material

References (RIS)

MS 390393-107
Published 23 January 2024

Funded by NSF OCE1326927

1. Background and objectives

Site U1583 (30°42.6175′S, 20°26.0336′W; proposed Site SATL-33B) is in the central South Atlantic Ocean at a water depth of ~4210 meters below sea level (mbsl), ~652 km west of the Mid-Atlantic Ridge (see Figure **F1** and Tables **T1**, **T2**, all in the Expedition 390/393 summary chapter [Coggon et al., 2024b]) on crust that formed at an intermediate half spreading rate of ~24 mm/y, which is close to the highest spreading rate in the study region (Kardell et al., 2019; Christeson et al., 2020) (see Figure **F7** in the Expedition 390/393 summary chapter [Coggon et al., 2024b]). With an estimated age of 30.6 Ma, Site U1583 is close to the median age of the South Atlantic Transect (SAT) campaign (International Ocean Discovery Program [IODP] Expeditions 390C, 395E, 390, and 393), and it is closest to the geographic midpoint.

1.1. Geologic setting

Unlike other sites visited during the SAT expeditions, Site U1583 is a new site occupied only during Expedition 393. It is located on the north-south–trending (355) Crustal Reflectivity Experiment Southern Transect (CREST) seismic crossing Line 03 at Common Depth Point 12300 about 3.3 km south of the main east–west (085) CREST Seismic Line 1C/1D (Figures **F1**, **F2**) (Reece et al., 2016; Reece and Estep, 2019). Interpretation of multichannel seismic and ocean-bottom seismograph data in this region suggests that the ocean crust is slightly thicker at the site (~7 km; Christeson et al., 2020) than normal ocean crust (6.15 ± 0.93 km; Christeson et al., 2019) and is associated with a peak in seamount density. At a water depth of 4210 m, Site U1583 falls within the depth range predicted by simple lithospheric cooling models (see Figure **F4** in the Expedition 390/393 summary chapter [Coggon et al., 2024b]) (e.g., Parsons and Sclater, 1977; Korenaga and Korenaga, 2008; Marty and Cazenave, 1989), unlike neighboring Sites U1558 and U1559, which are shallower than predicted because of their location on elevated features. Site U1583, in contrast, lacks the rugged basement topography present near Sites U1558 and U1559.

Site U1583 sits near the top of a ~180 m high (above regional seafloor), 30 km long, near north-south–trending (359), 10 km wide basement ridge (Figures **F1**, **F2**, **F3**). This basement ridge is one of many subparallel and 30–40 km long ridges, and it is continuously draped with sediments. Along the north-south–trending CREST Line 03 profile, sediment thickness increases from 30 m

at the intersection with the main east–west CREST Seismic Line 1 to 300 m at the southern end of the line (Figure **F2B**). The sediment thickness at Site U1583 is 106 m, which is close to the global average overburden thickness for basement of this age (~125 m; Spinelli et al., 2004; cf. Olson et al., 2016; Straume et al., 2019) and the mean sediment thickness encountered along CREST Seismic Lines 1C (31–48 Ma) and 1D (15–31 Ma) of 131 and 85 m, respectively (Estep et al., 2019).

Basement topography is much smoother along the long north–south axis of the Site U1583 ridge than across the profile (Figure **F2**). The seismic reflector interpreted to be the sediment/basement

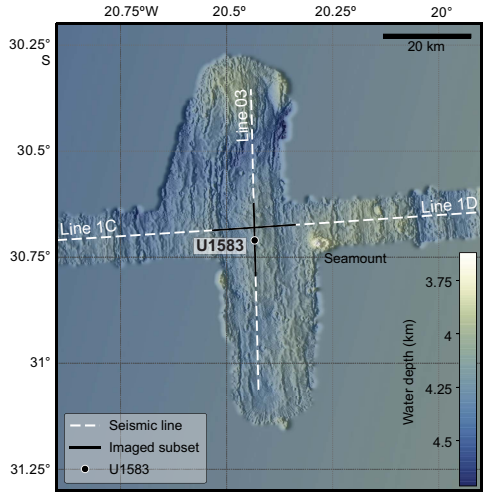

Figure F1. Bathymetric map of the 30.6 Ma SAT study area showing location of Site U1583 and CREST multichannel seismic (MCS) Reflection Lines 1C/1D and 03 (Christeson and Reece, 2020). Seismic reflection profiles were acquired during CREST cruise (Reece et al., 2016). Solid black lines = location of wide-angle MCS profiles for which seismic images are shown in Figure F2.

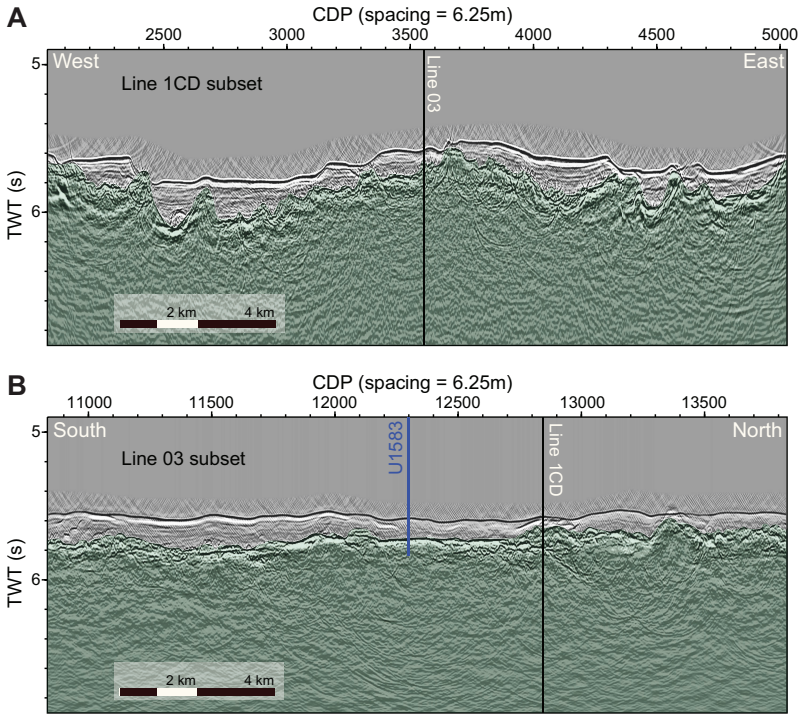

Figure F2. CREST multichannel seismic (MCS) reflection profiles on ~30.6 Ma crust showing local basement topography, Site U1583. A. West–east MCS Line 1C/1D that crosses Line 03 approximately 3.3 km north of Site U1583. B. North–south Line 03. Black lines = intersections of MCS reflection profiles. CDP = common depth point, TWT = two-way traveltime.

interface has a very strong and subhorizontal signature for distances of ~2.5 km north and ~5 km south of Site U1583. This strong reflector gradually deepens to the south, resulting in the increased sediment thickness. In contrast, along the east-west–trending CREST Line 1C/1D profile, a number of 1 km wide subbasins are imaged across both flanks of the basement ridge, separated by elevated features above the main basement level and each filled with ~160 to ~300 m of sediment (Figure **F2A**). These subbasins and elevated features are continuously draped with sediments.

The basement ridge on which Site U1583 is located plunges toward the north and creates a basin with water depths around ~4500 m (Figure **F1**). Backscatter reflections from multibeam profiles (Figure **F3**) reveal that a significant proportion of the seafloor near Site U1583 is blanketed by continuous sediment cover, which is in contrast to the other sites along the SAT. Therefore, ventilation of the volcanic rocks of the upper ocean crust through the ingress of seawater and egress of seawater-derived low-temperature hydrothermal fluids may be reduced compared to other sites. However, the unique presence of seamounts near Site U1583, which agrees with an observed peak in seamount density at 28–40 Ma along the SAT (Christeson et al., 2020), may influence the local fluid flow system with consequent impacts on heat flow, sediment pore waters, basement hydrothermal alteration, and microbial communities in both the marine sediments and underlying basalts. One large seamount forms a prominent feature on the local bathymetric and backscatter maps (Figures **F1**, **F3**). This seamount is ~17 km east of Site U1583, is ~5 km in diameter, and rises to ~3.7 km below sea level (Figures **F1**). High normalized reflectivity indicates very thin or no sediment cover (Figure **F3**).

1.2. Objectives

The operational objectives at Site U1583 during Expedition 393 were to (1) core the entire sediment section and a few meters into basement with the advanced piston corer (APC) and extended core barrel (XCB) systems in two holes to collect material that address the paleoceanographic, paleoclimate, and microbiological objectives of the SAT expeditions; (2) core 250 m into basement with the rotary core barrel (RCB) system in a third hole to collect material that addresses the petrologic, geochemical, and microbiological objectives of the SAT expeditions; and (3) collect wireline geophysical logging data through the basement section.

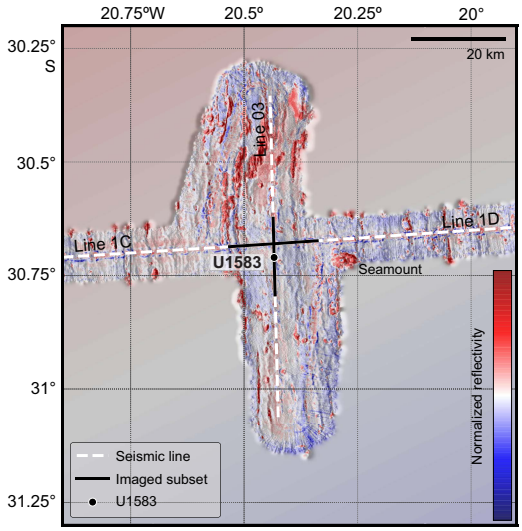

Figure F3. Backscatter reflections from Site U1583 region collected during CREST site survey cruise (Reece et al., 2016; Reece and Estep, 2019; Christeson et al., 2020). Red = higher normalized reflectivity values, blue = lower normalized reflectivity values. Solid black lines = location of wide-angle multichannel seismic profiles for which seismic images are shown in Figure F2.

2. Operations

2.1. Transit

At 0530 h on 5 July 2022, we started the 227 nmi transit to Site U1583 from Site U1558. The transit took 21.5 h at an average speed of 10.6 kt, and we arrived on site at 0300 h on 6 July.

2.2. Holes U1583A and U1583B

The ship switched to dynamic positioning mode at 0315 h on 6 July 2022, beginning operations in Hole U1583A. On site, we noted a 41 m seafloor depth discrepancy between the ship's precision depth recorder (PDR) 12 kHz estimate of 4234 mbsl and the estimate from the preexpedition seismic survey of 4193 mbsl in the *Scientific Prospectus* (Coggon et al., 2020). Sea conditions were rough, and ship heave was 3–4 m. The APC/XCB bottom-hole assembly (BHA) was made up and lowered to 4228.5 mbsl, 4.5 m above the PDR estimated depth. At 1030 h, led by Captain Tom Hartt, the Expedition 393 Science Party and others available on board held a short celebration of the life of Professor Dick Kroon (1957–2022) (see KROON in **Supplementary material**).

At 1545 h, we started Hole U1583A. Core 1H recovered 9.14 m of sediment, indicating that the bit was below the seafloor when the piston was shot, so the mudline depth could not be determined (Table **T1**). At 1715 h, we started Hole U1583B at approximately the same geographic location

Table T1. Core summary, Site U1583. DRF = drilling depth below rig floor, DSF = drilling depth below seafloor, CSF = core depth below seafloor, CSF-A = core depth below seafloor, Method A. Core type: H = advanced piston corer (APC), R = rotary core barrel (RCB), X = extended core barrel (XCB), numeric core type = drilled interval. ROP = rate of penetration. (Continued on next page.) **Download table in CSV format.**

Hole U1583A
Expedition: 393
Latitude: 30°42.6060′S
Longitude: 20°26.0340′W
Water depth (m): 4210.04
Date started (UTC): 06 Jul 2022; 0324 h
Date finished (UTC): 06 Jul 2022; 1615 h
Time on hole (days): 0.54
Seafloor depth DRF (m): 4221.5
Seafloor depth est. method: Offset from E
Rig floor to sea level (m): 11.41
Penetration DSF (m): 9.1
Cored interval (m): 9.1
Recovered length (m): 9.14
Recovery (%): 100.44
Drilled interval (m): 0
Drilled interval (*N*): 0
Total cores (*N*): 1
APC cores (*N*): 1

Hole U1583B
Expedition: 393
Latitude: 30°42.6062′S
Longitude: 20°26.0341′W
Water depth (m): 4210.04
Date started (UTC): 06 Jul 2022; 1615 h
Date finished (UTC): 06 Jul 2022; 1800 h
Time on hole (days): 0.07
Seafloor depth DRF (m): 4221.5
Seafloor depth est. method: Offset from E
Rig floor to sea level (m): 11.41
Penetration DSF (m): 9.4
Cored interval (m): 9.4
Recovered length (m): 9.38
Recovery (%): 99.79
Drilled interval (m): 0
Drilled interval (*N*): 0
Total cores (*N*): 1
APC cores (*N*): 1

Hole U1583C
Expedition: 393
Latitude: 30°42.6011′S
Longitude: 20°26.0343′W
Water depth (m): 4214.59
Date started (UTC): 06 Jul 2022; 1800 h
Date finished (UTC): 07 Jul 2022; 1540 h
Time on hole (days): 0.9
Seafloor depth DRF (m): 4226
Seafloor depth est. method: Mudline core (missed mudline)
Rig floor to sea level (m): 11.41
Penetration DSF (m): 107.5
Cored interval (m): 107.5
Recovered length (m): 110.19
Recovery (%): 102.5
Drilled interval (m): 0
Drilled interval (*N*): 0
Total cores (*N*): 13
APC cores (*N*): 12
XCB cores (*N*): 1

Hole U1583D
Expedition: 393
Latitude: 30°42.6288′S
Longitude: 20°26.0340′W
Water depth (m): 4210.04
Date started (UTC): 07 Jul 2022; 1540 h
Date finished (UTC): 07 Jul 2022; 1730 h
Time on hole (days): 0.08
Seafloor depth DRF (m): 4221.5
Seafloor depth est. method: Offset from E
Rig floor to sea level (m): 11.46
Penetration DSF (m): 9.5
Cored interval (m): 9.5
Recovered length (m): 10.04
Recovery (%): 105.68
Drilled interval (m): 0
Drilled interval (*N*): 0
Total cores (*N*): 1
APC cores (*N*): 1

Hole U1583E
Expedition: 393
Latitude: 30°42.6285′S
Longitude: 20°26.0340′W
Water depth (m): 4210.04
Date started (UTC): 07 Jul 2022; 1730 h
Date finished (UTC): 10 Jul 2022; 0430 h
Time on hole (days): 2.46
Seafloor depth DRF (m): 4221.5
Seafloor depth est. method: Mudline core
Rig floor to sea level (m): 11.46
Penetration DSF (m): 105.2
Cored interval (m): 105.2
Recovered length (m): 105.15
Recovery (%): 99.95
Drilled interval (m): 0
Drilled interval (*N*): 0
Total cores (*N*): 12
APC cores (*N*): 12

Hole U1583F
Expedition: 393
Latitude: 30°42.6175′S
Longitude: 20°26.0336′W
Water depth (m): 4210.05
Date started (UTC): 10 Jul 2022; 0430 h
Date finished (UTC): 18 Jul 2022; 0845 h
Time on hole (days): 8.18
Seafloor depth DRF (m): 4221.5
Seafloor depth est. method: Offset
Rig floor to sea level (m): 11.45
Penetration DSF (m): 239.5
Cored interval (m): 138.5
Recovered length (m): 45.79
Recovery (%): 33.06
Drilled interval (m): 101
Drilled interval (*N*): 1
Total cores (*N*): 28
RCB cores (*N*): 28

Table T1 (continued).

Core, type	Core on deck date (2022)	Core on deck time UTC (h)	Top depth drilled DSF (m)	Bottom depth drilled DSF (m)	Advanced (m)	Top depth cored CSF (m)	Bottom depth recovered CSF-A (m)	Recovered length (m)	Curated length (m)	Recovery (%)	Sections (*N*)	Real ROP (m/h)
393-U1583A-												
1H	06 Jul	1610	0.0	9.1	9.1	0.0	9.14	9.14	9.14	100	7	0.0
393-U1583B-												
1H	06 Jul	1745	0.0	9.4	9.4	0.0	9.38	9.38	9.38	100	8	0.0
393-U1583C-												
1H	06 Jul	1920	0.0	8.5	8.5	0.0	8.47	8.47	8.47	100	7	0.0
2H	06 Jul	2045	8.5	17.0	8.5	8.5	16.95	8.45	8.45	99	7	102.0
3H	06 Jul	2205	17.0	26.5	9.5	17.0	26.47	9.44	9.47	99	8	114.0
4H	06 Jul	2345	26.5	36.0	9.5	26.5	36.41	9.91	9.91	104	8	114.0
5H	07 Jul	0100	36.0	45.5	9.5	36.0	45.36	9.36	9.36	99	8	114.0
6H	07 Jul	0210	45.5	55.0	9.5	45.5	53.88	8.38	8.38	88	7	114.0
7H	07 Jul	0335	55.0	64.5	9.5	55.0	64.68	9.68	9.68	102	8	114.0
8H	07 Jul	0445	64.5	74.0	9.5	64.5	73.13	8.63	8.63	91	7	114.0
9H	07 Jul	0550	74.0	83.5	9.5	74.0	83.27	9.27	9.27	98	7	114.0
10H	07 Jul	0720	83.5	93.0	9.5	83.5	92.54	9.02	9.04	95	7	114.0
11H	07 Jul	0835	93.0	102.5	9.5	93.0	102.67	9.67	9.67	102	8	57.0
12H	07 Jul	0945	102.5	104.5	2.0	102.5	110.52	8.02	8.02	401	7	12.0
13X	07 Jul	1405	104.5	107.5	3.0	104.5	106.32	1.89	1.82	63	2	2.0
				Hole U1583C totals:	107.50			110.19	110.17	103		
393-U1583D-												
1H	07 Jul	1730	0.0	9.5	9.5	0.0	10.04	10.04	10.04	106	8	0.0
393-U1583E-												
1H	07 Jul	1900	0.0	4.0	4.0	0.0	4.03	4.03	4.03	101	4	0.0
2H	07 Jul	2245	4.0	13.5	9.5	4.0	13.89	9.89	9.89	104	8	114.0
3H	08 Jul	0050	13.5	23.0	9.5	13.5	23.03	9.53	9.53	100	8	114.0
4H	08 Jul	0255	23.0	32.5	9.5	23.0	32.49	9.49	9.49	100	8	114.0
5H	08 Jul	0425	32.5	42.0	9.5	32.5	42.68	10.18	10.18	107	8	57.0
6H	08 Jul	0535	42.0	51.5	9.5	42.0	50.39	8.39	8.39	88	7	114.0
7H	08 Jul	0645	51.5	61.0	9.5	51.5	61.46	9.96	9.96	105	8	114.0
8H	08 Jul	0810	61.0	70.5	9.5	61.0	70.73	9.73	9.73	102	8	114.0
9H	08 Jul	0915	70.5	80.0	9.5	70.5	79.14	8.64	8.64	91	7	114.0
10H	08 Jul	1020	80.0	89.5	9.5	80.0	89.66	9.66	9.66	102	8	114.0
11H	08 Jul	1120	89.5	99.0	9.5	89.5	99.02	9.52	9.52	100	8	114.0
12H	10 Jul	0745	99.0	105.2	6.2	99.0	105.13	6.13	6.13	99	6	37.2
				Hole U1583E totals:	105.20			105.15	105.15	100		
393-U1583F-												
11	11 Jul	0415	0.0	101.0			*****Drilled from 0.0 to 101.0 mbsf*****				0	110.2
2R	11 Jul	0645	101.0	109.5	8.5	101.0	107.43	6.43	6.43	76	6	11.3
3R	11 Jul	1150	109.5	114.3	4.8	109.5	113.03	3.52	3.53	73	3	1.3
4R	11 Jul	1605	114.3	119.2	4.9	114.3	119.28	4.70	4.98	96	4	1.9
5R	11 Jul	2200	119.2	128.9	9.7	119.2	124.58	4.05	5.38	42	4	2.2
6R	12 Jul	0220	128.9	133.7	4.8	128.9	128.98	0.07	0.08	1	1	1.8
7R	12 Jul	0745	133.7	138.6	4.9	133.7	135.05	1.32	1.35	27	1	1.3
8R	12 Jul	1325	138.6	143.4	4.8	138.6	138.60				0	1.2
9R	12 Jul	1750	143.4	146.3	2.9	143.4	143.75	0.35	0.35	12	1	3.5
10R	12 Jul	2210	146.3	148.4	2.1	146.3	147.80	1.20	1.50	57	1	1.7
11R	13 Jul	0255	148.4	153.2	4.8	148.4	149.20	0.94	0.80	20	1	1.6
12R	13 Jul	0910	153.2	158.1	4.9	153.2	157.99	4.36	4.79	89	4	1.1
13R	13 Jul	1435	158.1	162.9	4.8	158.1	162.88	4.19	4.78	87	4	1.1
14R	13 Jul	1845	162.9	166.8	3.9	162.9	163.82	0.75	0.92	19	1	2.3
15R	13 Jul	2325	166.8	171.6	4.8	166.8	168.08	1.00	1.28	21	1	1.6
16R	14 Jul	0400	171.6	176.5	4.9	171.6	174.67	2.49	3.07	51	3	1.8
17R	14 Jul	0950	176.5	181.3	4.8	176.5	177.77	1.09	1.27	23	1	1.3
18R	14 Jul	1440	181.3	186.2	4.9	181.3	183.15	1.56	1.85	32	2	1.8
19R	14 Jul	1755	186.2	191.0	4.8	186.2	186.66	0.32	0.46	7	1	3.2
20R	14 Jul	2300	191.0	195.9	4.9	191.0	191.76	0.63	0.76	13	1	1.8
21R	15 Jul	0350	195.9	200.7	4.8	195.9	197.63	1.56	1.73	33	2	1.5
22R	15 Jul	0725	200.7	205.6	4.9	200.7	202.35	1.40	1.65	29	2	2.5
23R	15 Jul	1140	205.6	210.4	4.8	205.6	206.96	1.17	1.36	24	1	2.9
24R	15 Jul	1540	210.4	215.3	4.9	210.4	211.51	0.92	1.11	19	1	2.9
25R	15 Jul	2015	215.3	220.1	4.8	215.3	215.60	0.20	0.30	4	1	3.2
26R	15 Jul	2345	220.1	225.0	4.9	220.1	220.39	0.21	0.29	4	1	3.3
27R	16 Jul	0420	225.0	229.8	4.8	225.0	225.42	0.46	0.42	10	1	1.6
28R	16 Jul	0835	229.8	234.7	4.9	229.8	230.42	0.53	0.62	11	1	2.1
29R	16 Jul	1230	234.7	239.5	4.8	234.7	235.16	0.37	0.46	8	1	3.2
				Hole U1583F totals:	138.50			45.79	51.51	33		

(Figure F4) with the drill bit 5 m shallower; however, Core 1H was similarly full, recovering 9.38 m of sediment, so the mudline depth again could not be determined.

2.3. Hole U1583C

The bit was raised 10 m shallower than the Hole U1583B shooting depth to 4213.5 mbsl, and the ship moved 10 m north (Figure F4). At 1845 h on 6 July 2022, we started Hole U1583C, and Core 1H recovered 8.5 m of sediment, giving an apparent mudline at 4214.6 mbsl (we did not know at the time that this core was also shot from below the mudline). Coring continued with the full-length APC system with the Icefield MI-5 core orientation tool run on each core. Temperature measurements were taken on Cores 4H, 7H, and 10H. Core 12H hit hard rock when it was fired, based on some damage to the cutting edge of the APC shoe. Basement contact was subsequently confirmed when the bit encountered hard formation 2 m below the top of Core 12H at 104.5 meters below seafloor (mbsf). Core 12H recovered 8.02 m of sediment, an apparent 401% recovery, most of which was disturbed sucked-in sediment and is not in place. This basement depth was ~33.5 m shallower than expected from the site survey seismic interpretation of basement depth at ~138 mbsf. Cores 1H–12H penetrated from 0 to 104.5 mbsf and recovered 108.3 m (103%).

The XCB coring system was then deployed for Core 393-U1583C-13X, which penetrated 3 m to 107.5 mbsf and recovered 1.9 m of fresh microcrystalline basalt (63%). The bit was then pulled out of the hole, clearing the seafloor at 1540 h on 7 July, ending Hole U1583C.

2.4. Hole U1583D

We started Hole U1583D 50 m south of Hole U1583C and 20 m south of the preexpedition site coordinates, which we reserved for hard rock coring in Hole U1583F. All holes at this site are located on a north–south line (Figure F4) because the site sits on the edge of a north-south–trending basin and the basement depth was anticipated to be more uniform in this direction compared to the east–west direction. Core 393-U1583D-1H recovered 10.04 m of sediment, and the mudline depth could not be determined. Coring was terminated, and Hole U1583D ended at 1730 h on 7 July 2022.

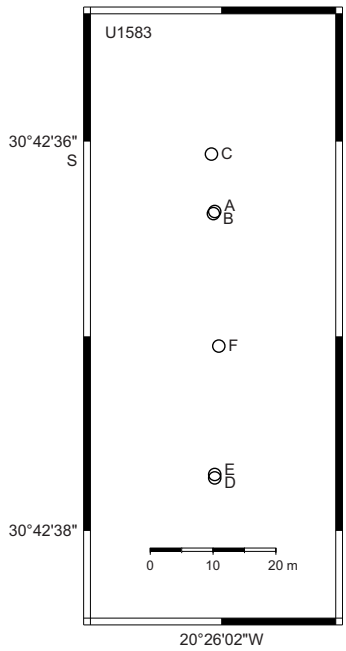

Figure F4. Map of holes drilled at Site U1583.

2.5. Hole U1583E

We raised the bit 5 m to 4204.5 mbsl, and at 1835 h on 7 July 2022 we started Hole U1583E in the same location as Hole U1583D. Core 393-U1583E-1H recovered 4.03 m of sediment, placing the mudline at 4210.0 mbsl. This seafloor depth was 24 m shallower than the PDR depth and 17 m deeper than the depth predicted from the preexpedition seismic survey. The difference from the seismic survey depth is consistent with observations at Sites U1556–U1560 along the transect, where mudline seafloor depths are deeper by 8–21 m than the depth estimated from the seismic survey. While retrieving Core 2H, the core winch weight indicator showed that the core barrel became detached from the core winch line. An overshot was made up using a core catcher and a RCB core barrel. The barrel was lowered, and the APC core barrel was retrieved. Coring continued through Core 12H at 105.2 mbsf. All cores were full-length APC cores, and the Icefield MI-5 core orientation tool was run on all but two cores (3H and 4H). Temperature measurements were taken on Cores 3H and 8H.

After cutting Core 393-U1583E-12H, the APC core barrel could not be pulled back into the BHA. From 1230 to 1545 h on 8 July, we tried to free the barrel by pumping and washing over it, but it would not move. We decided to deploy the Kinley wireline cutter and crimper to cut the winch core line just above the APC corer. The Kinley wireline cutter and crimper was deployed at 1610 h, and the hammer/actuator was deployed at 1640 h. However, based on the core winch line tension, the Kinley wireline cutter and crimper had stopped before reaching the bottom of the drill string and cut part way down. Approximately 1560 m of core winch line was pulled up to the ship, and we then started to raise the pipe. The drill pipe was pulled out of the hole to 2562 meters below rig floor (mbrf) when the severing tool was found in Stand 83. A second Kinley wireline cutter and crimper was deployed in an effort to sever the remaining core winch line from the sinker bar assembly. This was unsuccessful, and the rig crew continued to pull the drill string out of the hole, cutting and removing the remaining core winch line at each stand. The second severing tool was found at the top of Stand 55. The rig crew continued to pull the drill string to the surface, cutting and removing the core winch line as before. The bit reached the rig floor at 0435 h on 10 July, ending Hole U1583E. The rig floor team then disassembled the lower part of the BHA and found that the APC core barrel assembly had stuck in the landing saver sub because a shear pin had become wedged between the landing seat and the core barrel. The APC cutting shoe was undamaged, showing that it had not hit basement, and Core 12H recovered 6.1 m of sediment after a long trip to the surface. Cores 1H–12H penetrated from the seafloor to 105.2 m and recovered 105.2 m (100%).

2.6. Hole U1583F

We started Hole U1583F 20 m north of Hole U1583E, and it became the center location of all holes at this site. At 1000 h on 10 July 2022, we began assembling the RCB BHA with a C-7 bit and then lowered it to 4174 mbsl, where we paused to slip and cut the drill line and pick up the top drive. At 0030 h on 11 July, we started Hole U1583F and washed down through most of the sediment column to 101 mbsf (drilled interval 11). Core 2R penetrated from 101.0 to 109.5 mbsf and recovered 6.4 m (76%) of clayey nannofossil ooze. At the start of drilling Core 3R, hard formation was noted by the drillers at 109.7 mbsf, and the formation was subsequently confirmed to be basalt. Coring continued through Core 8R at 142.9 mbsf. With a hole in basement established, a free-fall funnel (named in honor of Professor Dick Kroon; see KROON in **Supplementary material**) was deployed (Figure **F5**) at 1450 h on 12 July to aid in reentry for downhole logging or for a bit change, which was still a possibility at the time. Coring continued with a typical RCB half-core advance of 4.8/4.9 m. To test for microbiological contamination, perfluoromethyldecalin (PFMD) tracer was run continuously in the drilling fluid until the supply was exhausted on Core 12R. From Core 12R, there was as much as 3 m of backfill in the hole after each core, and the drill string experienced high torque at times. It was uncertain whether the fill resulted from cuttings not being completely cleared from the hole or whether new material was falling down from the borehole wall. We ran 30–60 bbl mud sweeps after every core to flush out the cuttings. The last five cores (Cores 25R–29R) averaged only 7% recovery and the bit had been run for ~73 h of drilling time, so coring was terminated at 1230 h on 16 July after recovering Core 29R. Basement Cores 3R–29R penetrated from 109.5 to 239.5 mbsf and recovered 39.4 m (30%).

To prepare for wireline logging in Hole U1583F, we ran a 75 bbl mud sweep and released the RCB bit at the bottom of the hole. We set the end of the pipe at 102.8 mbsf in sediment ~7 m above the basalt flow that forms the uppermost basement to avoid the risk of dislodging rock pieces while the logging tools were below that depth. At 1730 h, we began to rig up the triple combo logging tool string, consisting of natural gamma radiation, neutron porosity, density, and electrical resistivity tools. Because of the hole conditions and ~3 m ship heave, which is high for logging, the density tool source and magnetic susceptibility tool were not included in the tool string, and the density tool was used only for the caliper log of the borehole diameter. The tool string was lowered down the pipe, but at ~540 mbsl it developed an electrical fault and had to be raised back to the ship. The fault was found in the electrical resistivity tool (the lowermost tool of the tool string), which was then replaced with the backup resistivity tool.

We started to lower the triple combo from the rig floor again at 0045 h on 17 July. Logs were recorded on the downward pass, and the tool string reached 237 mbsf, within 3 m of the bottom of the hole. Two logging passes were run in the open hole. During the first pass, the wireline heave compensator (WHC) cut out about halfway up the open hole but logging continued to the top of basement. While descending for the second pass, the tool string encountered an obstruction at 182 mbsf and could not pass below it. We raised the triple combo to the rig floor, disassembled it, and assembled the Formation MicroScanner (FMS)-sonic tool string. We lowered the FMS-sonic tool string to 182 mbsf and made a logging pass up to the top of basement at 109.5 mbsf. At that point, we found that the tool string could not go back down into basement, and overpull of approximately 8000 lb was observed when trying to pull the tool string back into the drill pipe. After pumping to remove any potential obstruction, the tool string still could not enter the pipe. Finally, we rotated the pipe 180°, and the tool string could be pulled in. When the tool string reached the rig floor, it was discovered that the FMS tool caliper arms had been damaged and one was missing. By 0000 h, we had disassembled the FMS-sonic tool string, ending downhole logging operations in Hole U1583F. The difficult borehole conditions and continuing high heave did not allow for the planned logging with the Ultrasonic Borehole Imager (UBI) tool string. We raised the pipe from 102.8 mbsf, clearing the seafloor at 0035 h on 18 July. The BHA reached the ship at 0645 h and was disassembled. The rig floor was secured for transit by 0840 h, and we raised the thrusters and began the transit to Site U1560.

Figure F5. Launch of a free-fall funnel, named in honor of Professor Dick Kroon, Hole U1583F (Credit: Erick Bravo, IODP JRSO).

3. Stratigraphic unit summary

At Site U1583, we recovered 108.3 m of sediment and 1.89 m of volcanic rock in Hole U1583C and 105.2 m of sediment in Hole U1583E before RCB coring in Hole U1583F penetrated 8.5 m of sediment and ~130 m of volcanic formations (39.4 m volcanic rock retrieved; ~30% recovery) from the uppermost ocean crust (total depth = 239.5 mbsf). The cores recovered from the six holes (U1583A–U1583F) record four major sedimentary units (Figure **F6**) overlying seven basement units (Figure **F7**). The units are numbered from the top of the holes, with units in the sedimentary section designated by Roman numerals (e.g., I and II) and units in the basement designated by Arabic numerals (e.g., 1 and 2); subunits are designated with letters (e.g., IA, IB, 2A, and 2B).

3.1. Sediment units

Biogenic and siliciclastic sediments were recovered from three holes cored at Site U1583. Biogenic sediments consist primarily of calcareous nannofossil ooze with varying amounts of clay and foraminifera. Intervals with siliciclastic sediments are represented by clays with variable nannofossil and foraminifera content. Four lithostratigraphic units (I–IV) are defined (Figure **F6**; Table **T2**). Unit I is composed of 3 m of Pliocene/Pleistocene sediments, consisting of interbedded nannofossil-rich clay with foraminifera and clayey nannofossil ooze, and was only recovered in Hole U1583E. Unit II is composed of up to 11.3 m of Pliocene/Pleistocene sediments, predominantly beds of nannofossil ooze with clay and foraminifera interbedded with beds of nannofossil ooze with clay. Unit III consists of up to 11.9 m of clay and nannofossil ooze with varying amounts of clay. Unit IV is divided into three subunits (IVA–IVC; see **Sedimentology**). Subunit IVA is up to 64.4 m thick and consists of nannofossil ooze with clay and varying amounts of foraminifera. Subunit IVB comprises up to 6.1 m of nannofossil ooze with clay and decimeter-thick beds of calcareous ooze. Subunit IVC is up to 24.4 m thick and consists of nannofossil ooze with clay and varying amounts of foraminifera.

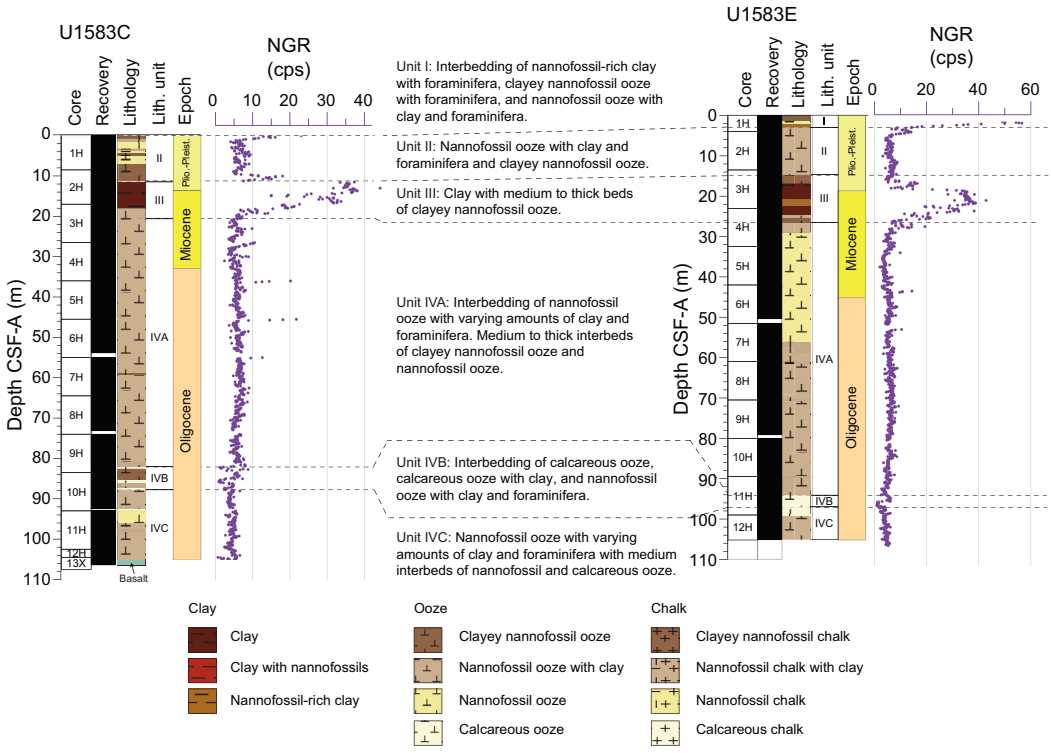

Figure F6. Lithostratigraphic summary of sediment units and correlation of full sediment sequences, Holes U1583C and U1583E. For epochs, see Age model and mass accumulation rates. For unit contact depths and thicknesses, see Table T2. Dashed lines = correlation between units. cps = counts per second.

3.2. Volcanic sequences

Both Holes U1583C and U1583F intersected a ~11 m thick massive lava flow at 107.5 and 109.7 mbsf, respectively, which is about 30 m shallower than predicted by seismic site surveys (Kardell et al., 2019). Only Hole U1583F advanced deeply into basement, reaching 239.6 mbsf or 129.8 meters subbasement (msb) with ~30% average recovery (Figure **F7**; Table **T4**).

Hole U1583F intersected three volcanic sequences (A, B, and C), with 62, 35, and 33 m expanded thicknesses, respectively, separated by two sedimentary breccia units (4 and 6) with thicknesses estimated between 0.8 and 3.4 m (Figure **F7**; Table **T4**). The upper Sequence A (109.7–171.6 mbsf) consists of Unit 1, which is an 11 m thick massive lava flow; Unit 2, which is made of moderately phyric pillow lavas and sheet flows; and Unit 3, which is composed of aphyric pillow lavas and sheet flows that are markedly more primitive than all of the other units in the hole (Table **T4**). The middle Sequence B is capped by sedimentary breccia Unit 4 and additionally consists of moderately phyric pillow basalts (Subunits 5A and 5C) and another thin breccia horizon (Subunit 5B). The lower Sequence C is again capped by a sedimentary breccia (Unit 6) above sparsely to moderately phyric pillow basalts that are chemically and lithologically similar to Sequence B. Volcanic clasts within the sedimentary breccias (Units 4 and 6) are consistent with derivation from the immediately underlying lava flows (Subunits 5A and 7A).

Lava composition assessed by portable X-ray fluorescence (pXRF) varies both gradationally and in a stepwise fashion across petrologically defined unit boundaries. Incompatible element concentrations and Zr/Ti ratios are consistent with a relatively primitive, normal mid-ocean-ridge basalt (N-MORB)-like composition for the lavas at Site U1583. In contrast to the sequence stratigraphy defined by the presence of sedimentary breccias, pXRF measurements reveal that Unit 3 has a uniquely primitive composition in Hole U1583F, splitting the hole into three major chemostratigraphic packages: Igneous Units 1 and 2, 3, and 5–7.

3.3. Sediment/basement interface

Expedition 393 Holes U1583C and U1583F recovered basement volcanic rocks that were encountered ~30 m shallower than predicted from the seismic site survey (Coggon et al., 2020) at 107.5 and 109.7 mbsf (drilling depth below seafloor [DSF] scale), respectively. The interface was not

Table T2. Sedimentary units and subunits, contacts, and thicknesses, Site U1583. * = Unit II/III boundary lies in a core section taken for microbiology and interstitial water samples. Therefore, unit boundaries were moved to the midpoint between recovered cores, in this case, extended by 15 cm for each unit. **Download table in CSV format.**

Unit	Hole	Depth (mbsf)	Thickness (m)	Age	Core, section, interval (cm)	Lithologic summary
	393-					
I	U1583E	0.0–3.0	3.00	Pliocene/Pleistocene	1H-1, 0, to 1H-2, 150	Interbedded brown (7.5YR 5/4) nannofossil-rich clay with foraminifera and light brown (7.5YR 6/4) clayey nannofossil ooze with foraminifera with a few beds of pink (7.5YR 7/3) nannofossil ooze with foraminifera.
	U1583D	0.0–1.0	1.00		1H-1, 0, to 1H-1, 99	
II	U1583B	0.0–5.4	5.4	Pliocene/Pleistocene	1H-1, 0, to 1H-4, 94	Interbedded pink (7.5YR 73-7/4) nannofossil ooze with clay and foraminifera with decimeter-scale beds of light brown (7.5YR 6/4) nannofossil ooze with clay.
	U1583C	0.0–11.3*	11.3*		1H-1, 0, to 2H-2, 135	
	U1583D	1.0–10.0	9		1H-1, 99, to 1H-CC, 22	
	U1583E	3.0–14.6	11.6		1H-2, 150, to 3H-1, 114	
III	U1583A	0.0–1.2	>1.2	Middle to Early Miocene	1H-1, 0, to 1H-1, 122	Dark brown (7.5YR 3/3) to brown (7.5YR 5/3-4/4) clay and brown (7.5YR 5/3-4/4) to light brown (7.5YR 6/4) nannofossil ooze with varying amounts of clay, becoming interbedded nannofossil ooze with clay and clayey nannofossil ooze in the lower 3 m.
	U1583B	5.4–9.4	>4.9		1H-4, 60, to 1H-CC, 14	
	U1583C	11.3*–19.4	>8.1*		2H-2, 135, to 3H-2, 86	
	U1583E	14.6–26.5	11.9		3H-1, 114, to 4H-3, 45	
IVA	U1583A	2.7–9.1	6.4	Early Miocene to early Oligocene	1H-2, 122, to CC, 19	Pink (7.5YR 7/4), brown (7.5YR 5/4), light brown (7.5YR 6/4-6/3), to very pale brown (10YR 7/4) nannofossil ooze with clay with varying amounts of foraminifera.
	U1583C	19.4–82.0	62.6		3H-2, 86, to 9H-6, 51	
	U1583E	26.5–90.9	64.4		4H-3, 45, to 11H-4, 7	
IVB	U1583C	82.0–87.8	5.8	early Oligocene	9H-6, 51, to 10H-3, 123	Pink (7.5YR 7/3-7/4) to light brown (7.5YR 6/4) nannofossil ooze with clay with decimeter to meter thick beds of pinkish white (7.5YR 8/2) calcareous ooze.
	U1583E	90.9–97.0	6.1		11H-4, 7, to 11H-CC, 20	
IVC	U1583C	87.8–110.2	24.4	early Oligocene	10H-3, 123, to 12H-CC, 17	Light brown (7.5YR 6/4) to pink (7.5YR 7/4) nannofossil ooze with clay and varying amounts of foraminifera.
	U1583E	97.0–105.1	8.1		11H-CC, 20, to 12H-5, 59	
	U1583F	101.0–107.4	6.4		2R-1, 0, to 2R-CC, 19	

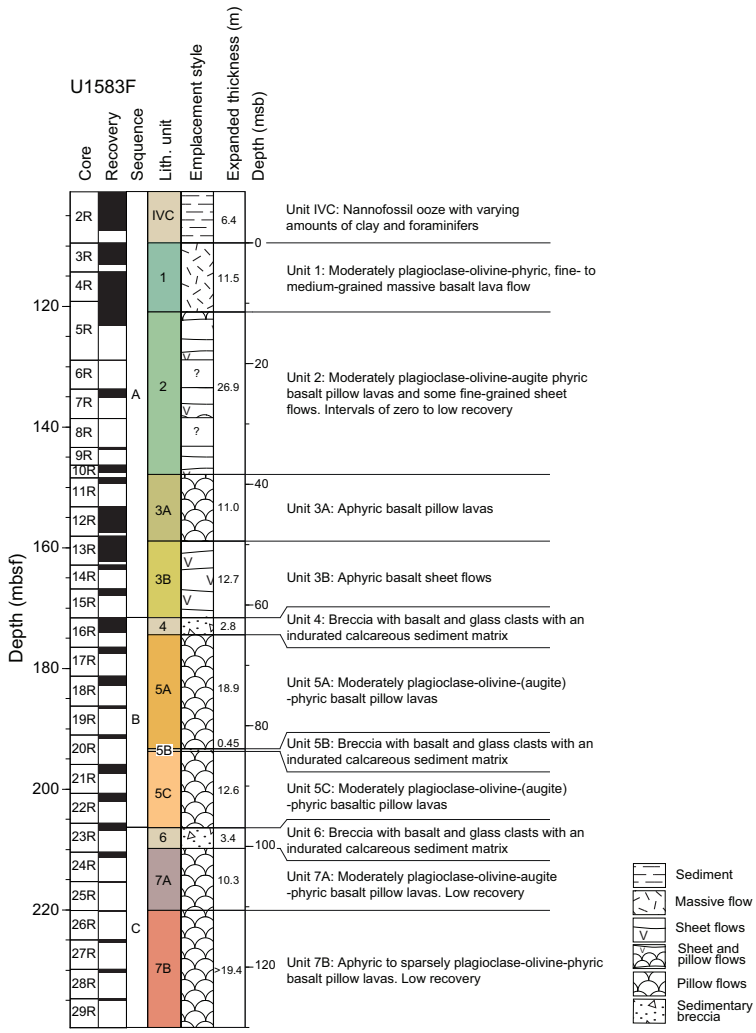

Figure F7. Lithostratigraphic summary of volcanic units, Hole U1583F. Unit contact depths and thicknesses are expanded to account for <100% recovery (see Table T4 for curated and expanded contact depths).

recovered in either hole; however, based on what was recovered, it is thought to consist of sediments of unknown lithification directly overlying the glassy, chilled top of a massive lava flow that extends over the entire site. The depth at which basement was encountered during drilling of the deepest hole (U1583F) at 109.7 mbsf (DSF scale) is taken as the sediment/basement interface depth for Site U1583.

4. Sedimentology

Two of the six holes at Site U1583 cored the majority of the sediment section: Hole U1583C missed the mudline but was cored to basement and Hole U1583E recovered the mudline but was stopped a few meters above basement (Figure **F8**). Hole U1583F recovered 6.43 m of sediments in Core 2R above the sediment/basement interface (Figure **F8**) before changing to RCB coring in this hole. Holes U1583A, U1583B, and U1583D all missed the mudline and were single-core holes (Figure **F8**). The uppermost sediments are represented by Pliocene–Pleistocene nannofossil ooze with clay (see **Age model and mass accumulation rates** for the ages) underlain by a condensed Pleistocene to Middle Miocene interval consisting of clay and nannofossil-rich clay, below which Middle Miocene to Oligocene nannofossil oozes with clay and varying foraminiferal abundances were recovered. The clay-rich interval is interpreted to reflect a change in the seafloor position relative to the carbonate compensation depth (CCD), which could be due to deepening of the CCD with

time and/or thermal or tectonic movement of the basement at this location. In contrast, the nannofossil oozes were deposited when the CCD was deeper than the seafloor.

The sediments are divided into four lithostratigraphic units (I–IV; youngest to oldest) based on sediment composition in smear slides and visual core description (Figures **F8**, **F9**, **F10**, **F11**, **F12**, **F13**). The lowermost unit is divided into three subunits (IVA–IVC) based on the appearance of white calcareous ooze, which divides the two sections of nannofossil ooze with varying amounts of clay and foraminifera. This division is supported by macroscopic and microscopic interpretations as well as $CaCO_3$ weight percent and other physical properties data.

4.1. Unit descriptions

4.1.1. Unit I

Intervals: 393-U1583D-1H-1, 0 cm, to 1H-1, 99 cm; 393-U1583E-1H-1, 0 cm, to 1H-2, 150 cm
Depths: Hole U1583D = 0.0–1.0 m core depth below seafloor, Method A (CSF-A); Hole U1583E = 0.0–3.0 m CSF-A
Thickness: Hole U1583D = >1.0 m; Hole U1583E = 3.0 m
Age: Pliocene–Pleistocene
Lithology: interbedded nannofossil-rich clay with foraminifera and nannofossil ooze with clay and foraminifera

Lithostratigraphic Unit I is composed of centimeter- to decimeter-scale interbeds of brown nannofossil-rich clay with foraminifera, light brown clayey nannofossil ooze with foraminifera, and pink nannofossil ooze with clay and foraminifera (Figures **F8**, **F9**, **F10**, **F11**, **F12**). The characteristic high mud content of this unit is supported by high natural gamma radiation (NGR) and low light reflectance values (Figure **F9**). This unit was partially recovered in Hole U1583D (0–1.0 m) and fully recovered in Hole U1583E.

Lithologic contacts in Unit I are bioturbated and horizontal. Mottling is the dominant sedimentary structure (Figure **F11**). Biogenic mottling is common, with distinct ichnofossils identified that include *Planolites, Thalassinoides, Skolithos*, and *Zoophycos* (Figure **F13**). Bioturbation intensity is

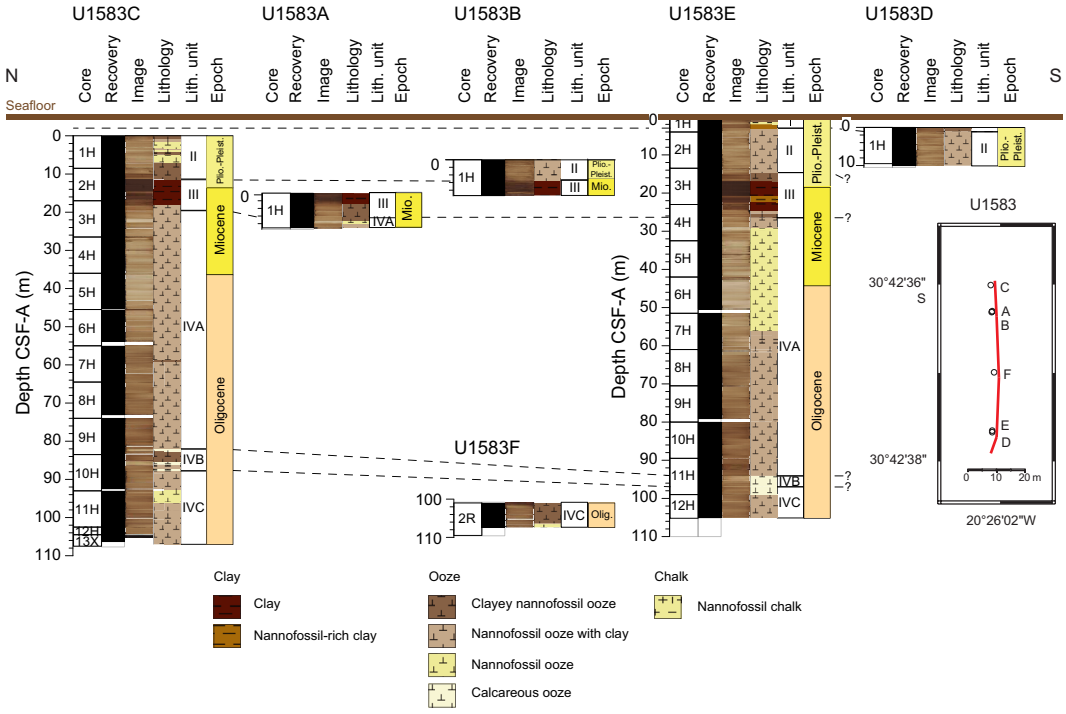

Figure F8. Lithologic correlation of sediment holes, Site U1583. For epochs, see Age model and mass accumulation rates. Dashed lines = correlation between units. Bottom right: map with positions of each hole relative to one another.

absent to intense (bioturbation index [BI] = 0–5). Ichnofossil diversity ranges 1–3 ichnogenera, with a maximum diameter ranging 4–12 mm (Figure **F13**).

The primary minerals identified using bulk X-ray diffraction (XRD) in Unit I include calcite, quartz, plagioclase, and clay minerals such as illite, smectite, and chlorite (Figure **F14**; Table **T3**). Calcite and quartz form the main peaks in this unit, with the calcite peak being the largest. In the clay-rich beds, feldspar, illite, and chlorite are present. The smectite peak at 5.6°2θ is identified in all samples of this unit.

The lithologic boundary between Units I and II is marked by an abrupt decrease in clay content and a brightening in sediment color coupled with a decrease in magnetic susceptibility (MS) (Figure **F9**).

4.1.2. Unit II

Intervals: 393-U1583B-1H-1, 0 cm, to 1H-4, 60 cm; 393-U1583C-1H-1, 0 cm, to 2H-2, 135 cm; 393-U1583D-1H-1, 99 cm, to 1H-CC, 22 cm; 393-U1583E-1H-2, 150 cm, to 3H-1, 114 cm
Depths: Hole U1583B = 0.0–0.9 m CSF-A; Hole U1583C = 0.0–11.3 m CSF-A; Hole U1583D = 1.0–10.0 m CSF-A; Hole U1583E = 3.0–14.6 m CSF-A

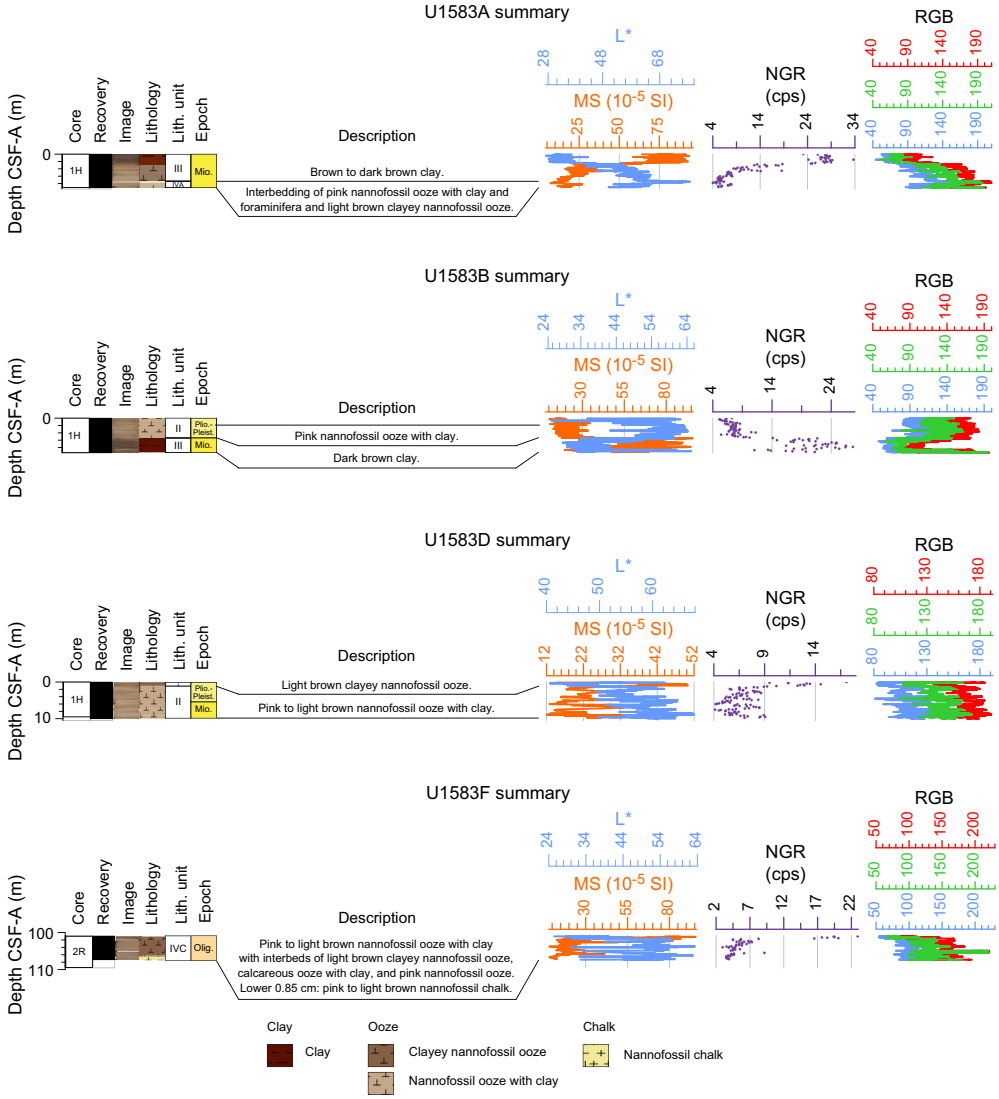

Figure F9. Lithologic summaries, Site U1583. For epochs, see Age model and mass accumulation rates. cps = counts per second, RGB = red-green-blue. (Continued on next page.)

Thickness: Hole U1583B = >0.9 cm; Hole U1583C = >11.3 m; Hole U1583D = >9.0 m; Hole U1583E = 11.6 m
Age: Pliocene–Pleistocene
Lithology: nannofossil ooze with varying amounts of clay and foraminifera

Lithostratigraphic Unit II consists of interbedded pink nannofossil ooze with varying amounts of clay and foraminifera with light brown clayey nannofossil ooze (Figures **F8**, **F9**, **F10**, **F11**, **F12**, **F13**). Low NGR values, relatively low MS, and high reflectance data (L*) characterize this unit (Figure **F9**). The foraminifera content generally ranges between 10% and 25% except in darker intervals, such as light brown nannofossil ooze with clay and clayey nannofossil ooze, where foraminifera content falls below 10%. In the lowermost 1.5 m of this unit, the sediment darkens to

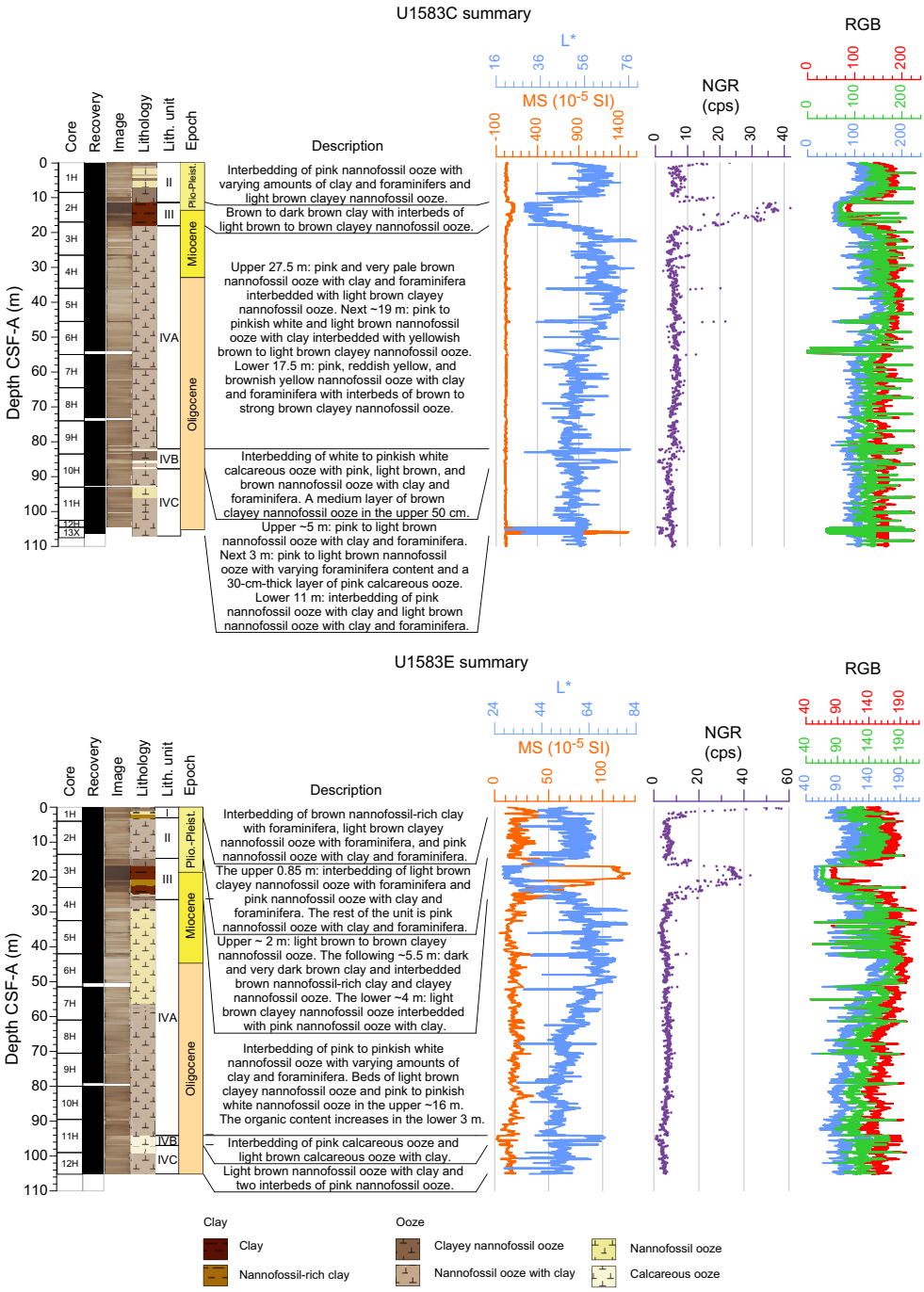

Figure F9 (continued).

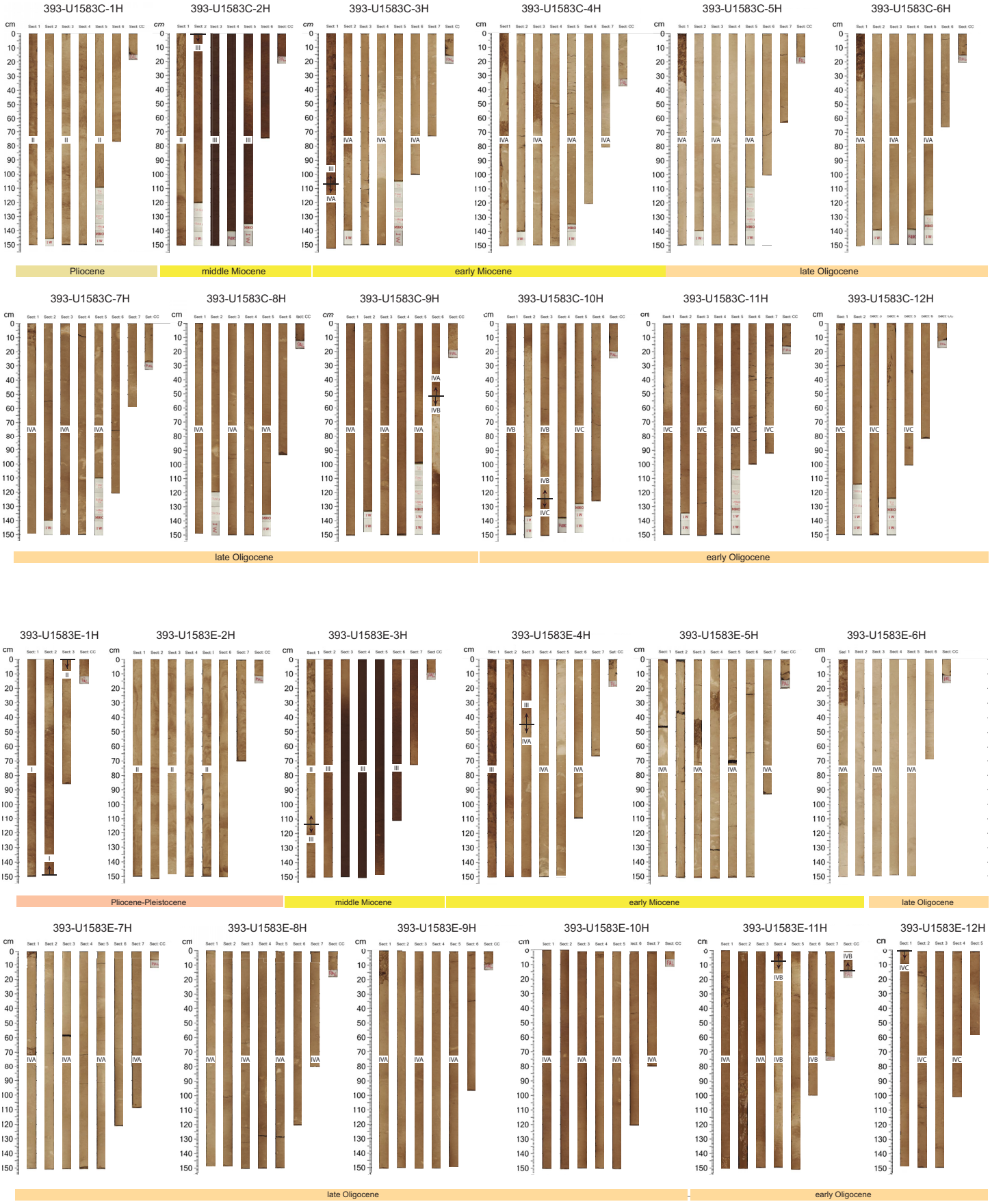

Figure F10. Ages and units, Holes U1583C and Hole U1583E.

brown as clay content increases. This increase is supported by an increase in NGR and higher MS values coupled with lower light reflectance (L*) values (Figure **F9**). This increase in clay and decrease in carbonate content is interpreted to reflect a change in the seafloor position relative to the CCD. Here specifically, this could be deepening of the CCD with time and/or thermal or tectonic movement of the basement.

Mottling and massive bedding are the primary sedimentary structures (Figures **F11**, **F13**). Pinkish white halos (2–2.5 cm) and rare small black blebs (probably iron or manganese oxides) are present throughout this unit. Biogenic mottling is common, with bioturbation intensity ranging from absent to intense (BI = 0–5). Distinct ichnogenera were identified and include *Planolites, Thalassinoides, Chondrites*, and more rarely *Skolithos* and *Nereites* (Figure **F13**). Ichnogenera diversity ranges 1–4, with the maximum ichnofossil diameter ranging 3–28 mm (Figure **F13**).

The primary minerals identified with bulk XRD in Unit II include calcite, quartz, plagioclase, and clay minerals such as illite and smectite (Figure **F14**; Table **T3**). Calcite and quartz form the dominant peaks, with calcite having the largest peak.

Severe drilling disturbances occurred in large portions of Unit II. These disturbances resulted in complete disruption of more than half of the sediments in Core 393-U1583E-2H. The lithologic boundary between Units II and III is marked by an abrupt lithologic change from light brown nannofossil ooze with clay and foraminifera above to dark brown clay below, which is interpreted to be an abrupt deepening of the CCD with time across this unit boundary and/or thermal or tectonic movement of the basement (Figures **F8**, **F9**).

4.1.3. Unit III

Intervals: 393-U1583A-1H-1, 0 cm, to 1H-1, 122 cm; 393-U1583B-1H-4, 60 cm, to 1H-CC, 14 cm; 393-U1583C-2H-2, 135 cm, to 3H-2, 86 cm; 393-U1583E-3H-1, 114 cm, to 4H-3, 45 cm

Depths: Hole U1583A = 0.0–1.2 m CSF-A; Hole U1583B = 4.5–9.4 m CSF-A; Hole U1583C = 11.35–19.4 m CSF-A; Hole U1583E = 14.6–26.5 m CSF-A

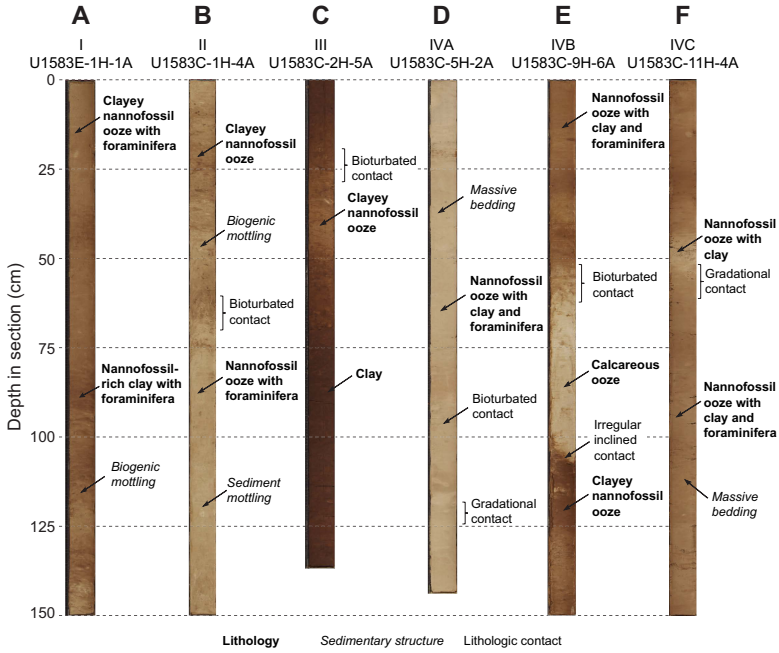

Figure F11. Typical lithologies of each unit, Site U1583. A. Unit I alternating nannofossil-rich clay with foraminifera and nannofossil ooze with clay and foraminifera. B. Unit II nannofossil ooze with varying amounts of clay and foraminifera. C. Unit III clay with varying amounts of nannofossils and clayey nannofossil ooze. D. Subunit IVA nannofossil ooze with varying amounts of clay and foraminifera. E. Subunit IVB alternating calcareous ooze and nannofossil ooze with clay and foraminifera. F. Subunit IVC nannofossil ooze with varying amounts of clay and foraminifera.

Thickness: Hole U1583A = >1.2 m; Hole U1583B = >4.9 m; Hole U1583C = 8.0 m; Hole U1583E = 11.8 m
Age: Middle to Early Miocene
Lithology: clay with varying amounts of nannofossils and clayey nannofossil ooze

Lithostratigraphic Unit III in Hole U1583C consists of brown to dark brown clay with interbeds of light brown to brown clayey nannofossil ooze (Figures **F8**, **F9**, **F10**, **F11**, **F12**, **F13**). Foraminifera content is consistently below 10%. Its composition is more complex in Hole U1583E, where the upper ~2 m is light brown to brown clayey nannofossil ooze and the underlying ~5.5 m is predominantly dark to very dark brown clay with interbedded brown nannofossil-rich clay and clayey nannofossil ooze. The lowermost ~4 m consists of light brown clayey nannofossil ooze with decimeter-scale beds of pink nannofossil ooze with clay.

Lithologic contacts are bioturbated to gradational. Bedding is massive, and mottling is common in this unit. In addition, rare, small (0.5 cm) black blebs occur. (probably the manganese/iron oxides identified by XRD; Table **T3**) Bioturbation intensity in Unit III ranges from absent to intense (BI = 0–5), with distinct ichnogenera identified as *Planolites, Skolithos, Chondrites, Zoophycos*, and more rarely *Thalassinoides, Helminthopsis*, and *Phycosiphon* (Figure **F13**). Trace fossil diversity ranges 1–6, and the maximum ichnofossil diameter ranges 3–23 mm (Figure **F13**).

The primary minerals identified with bulk XRD in Unit III include quartz, feldspar, plagioclase, and clay minerals such as illite, smectite, kaolinite, and chlorite (Figure **F14**; Table **T3**). Calcite and quartz form the main peaks in this unit, where the calcite peak is the largest. In the clay-prone beds, quartz, illite, and feldspars form the dominant peaks.

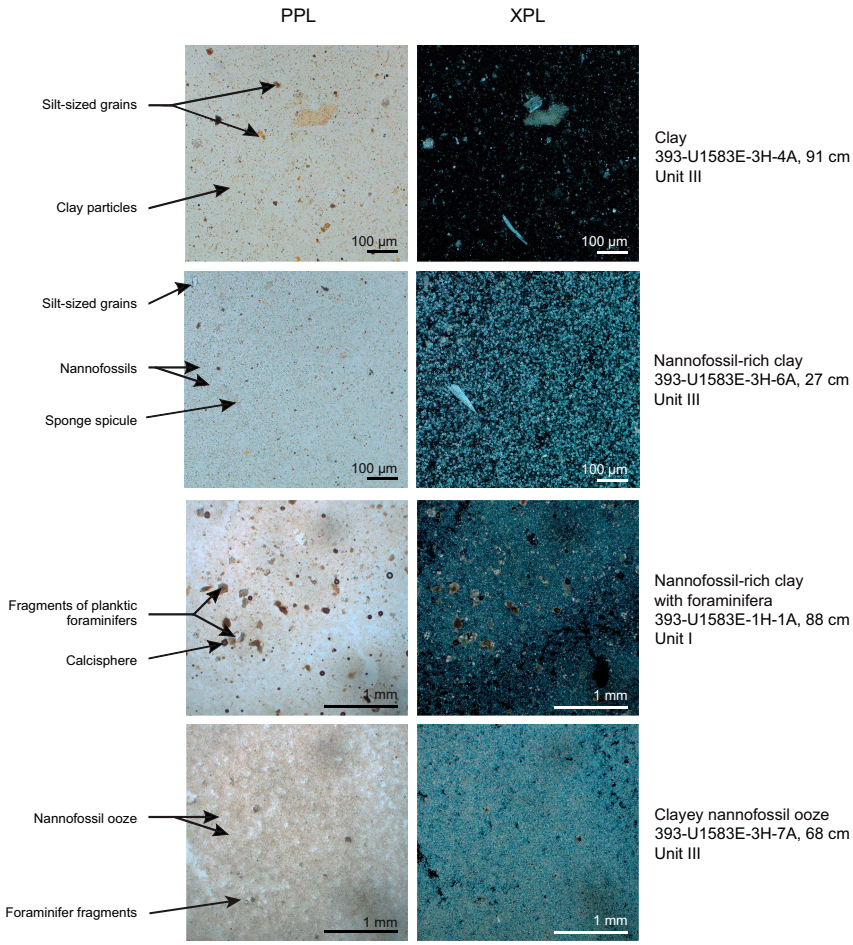

Figure F12. Principal sediment types, Site U1583. Nannofossil-rich clays and nannofossil oozes/chalks. PPL = plane-polarized light, XPL = cross-polarized light. (Continued on next page.)

The boundary between Unit III and Subunit IVA is characterized by a dramatic decrease in clay content, an increase in MS, and lighter sediment colors (Figure **F8**, **F9**, **F10**), which is interpreted to be a change in the seafloor position relative to the CCD. Here specifically, this could be an abrupt shallowing of the CCD with time across this unit boundary and/or thermal or tectonic movement of the basement.

4.1.4. Unit IV

Intervals: 393-U1583A-1H-2, 122 cm, to 1H-CC, 19 cm; 393-U1583C-3H-2, 86 cm, to 12H-CC, 17 cm; 393-U1583E-4H-3, 45 cm, to 12H-5, 59 cm; 393-U1583F-2R-1, 0 cm, to 2R-CC, 19 cm
Depths: Hole U1583A = 2.7–9.1 m CSF-A; Hole U1583C = 18.1–110.2 m CSF-A; Hole U1583E = 26.5–105.1 m CSF-A; Hole U1583F = 101.0–107.4 m CSF-A
Thickness: Hole U1583A = 6.4 m; Hole U1583C = 90.9 m; Hole U1583E = 78.6 m; Hole U1583F = 6.4 m
Age: Early Miocene to early Oligocene
Lithology: nannofossil ooze with varying clay and foraminifera content

Lithostratigraphic Unit IV is predominantly composed of pink to pinkish white nannofossil ooze with varying amounts of clay and foraminifera (Figures **F8**, **F9**, **F10**, **F11**, **F12**, **F13**). Foraminiferal abundances generally range from rare (<10%) to common (10%–25%). Several decimeter-thick beds of calcareous ooze occur between 82.0 and 87.8 m CSF-A in Hole U1583C and between 90.9 m and 97.0 m CSF-A in Hole U1583E.

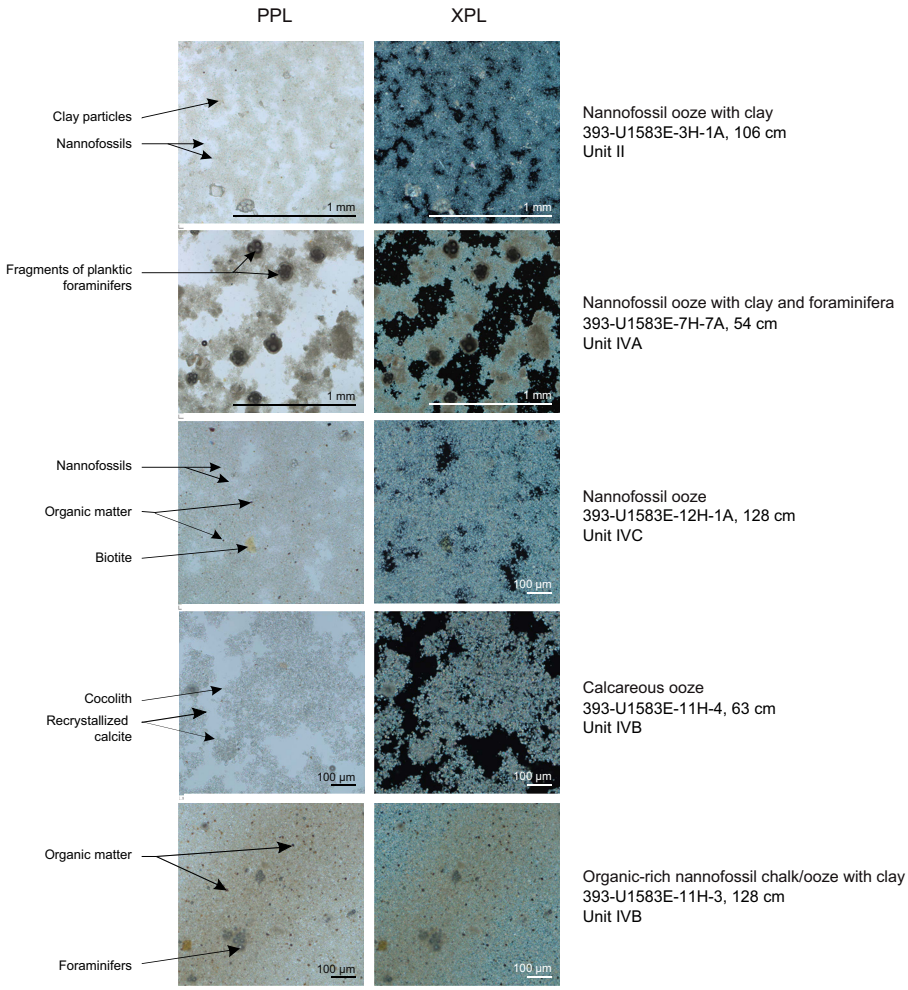

Figure F12 (continued).

Lithologic contacts in Unit IV are typically gradational to bioturbated, horizontal to inclined, and curved (the latter two may be due to slight drilling disturbances). Massive bedding is dominant in the upper ~30 m in this unit, with mottling dominating the lower part (Figure **F11**). No discernible breaks in the lithology and no hiatuses were identified (see **Biostratigraphy**). Biogenic mottling is common throughout this unit, with the bioturbation index ranging from absent to complete (BI = 0–6) and averaging between sparse and moderate (BI = 1–3) (Figure **F13**). In addition, distinct ichnogenera identified in this unit include *Planolites, Thalassinoides, Chondrites, Zoophycos, Skolithos*, and more rarely *Palaeophycus* and *Arenicolites* (Figure **F13**).

XRD and CARB data indicate uniform mineralogy in Unit IV. Calcite dominates the mineral assemblage with terrigenous minerals such as quartz, plagioclase, and clay minerals constituting minor components of this unit (Figure **F14**; Table **T3**). The smectite peak at 5.6°2θ remains fairly constant throughout Unit IV. Slight variations in relative peak intensities of quartz, feldspar, illite, kaolinite, and chlorite suggest minor changes in the relative amount of the other terrigenous components.

Unit IV is divided into three subunits (IVA–IVC) that are described below.

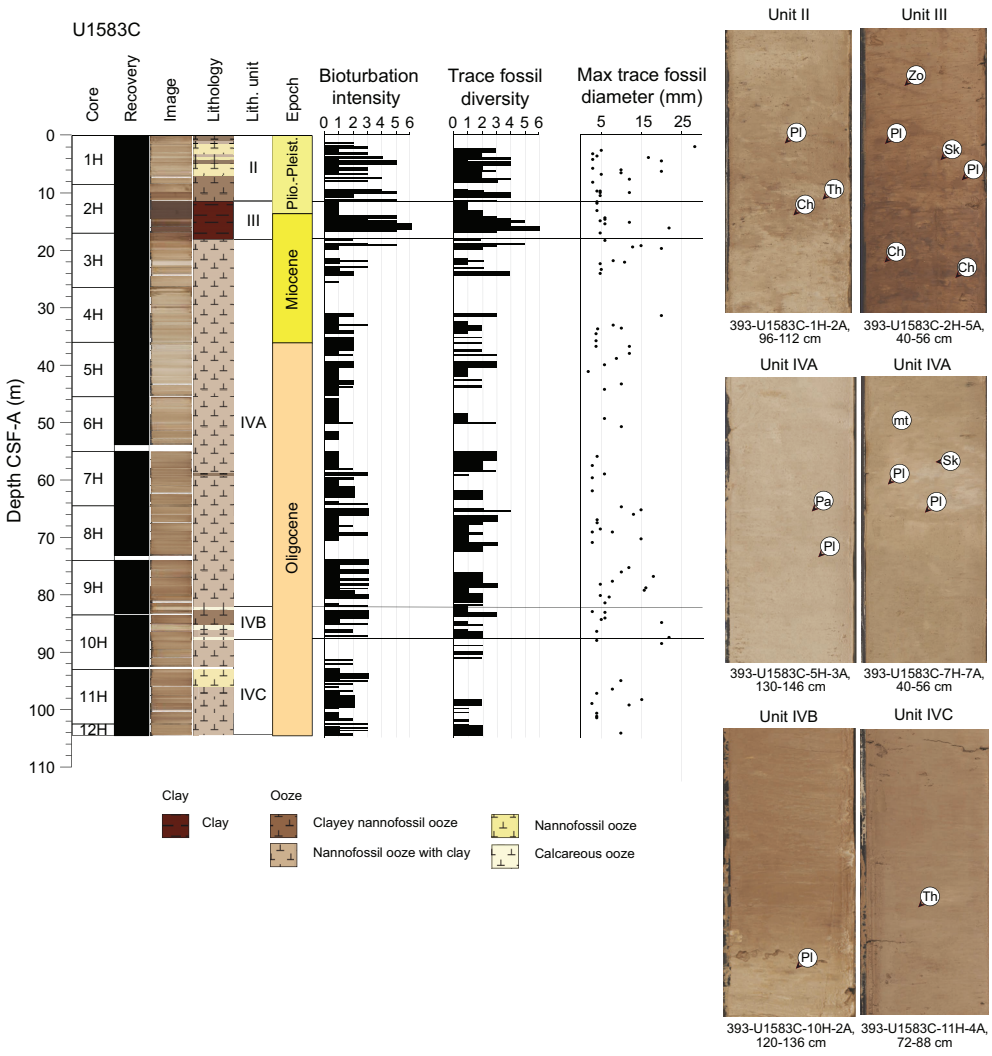

Figure F13. Characterization of bioturbation signatures and core photographs of typical trace fossil assemblages for each unit, Holes U1583C and Hole U1583E. For epochs, see Age model and mass accumulation rates. Zo = *Zoophycos*, Pl = *Planolites*, Th = *Thalassinoides*, Ch = *Chondrites*, Sk = *Skolithos*, Pa = *Palaeophycus*, mt = biogenic mottling, Ne = *Nereites*. (Continued on next page.)

4.1.4.1. Subunit IVA

Intervals: 393-U1583A-1H-2, 122 cm, to 1H-CC, 19 cm; 393-U1583C-3H-2, 86 cm, to 9H-6, 51 cm; 393-U1583E-4H-3, 45 cm, to 11H-4, 7 cm
Depths: Hole U1583A = 2.7–9.1 m CSF-A; Hole U1583C = 19.4–82.0 m CSF-A; Hole U1583E = 26.5–90.9 m CSF-A
Thickness: Hole U1583A = 6.4 m; Hole U1583C = 62.6 m; Hole U1583E = 64.5 m
Age: Early Miocene to early Oligocene
Lithology: nannofossil ooze with varying clay and foraminifera content

The upper 27.5 m in Hole U1583C and ~35 m in Hole U1583E of Subunit IVA are pink and very pale brown nannofossil ooze with clay and foraminifera with centimeter-scale interbeds of light brown clayey nannofossil ooze (Figures **F10**, **F12**). The underlying ~19 m in Hole U1583C and ~10 m in Hole U1583E constitute pink to pinkish white, very pale brown, light yellowish brown, and light brown nannofossil ooze with clay interbedded with centimeter- to decimeter-scale yellowish brown to light brown clayey nannofossil ooze (Figures **F10**, **F12**). The lower 17.5 m in Hole U1583C and ~23 m in Hole U1583E predominantly consist of pink, reddish yellow, and brownish yellow nannofossil ooze with clay and foraminifera with centimeter-scale interbeds of brown to dark brown clayey nannofossil ooze (Figure **F12**). Foraminifera content varies in this subunit: common (10%–25%) in the upper 27.5 m in Hole U1583C and ~35 m in Hole U1583E, rare (<10%)

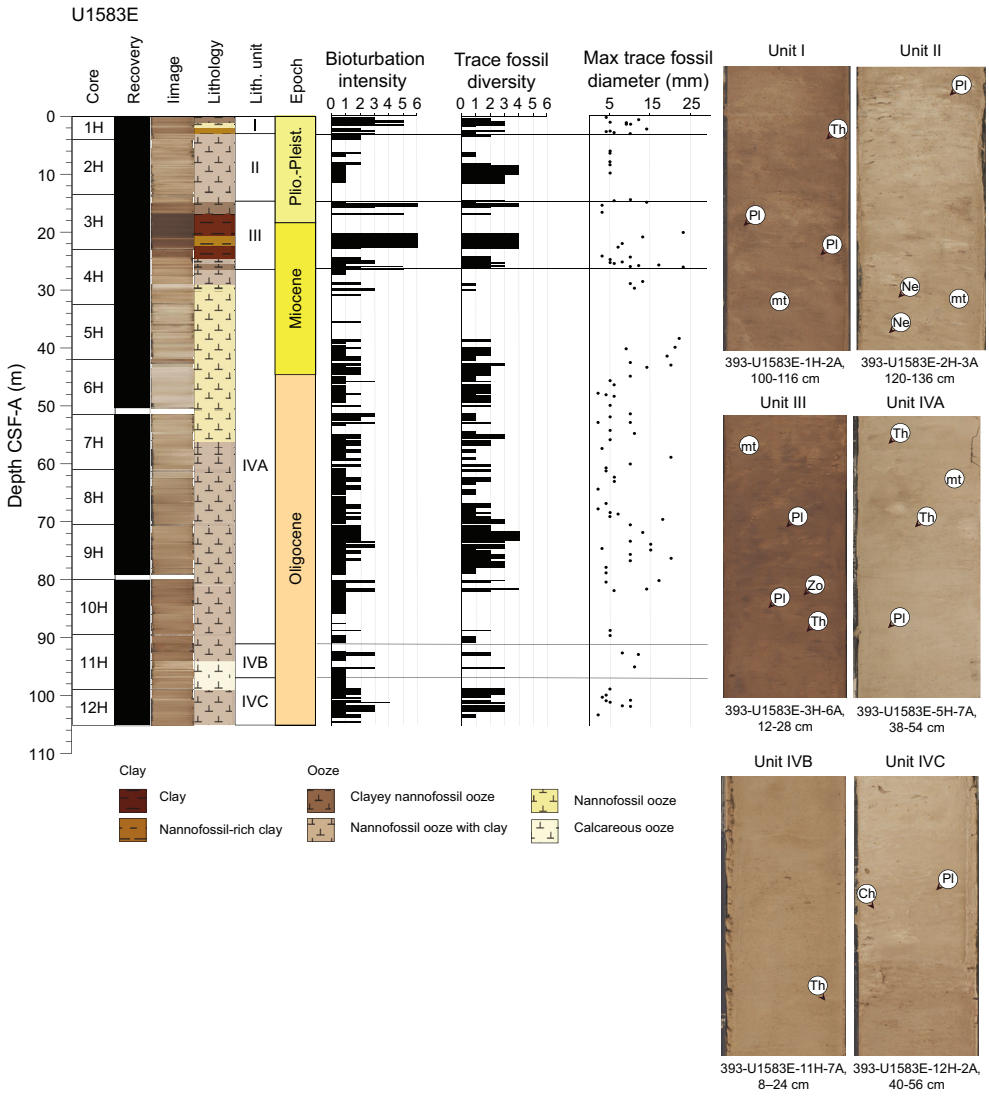

Figure F13 (continued).

in the middle ~19 m in Hole U1583C and ~10 m in Hole U1583E, and common (10%–25%) again in the lower 17.5 m in Hole U1583C and ~23 m in Hole U1583E.

Most lithologic contacts are gradational, although the lower contacts of clayey nannofossil ooze beds can be sharp to irregular. The bedding is typically massive, and mottling is common (Figure **F11**). Pinkish white halos and lenses (2–4 cm in diameter) sporadically occur throughout Subunit IVA. Ichnofossils were identified within decimeter-thick beds and include *Thalassinoides, Planolites, Skolithos, Chondrites*, and rarely *Arenicolites* and *Zoophycos* (Figure **F13**). Bioturbation

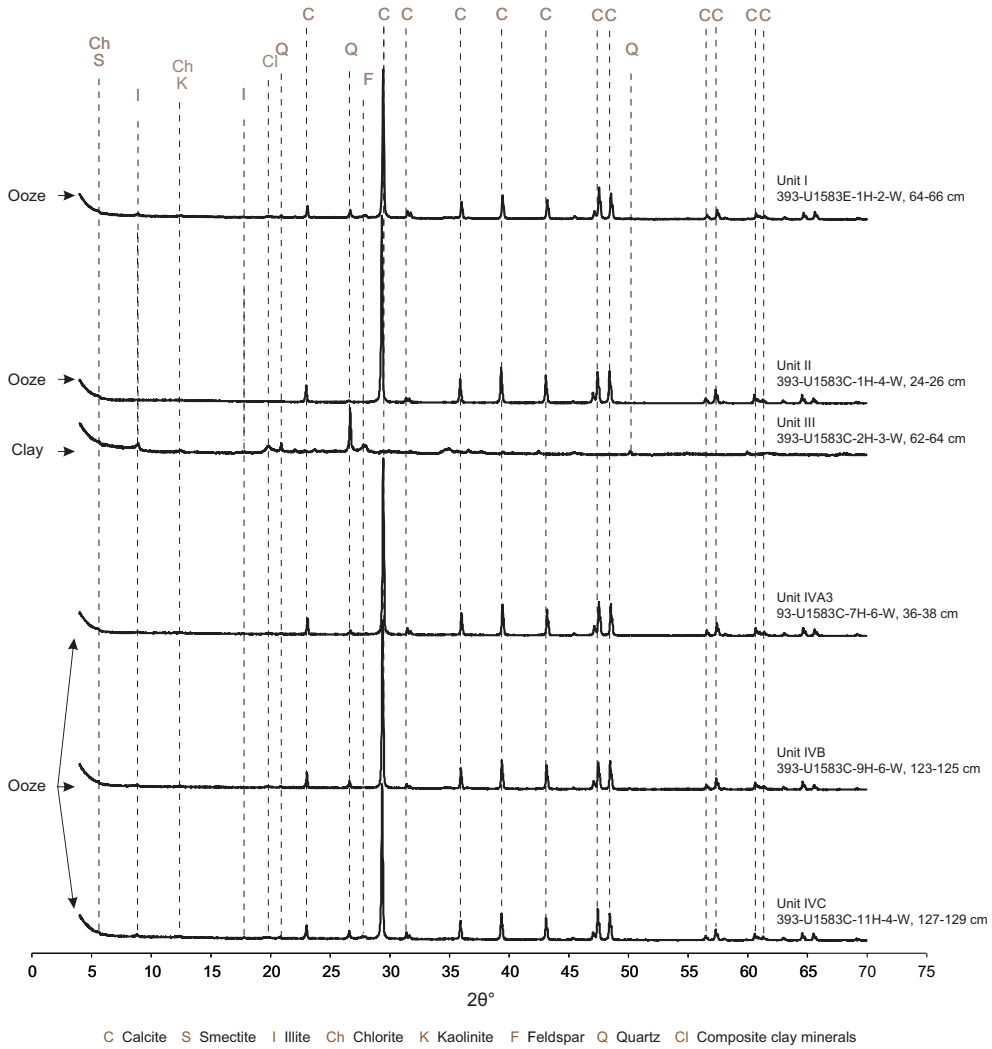

Figure F14. Representative X-ray diffractograms of bulk sediments, Holes U1583C and U1583E.

Table T3. XRD qualitative estimation of main mineralogical components, Hole U1583C. XRD analysis of Unit I was performed for Hole U1583E. * = approximate depth/thickness because of microbiological whole-round sampling across boundary between lithostratigraphic units. **Download table in CSV format.**

Lith. unit	Lithologic description	Depth range CSF-A (m)	Thickness (m)	Dominant peak(s)	Secondary peaks
I	Interbedded nannofossil-rich clay with foraminifera and nannofossil ooze with clay and foraminifera	0.00–3.0	3.0	Calcite, Quartz	Feldspar, Illite, Smectite, Chlorite
II	Nannofossil ooze with varying amounts of clay and foraminifera	0.0–11.3*	11.3*	Calcite, Quartz	Feldspar, Smectite
III	Clay with varying amounts of nannofossils and clayey nannofossil ooze	11.3*–18.1	6.7*	Quartz, Calcite	Feldspar, Mg/Fe oxides, Illite, Smectite, Chlorite, Kaolinite
IVA	Nannofossil ooze with varying clay and foraminifera	8.1–82.0	64.0	Calcite, Quartz	Illite, Smectite, Kaolinite, Feldspars
IVB	Alternating calcareous ooze and nannofossil ooze with clay and foraminifera	82.0–87.8	5.7	Calcite	Quartz, Smectite, Illite, Kaolinite
IVC	Nannofossil ooze with varying amounts of clay and foraminifera	Hole C: 87.8–110.2	22.8	Calcite	Quartz, Smectite, Illite, Kaolinite

intensity varies from absent to intense (BI = 0–5) and is predominantly sparse to moderate (BI = 1–3) (Figure **F13**). Ichnofossil diversity ranges 1–4 ichnogenera and averages 2. The maximum trace fossil diameter ranges 2–22 mm (Figure **F13**).

XRD and carbonate (CARB) data indicate that calcite and quartz are the main minerals constituting Subunit IVA, with calcite being the most abundant (Figure **F14**; Table **T3**). The irregular presence of plagioclase (27.8°–28.0°2θ) and kaolinite (~12.4°–19.8°2θ) peaks suggests changes in the relative amount of these minerals throughout this subunit. Illite is present in all samples, although variations in illite peak intensities at ~8.9°2θ may indicate changes in the abundance of this mineral.

Drilling disturbances occurred within this subunit in Hole U1583E that resulted in severely destroyed sediments, primarily in the upper decimeters to 1 m of Sections 393-U1583E-6H-1, 7H-1, and 9H-1 as well as in Section 5H-1 through Core 4H. The boundary between Subunits IVA and IVB is defined by the first occurrence of white calcareous beds and a decrease in foraminiferal abundances.

4.1.4.2. Subunit IVB

Intervals: 393-U1583C-9H-6, 51 cm, to 10H-3, 123 cm; 393-U1583E-11H-4, 7 cm, to 11H-CC, 20 cm
Depths: Hole U1583C = 82.0–87.8 m CSF-A; Hole U1583E = 90.9–97.0 m CSF-A
Thickness: Hole U1583C = 5.7 m; Hole U1583E = 6.0 m
Age: early Oligocene
Lithology: alternating calcareous ooze and nannofossil ooze with clay and foraminifera

Subunit IVB represents decimeter- to meter-thick interbedding of white to pinkish white calcareous ooze with pink, light brown, and brown nannofossil ooze with clay and foraminifera (Figures **F10**, **F11**, **F12**). In addition, decimeter-thick beds of brown nannofossil ooze with clay occur between the two upper calcareous ooze beds. Foraminiferal content is <10% for the calcareous ooze and the brown nannofossil ooze with clay and ranges between 10% and 25% for the pink and light brown nannofossil ooze with clay and foraminifera.

Lithologic contacts between the light brown nannofossil ooze with clay and calcareous ooze and brown nannofossil ooze with clay are typically sharp, often curved likely due to drilling disturbance (Figure **F11**), and rarely bioturbated. In contrast, color changes from pink to light brown nannofossil ooze with clay are gradational. The decimeter- to meter-thick beds of darker (e.g., brown versus light brown) nannofossil ooze with clay appear to contain organic particles based on smear slide observations (Figure **F12**). In addition, NGR values remain relatively low for these brown sediments compared to the sediments with a similar Munsell color (i.e., brown; 7.5YR 5/4) at Site U1558. For example, a similar lithology and color (brown; 7.5YR 5/4) at Site U1558 occurs between 111.9 and 112.4 m CSF-A (interval 393-U1558F-16F-2, 0 cm, to 16F-2, 50 cm) and contains NGR values ranging 13–29 counts/s (see **Physical properties and downhole measurements** in the Site U1558 chapter [Teagle et al., 2024a]). In comparison, NGR values for this brown nannofossil ooze with clay at Site U1583 range 2–6 counts/s (Figure **F9**; see **Physical properties and downhole measurements**). In addition, the $CaCO_3$ weight percent value for this brown interval in Hole U1583C remains relatively high (72 wt%). We hypothesize that 1–10 wt% disseminated organic matter may cause darker coloration of the sediments.

Mottling and massive bedding are common in this subunit. Biogenic mottling is pervasive, with the bioturbation index ranging from absent to moderate (BI = 0–3). Distinct ichnogenera are present and include *Planolites, Skolithos, Thalassinoides, Chondrites*, and rarely *Palaeophycus* (Figure **F13**). Diversity ranges 1–3, and the maximum trace fossil diameter ranges 4–22 mm (Figure **F13**). The boundary between Subunits IVB and IVC is based on the last occurrence of the white to pinkish white calcareous ooze.

XRD and CARB data (see **Geochemistry**) indicate that calcareous ooze beds of Subunit IVB contain predominantly calcite ($CaCO_3$ = 97 wt%) with low smectite, illite, and quartz contents (Figure **F14**; Table **T3**).

4.1.4.3. Subunit IVC

Intervals: 393-U1583C-10H-3, 123 cm, to 12H-CC, 17 cm; 393-U1583E-11H-CC, 20 cm, to 12H-5, 59 cm; 393-U1583F-2R-1, 0 cm, to 2R-CC, 19 cm
Depths: Hole U1583C = 87.8–110.2 m CSF-A; Hole U1583E = 97.0–105.1 m CSF-A; Hole U1583F = 101.0–107.4 m CSF-A
Thickness: Hole U1583C = 22.8 m; Hole U1583E = 7.2 m; Hole U1583F = 6.4 m
Age: early Oligocene
Lithology: nannofossil ooze with varying amounts of clay and foraminifera

The upper ~5 m of Subunit IVC consists of pink to light brown nannofossil ooze with clay and foraminifera (Figures **F8**, **F9**, **F10**, **F11**, **F12**). The underlying 3 m contains pink to light brown nannofossil ooze with varying foraminifera content and a 30 cm thick layer of pink calcareous ooze in Hole U1583C and two decimeter-scale interbeds of pink nannofossil ooze in Hole U1583E (Figure **F12**). The lower 11 m shows interbedding of pink nannofossil ooze with clay and light brown nannofossil ooze with clay and foraminifera (Figure **F12**).

Although lithologic contacts are typically gradational over many decimeters, the upper contacts of the pink sediments contain sharp boundaries. Slight color variations are present throughout Subunit IVC, but the color changes are commonly subtle and fall within one Munsell color. Bedding is massive throughout this subunit (Figure **F11**). Two 1 cm thick semilithified beds occur in Sections 393-U1583E-12H-2, 106 cm, and 12H-3, 134 cm. Biogenic mottling is abundant, with bioturbation intensity ranging from absent to high (BI = 0–4). Distinct ichnogenera include *Planolites, Chondrites, Skolithos, Thalassinoides*, and rarely *Arenicolites* (Figure **F13**). Trace fossil diversity ranges 1–3, and the maximum diameter ranges 2–22 mm (Figure **F13**).

Drilling disturbances affect parts of this subunit in Holes U1583C and U1583E. In Core 393-U1583C-12H, drilling disturbances manifest as midcore flow-in and destroyed sediments in Sections 12H-2 through 12H-CC. There was only a 2 m advance between the top of Core 12H and the basement interface at the top of Core 13X, so very little of the 8 m of recovered sediment in Core 12H is in place. Sediments were also severely disturbed to destroyed in the upper sections of Cores 393-U1583E-5H and 11H.

XRD and CARB data (see **Geochemistry**) indicate that calcite is the major component of Subunit IVC. Quartz, illite, and kaolinite are present irregularly throughout this subunit, whereas feldspars are absent (Figure **F14**; Table **T3**).

5. Igneous petrology

Hole U1583F targeted ~30.6 Ma upper oceanic crust along the SAT. Hole U1583F reached volcanic basement at 109.7 mbsf and penetrated a further 129.8 m, reaching 295.5 mbsf and recovering 45.79 m of core for an average basement recovery of 35% (Figure **F7**; Table **T4**). Recovery was generally higher in the upper part of the hole, with an average of 46% (ranging 0%–96%) between Cores 393-U1583F-2R and 13R (0–50 msb). Recovery steadily dropped for the remainder of the hole to an average of 19% between Cores 14R and 29R (50–130 msb). Overall, this recovery was sufficient for preliminary unit boundaries, lava types, and volcanic emplacement styles to be determined with confidence throughout most of the hole but inadequate for many other science goals.

Unless stated otherwise, all cores, sections, and intervals refer to Hole U1583F. Depths are described in meters below seafloor (mbsf; on CSF-A scale) and meters subbasement (msb; CSF-A depth minus 109.7 m). Sample, interval, and contact depths are curated depths unless stated otherwise. This section documents the lithostratigraphy of the volcanic basement at Site U1583 and then summarizes observations and results for the phenocryst phases, breccias, and igneous chemostratigraphy as measured by pXRF.

5.1. Lithostratigraphic units

The basement volcanic sequence at Site U1583 is divided into three main eruptive sequences and seven main volcanic and intravolcanic breccia units. Unit 3 is divided into two subunits (3A and 3B), Unit 5 is divided into three subunits (5A–5C), and Unit 7 is divided into two subunits (7A and 7B). These units and their thicknesses, emplacement styles, contacts, and lithologic details are summarized in Table T4, illustrated in Figure F7, and documented in detail in this section.

Table T4. Volcanic units, contacts, thicknesses, and emplacement styles, Hole U1583F. See the Expedition 390/393 methods chapter (Coggon et al., 2024a) for explanation of expanded and minimum depths and thicknesses. Plag = plagioclase, ol = olivine, cpx = clinopyroxene. **Download table in CSV format.**

Sequence	Unit	Upper unit contact					Unit thickness (m)			Rock type	Flow interior groundmass	Phenocrysts	Evidence for emplacement style	Nature of upper contact
		Core, section, interval (cm)	Curated (mbsf)	Curated depth (msb)	Expanded depth DSF (m)	Expanded hole depth (msb)	CSF-A	Minimum	Expanded					
S	IVC	393-U1583F-2R-1, 0	101.00	—	101.00	—	109.50	109.5	109.5	Nannofossil ooze with varying amounts of clay and foraminifera	—	—	—	—
A	1	3R-1, 0	109.5	0.00	109.70	0.00	11.31	11.2	11.2	Sparsely plag-ol-phyric fine–medium grained massive lava flow	Fine–medium grained	Plag, ol	Gradational grain size change from cryptocrystalline chilled flow top to medium-grained lower flow interior	Incompletely recovered chilled cryptocrystalline flow top
	2	5R-2, 17	120.81	11.31	120.95	11.25	26.61	20.9	26.9	Moderately plag-ol-augite phyric basalt pillow lavas and sheet flows; intervals of no–low recovery	Microcrystalline–fine grained	Plag, ol, cpx	Variably dipping curved glassy margins	Glassy margin at massive flow base and at Unit 2 pillow top
	3A	10R-1, 112	147.42	37.92	147.87	38.17	11.50	10.7	11.1	Aphyric basalt pillow lavas	Microcrystalline–fine grained	Plag	Nonparallel common glassy margins; completely recovered pillow flows	Corrugated glassy flow top margin
	3B	13R-1, 82	158.92	49.42	158.92	49.22	12.68	9.2	12.7	Aphyric basalt sheet flows	Fine grained	Plag	Subhorizontal planar margins and continuous, fine grained over >1 m	Planar, subhorizontal glassy margin
B	4	16R-1, 0	171.60	62.10	171.60	61.90	2.17	1.8	2.8	Breccia of basalt and glass clasts in indurated calcareous sediment matrix	Microcrystalline–glassy clasts	Plag, ol in clasts	Clasts of Unit 5 basalt in sedimentary matrix	Not recovered
	5A	16R-2, 110	173.77	64.27	174.43	64.73	17.59	14.8	18.9	Moderately plag-ol-phyric basalt pillow lavas with rare augite phenocrysts	Microcrystalline	Plag, ol ± cpx	Vertical and curved glassy margins with adhering hyaloclastite	Chilled margin at flow top but not continuously recovered
	5B	20R-1, 26	191.36	81.86	193.32	83.62	0.07	0.16	0.45	Breccia of basalt and glass clasts in indurated calcareous sediment matrix	Microcrystalline–glassy clasts	Plag, ol in clasts	Clasts of Subunit 5C basalt in sedimentary matrix	Not recovered
	5C	20R-1, 43	191.43	81.93	193.77	84.07	14.40	10.1	12.6	Moderately plag-ol-phyric basalt pillow lavas with rare augite phenocrysts	Microcrystalline	Plag, ol ± cpx	Common, variably dipping, and curved glassy margins	Not recovered
C	6	23R-1, 23	205.83	96.33	206.41	96.71	0.97	0.8	3.4	Breccia of basalt and glass clasts in indurated calcareous sediment matrix with intervening lava	Microcrystalline–glassy clasts	Plag, ol in clasts	Clasts of Unit 7 basalt in sedimentary matrix	Not recovered
	7A	23R-1, 120	206.80	97.30	209.84	100.14	13.30	9.9	10.3	Moderately plag-ol-augite-phyric basalt pillow lavas; low recovery	Microcrystalline	Plag, ol, cpx	Curved glassy margins	Breccia resting sharply on glassy pillow top
	7B	26R-1, 0	220.10	110.60	220.10	110.40	>19.40	14.9	>19.4	Aphyric to sparsely plag-ol-phyric basalt pillow lavas; low recovery	Cryptocrystalline–fine grained	Plag, ol ± cpx	Variable texture and some curved glassy margins	Gradational reduction in phenocryst abundance: 25R-1 to 26R-1
	EOH	29R-1, 46	239.50	130.00	239.50	129.80								

5.1.1. Sediment/basement interface

The shallowest occurrences of volcanic rocks and the deepest occurrences of sediment within the sediment/basement interface for all holes at Site U1583 are summarized in Table **T5** and illustrated in Figure **F15**. Only Holes U1583C and U1583F recovered basement volcanic rocks, with Holes U1583A, U1583B, U1583D, and U1583E not advancing to sufficient depths.

Volcanic basement was encountered ~30 m shallower than predicted from the seismic site survey in both Holes U1583C and U1583F at 107.5 and 109.7 mbsf, respectively, whereas the estimated sediment thickness was 138 m (e.g., Coggon et al., 2020; Kardell et al., 2019). In Hole U1583C, this discrepancy resulted in an APC core being fired close to the sediment/basement interface, which was neither penetrated nor recovered, and resulted in several meters of sediment getting sucked into the APC core along with some small fragments of altered glass from the top of basement (interval 393-U1583C-12H-5, 33–35 cm; Figure **F15A**). After changing to XCB drilling, the chilled cryptocrystalline top and several meters of continuous Unit 1 massive lava flow were recovered in the subsequent core (Figure **F15A**).

Table T5. Sediment/basement interface depths and descriptions, Site U1583. **Download table in CSV format.**

Sediment/basement interface core, section, interval (cm)	Basement depth DSF (m)	Shallowest volcanic piece depth CSF-A (m)	Deepest sediment at interface depth CSF-A (m)	Nature and recovery of sediment/basement interface
393-U1583C-13X-1, 0	104.5	104.5	104.5	Fragments of altered glass in disturbed sediment and cryptocrystalline massive flow chilled margin. Indurated sediment veins in upper section.
393-U1583F-3R-1, 0	109.7	109.5	107.43	Not recovered, microcrystalline massive flow top. Indurated sediment veins in upper pieces.

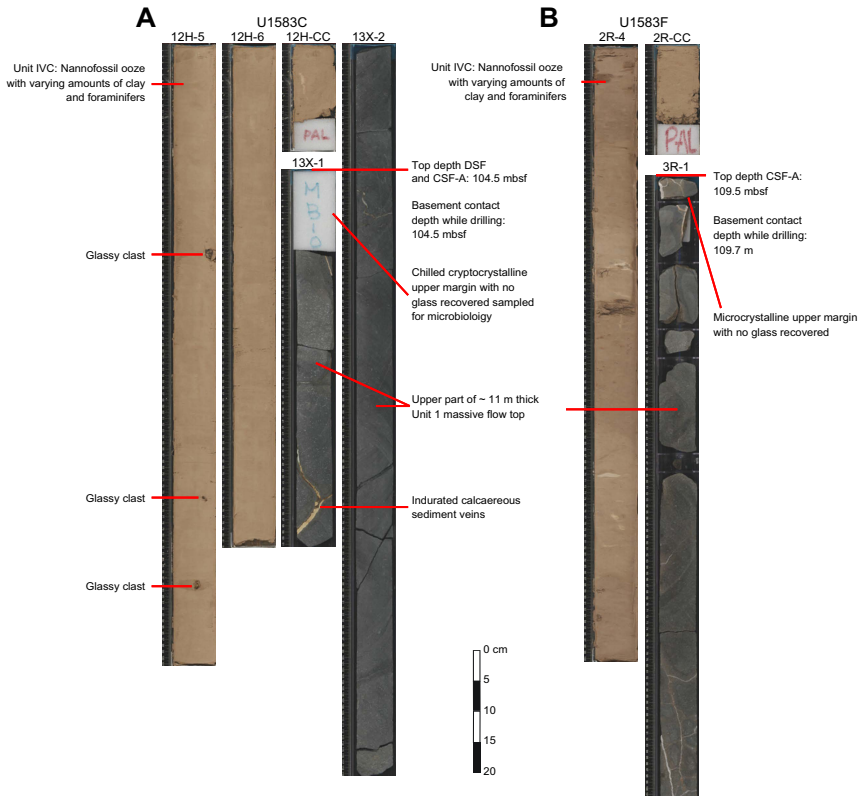

Figure F15. Sediment/volcanic basement interface, Holes U1583C and U1583F. A. Glassy clasts and unrecovered sediment/basement contact. Note that Core 12H had 401% recovery following rebound of APC cutting shoe from unexpectedly hitting basalt interface, sucking in highly disturbed sediment. Consequently, stratigraphic positions of glassy fragments in this core are likely meaningless. Cryptocrystalline upper margin of Unit 1 was sampled for microbiology, and veins of indurated calcareous sediment are present in top of massive flow. B. Similar unrecovered sediment/basement contact with some indurated calcareous sediment veins.

In Hole U1583F, the sediment/basement interface was also not continuously recovered but the chilled microcrystalline top of the Unit 1 massive flow was recovered. By comparison to other flows drilled along the transect, the sediment/basement interface is inferred to be within tens of centimeters of the flow top. No single cores containing both sediment and basalt were recovered in any of the holes at Site U1583. However, veins of indurated calcareous sediment are present in the uppermost sections of both Holes U1583C and U1583F (e.g., intervals 393-U1583C-13X-1, 45–60 cm, and 393-U1583F-3R-1, 0–11 cm; Figure **F15**).

5.1.2. Division of volcanic sequences

The volcanic basement at Site U1583 was divided into three eruptive sequences (A–C; Figure **F7**; Table **T4**). This division was made principally based on the presence of two sedimentary breccias, with their upper contacts at 171.6 mbsf (62.10 msb; Unit 4) and 205.83 mbsf (96.33 msb). These breccias are interpreted to have accumulated during volcanic hiatuses and are described in detail below.

5.1.3. Sequence A

Lithology: aphyric to moderately plagioclase-olivine-phyric pillow, sheet, and massive lava flows

Volcanic Sequence A consists of Units 1–3, which have relatively diverse lithologies and emplacement styles, ranging from aphyric to moderately phyric basalts and from pillow lavas to an ~11 m thick massive flow (Table **T4**; Figure **F7**).

5.1.3.1. Unit 1

Lithology: moderately plagioclase-olivine-phyric fine- to medium-grained massive lava flow

Unit 1 is the uppermost volcanic unit at Site U1583, and it consists of an ~11.2 m thick massive lava flow that was intersected by both of the holes that reached basement (Figure **F15**). The Unit 1 massive flow consists of moderately plagioclase(-olivine) phyric basalt with a fine- to medium-grained interior groundmass, much of which is relatively fresh (e.g., Figure **F16E, F16F**).

Emplacement as a single massive lava flow rather than a sill or a series of sheet flows was deduced from several lines of evidence. Firstly, the unit is situated at the top of the volcanic section, and no sediments are present in the well-recovered core beneath Unit 1 (Section 393-U1583F-5R-2). Secondly, the textural gradations related to cooling of the unit are asymmetric, with a deeply chilled cryptocrystalline upper margin and a variolitic upper flow interior (Figure **F16**). From this flow top, the groundmass grades to medium grain size over ~7 m, reaching a peak around ⅔ to ¾ of the way down through the flow (Figure **F17**). The transition from medium grain size back to the lower glassy margin occurs over ~1.5 m. This asymmetric textural gradation suggests that the top of this flow cooled more rapidly than the bottom, which is consistent with its top being emplaced into seawater and the base being emplaced onto rock.

The upper interior of the flow, starting from ~10 cm below the top of the uppermost recovered basalt piece (interval 393-U1583F-3R-1, 10–50 cm) is moderately vesicular with spherical vesicles. These are interpreted to record magmatic volatiles that exsolved from lower in the flow upon emplacement and, having migrated upward, became trapped under the chilled flow top (Figure **F16D**).

5.1.3.2. Unit 2

Lithology: moderately plagioclase-olivine-augite phyric basalt pillow lavas and sheet flows

Volcanic Unit 2 is a 27 m thick unit of moderately plagioclase-olivine-phyric pillow and sheet lava flows (Table **T4**). The upper part of Unit 2 (120–124 mbsf; Sections 393-U1583F-5R-2 and 5R-3) is composed of pillow lavas that are 30–60 cm thick, with numerous glassy margins that are fresh, dipping, and commonly curved (Figure **F18A**). The central part of Unit 2 (124–135 mbsf; Sections 5R-4 through 7R-1) contains a series of ~1 m thick sheet or possibly large pillow flows, with long intervals of continuous fine-grained flow interiors. The lower part of Unit 2 (135–146 mbsf; Sec-

tions 8R-1 through 10R-1) is again emplaced as pillow lavas, as indicated by greater variation in grain size and common glassy margins.

Core 393-U1583F-6R had 1% recovery, and Core 8R was skunked (0% recovery). Both of these cores are entirely within Unit 2. Except for the difference in recovery, there is no evidence from the cores recovered that these very poorly recovered intervals contain different rock types from the rest of Unit 2. Further examination of wireline and rate of penetration logs may elucidate whether breccias or some other difficult-to-recover lithology were missed over these intervals (question marks in Figure **F7**).

Like much of the Sequence A lavas, except for the Unit 1 massive flow, the interiors of Unit 2 pillow lavas exhibit characteristically microcrystalline or even fine-grained groundmass up to within a few centimeters of the chilled margins (Figure **F18C**). Where they were well recovered, these margins are relatively thick (1–2 cm), fresh, and contain the same phenocrysts as the flow interiors (Figure **F18B, F18D, F18E**). These glassy margins grade from exterior glass with phenocrysts through a spherulitic transition into a cryptocrystalline groundmass of extremely fine, fibrous minerals (clinopyroxene and plagioclase?) (Figure **F18E, F18F**).

Despite these differences in emplacement style, phenocryst character is relatively consistent through Unit 2, dominated by ~1 mm plagioclase (3–6 mod%), with lesser amounts of 0.5 mm olivine (~0.5–1 mod%) that is variably fresh and pale green or altered to pale clay. Some olivine grains are altered to orange clay + Fe oxyhydroxide. In addition, there are extremely sparse but distinctive black, prismatic augite phenocrysts (0.1%–0.5%; 0.3–1 mm).

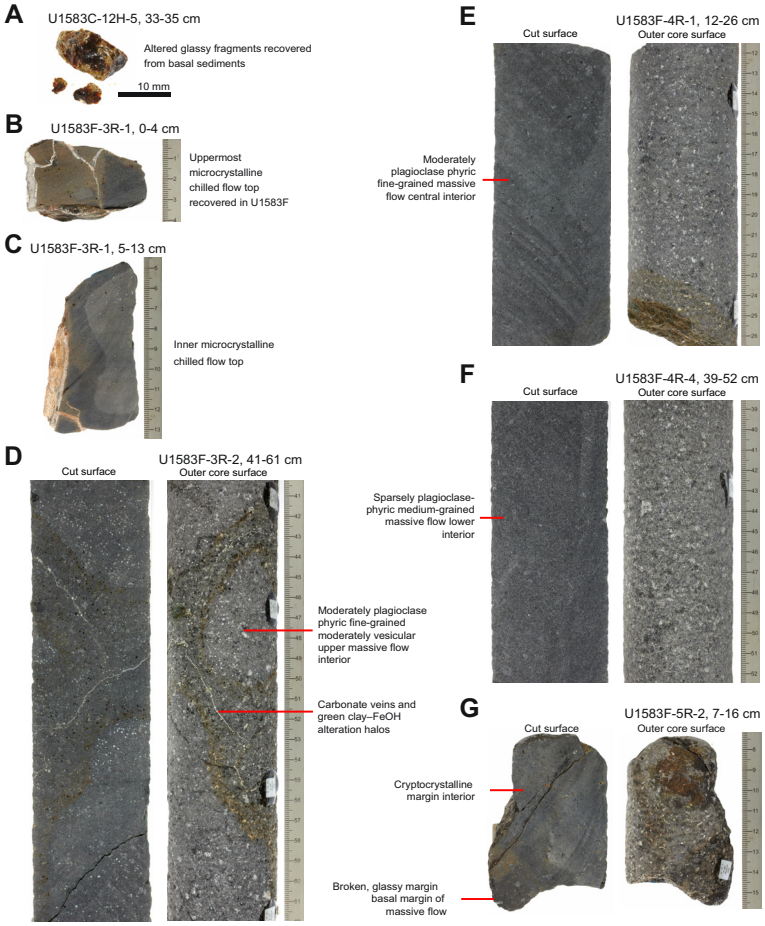

Figure F16. Unit 1 massive lava flow and glass near sediment/basement interface, Holes U1583C and U1583F. A. Fragments of altered glass from recovered sediment. B, C. Unit 1 massive flow microcrystalline chilled flow top. D. Vesicular upper interior of massive flow. E. Fine-grained central massive flow interior. F. Medium-grained lower massive flow interior. G. Probable cryptocrystalline and glassy basal margin of massive flow.

5.1.3.3. Subunit 3A

Lithology: aphyric basalt pillow lavas and rare sheet flows

Subunit 3A has an expanded thickness of 11 m and is composed of aphyric basalt pillow lavas and rare sheet flows that are 0.3–1 m thick (Table **T4**). The glassy margins of Unit 3 are typically thinner than those in Unit 2, and the flow interiors are distinctly variolitic within ~20 cm of the rim (Figure **F19A, F19D**). Although they are classified as aphyric, Subunit 3A lavas have between 0.1% and 0.5% plagioclase phenocrysts (e.g., Figure **F19C**) as well as rare (0%–0.3%) olivine and augite phenocrysts, with fresh olivine present in the upper part of the unit.

One unique feature of Subunit 3A is that its uppermost flow has a corrugated glassy flow top similar to the upper surface of pahoehoe lavas (e.g., Figure **F19B**). All the Subunit 3A basalts have a low abundance (0.5%–1%) of small (mode = 0.2–0.3 mm) spherical vesicles, mostly filled with clay of varying color. An interflow breccia was recovered from Subunit 3A at interval 393-U1583F-13R-1, 41–46 cm, that includes glassy clasts in an indurated calcareous sediment matrix (Figure **F19E**).

5.1.3.4. Subunit 3B

Lithology: aphyric basalt sheet flows

Subunit 3B is lithologically similar to Subunit 3A but consists of aphyric basalt sheet flows instead of pillow lavas, with three continuously recovered flows having thicknesses of 80, 120, and 130 cm and the unit having a total expanded thickness of 12.7 m (Table **T4**). These sheet flows have gently dipping, planar glassy margins and fine-grained interiors, with similarly variolitic inner margins to Subunit 3A (Figure **F19D**). The similar lithology but contrasting emplacement style between Subunits 3A and 3B affords an excellent opportunity to test the effects of emplacement style and grain size on physical and magnetic properties (see **Basement** in Physical properties and downhole measurements and **Basement** in Paleomagnetism).

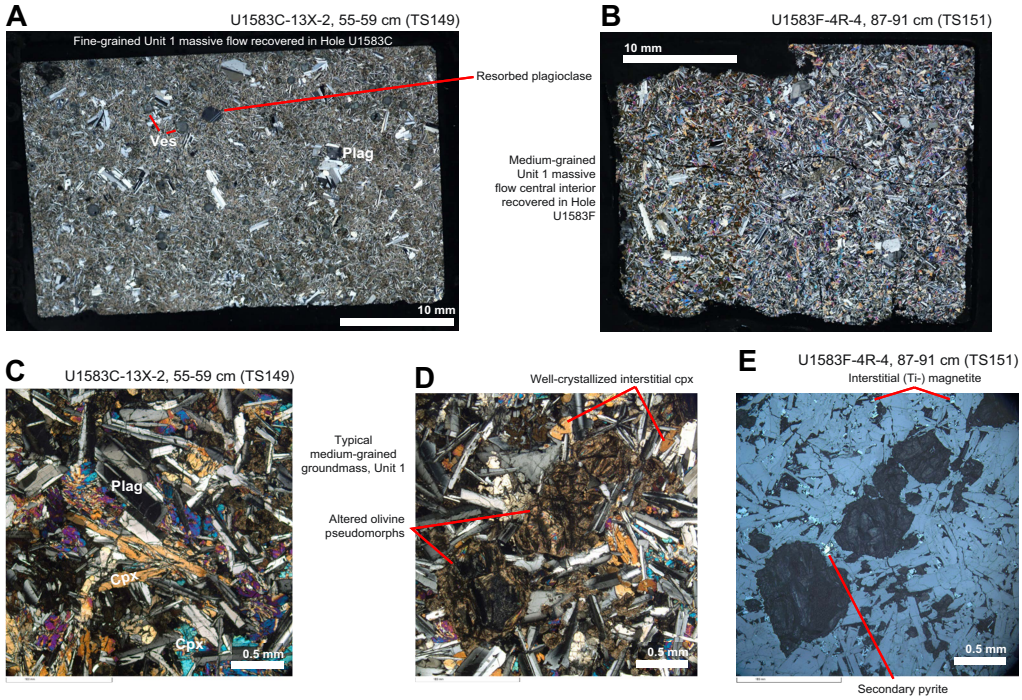

Figure F17. Unit 1 massive lava flow, Holes U1583C and U1583F. A. Vesicular, fine-grained basalt with plagioclase (Plag) phenocrysts ~1 m from flow (XPL). Ves = vesicle. B. Medium-grained central/lower massive flow interior with well-crystallized subophitic texture (XPL). C. Plagioclase laths and mostly interstitial clinopyroxene (Cpx) in upper flow interior, groundmass (XPL). D. Altered olivine phenocrysts and well-crystallized interstitial clinopyroxene in central to lower massive flow interior (XPL). E. Relatively abundant, coarse interstitial (Ti-)magnetite and sparse secondary pyrite (reflected light).

5.1.4. Sequence B

Lithology: moderately plagioclase-olivine-(augite)-phyric basalt pillow lavas and sedimentary breccia

The boundary between Volcanic Sequences A and B occurs at the top of sedimentary breccia Unit 4 (Section 393-U1583F-16R, 0 cm; 171.6 mbsf; 62.1 msb) and is interpreted to coincide with a short hiatus in volcanism at Site U1583 (Figure **F7**). All the lavas of Sequence B belong to Unit 5 and have a relatively uniform lithology of moderately plagioclase-olivine-(augite)-phyric microcrystalline basalt and emplacement style of pillow lavas.

5.1.4.1. Unit 4

Lithology: breccia of basalt and glass clasts in an indurated calcareous sediment matrix

Unit 4 is a well-recovered sedimentary breccia in Core 393-U1583F-16R with a minimum thickness of 1.8 m and an expanded thickness of 2.8 m, situated between 171.6 and 173.8 mbsf (62.1–64.3 msb) at the boundary between volcanic Sequences A and B (Table **T4**). The breccia consists of large broken basalt clasts and smaller altered glass clasts in an indurated calcareous sediment matrix, cemented to varying extents by coarsely crystalline carbonate (Figure **F20**). The basalt and glass clasts in Unit 4 are all moderately plagioclase-olivine phyric (Figure **F20A, F20B, F20D**) and hence derive from the underlying Unit 5 basalts with similar lithologic characteristics and rather than from the overlying aphyric basalts. This assertion is supported by pXRF analyses of breccia clasts (see **High-resolution chemostratigraphy**). This, as well as the angularity of the clasts and the indurated sedimentary carbonate matrix, shows that Unit 4 is a sedimentary breccia formed

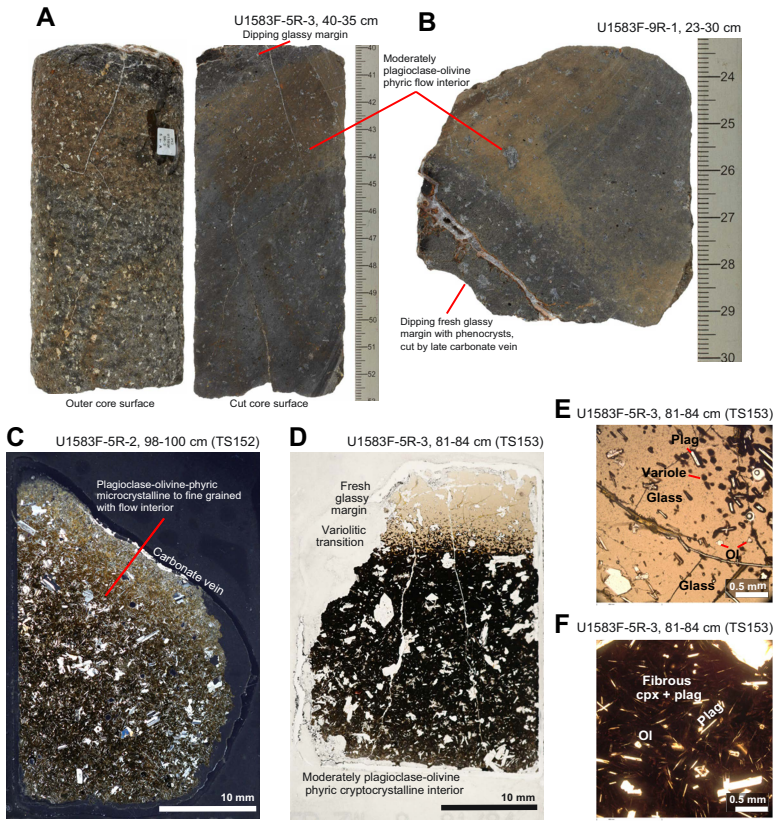

Figure F18. Volcanic Unit 2, Hole U1583F. A. Typical Unit 2 moderately plagioclase-olivine-phyric upper pillow margin and interior, both outer and cut core surfaces. B. Dipping glassy margin of Unit 2 pillow lava. Whole thin section images of (C) plagioclase-olivine-phyric microcrystalline basalt altered around thin carbonate vein (XPL) and (D) fresh glassy margin and moderately plagioclase-olivine-phyric flow interior. E. Close up photomicrograph of glassy selvage and edge of spherulitic transition, with fresh plagioclase (Plag) and olivine (Ol) microlites. F. Photomicrograph of cryptocrystalline groundmass of fibrous clinopyroxene (cpx) and plagioclase laths with sparse olivine microlites.

on the seafloor probably by the self-collapse and disaggregation of local volcanic outcrops, as has been observed in hummocky terrains along the modern Mid-Atlantic Ridge (e.g., Smith and Cann, 1990; Yeo et al., 2012).

The estimated thickness of Unit 4 is greater than the sum of the continuous breccia pieces because the pieces of basalt above the well-recovered breccia are interpreted to be breccia clasts that have lost their matrix during drilling (interval 393-U1583F-16R-1, 0–26 cm). This interpretation is based on the moderately plagioclase-olivine-phyric texture of these clasts, which matches the clasts in the underlying well-recovered breccia but not the overlying aphyric Unit 3 lavas. The pieces are also well within the size range of the clasts in the well-recovered breccia intervals, and one has a veneer of sediment adhering to a broken basalt surface (interval 16R-1, 0–6 cm), which would be consistent with relict matrix.

One anomalous breccia piece from Unit 4 has a much higher proportion of glassy clasts and no sedimentary matrix but instead a coarse crystalline carbonate cement (Figure **F20E**).

5.1.4.2. Subunits 5A–5C

Lithology: moderately plagioclase-olivine-phyric basalt pillow lavas with rare augite phenocrysts

Unit 5 consists of three subunits (5A–5C) with a total expanded thickness of 32 m (Table **T4**). The lavas of Unit 5 are lithologically uniform, moderately plagioclase-olivine-phyric lavas with rare augite phenocrysts. Curved glassy margins with varying dips were commonly recovered, indicating emplacement as pillow lavas (Figure **F21A, F21C**). Unit 5 was divided because of the recovery of a ~16 cm piece of sedimentary breccia of basalt and altered glassy clasts in a matrix of indurated calcareous sediment at interval 393-U1583F-20R-1, 33–43 cm (191.36 mbsf; 81.9 msb), that is similar in character to the Unit 4 breccias (Figure **F21A, F21C**). The expanded thickness of Subunit 5B is 0.45 m, so it is a permissibly significant breccia horizon (Table **T4**).

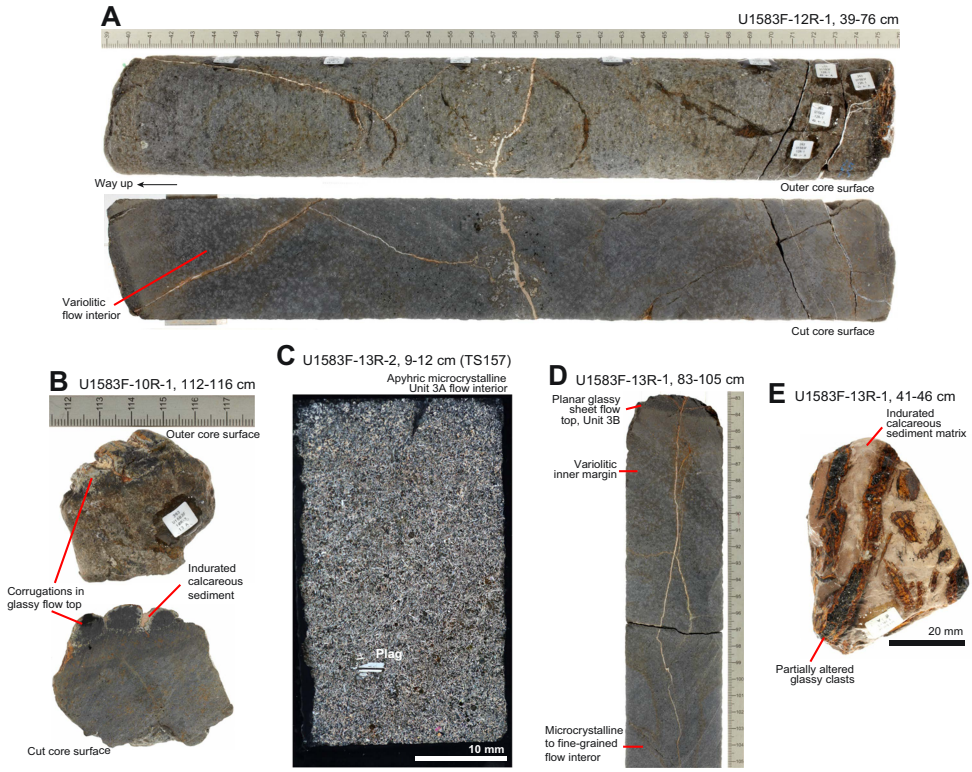

Figure F19. Volcanic Unit 3, Hole U1583F. A. Aphyric, completely recovered ~30 cm thick Subunit 3A pillow lava with two glassy margins, cut by calcareous sediment veins. B. Corrugated glassy flow top. C. Aphyric microcrystalline flow interior. D. Planar glassy flow top and upper interior of Subunit 3B sheet flow. E. Interflow breccia from Subunit 3A.

The lavas of Unit 5 are relatively plagioclase-phyric, with 4%–6% plagioclase, 0.5%–1% olivine mostly altered to orange clay and Fe oxyhydroxide, and some intervals with 0.2%–1% black augite phenocrysts that are commonly subophitic with plagioclase. The flow interior groundmass for Unit 5 pillow lavas is typically microcrystalline, with plagioclase laths that are weakly oriented (e.g., Figure **F21D, F21E**).

5.1.5. Sequence C

5.1.5.1. Unit 6

Lithology: breccia of basalt and glass clasts in an indurated calcareous sediment matrix with intervening lava

Unit 6 consists of breccias with basalt and glassy clasts in an indurated calcareous sediment matrix with a possible intervening lava flow (Figure **F22A**). This package has a total expanded thickness of 3.4 m (Table **T4**). The top of the Unit 6 breccias at 205.83 mbsf (96.33 msb) marks the boundary between Sequences B and C (Section 393-U1583F-23R-1, 23 cm).

The Unit 6 breccias are clast supported, with clasts of moderately plagioclase-phyric, microcrystalline to cryptocrystalline basalt, some with glassy margins, and variably fresh to altered glass (Figure **F22B**). These clasts are set in a yellowish, pale brown (Munsell 2.5Y 7/3) matrix of indurated calcareous sediment that is variably altered yellowish red (5YR 5/8) with black (Mn?) oxide spots. The matrix also has a component of comminuted and altered glass that contributes to the variegation in color (Figure **F22B, F22C**). Given the sedimentary matrix and the denser packing of clasts above the basal contact of the breccia (Figure **F22C**), these breccias are interpreted to be of the same origin as the breccias in Unit 4 and Subunit 5B. They are inferred to have accumulated during a pause in volcanism in which outcrops of Unit 7 lavas collapsed onto a seafloor upon which sediment was progressively accumulating.

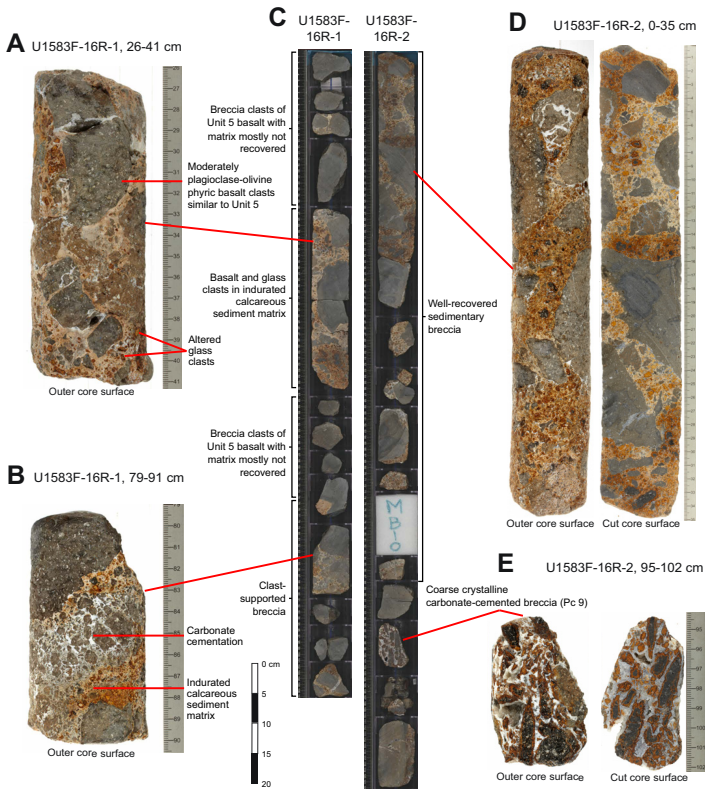

Figure F20. Unit 4 sedimentary breccia and Sequence A/B boundary, Hole U1583F. A. Sedimentary breccia of moderately phyric basalt clasts and altered glass in matrix of indurated calcareous sediment. B. Similar breccia, with disaggregated and carbonate-cemented domain. C. Archive half images of entire Unit 4 breccia zone. D. 35 cm continuous breccia piece. E. Piece of carbonate-cemented, matrix-free breccia with mostly glass clasts.

The continuously recovered basal contact of the Unit 6 breccias with the Unit 7 lavas is unique among the breccia units recovered in Hole U1583F (Figure **F22C**). This contact shows the breccias accumulated above a fractured and broken surface rather than intact pillows. In the center of the unit (interval 393-U1583F-23R-1, 70–106 cm), there are four pieces of lava without adhering matrix. There is no evidence to suggest these are breccia clasts parted from their matrix during drilling, so these are interpreted to be an intervening lava flow. Recovery is relatively low for Core 23R-1 (24%); therefore, using expanded contact depths and assuming the interval mentioned above is a lava flow, the total thickness of breccia in Unit 6 is 2.2 m and intervening lava is 1.3 m. Judging from the size and lithology of these pieces of intervening lava; however, it is still permissible that these are breccia clasts, in which case the total thickness of breccia in Unit 6 would be the same as the 3.4 m expanded thickness as the entire unit.

These two contrasting interpretations may have significant consequences for calculations of hydrothermal exchanges in Hole U1583F and could be further tested by examination of the paleomagnetic inclination of the oriented clasts and the limited wireline logging carried out in this hole.

5.1.5.2. Subunit 7A

Lithology: moderately plagioclase-olivine-augite-phyric basalt pillow lavas

Subunit 7A consists of moderately plagioclase-olivine-augite-phyric basalt pillow lavas. Recovery of curved glassy margins is common, and pillow interiors range from cryptocrystalline to microcrystalline (Figure **F23**). The subunit has an expanded thickness of 10.3 m (Table **T4**).

Only 10% of Unit 7 was recovered by coring, which is low for Hole U1583F and hints that, in addition to pillow lavas, less durable rock types such as breccia were preferentially not recovered. Of the material recovered, the Subunit 7A pillow lavas have 3%–4% plagioclase phenocrysts, 0.3%–1%

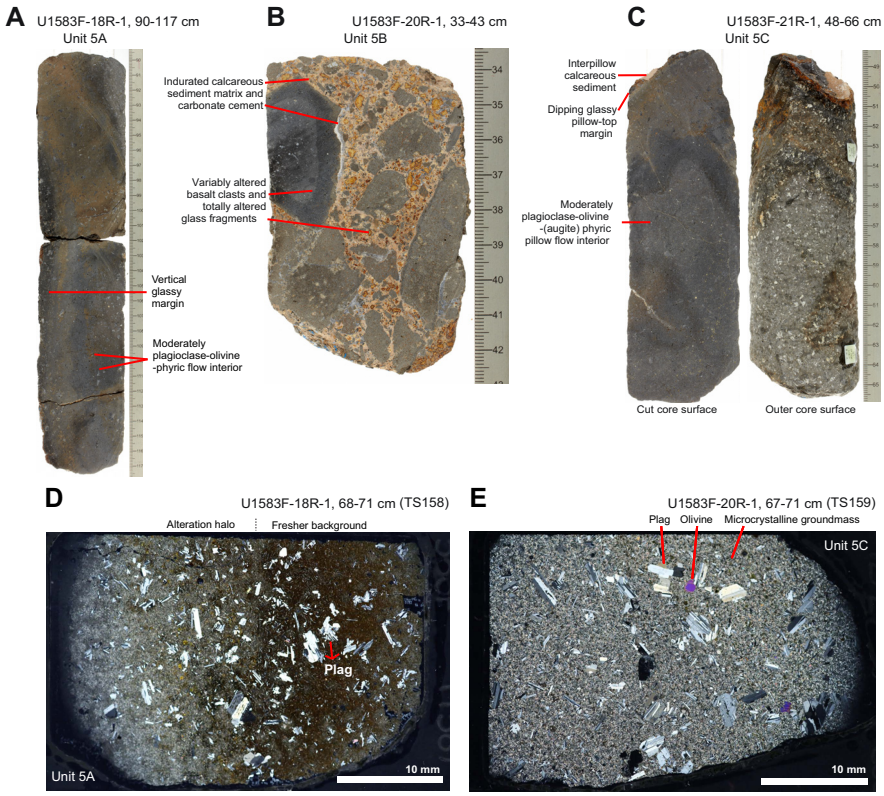

Figure F21. Volcanic Unit 5, Hole U1583F. A. Moderately plagioclase (Plag)-olivine-phyric Subunit 5A basalt pillow lava with steeply dipping lower margin along left side of piece. B. Thin sedimentary breccia Subunit 5B. C. Moderately plagioclase-olivine-augite phyric Subunit 5C pillow lava top, altered along (radial?) fractures, cut and outer core surfaces. D. Whole thin section image of alteration halo and fresher background from Subunit 5A flow interior (XPL). E. Fresh plagioclase-augite phyric microcrystalline Subunit 5C basalt (XPL).

olivine phenocrysts, and the variable presence of 0.5%–1% black augite phenocrysts. Olivine phenocrysts are entirely altered to orange mixtures of clay and Fe oxyhydroxides. Common glassy margins, several of which are curved, indicate emplacement of Subunit 7A as pillow lavas. These pillows typically have mottled to variolitic inner margins, with this texture accentuated by brown clay alteration (Figure **F23A, F23D**). In thin section, plagioclase is the dominant phenocryst, with larger crystals commonly having anhedral, resorbed rims (Figure **F23D**). These are set in a groundmass of plagioclase laths and olivine microlites with interstitial plumose or fibrous clinopyroxene, with sparse (0.5%–1%) 0.1–0.5 mm spherical vesicles (Figure **F23C, F23D**).

5.1.5.3. Subunit 7B

Lithology: aphyric to sparsely plagioclase-olivine-phyric basalt pillow lavas

Subunit 7B lavas were the deepest rocks recovered in Hole U1583F and consist of aphyric to sparsely plagioclase-olivine-phyric basalt pillow lavas with an expanded unit thickness of at least 19.4 m (Table **T4**). The reduction in total phenocryst abundance from 4%–6% in Subunit 7A to 2%–4% in the uppermost rocks of Subunit 7B occurs gradually over Cores 393-U1583F-25R and 26R (Figure **F24B**). However, in the lower portions of Subunit 7B (below Section 27R-1, 0 cm), the modal abundance of small, 0.1–1 mm olivine phenocrysts increases to the same level as plagioclase (2%), which is unique for Hole U1583F.

Apart from these subtle variations in low-level phenocryst abundances, lavas through Subunits 7A and 7B are lithologically similar, with Subunit 7B also having augite phenocrysts; fresh, curved glassy margins; and mottled to variolitic pillow interiors (Figure **F23B, F23E**). Cores 393-U1583F-27R and 28R have the highest numbers of glasses per meter of recovered core in Hole U1583F (Figure **F24E**). The final cores of Subunit 7B have poor recovery, but lavas recovered have a fine-grained groundmass and glassy margins are uncommon (Cores 28R and 29R). This may indicate lava emplacement as large pillows or sheet flows toward the bottom of the hole. However, recovery was insufficient for a confident assignment of emplacement style for lowermost Subunit 7B.

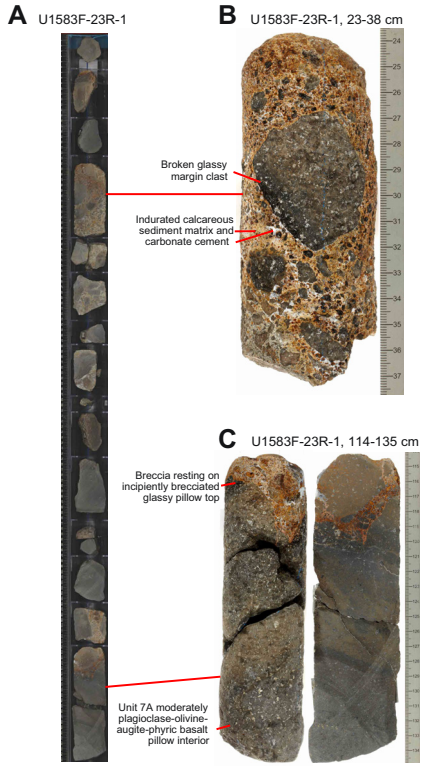

Figure F22. Basalt and sedimentary breccia Unit 6, Hole U1583F. A. Mixed basalt and breccia pieces. B. Whole-round close-up of upper breccia. C. Whole-round and cut surface images of recovered contact between breccia and Subunit 7A pillow lava.

5.2. Phenocryst phases

Phenocryst assemblages in Hole U1583F were relatively uniform, with plagioclase mostly being the dominant phase over olivine. Macroscopically identifiable augite occurs only in some of the most phenocryst-rich rocks. However, the abundance of phenocrysts varies characteristically between the units, ranging from <1% (aphyric) in Unit 3 to 6%–7% in Units 2 and 5 (Figure **F24**). This variation in phenocryst abundance is paralleled by Cr/Ti variation downhole, with the uniquely aphyric Unit 3 also having the highest Cr/Ti in Hole U1583F (Figure **F24**).

Unit 7 exhibits a particularly interesting relationship between phenocryst abundance and lava composition, with a zigzag downhole pattern in Cr/Ti that is roughly paralleled by total phenocryst abundance, with the low point for both occurring at the Subunit 7A/7B boundary (Figure **F24**).

Some of the larger plagioclase phenocrysts observed in thin section in Hole U1583F are anhedral and exhibit rounded, resorbed corners (e.g., Figures **F17A**, **F23D**). This is evidence for disequilibrium between the phenocrysts and the melt that transported them to the surface. However, most plagioclase and olivine phenocrysts are euhedral, so this effect must have been limited or perhaps occurred to a single population of phenocrysts deeper in the magmatic system.

5.3. Breccias

Hole U1583F recovered two main breccia units (4 and 6) as well as thinner breccias of similar character in Subunit 5B. These breccias have angular basalt and altered glass clasts that are either clearly or permissibly derived from the underlying volcanic unit, set in a matrix of indurated calcareous sediment. These features indicate that the breccias are sedimentary in nature, formed

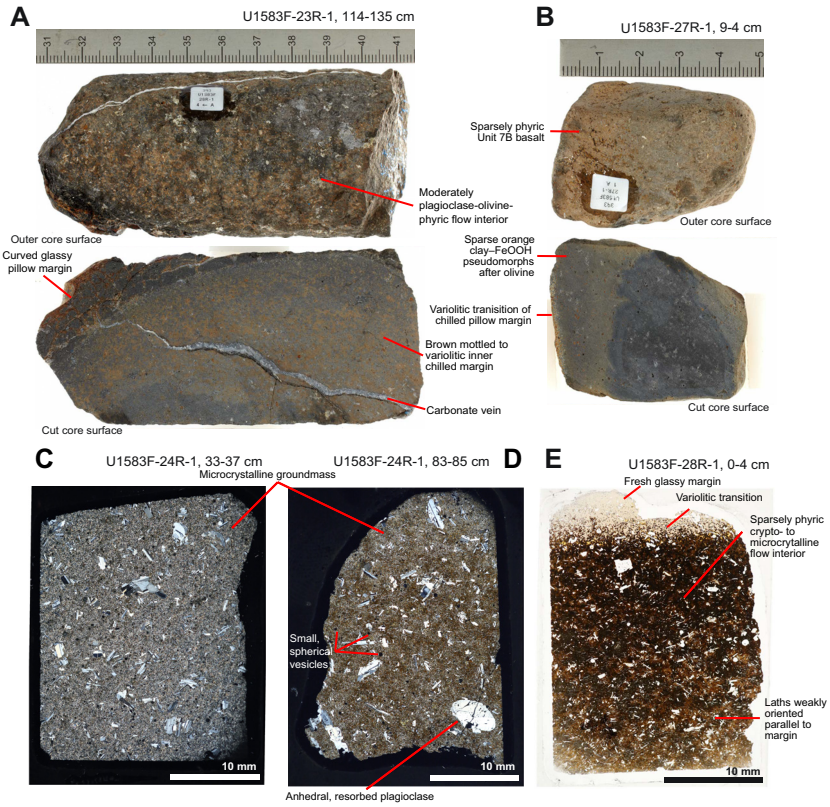

Figure F23. Volcanic Unit 7, Hole U1583F. A. Curved glassy margin of moderately plagioclase-olivine-augite phyric Subunit 7A pillow basalt, outer and cut core surfaces. B. Inner chilled margin of sparsely plagioclase-olivine phyric Subunit 7B lava, outer and cut core surfaces. Thin section photomicrographs of (C) moderately plagioclase-phyric, microvesicular Subunit 7A pillow lava flow interior and (D) comparable primary lithology to C, but with mottled texture and resorbed plagioclase phenocrysts. E. Fresh glassy margin of Subunit 7B pillow lava that grades from glassy to microcrystalline groundmass.

during hiatuses in volcanism by collapse of seafloor pillow lava outcrops, with broken pillow clasts and margins falling into and sedimented by background carbonate sedimentation on or near the ridge axis (e.g., Yeo et al., 2012). It is difficult to rule out that some proportion of this apparently sedimentary matrix may be a very fine hydrothermal precipitate, as documented at Site U1557, but future petrographic analysis should resolve this. According to the sedimentary interpretation, these breccias should mark paleoseafloor horizons, comparable to those encountered in Hole U1558D. These rocks and the underlying lavas present compelling targets for investigating multi-stage seafloor weathering in sequentially accreted slow-spreading crust. It is also possible that Cores 393-U1583F-6R and 8R, with 1% and 0% recovery in Unit 2, failed to sample breccia or other difficult-to-recover rock types. Wireline and drilling data are required to better estimate the nature of the missing >99% of basement core in these intervals.

5.4. High-resolution chemostratigraphy

The cut surfaces of the archive halves from Hole U1583F were measured by pXRF for selected elemental concentrations in 207 locations. These measurements were made at locations with background levels of alteration, selected from the most visibly fresh rock present, alteration halos around veins or flow margins, and breccia matrix with variable amounts of altered glass. This allows both primary igneous compositions and chemical perturbations by hydrothermal alteration

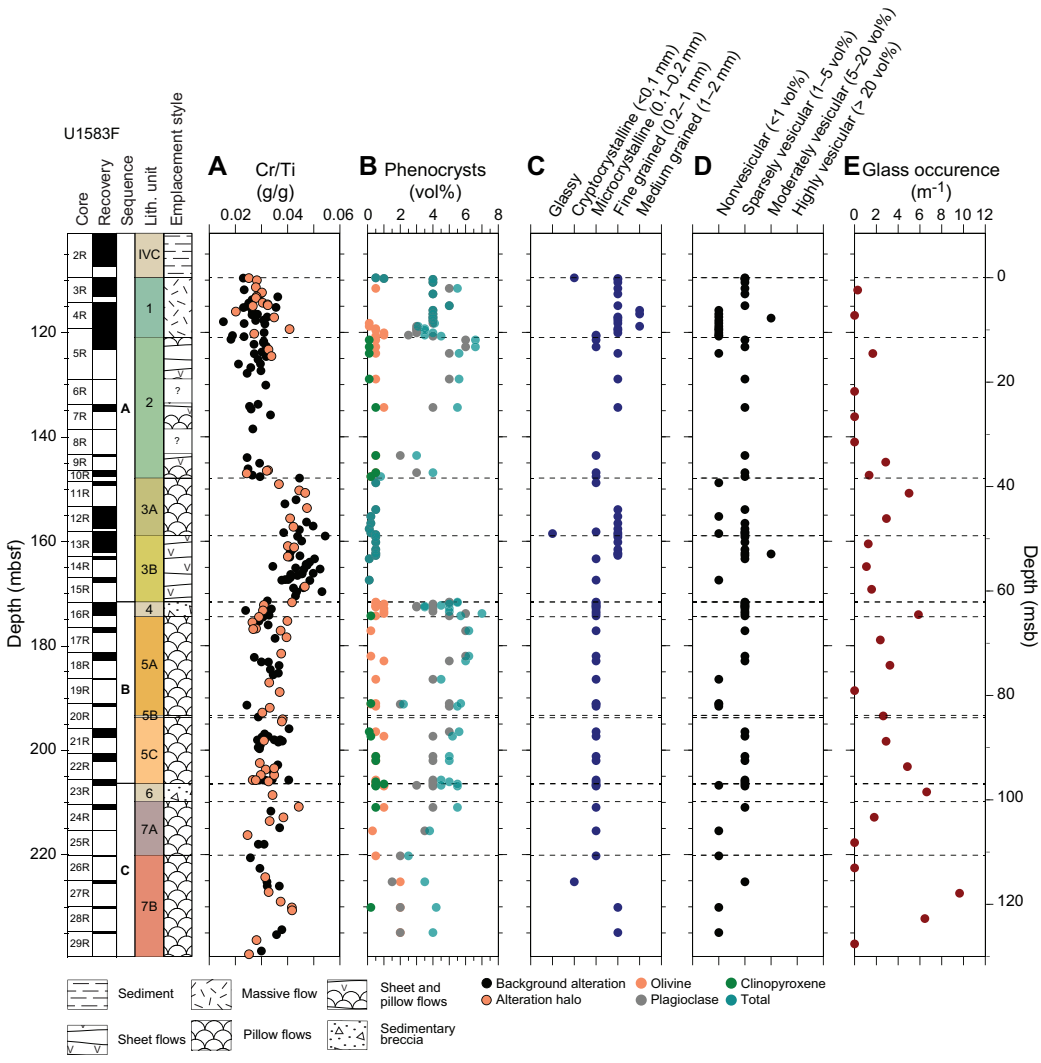

Figure F24. Macroscopic core observations, Hole U1583F. A. Cr/Ti ratios from pXRF analysis of split core surfaces (see Figure F25 for additional results). B. Phenocryst abundance. C. Flow interior grain size. D. Vesicularity. E. Glass occurrences per meter of recovered core for each core.

to be considered downhole. Of the 207 locations measured, 133 were from the background areas, 65 were from undifferentiated alteration halos, and 9 were from breccia matrix, which are provided at the end of Table **T6** but not plotted together with the basalt analyses in Figure **F25**. Shipboard analyses of whole-rock samples by inductively coupled plasma–atomic emission spectroscopy (ICP-AES) are additionally plotted for comparison to the pXRF data, which compare favorably for the utilized elements, with only TiO_2 being significantly lower for pXRF measurements relative to ICP-AES. This suggests the TiO_2 pXRF calibration curves could be refined or the influence of phenocrysts considered in future work. Given relative standard deviations of <6% measured on rock standard surfaces over the course of Expedition 393 for TiO_2 (see **Geochemistry** in the Expedition 390/393 methods chapter [Coggon et al., 2024a]), the relative variation between 1 and 1.5 wt% in Hole U1583F should nevertheless be considered with confidence.

5.4.1. Variation with depth and similarities between sites

Figure **F25** shows variation in key major element oxides and trace elements with depth for Hole U1583F, both measured by pXRF on split core surfaces (Table **T6**) and by ICP-AES on powdered discrete whole rock samples (Table **T35**).

The volcanic rocks at Site U1583 are split into three main chemostratigraphic groups, with their transitions at the top of Unit 4 (Sequence A/B boundary) and the top of Unit 3 (Figure **F25**). No major compositional change occurs across the Sequence B/C boundary. The three chemostratigraphic groups are principally defined by the high Cr and low Ti and Zr composition of the Unit 3 lavas relative to all the other lavas above and below. These relatively high concentrations of compatible Cr and low concentrations of incompatible Ti and Zr at relatively constant Zr/Ti indicates Unit 3 is potentially less fractionated than the other magmatic units at Site U1583.

Table T6. pXRF data on split core surfaces, Hole U1583F. **Download table in CSV format.**

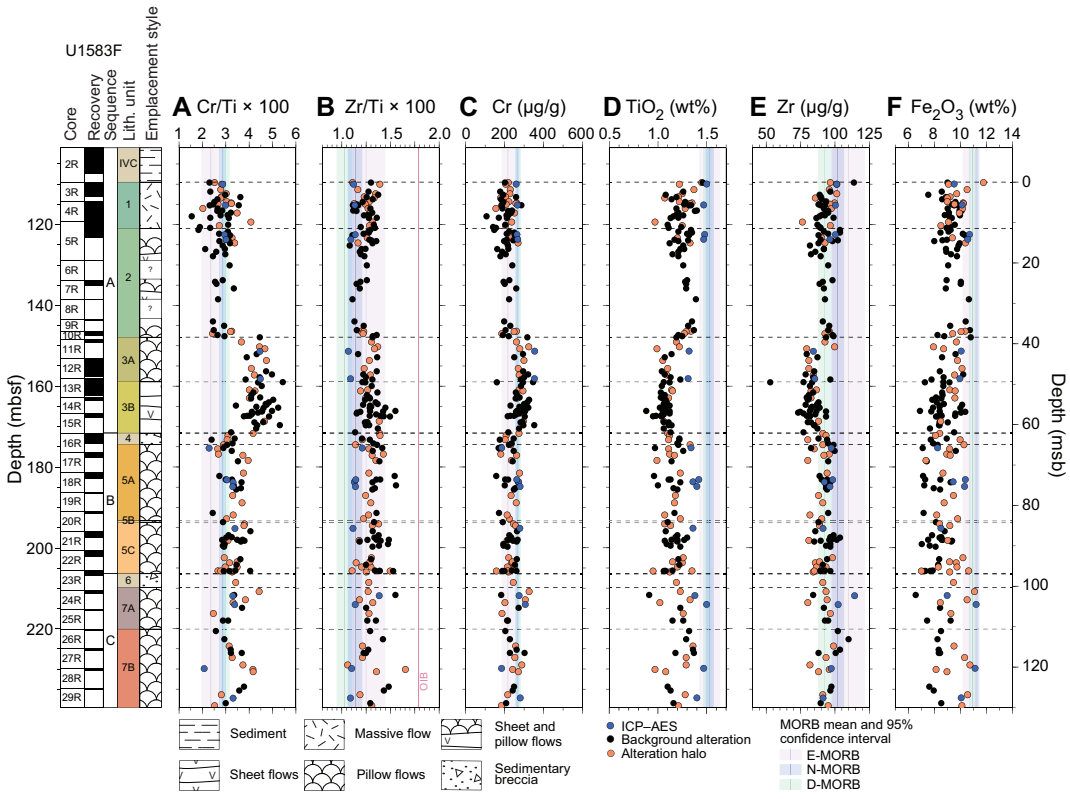

Figure F25. A–F. Shipboard split core surface pXRF and ICP-AES whole rock powder analyses of major and trace element concentrations and ratios, Hole U1583F. Total Fe is calculated as Fe_2O_3. MORB reference means and 95% confidence intervals from Gale et al. (2013). pXRF data available in Table T6; ICP-AES data available in Table T35. D-MORB = depleted MORB.

Unit 3 is also the least rich in phenocrysts (Figure **F24A, F24B**). This coincidence of high Cr/Ti and low phenocryst abundance occurring as the second major chemostratigraphic unit in the hole closely parallels the volcanostratigraphy of Holes U1558D and U1560A (see Figure **F30** in the Site U1558 chapter [Teagle et al., 2024a] and Figure **F27** in the Site U1560 chapter [Teagle et al., 2024b]). Holes U1583F and U1560B also have massive lava flows of comparable 6–11 m thickness in the uppermost chemostratigraphic unit (Figure **F7**; see Figure **F7** in the Site U1560 chapter [Teagle et al., 2024b]).

The volcanostratigraphic similarities between these holes provide an excellent opportunity for assessment of ridge flank hydrothermal maturation, offering a like-for-like comparison in terms of protolith compositions and emplacement styles between 15 and 50 Ma.

Looking at the Hole U1583F chemostratigraphy in more detail, the transition from Unit 3 to Unit 2 is gradational, with anticorrelated Cr and Ti changing over Cores 393-U1583F-9R through 11R (145–155 mbsf; Figure **F25C, F25D**). As mentioned in the Unit 7 description, Cr/Ti values follow a zigzag pattern through Unit 7, possibly recording a pulsation between the eruption of more and less evolved lavas within this unit (Figure **F25A**).

Another interesting feature in the downhole pXRF data are the higher Fe concentrations in alteration halos relative to the fresher background rocks for samples below ~80 msb (Figure **F25F**). A similar Fe enrichment in halos over background compositions is seen in Hole U1558D starting at 100 msb and Hole U1560B starting at 110 msb. Ratios of Zr/Ti are scattered but relatively uniform downhole in Hole U1583F, with compositions within the N-MORB to enriched MORB (E-MORB) range, similar to lavas in Hole U1558D (Figure **F25**).

5.5. Summary

Site U1583 was established in ~30.6 Ma crust during Expedition 393, and Holes U1583C and U1583F recovered volcanic basement. These holes both intersected a ~11 m thick massive lava flow at 107.5 and 109.7 mbsf, respectively, ~30 m shallower than predicted by seismic site surveys (Kardell et al., 2019). Only Hole U1583F advanced deeply into basement, reaching 239.6 mbsf (129.8 msb) and recovering 45.8 m of basement lavas and breccias for a total recovery of 35% (Figure **F7**; Table **T4**).

Hole U1583F intersected three volcanic sequences (A, B, and C) with 62, 35, and 33 m expanded thicknesses, respectively, separated by two sedimentary breccia units (4 and 6) with thicknesses estimated between 0.8 and 3.4 m (Table **T4**). The upper Sequence A (109.7–171.6 mbsf) consists of Unit 1, which is an 11 m thick massive lava flow; Unit 2, which is a package of moderately phyric pillow lavas and sheet flows; and aphyric Unit 3, which is less evolved than all the other units in the hole (Table **T4**; Figure **F25**). The middle Sequence B consists of moderately phyric pillow basalts and a thin breccia horizon and is capped by the sedimentary breccia of Unit 4. The lower Sequence C is again capped by a sedimentary breccia (Unit 6) that lies above sparsely to moderately phyric pillow basalts that are chemically and lithologically similar to Sequence B (Figure **F25**).

Lava composition assessed by pXRF varies downhole both gradually and in a stepwise fashion across petrologically defined unit boundaries (Figure **F25**). Zr/Ti ratios are consistent with a N-MORB-like composition for the lavas at Site U1583. In contrast to the sequence stratigraphy defined by the presence of sedimentary breccias, pXRF measurements reveal that Unit 3 has one of the least fractionated compositions in Hole U1583F, splitting the hole into three main chemostratigraphic packages: Igneous Units 1 and 2, 3, and 5–7.

6. Alteration petrology

The basement rocks recovered from Site U1583 all preserve evidence of reaction with seawater-derived hydrothermal fluids to varying extents. This alteration is manifest as secondary minerals in three main contexts: (1) replacing interstitial mesostasis and glass, (2) replacing groundmass and phenocrysts, and (3) precipitating in open porosity to partially or completely fill fractures to form veins and vesicles. These three manifestations occur in a range of spatial contexts in Site

U1583 basement, namely background alteration representing fluid-rock reaction that has pervasively permeated the bulk rock along grain boundaries and alteration halos that are generally related to previous open porosity that has facilitated channeled fluid flow and more extensive fluid–wall rock reaction (e.g., around veins and vugs or along igneous margins). In addition, the breccias recovered from Site U1583 record extensive alteration of clasts and matrix and are cemented by secondary minerals. The replacement minerals, styles, and intensity of alteration, along with the secondary minerals precipitated in veins, vesicles, and breccias, provide a record of the hydrothermal alteration taking place in 30 My of crustal aging. This section focuses on Hole U1583F, although similar alteration features were observed in the basement recovered by XCB coring in Hole U1583A.

Overall, Hole U1583F is characterized by low-temperature alteration downhole with changing abundance and types of alteration halos and background alteration that are also accompanied by changes in the secondary minerals precipitating in veins (Figure **F26**).

6.1. Alteration of glass

Volcanic glass associated with chilled margins and breccias is present throughout most of Hole U1583F and shows a full spectrum of alteration from fresh to completely altered to clay minerals. The intervals with the highest percent abundance of glass (Figure **F26**) (e.g., Sections 393-U1583F-9R-1 and 28R-1) also have the highest abundance of fresh glass, but this percentage is skewed by the recovery of thick (>1 cm) glassy margins in short sections rather than intervals with many chilled margins. In some chilled margins, where altered, glass is uniformly altered to orange clays (5YR 4/6 yellowish red) (Figure **F27**) but to varying extents of replacement. In breccias, glass alters to clays with a range of colors from orange to green with increasing replacement by clay minerals (see **Breccia**).

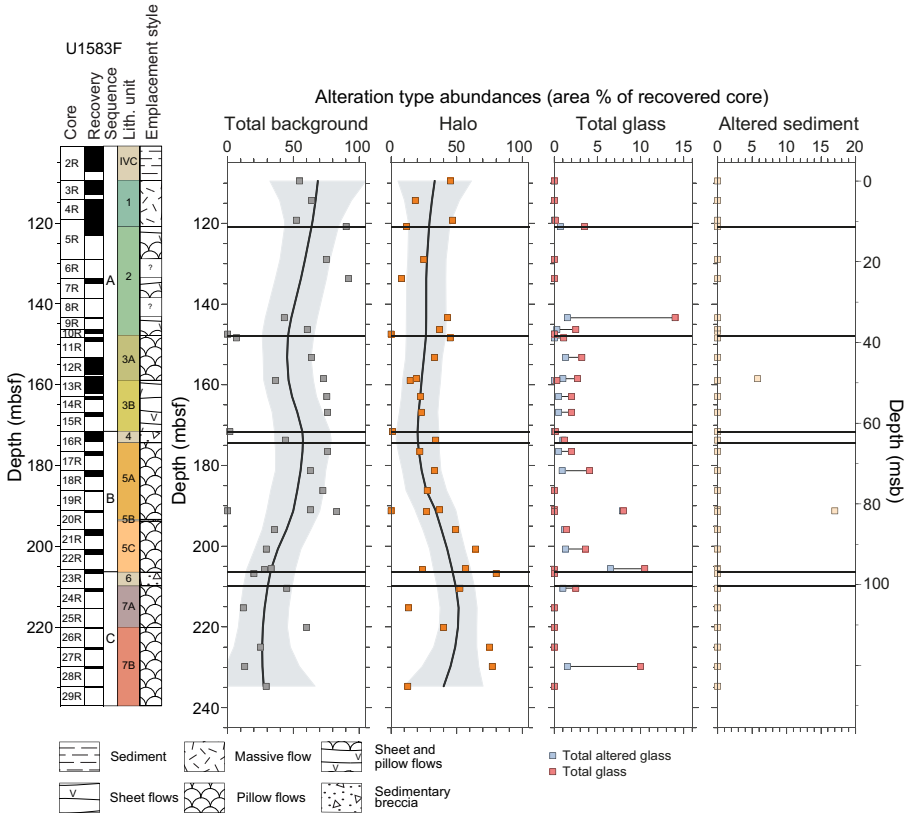

Figure F26. Alteration overview showing abundance of background alteration, alteration halos, fresh and altered glass, and altered sediment, Hole U1583F. Data are plotted at individual core level, except where igneous units straddle a core, in which case data are separated by igneous unit. Data are plotted at top of cored intervals. Black trend lines = locally weighted scatter plot smoothing (LOWESS) nonparametric regression, gray shaded areas = 2σ of mean.

6.2. Background alteration

Background alteration is present throughout Hole U1583F and occurs in two types: gray background and mottled gray chilled margin background. Orange speckled background (recognized by the replacement of olivine to clays + Fe oxyhydroxides) is absent from this hole (Figure **F28**). Background alteration occupies 11%–90% of the area of the cores and shows a marked change in abundance downhole. Above 195.9 mbsf, background alteration is the dominant alteration type, occupying an average area of ~60% of the core. Below this depth, the background alteration area decreases to 30% on average. This shift is mirrored by the downhole increase in abundance of alteration halos.

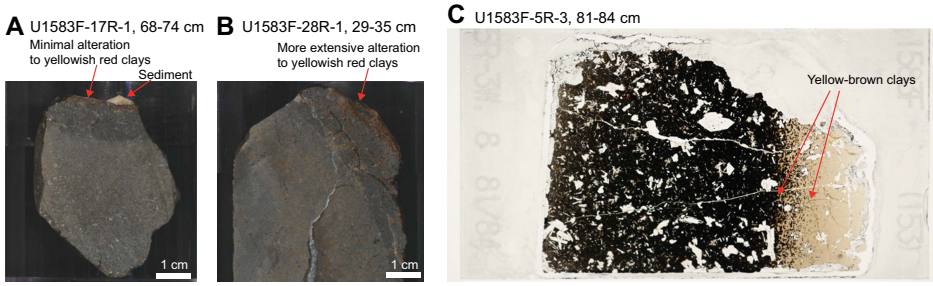

Figure F27. Glass alteration along chilled margins, Hole U1583F. A. Thick (>10 mm) glass margin with minimal alteration to clays on outer edge, overlain by remnants of sediment vein. B. Similarly thick (>10 mm) glassy margin that is more altered, with thicker band of clays on outer edge, and incipient alteration around veins and fractures within margin itself. C. Chilled margin where glass is beginning to alter to yellow-brown clay minerals at inner edge of margin and along veins.

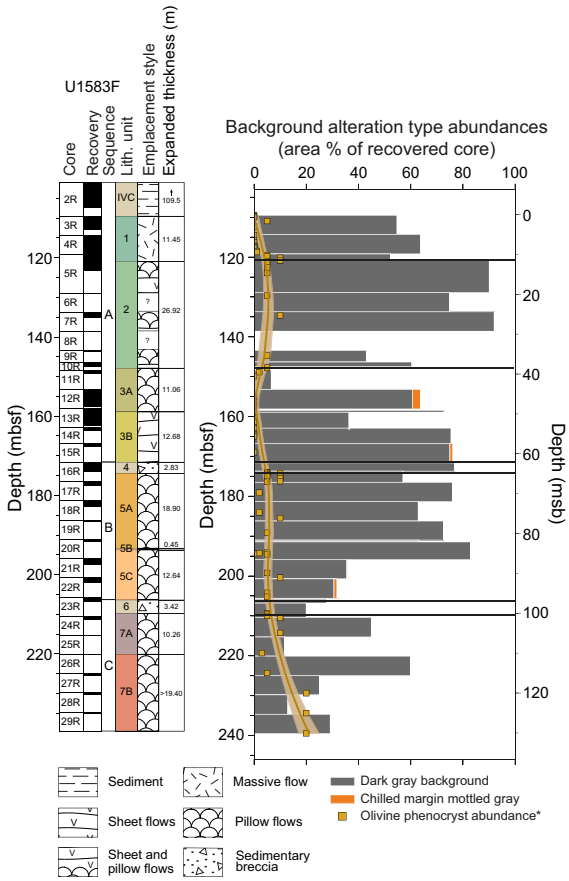

Figure F28. Downhole distribution of background alteration types calculated on section unit scale, Hole U1583F. Olivine phenocryst abundance (*) shown for context and plotted as olivine phenocryst abundance (area percent) × 10.

6.2.1. Gray background

Gray background dominates the background alteration, is similar to Sites U1559, U1558, and U1560, and is commonly associated with a uniform texture and color (GLEY 1 5/N) (Figure **F29**). In contrast to Sites U1559 and U1558, the background alteration in Hole U1583F shows greater variation in color and texture. Color ranges from gray (GLEY 1 5/N) to dark gray (5YR 4/1) to very dark gray (2.5Y 3/1), with the latter occurring in one-third of the logged intervals. The very dark gray color is browner and typically associated with a more patchy, commonly mottled, appearance (Figure **F29**). Alteration is primarily focused on the replacement of mesostasis and groundmass, but examples of plagioclase phenocrysts altering to white to creamish clays are present. Olivine phenocrysts are variably altered to clays (of varying colors) ± Fe oxyhydroxides. The orange speckled background is not found in Hole U1583F because of this variation in olivine alteration (cf. Hole U1558D).

In thin section, yellow-brown clays replace mesostasis and groundmass in areas of background alteration (Figure **F29**). The abundance of secondary minerals is variable from 11% to 78%, with most of examples between 11% and 28% in thin sections. Vesicles are filled to varying amounts (10%–100% filled) with yellow-brown and green clays, calcium carbonate, and/or zeolites.

6.2.2. Mottled gray chilled margin background

In Hole U1583F, pillow lava chilled margins show a distinct zone of alteration that lies between the glassy margin and the cryptocrystalline pillow interior and highlights the transition in crystallinity away from the glassy margin. This zone is characteristically mottled gray and varies in width from 2 to 20 mm. This zone is commonly overprinted by later orange alteration halos. It is most pronounced in pillow lavas that display a patchy to variolitic texture in the core of the pillow, suggesting that the gray mottling is related to groundmass texture (Figure **F29**).

6.3. Alteration halos

Halo alteration in Hole U1583F is more complex than in Holes U1559B or U1558D and shows different but similarly variable halo alteration to Site U1560. Halos show greater variation in color, some are multilayered, and some show more diffuse boundaries, but in general the alteration is commonly of lower intensity. Downhole, the area abundance of halos varies at core level, from 11% to 80%, and there is a prominent shift in abundance partway through Subunit 5C at 195.9 mbsf (Figure **F30**). Above 195.9 mbsf, the average area of a core occupied by halos is 27%, whereas below 195.9 mbsf this increases to 50%. This increase in halo abundance is represented by the increase in abundance of brown and orange halos (Figure **F30**).

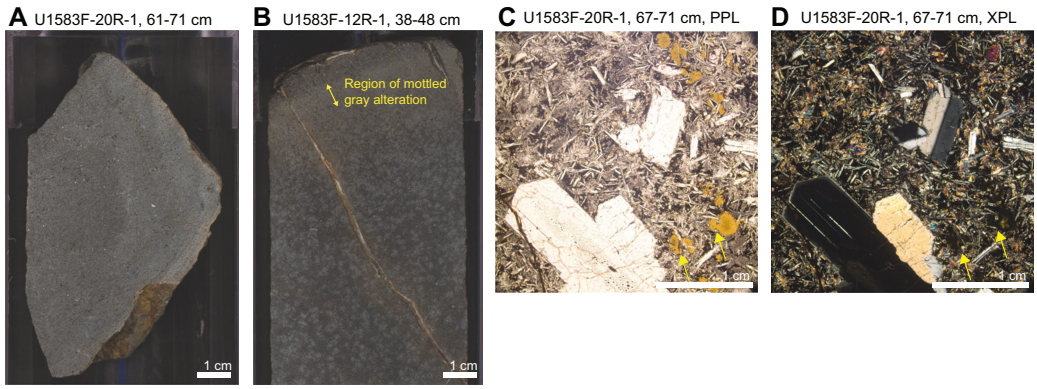

Figure F29. Background alteration, Hole U1583F. A. Typical uniform, gray (GLEY 1 5/N) pseudomorphic background alteration. B. Narrow band of mottled gray alteration that transitions into dark gray (2.5Y 3/1) patchy to variolitic background alteration away from chilled margin at top of image. C, D. Typical replacement of mesostasis and groundmass to yellow-brown clays (arrows) in background. Phenocrysts are unaltered.

6.3.1. Dark gray halos

Dark gray halos are found in most but not all cores (Figure **F30**) and at core level represent 6.1% of the cut surface. Dark gray halos (GLEY 1 4/N), typical of other holes along the SAT, are present and almost always occur as a single band of halo (average width = 4.3–5.3 mm; maximum = 26 mm; Table **T7**). The multiple millimeter-sized dark gray halos seen in the other SAT holes (e.g., Hole U1558D) are rarely present in Hole U1583F and only occur in Section 393-U1583F-20R-1. Some dark gray halos also exhibit a distinct color (GLEY 2 4/10B dark bluish gray) in addition to the GLEY 1 4/N seen at other sites.

Dark gray halos occur with many other halo types. They are almost always present with the light brownish gray halos that are common in Holes U1559B, U1558D, and U1560B. Another combina-

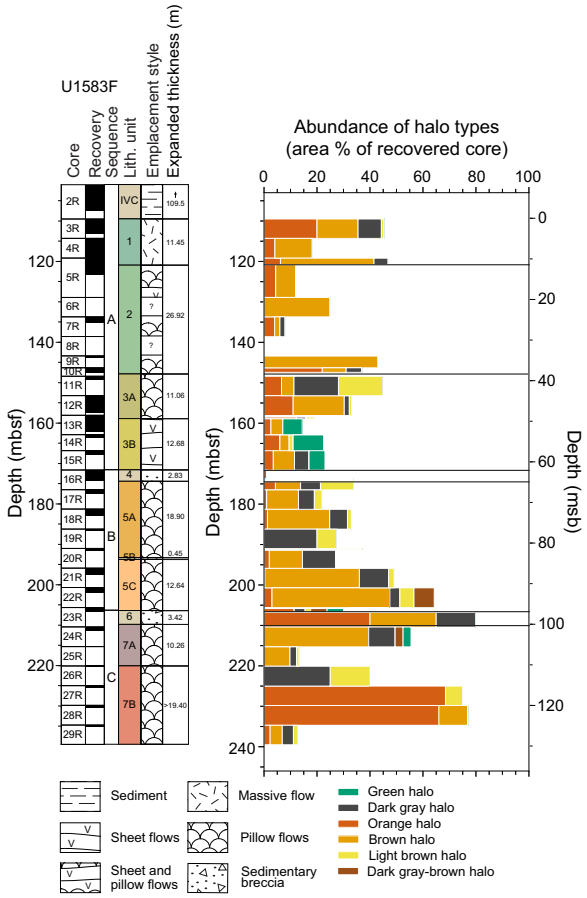

Figure F30. Downhole variation in area abundance of alteration halo types calculated on section unit basis, Hole U1583F. Height of each bar scaled to advance in depth. Halo abundance increases downhole, driven by increasing abundance of orange and brown halos below 205 mbsf.

Table T7. Halo type abundance and average half-width when found bordering veins, Site U1583. Note that orange halos rarely occur with veins. **Download table in CSV format.**

Halo type	Average abundance per section unit (area %)	Average half-width around veins (mm)
Dark gray	6.1	4.3
Dark bluish gray		5.3
Light brownish gray	3.0	4.6
Light yellowish brown	13.5	12.2
Brown		4.7
Orange	10.3	4.7
Greenish gray	1.3	9.2

tion present is the dark bluish gray halo together with orange halos, first appearing in Sample 393-U1583F-10R-1, 104 cm (Figure **F31**). The dark bluish gray variety of the dark halos also co-occurs in multicolored halos (see **Multiple layer halos**). In thin section, the dark gray halos have abundant yellow-brown clay as the principal alteration mineral.

6.3.2. Light brownish gray halos

The light brownish gray halos are present in half of the core intervals but on average occupy only 3% of the area of a core. They are absent between 114.3 and 148.4 mbsf. They are light brownish gray (10YR 6/2) and most commonly occur with dark gray halos (Figure **F32**). Light brownish gray halos have also developed around vugs.

6.3.3. Brown halos

Brown halos are present in most cores and show a strong variation in abundance downhole in Hole U1583F. Above 195 mbsf, brown halo abundance is on average 12% of the area of the core, and between 195 and 215 mbsf, brown halo abundance peaks at 24%–48% before decreasing sharply to 0%–11% (Figure **F30**). The brown halos show a range of colors (7.5YR 5/2 brown, 7.5YR 5/3 brown, 10YR 5/3 brown, 10YR 6/4 light yellowish brown, and 10YR 4/1 dark gray), likely reflecting a range of intensities of replacement of olivine and oxidation of iron (Figure **F33**). The dark gray variety (10YR 4/1) is only present within the brown halo peak between 195 and 215 mbsf (Figure **F31**), where it exhibits the strongest brown tone and is interpreted to be the most intense example of brown alteration. This halo type occurs only in discrete pieces that are entirely composed of brown halo and do not have any preserved veins or margins that indicate the origin of the alteration.

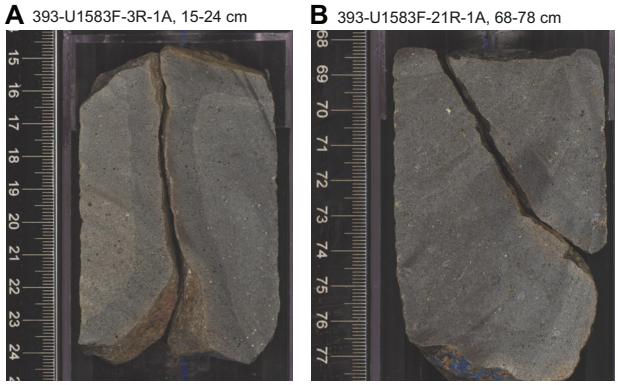

Figure F31. Dark gray halos, Hole U1583F. A. Dark bluish gray halo around clay vein. B. Dark gray halo around clay vein. In both examples, halos form pervasive bands of alteration flanking veins.

Figure F32. Light brownish gray halos, Hole U1583F. This halo type commonly co-occurs as an inner halo to dark gray halos around veins and vugs.

When bordering veins that are actually recovered, the brown halos generally occur as a single halo although some display a dark bluish gray outer halo. Brown halos have an average half-width of ~12 mm (Table **T7**). Brown halos also occur as alteration zones extending from chilled margins into the groundmass of host lava flow. In this setting, the halos are thicker (up to 40 mm) and show both sharp and gradational boundaries with the background alteration.

The brown halos host vesicles that are filled by either multiple minerals (e.g., clay + Fe oxyhydroxide) or clay of different colors such that the vesicles display concentric layering. Common pairings of vesicle fill include lining of Fe oxyhydroxide with a green clay center or a variably colored clay lining with a carbonate central filling.

6.3.4. Orange halos

Orange halos occur in most cores, but they have the most variable abundance of all halo types in Hole U1583F (Figure **F30**). Orange halos show a peak in area abundance in the first basement core (393-U1583F-3R) before remaining at relatively low abundances (0%–22%, mostly <10%) to 205 mbsf (the top of Unit 6), below which the abundance of orange halos is higher, and this style of halo is dominant in Subunit 7B (up to 68.5% of a core). The orange halos are either reddish brown (5YR 5/4) or reddish yellow (5YR 6/6), with the latter shade more abundant below 205 mbsf. The orange color originates from the formation of clays and Fe oxyhydroxides. The orange halos, similar to the brown halos, occur bordering veins and vugs and as alteration zones extending from chilled margins (Figure **F34**). When bordering recovered veins, they have an average half-width of 4.7 mm and are reddish brown (5YR 5/4) (Table **T7**). These vein-related orange halos appear diffuse, with the majority of the halo characterized by low intensity of replacement. However, a very prominent and sharp outer edge shows up clearly on a wet surface. Reddish brown halos also occur in the multihalos (see **Multiple layer halos**).

Vesicles are generally more filled in orange halos, typically with Fe oxyhydroxides ± clays partially to completely filling the vesicles. Where more than one mineral fills a vesicle, the Fe oxyhydroxide forms the lining, indicating early formation.

6.3.5. Multiple layer halos

Multiple layer halos, or multihalos, are defined as halo color combinations that always occur together, typically as narrow bands. The colors present in multihalos mostly fall into halo colors (orange, brown, and dark gray) seen elsewhere in Hole U1583F, with the exception of greenish gray halos that are only present in multihalos. Hole U1583F has multihalos with 3 or 4 different halo colors; some of these combinations are unique to this hole. For example, dark bluish gray–reddish brown halos occur throughout most of the hole, most commonly the reddish brown forms the inner halo but some reversed examples exist. In a few examples, the reddish brown forms 2 layers separated by a band of dark bluish gray (Figure **F35**). In contrast, some of the multihalo types are

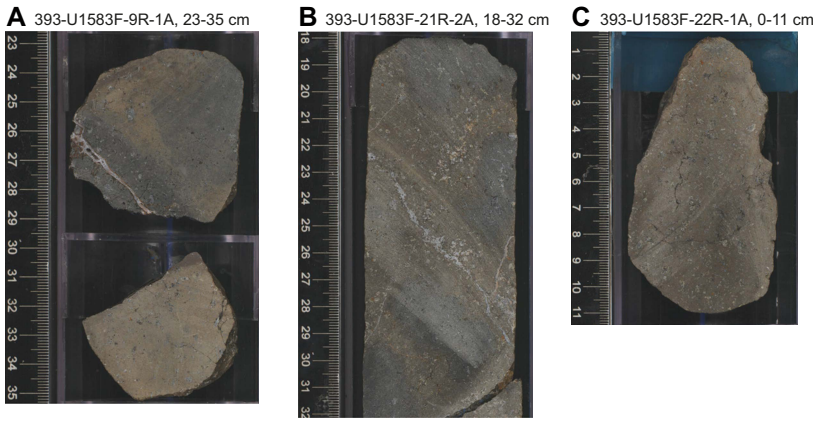

Figure F33. Brown halo types, Hole U1583F. A. Irregular (23–29 cm) and pervasive (30–35 cm) brown (7.5YR 5/3) alteration around chilled margins. B. Brown (7.5YR 5/2) halos around veins with diffuse boundary with gray background (23–32 cm). C. Extensive dark gray (brown) alteration with no recovered vein or chilled margin.

found within specific zones in Hole U1583F. The multihalos of greenish gray–reddish brown–light yellowish brown–dark bluish gray halos occur mostly in the sheet flows of Subunit 3B (158–171 mbsf). These halos most commonly border veins that have variable mineral fillings along the length of the vein, from green clay to Fe oxyhydroxide ± clay rich compositions. These veins have sharp boundaries between these compositional changes that can be traced around the core to

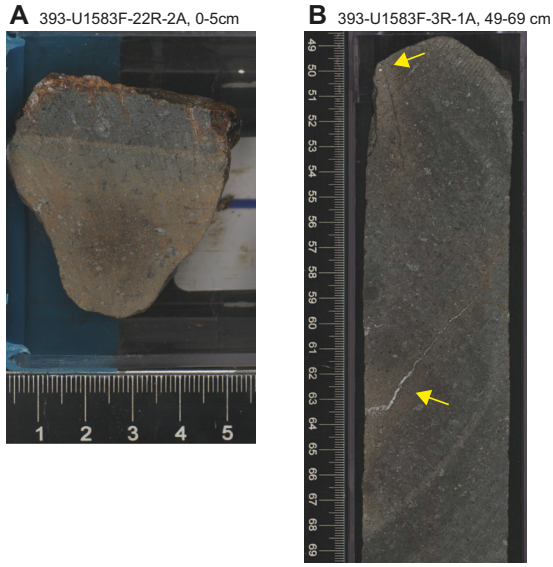

Figure F34. Orange halo types, Hole U1583F. A. Orange (reddish yellow) alteration zone related to chilled margins. B. Orange (reddish brown) irregular halos around carbonate veins (arrows).

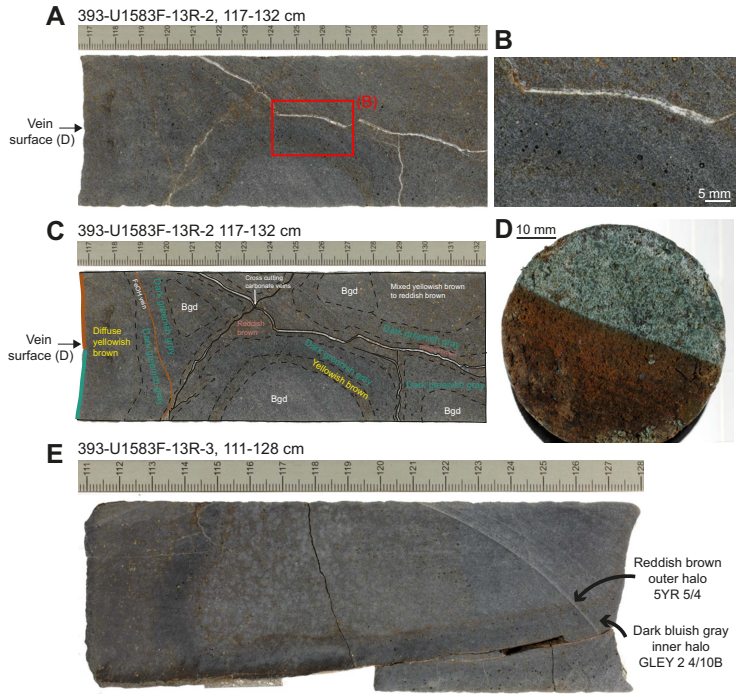

Figure F35. Multihalo types, Hole U1583F. A–D. Layered halos of light yellowish brown–dark greenish gray and reddish brown. Each halo type is identified in C. B. Close up of A showing enlargement of groundmass to illustrate variable vesicle fills across halo types. Dark greenish gray halos host green clay–filled vesicles and light yellowish brown vesicles with orange-brown clays ± FeOH. D. End on view of vein present on left side of A. This vein composition changes across vein surface, from green clay to dark orange-brown clay ± FeOH, with sharp boundary between compositions. E. Dark bluish gray halo with sharp outer boundary of reddish brown. Bgd = background.

mimic the halo boundaries. Similar to the reddish brown halos described above (see **Orange halos**), a key characteristic of these multilayered halos is that they are diffuse for most of the halo but have sharp boundaries where the replacement to various clay ± Fe oxyhydroxides is concentrated. The secondary minerals creating the various colors are best displayed in the sequential fill of vesicles. As expected, the greenish gray halos host green clay filled vesicles and the redder the halo the more yellow-orange clay + Fe oxyhydroxide fills vesicles. In interval 393-U1583F-13R-2, 117–132 cm, there is a multihalo around a carbonate + Fe oxyhydroxide vein that is locally overprinted by light yellowish brown halos, indicating multiple phases of fluid/rock reactions (Figure **F35**).

6.4. Breccia

Breccia was recovered in two main units in Hole U1583F (Units 4 and 6), with smaller occurrences in Subunit 5B (Figure **F26**). They are interpreted to represent paleoseafloor horizons (see **Igneous petrology**). These breccias are fragmented rock types that have undergone multiple stages of fluid/rock reaction and because of their high porosity, likely act as important loci for fluid/rock exchange in the uppermost basement. The breccias in Hole U1583F contain previously hydrothermally altered clasts including abundant volcanic glass, variable matrixes of indurated calcareous sediment and comminuted rock, and cements of calcium carbonate and/or zeolites. They also preserve evidence of postformation hydrothermal alteration by the presence of overprinting hydrothermal veins, commonly filling open space.

6.4.1. Clast alteration: basalt

The basaltic clasts in the Hole U1583F breccias have all undergone hydrothermal alteration to varying extents, and based on the variability of alteration and the truncation of alteration halos, this alteration is interpreted to predate the formation of the breccia (Figure **F36**). The clasts contain a mixture of background alteration (GLEY 1 5/N or 2.5Y 3/1) and almost the full spectrum of alteration halos recovered in Hole U1583F (dark gray, light brownish gray, brown, and orange). The only halo type not observed in breccia clasts are multihalos. The ratio of background to halo within clasts is highly variable from 80:20 up to 10:90. The overall intensity of alteration within the basaltic clast is estimated between 20% and 60%, reflecting the large range in background:halo ratio. The basaltic clasts contain vesicles variably filled with clay ± carbonate ± Fe oxyhydroxides, assemblages that are also consistent with the rest of Hole U1583F. In some places, fragments of carbonate vein are present within clasts but whether such veins crosscut or predate the matrix is unclear.

6.4.2. Clast alteration: volcanic glass

Clasts of volcanic glass range from <1 mm up to 20 mm, and the extent of alteration of the glass to clay minerals is broadly correlated with clast size. The larger glass clasts typically display 1–2 mm wide alteration rims (5YR 5/4 reddish brown) and preserve at least some fresh glass in the core of the clast. The smaller glass clasts are completely replaced by clay minerals of varying colors (5YR 5/8 and 5YR 4/6 yellowish red and 10YR 7/6 yellow) (Figure **F36**).

6.4.3. Matrix alteration

The matrix in Hole U1583F breccias is a mixture of predominantly indurated calcareous sediment with minor fragments of volcanic glass. These altered sediments display a range of colors from white to pink and textures from clastic to micritic (see **Igneous petrology**). In thin section, there is strong evidence for the recrystallization of the sediment and dissolution and reprecipitation of biogenic calcareous and siliceous materials (Figure **F37**).

6.4.4. Cement

Secondary minerals (calcite and phillipsite; see Table **T8**) have precipitated in the pore space between clasts and the matrix. Residual open space may represent dissolution cavities or original porosity. In most breccia pieces, the volume of cement is low and is typically less than 5% of the volume of the interval. There are some examples where the cement is more abundant (e.g., interval 393-U1583F-16R-2, 94.5–103.5 cm; Figure **F36**), and in these cases it is dominated by calcite. Zeolites also occur in some cements as thin (<1 mm) coatings on the external surfaces of breccia

clasts, indicating that the formation of zeolites occurred over a prolonged time, spanning syn- and postbreccia formation.

6.5. Veins

Hydrothermal veins occur throughout Hole U1583F and provide a record of the precipitation of secondary mineral assemblages from seawater-derived hydrothermal fluids. The mineralogy and physical characteristics of 1144 veins were logged, including structural orientations for 429 veins. A total of 363 veins are associated with at least a single alteration halo. The width of veins ranges 0.1–7 mm and generally yields a geometric distribution, with a median value of 0.2 +1/–0.1 mm (1σ equivalent), mean of 0.4 mm, and mode of 0.1 mm (Figure **F38**). Downhole total vein density varies between 10 and 44 veins/m of recovered core with a median and mean of 28 veins/m (Figure **F39**). The volume of core occupied by veins is 1.3% (Figure **F40**).

The occurrence and abundance of secondary minerals in veins vary downhole with the total volume percentage of core filled by veins decreasing downhole (Figure **F40**). Secondary minerals filling veins include calcium carbonate, clays, zeolites, Fe oxyhydroxides, and sediment (Figures **F41**, **F42**; Table **T8**). Approximately 34% of all veins are filled with one mineral type, 52% are filled with two minerals, and 14% are filled with three or four mineral types. Calcium carbonate + clay is the dominant mineral vein assemblage. XRD analysis indicates aragonite in Core 393-U1583F-4R, but in the remainder of Hole U1583F XRD analysis indicates that the carbonate present is calcite. The

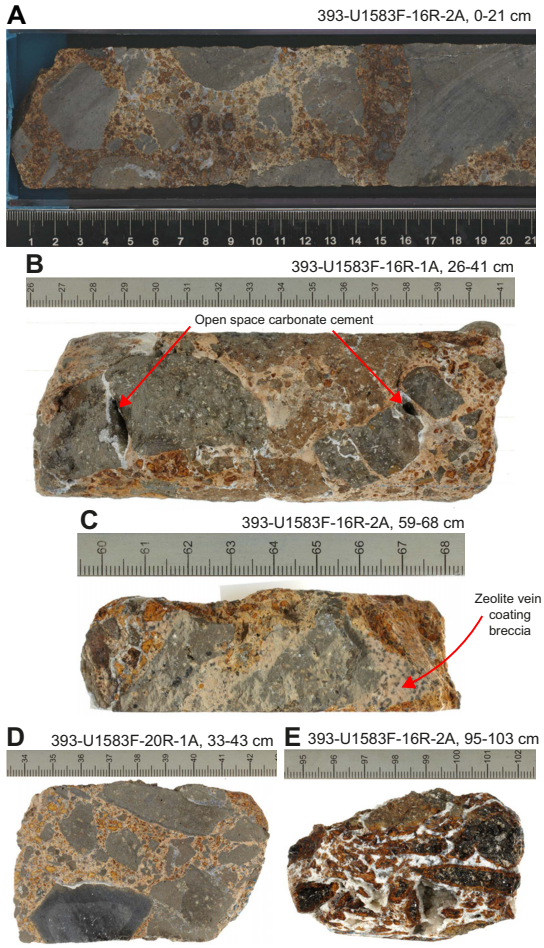

Figure F36. Breccias, Hole U1583F. A. Clasts within breccia that are variably altered to gray background and range of halo types. B. Open space filling carbonate cement on outside surface. Open spaces exist close to edges of larger clasts. C. Breccia with zeolite vein (0.1–0.2 mm thick) that coats edge of sample and must postdate formation of breccia. D. Breccia with clasts that show prominent alteration halos around edges of clasts. E. Breccia of volcanic glass clasts that has almost no matrix and is cemented by calcium carbonate. Glass clasts show strong alteration to brown clays along rims of clasts.

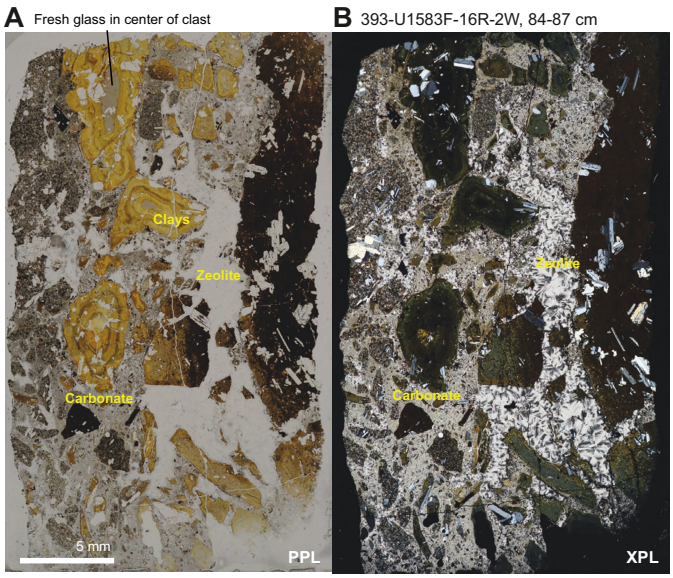

Figure F37. A, B. Breccia showing altered glass clasts extensively replaced by clay minerals forming concentric rings and basaltic clasts that are variably altered, Hole U1583F. Clasts are cemented by calcium carbonate and zeolite. Zeolite is preferentially found adjacent to glass clasts.

Table T8. XRD results for mineral separates, Site U1583. **Download table in CSV format.**

Core, section, interval (cm)	Top depth CSF-A (m)	Bottom depth CSF-A (m)	Minerals identified (semiquantitative % proportion)	Sampling note
393-U1583C-				
12H-5, 88–90	109.39	109.41	Zeolite (perlialite?, 91%), anorthite-sodian (9%)	Altered basalt(?) clast in sediment core
12H-5, 88–90	109.39	109.41	Zeolite (tschernichite, 70%), anorthite-sodian (30%)	Altered basalt(?) clast in sediment core
13X-1, 0–15	104.50	104.65	Calcite-magnesian (82%), goethite (18%), additional minor clay peaks	MBIO sample
13X-1, 50–51	105.0	105.01	Calcite-magnesian (97%), sepiolite (3%)	White-yellow-brown vein with precipitate and metamorphosed sediment
13X-1, 50–51	105.0	105.01	Anorthite (51%), calcite-magnesian (25%), augite (24%)	White-yellow-brown vein with precipitate and metamorphosed sediment
13X-2, 53–57	105.65	105.69	Anorthite-sodian (96%), ulvöspinel-ferrian (4%)	Vein
13X-2, 69–70	105.81	105.82	Augite (100%), additional major clay peaks (montmorillonite?)	Green clay vein
393-U1583F-				
3R-1, 0–4	109.50	109.54	Calcite-magnesian (97%), phillipsite-Na (3%)	Vein with white precipitate and metamorphosed sediment
3R-1, 5–7	109.55	109.57	Calcite-magnesian (96%), phillipsite-Na (4%), additional minor clay peaks	Vein with white precipitate and metamorphosed sediment
3R-2, 111–128	112.01	112.18	Calcite-magnesian (89%), anorthite-sodian (10%), vermiculite mica (1%)	MBIO sample
4R-2, 122–124	116.70	116.72	Calcite-magnesian (100%)	Vug with white precipitate and metamorphosed sediment
4R-2, 122–124	116.70	116.72	Phillipsite-Na (48%), albite (28%), calcite-magnesian (24%)	Vug with white precipitate and metamorphosed sediment
4R-2, 122–124	116.70	116.72	Albite (68%), calcite-magnesian (32%), additional peaks (phillipsite-K and/or chamosite?)	Vug with white precipitate and metamorphosed sediment
4R-3, 64–68	117.53	117.57	Calcite-magnesian (55%), aragonite (43%), sepiolite (2%)	Green clay vein
4R-4, 12–15	118.25	118.28	Aragonite (36%), calcite-magnesian (34%), anorthite-sodian (29%)	Yellow clay vein
4R-4, 36–38	118.49	118.51	Aragonite (74%), ganophyllite (25%), vermiculite mica (1%)	Clay vein
4R-4, 63–66	118.76	118.79	Sepiolite (57%), vermiculite mica (23%), calcite-magnesian (20%)	Green clay vein
10R-1, 36–46	146.66	146.76	Calcite-magnesian (100%), additional clay peaks	MBIO sample
11R-1, 0–3	148.40	148.43	Calcite-magnesian (96%), phillipsite-Na (4%)	Vein in glassy margin
12R-1, 16–31	153.36	153.51	Calcite-magnesian (84%), phillipsite-Na (16%)	MBIO sample
12R-4, 0–2	157.27	157.29	Phillipsite-Na (45%), albite-potassian (32%), calcite-magnesian (23%)	Vein in glassy margin
13R-2, 59–74	160.02	160.17	Calcite-magnesian (100%), additional minor clay peaks	MBIO sample
16R-2, 73–83	173.40	173.50	Phillipsite-Na (83%), calcite-magnesian (17%)	MBIO sample
16R-3, 75–77	174.645	174.665	Calcite-magnesian (100%), additional minor feldspar and clay peaks	Vein
17R-1, 68–73	177.18	177.23	Phillipsite-Na (64%), anorthite (36%), additional minor clay peaks	Precipitate on glassy margin
18R-1, 0–6	181.30	181.36	Phillipsite-Na (72%), anorthoclase (28%), additional minor clay peaks	Vein
20R-1, 33–43	191.33	191.43	Anorthite (72%), calcite-magnesian (18%), gobbinsite zeolite (10%)	Interpillow breccia
20R-1, 33–43	191.33	191.43	Calcite-magnesian (100%), additional minor peaks (chlorite?)	Interpillow breccia
22R-1, 26–36	200.96	201.06	Phillipsite-Na (58%), calcite-magnesian (42%), additional minor clay peaks	MBIO sample
23R-1, 38–44	206.28	206.30	Augite (66%), calcite-magnesian (34%), additional feldspar and zeolite peaks	Interpillow breccia
27R-1, 17–21	225.17	225.21	Phillipsite-Na (100%), additional feldspar and minor clay peaks	Vein in glassy margin
28R-1, 15–29	229.95	230.09	Calcite-magnesian (100%), additional minor feldspar peaks	MBIO sample

distribution of calcium carbonate veins is variable downhole with higher abundance in Unit 3 (148–171 mbsf) and lower abundance in Unit 5 (174–207 mbsf) (Figure **F40**). The abundance of Fe oxyhydroxide ± orange clay veins decreases with depth, and they are absent in some cores below 170 mbsf (Figure **F40**). Zeolite, in particular phillipsite, first occurs in veins at 160 mbsf, and is most abundant in Unit 5. Zeolite veins are generally associated with chilled margins, forming discrete <3 mm wide crack-seal syntaxial veins and as coatings on fresh and altered glass (Figures **F41**, **F42**). In contrast to calcium carbonate, Fe oxyhydroxide, and zeolite veins, the abundance of clay minerals in veins is generally uniform downhole (Figure **F40**). Sediment vein abundance is highest in Unit 1, and its occurrence is variable downhole, forming irregular veins up to 7 mm wide (Figure **F40**). Secondary mineral abundance and vein density generally co-vary downhole for all minerals (Figures **F39**, **F40**).

Vein textures indicate that 64% of veins in Hole U1583F display some evidence of multiple episodes of fracturing and precipitation as multiple mineral types occur within a single discrete vein (Figures **F41**, **F42**). Occurrences of veins that display clear crosscutting relationships are rare, and no systematic relationship occurs between calcium carbonate, Fe hydroxide, and clay veins or fillings.

In some occurrences of green clay veins, the composition of vein filling material changes along the vein with a discrete contact between green clay and clay + Fe oxyhydroxide; this change is associated with the changing characteristics of the associated halo (Figure **F41E**; e.g., intervals 393-U1583F-13R-2, 115.5–116 cm, and 13R-2, 39.5–40 cm). The distribution of measured vein widths does not vary between vein type, with a broadly geometric distribution occurring for all vein types (Figure **F43**).

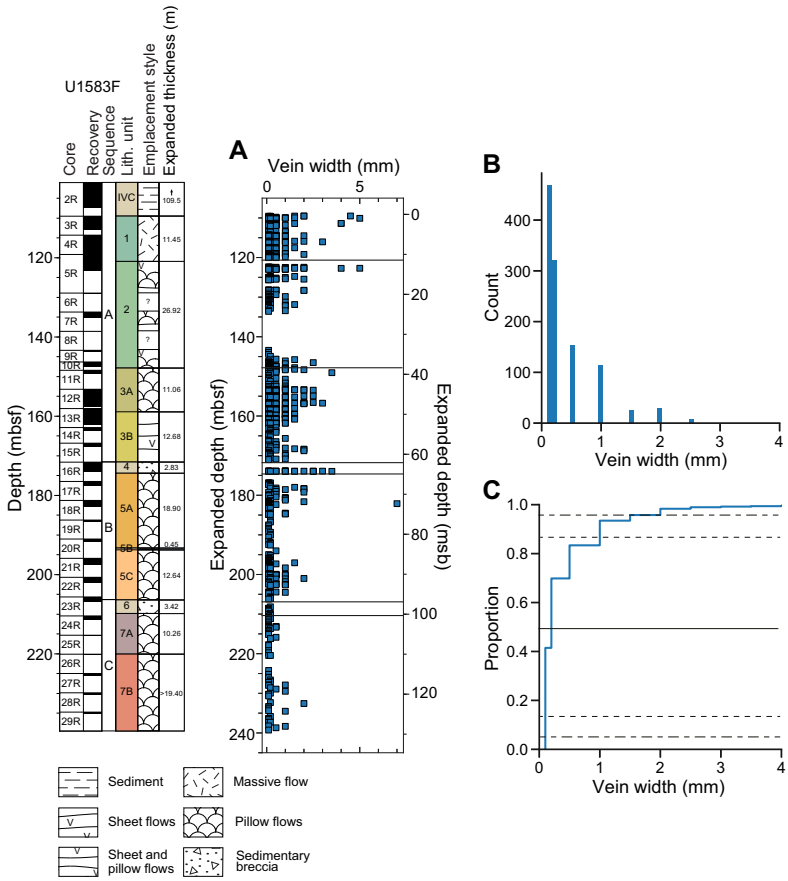

Figure F38. A–C. Vein width characteristics, Hole U1583F. C: solid line = median value (0.5 proportion), dashed lines = 1σ equivalent range of median, dot-dashed lines = 2σ equivalent range of median. Expanded depth scale stretches curated depths within each core advance to compensate for incomplete recovery (see the Expedition 390/393 methods chapter [Coggon et al., 2024a]).

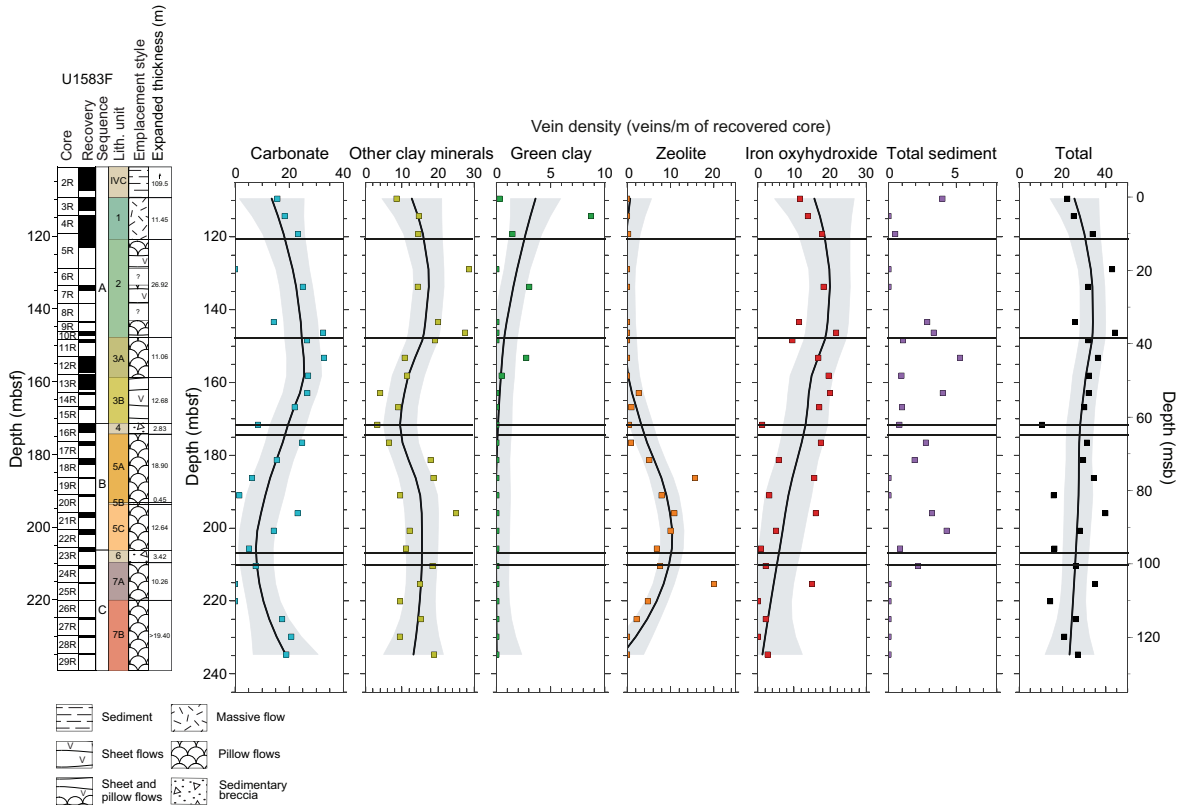

Figure F39. Vein density per meter normalized to core recovery, Hole U1583F. Total veins are separated by secondary mineral fill. Data plotted at the top depth of each core. Black trend lines = locally weighted scatter plot smoothing (LOWESS) nonparametric regression, gray shaded areas = 2σ of mean.

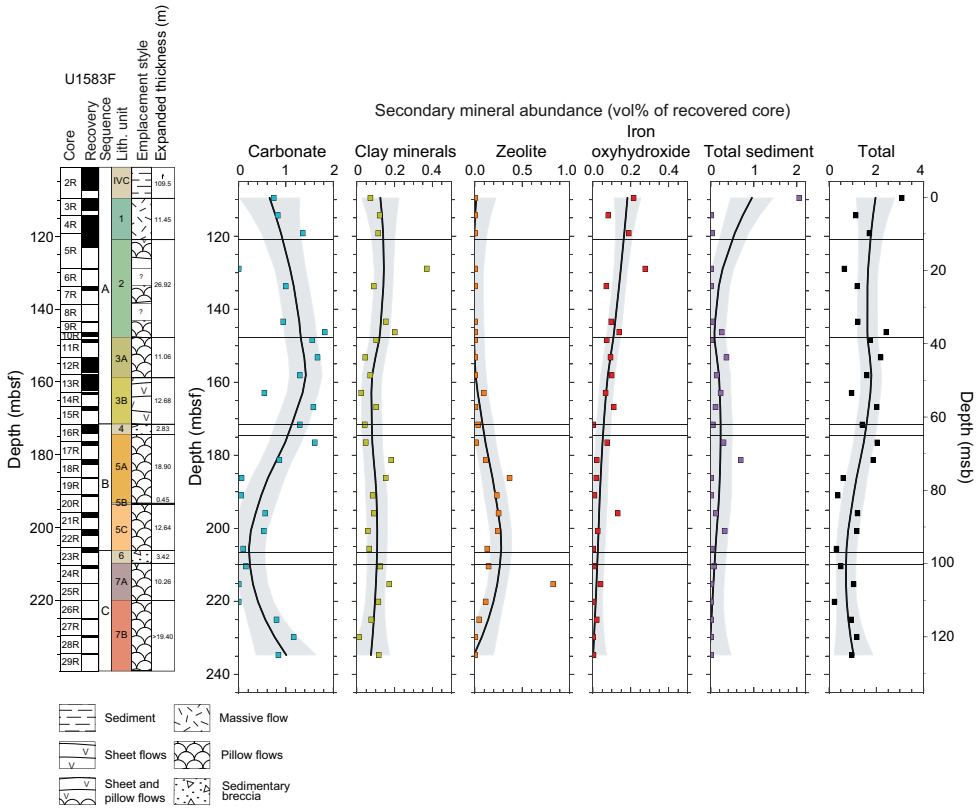

Figure F40. Secondary mineral abundance normalized to core recovery, Hole U1583F. Black trend lines = locally weighted scatter plot smoothing (LOWESS) nonparametric regression, gray shaded areas = 2σ of mean.

The vein width distribution of veins associated with a halo is broadly log normal and contrasts with the generally geometric distribution of veins that are not associated with a halo (Figure **F44**).

6.6. Structural data

The dip direction and dip angle of ~40% of logged veins were measured with true dip angles ranging 1°–89° (Figure **F45**). The median and mean vein true dip angle of measured veins is 48° (Figure **F45**). The distribution of all measured vein true dip angles generally yields a multimodal distribution (Figure **F45**). No systematic relationship between true vein dip angle and depth occurs (Figure **F45**). The true vein dip angle of single event veins generally yields a uniform distribution (Figure **F43**). Multiple event veins are the dominant vein type and display a broadly multimodal distribution with most orientated veins occurring at 30° dip angle (Figure **F43**). Measured true dip angles

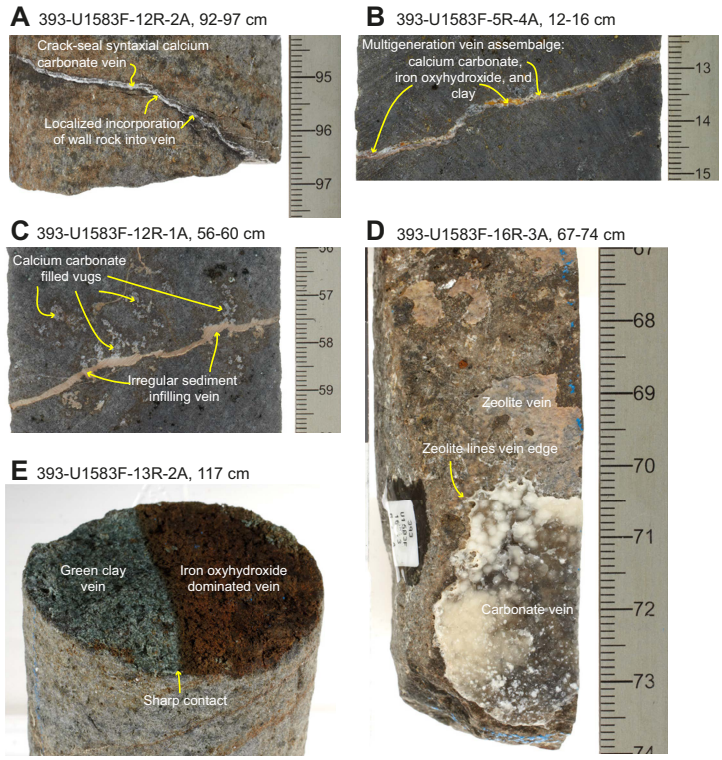

Figure F41. Typical vein assemblages, Hole U1583F. A. Crack-seal syntaxial calcium carbonate vein showing localized incorporation of wall rock into vein assemblage. B. Multiple generation vein assemblage composed of calcium carbonate, Fe oxyhydroxide, and clay. C. Irregular sediment infilling vein with vugs filled by calcium carbonate. D. Vein assemblage composed of calcium carbonate and zeolite with zeolite lining vein edge. E. Green clay and Fe oxyhydroxide vein with change in composition occurring along vein, resulting in discrete sharp contact.

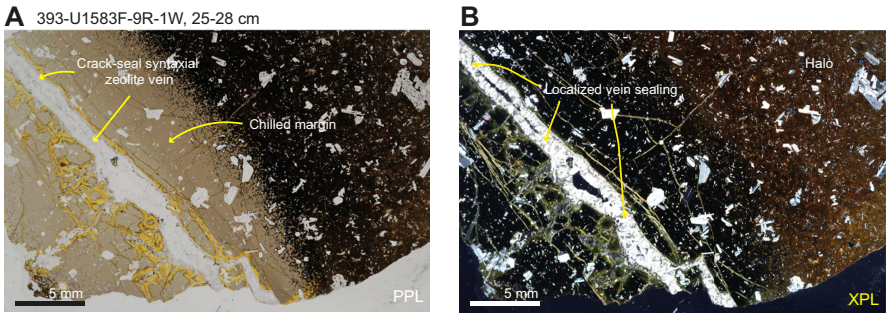

Figure F42. A, B. Internal structure of zeolite vein, Hole U1583F. Crack-seal syntaxial zeolite vein occurring in variably altered chilled margin associated with halo.

of veins associated with and without a halo yield similar multimodal distributions with little variation between veins associated with and without a halo (Figure **F43**).

6.7. XRD

XRD spectra were generated for alteration products and precipitates as well as strongly altered and recrystallized sedimentary material collected from veins and vugs, interpillow breccias,

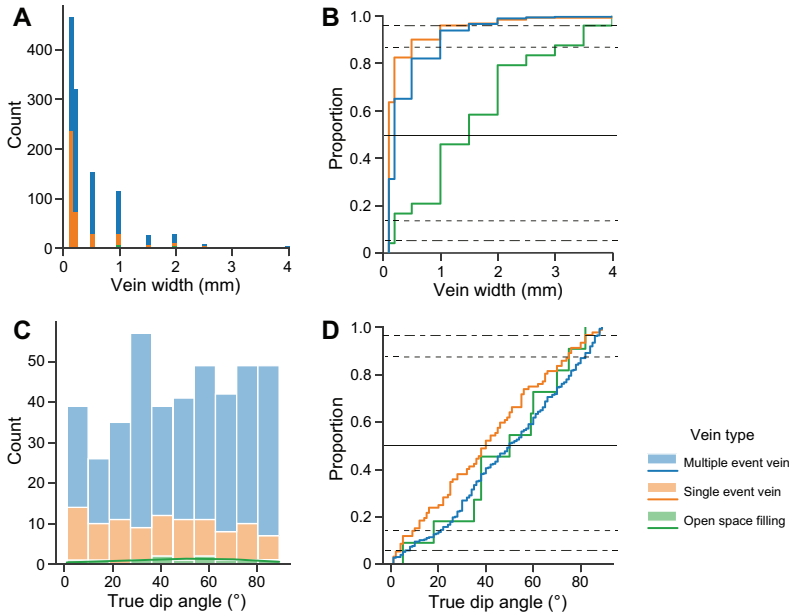

Figure F43. Vein width and dip angle statistics, Hole U1583F. A. Vein width histogram of vein types: single event veins (massive veins; see Alteration petrology in the Expedition 390/393 methods chapter [Coggon et al., 2024a]), multiple event veins (polycrystalline veins and crack-seal veins), and open space fillings. B. Vein width cumulative frequency of differing vein types. C. Vein dip angle histogram of vein types with respective probability density. D. Vein dip angle cumulative frequency of differing vein types.

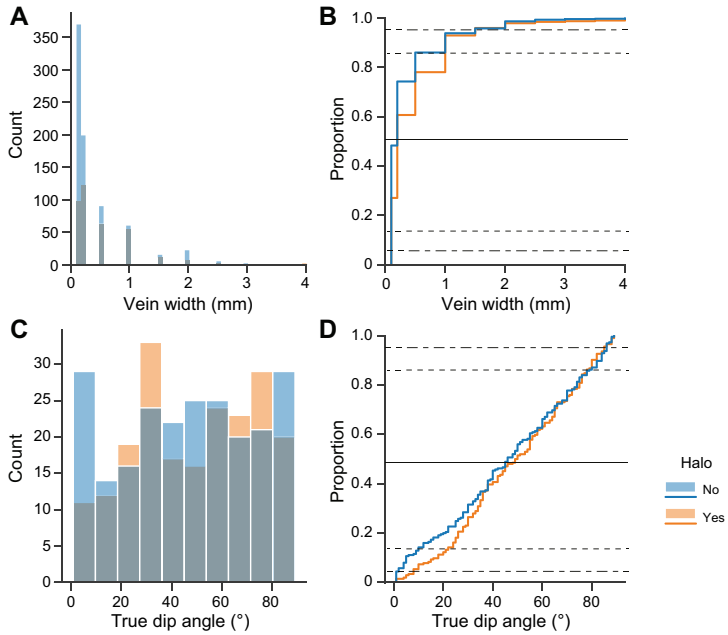

Figure F44. Vein width and dip angle statistics differentiated by halo association, Hole U1583F. A. Vein width histogram. B. Vein width cumulative frequency. C. Vein dip angle histogram. D. Vein dip angle cumulative frequency.

microbiology (MBIO) samples, and altered rock clasts in sediment cores (Table **T8**). XRD results for vein and vug fillings reveal mainly (magnesian) calcite, Na-phillipsite, and/or feldspar, with minor clay components, aragonite, clinopyroxene, oxides, and sepiolite. Additional peaks suggest the presence of other phyllosilicates, K-bearing feldspar, and possibly chamosite. Hydrothermal vein precipitates in Sections 393-U1583F-4R-3 and 4R-4 contain both calcite and aragonite. Samples from interpillow breccias are dominated by (magnesian) calcite, feldspar, and clinopyroxene with minor zeolite and possibly chlorite. XRD spectra from MBIO samples reveal (magnesian) calcite, Na-phillipsite, clays, feldspar, and goethite. The spectra of two altered basalt clasts in sediment Core 12H imply the presence of feldspar and zeolites. The evaluation of bulk rock powder spectra suggests dominantly calcic to sodic feldspars and clinopyroxene as well as minor amounts of olivine, Fe oxides, and additional spectral peaks that indicate the variable presence of clays and calcite (see U1583F_XRD.xlsx in ALTPET in **Supplementary material**).

6.8. Summary

Hole U1583F records fluid/rock reactions over the full range of spatial contexts expected for the uppermost basement. The secondary minerals forming, predominantly various clays, carbonate and Fe oxyhydroxides, are consistent with reactions at low temperatures with seawater-derived fluids. In Hole U1583F, it is possible to identify zones of alteration that have distinct characteristics (Figure **F46**). In the uppermost 70 m of the hole, background alteration dominates, and cores are characterized by the presence of green clay filling vesicles (in background and alteration halos) and a generally low abundance of alteration halos (generally less than 30% of the area of the core). This zone also hosts the most calcium carbonate, and carbonate abundance increases downhole

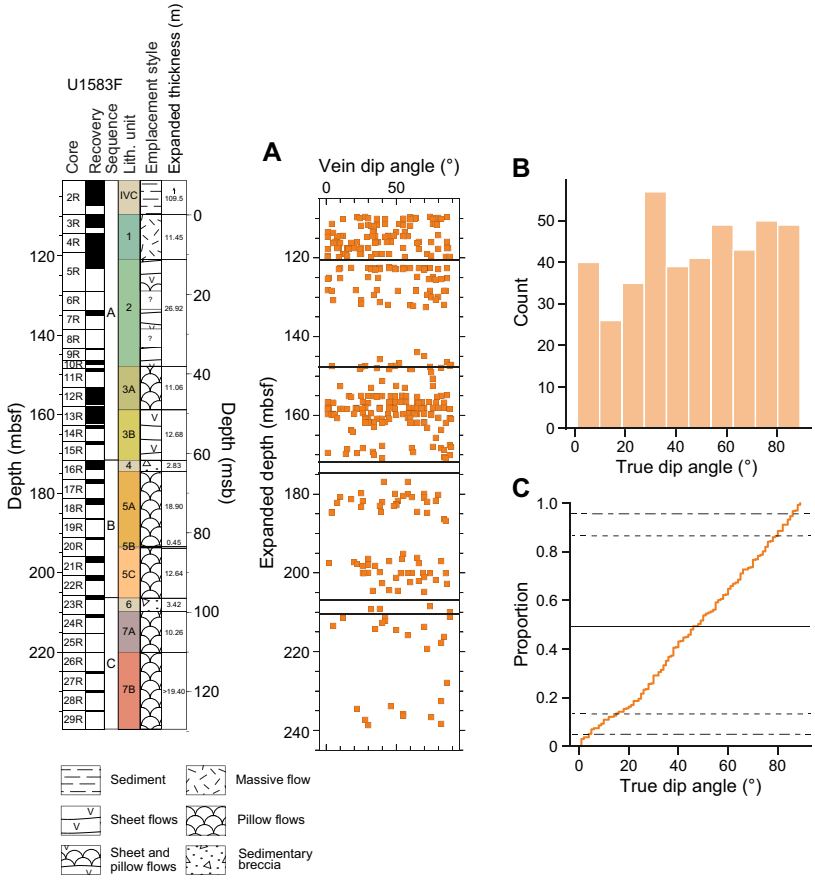

Figure F45. A. Vein dip angles, Hole U1583F. B. Histogram is binned into 12 distinct groups (spaced 7.5° each) showing multimodal distribution. C. Dip angle proportions. Solid line = median value (0.5 proportion), dashed lines = 1σ equivalent range of median, dot-dashed lines = 2σ equivalent range of median. Expanded depth scale stretches curated depths within each core advance to compensate for incomplete recovery (see the Expedition 390/393 methods chapter [Coggon et al., 2024a]).

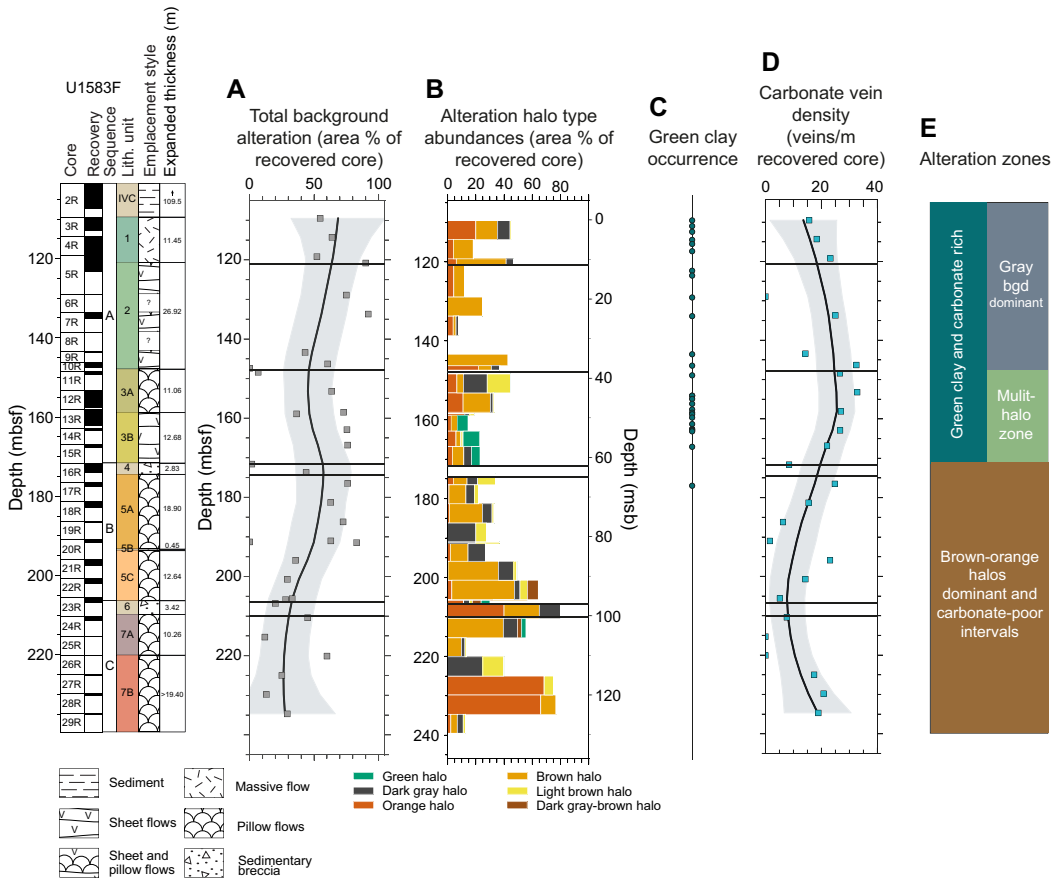

Figure F46. A–E. Overview of alteration zones, Hole U1583F.

through this zone. From 40 to 70 msb, the multihalos appear and exhibit diffuse but also sharp halo sequences that are variably mutually overprinting. These multihalos are best displayed by the changing sequences of vesicle infill. Below 70 msb, green clay filled vesicles are absent and the abundance of carbonate filled veins decreases. These changes are accompanied by a greater proportion of halos, and the abundance of brown halos increases downhole. Below 95 msb, orange halos are most common and there is a slight increase in the abundance of carbonate veins.

7. Biostratigraphy

The sedimentary succession of pelagic nannofossil oozes and clays at Site U1583 ranges in age from early Oligocene to Late Pleistocene. The integrated calcareous nannoplankton and planktic foraminiferal biozonation for Site U1583 is summarized in Figure **F47** and Tables **T9** and **T10**. The age-depth table and plots of biohorizons and paleomagnetic reversals for Holes U1583C and U1583E can be found in **Age model and mass accumulation rates** (Tables **T21**, **T22**; Figures **F65**, **F66**). Benthic foraminifera were not analyzed at this site.

All core catcher samples from Holes U1583C and U1583E were analyzed, and two additional samples were taken from the working halves of Hole U1583C to refine the nannofossil biostratigraphy. These samples were selected to avoid clay-rich intervals and maximize microfossil diversity.

In the mudline sample from Hole U1583C, planktic foraminiferal assemblages consist of extant and Late Pleistocene species, whereas the calcareous nannofossil assemblages indicate an Early Pleistocene age. In contrast, the mudline sample from Hole U1583E contains modern assemblages of both planktic foraminifera and calcareous nannoplankton. Pliocene to Pleistocene sediments are found above 11.14 m core depth below seafloor, Method B (CSF-B), in Hole U1583C and 13.46 m CSF-B in Hole U1583E. A condensed interval, mainly composed of dark clay (Lithostratigraphic

Unit III; see **Sedimentology**), spans ~9 My across the Miocene/Pliocene boundary and measures ~6.5 m thick in Hole U1583C and 11.83 m thick in Hole U1583E. Early Middle Miocene fossils span 14.84–35.97 m CSF-B in Hole U1583C and 22.95–41.96 m CSF-B in Hole U1583E. The Oligocene/Miocene boundary in Hole U1583C occurs in Core 393-U1583C-5H, and in Hole U1583E it occurs in Core 393-U1583E-6H, as inferred from calcareous nannofossil biostratigraphy. Oligocene sediments are ~71 m thick in Hole U1583C and ~54 m thick in Hole U1558E.

7.1. Age of basement

Three indurated calcareous sediment samples from directly above and within the lava flows recovered from Hole U1583F were analyzed, but no nannofossils were observed because of poor preservation. The most robust age determination is observed in the deepest sediment samples from Holes U1583C (Sample 393-U1583C-12H-CC, 12–17 cm; 104.58 m CSF-B) and U1583E (Sample 393-U1583E-12H-CC, 0–1 cm; 105.12 m CSF-B), both of which contain the calcareous nanno-

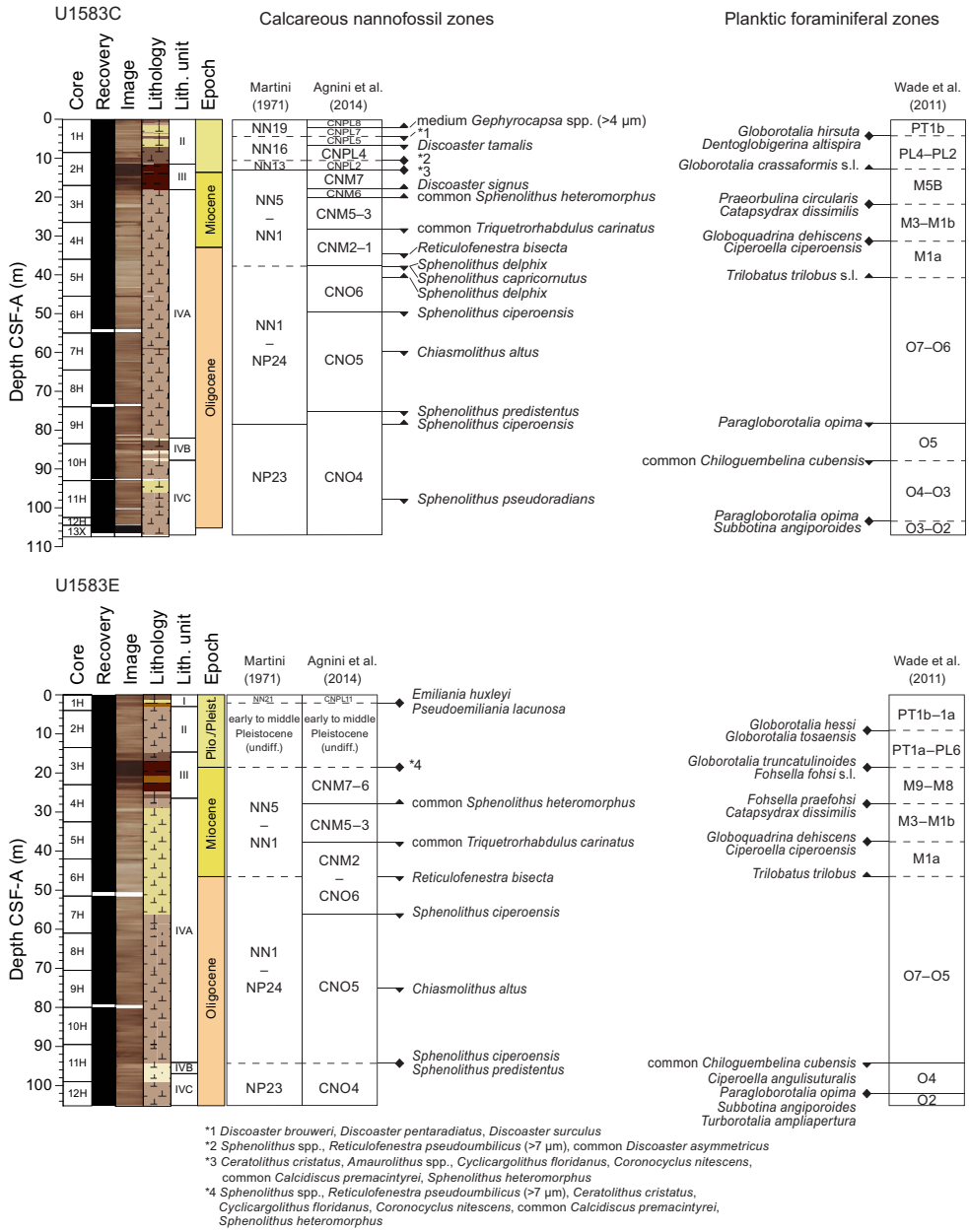

Figure F47. Calcareous nannofossil and planktic foraminiferal biostratigraphic zones and datums, Holes U1583C and U1583F. Upward arrows = bioevent base (first occurrence), downward arrows = bioevent top (last occurrence).

fossil species *Sphenolithus distentus*, suggesting that sediments near the sediment/basement interface are younger than 30.0 Ma. Planktic foraminiferal assemblages in the same two samples contain *Subbotina angiporoides* and record the disappearance of *Paragloborotalia opima*, suggesting an age older than 30.8 Ma. These results are in good agreement with the projected crustal age of ~30.6 Ma at Site U1583 (see **Background and objectives**).

7.2. Calcareous nannofossils

We examined all core catcher samples from Holes U1583C and U1583E to establish the calcareous nannofossil biostratigraphy and analyzed additional smear slide samples from the working halves of Hole U1583C to refine biohorizons. Nannofossil distributions are displayed in Tables **T11** and **T12**, which summarize the occurrences of age-diagnostic and other notable taxa. Calcareous nannofossil preservation and abundances are illustrated in Figure **F48**, and photomicrographs of key calcareous nannofossil specimens from Site U1583 are presented in Figure **F49**. At Site U1583, nannofossils are generally abundant, but their preservation varies from poor to good depending on lithology (Figure **F48**). In nannofossil-rich samples (Lithostratigraphic Units I and II and Subunits IVA and IVC; see **Sedimentology**), nannofossils are generally abundant with moderate to good preservation. In contrast, nannofossils are common to abundant with poor to moderate preservation in clay-rich intervals (Unit III) and calcareous ooze (Subunit IVB).

Table T9. Integrated calcareous nannofossil and planktic foraminiferal datums, Hole U1583C. T = top, B = bottom, Bc = base common, HCO = highest consistent occurrence. Nannofossil zones follow Martini (1971), Backman et al. (2012), and Agnini et al. (2014), and planktic foraminiferal biozonation is based on Wade et al. (2011). **Download table in CSV format.**

Biozone	Datum type/Taxon	Age (Ma)	Core, section, interval above (cm)	Sample above depth CSF-A (m)	Sample above depth CSF-B (m)	Core, section, interval below (cm)	Sample below depth CSF-A (m)	Sample below depth CSF-B (m)	Midpoint depth CSF-A (m)	Midpoint depth CSF-B (m)	Depth error (±) CSF-A (m)	Depth error (±) CSF-B (m)
			393-U1583C-			393-U1583C-						
top CNPL7	B medium *Gephyrocapsa* spp.	1.71	1H-1, 135–135	1.35	1.350	1H-2, 125–127	2.77	2.770	2.06	2.06	0.71	0.71
top CNPL6	T *Discoaster brouweri*	1.93	1H-3, 32–32	3.32	3.320	1H-4, 83–83	5.33	5.330	4.33	4.33	1.01	1.01
top CNPL5	T *Discoaster pentaradiatus*	2.39	1H-3, 32–32	3.32	3.320	1H-4, 83–83	5.33	5.330	4.33	4.33	1.01	1.01
in CNPL5	T *Discoaster surculus*	2.53	1H-3, 32–32	3.32	3.320	1H-4, 83–83	5.33	5.330	4.33	4.33	1.01	1.01
top CNPL4	T *Discoaster tamalis*	2.76	1H-4, 101–103	5.51	5.510	1H-6, 11–13	7.63	7.630	6.57	6.57	1.06	1.06
in CNPL4	T *Sphenolithus* spp.	3.61	2H-1, 130–130	9.80	9.800	2H-2, 114–116	11.16	11.160	10.48	10.48	0.68	0.68
top CNPL3	T *Reticulofenestra pseudoumbilicus* (>7 µm)	3.82	2H-1, 130–130	9.80	9.800	2H-2, 114–116	11.16	11.160	10.48	10.48	0.68	0.68
top CNPL2	Bc *Discoaster asymmetricus*	4.04	2H-1, 130–130	9.80	9.800	2H-2, 114–116	11.16	11.160	10.48	10.48	0.68	0.68
in CNPL1	B *Ceratolithus cristatus*	5.08	2H-2, 114–116	11.14	11.140	2H-5, 34–36	14.86	14.860	13.00	13.00	1.86	1.86
top CNM16	B *Amaurolithus* spp.	7.45	2H-2, 114–116	11.14	11.140	2H-5, 34–36	14.86	14.860	13.00	13.00	1.86	1.86
in CNM9	T *Cyclicargolithus floridanus*	11.85	2H-2, 114–116	11.14	11.140	2H-5, 34–36	14.86	14.860	13.00	13.00	1.86	1.86
in CNM9	T *Coronocyclus nitescens*	12.45	2H-2, 114–116	11.14	11.140	2H-5, 34–36	14.86	14.860	13.00	13.00	1.86	1.86
top CNM8	Tc *Calcidiscus premacintyrei*	12.57	2H-2, 114–116	11.14	11.140	2H-5, 34–36	14.86	14.860	13.00	13.00	1.86	1.86
top CNM7	T *Sphenolithus heteromorphus*	13.66	2H-2, 114–116	11.14	11.140	2H-5, 34–36	14.86	14.860	13.00	13.00	1.86	1.86
top CNM6	B *Discoaster signus*	15.85	2H-CC	16.90	16.900	3H-1, 133–133	18.33	18.330	17.62	17.62	0.71	0.71
top CNM5	Bc *Sphenolithus heteromorphus*	17.65	3H-2, 91–91	19.44	19.440	3H-3, 91–91	20.94	20.940	20.19	20.19	0.75	0.75
top CNM2	Tc *Triquetrorhabdulus carinatus*	19.18	3H-CC	26.42	26.420	4H-3, 17–19	29.70	29.567	28.06	27.99	1.64	1.57
in CNO6	T *Reticulofenestra bisecta*	23.13	4H-5, 34–36	32.86	32.597	4H-CC	36.41	36.000	34.64	34.30	1.77	1.70
top CNO6	T *Sphenolithus delphix*	23.11	4H-CC	36.36	35.952	5H-3, 4–6	39.06	39.060	37.71	37.51	1.35	1.55
top CNO6	T *Sphenolithus capricornutus*	23.11	4H-CC	36.36	35.952	5H-3, 4–6	39.06	39.060	37.71	37.51	1.35	1.55
in CNO6	B *Sphenolithus delphix*	23.72	5H-3, 4–6	39.04	39.040	5H-5, 9–11	42.12	42.120	40.58	40.58	1.54	1.54
top CNO5	T *Sphenolithus ciperoensis*	24.36	6H-2, 120–122	48.21	48.210	6H-4, 93–95	50.97	50.970	49.59	49.59	1.38	1.38
in CNO5	T *Chiasmolithus altus*	25.44	7H-3, 10–12	58.11	58.052	7H-5, 20–22	61.25	61.134	59.68	59.59	1.57	1.54
top CNO4	T *Sphenolithus predistentus*	26.93	8H-CC	73.08	73.080	9H-3, 9–11	77.11	77.110	75.10	75.10	2.02	2.02
in CNO4	B *Sphenolithus ciperoensis*	27.13	9H-3, 9–11	77.09	77.090	9H-4, 139–141	79.92	79.920	78.51	78.51	1.42	1.42
in CNO4	T *Sphenolithus pseudoradians*	28.73	11H-3, 14–16	96.14	96.085	11H-5, 29–31	99.32	99.209	97.73	97.65	1.59	1.56
in PT1b	B *Globorotalia hirsuta*	0.45	Mudline	0.00	0.000	1H-CC, 14–19	8.47	8.470	4.24	4.24	4.24	4.24
top PL4	T *Dentoglobigerina altispira*	3.00	Mudline	0.00	0.000	1H-CC, 14–19	8.47	8.470	4.24	4.24	4.24	4.24
in PL2	B *Globorotalia crassaformis*	4.30	1H-CC, 14–19	8.42	8.420	2H-CC, 16–21	16.95	16.950	12.69	12.69	4.27	4.27
in M5b	B *Praeorbulina circularis*	15.98	2H-CC, 16–21	16.90	16.900	3H-CC, 16–21	26.47	26.470	21.69	21.69	4.79	4.79
top M3	T *Catapsydrax dissimilis*	17.51	2H-CC, 16–21	16.90	16.900	3H-CC, 16–21	26.47	26.470	21.69	21.69	4.79	4.79
base M1b	B *Globoquadrina dehiscens*	22.50	3H-CC, 16–21	26.42	26.420	4H-CC, 32–37	36.41	36.000	31.42	31.21	4.99	4.79
in M1a	T *Ciperoella ciperoensis*	22.81	3H-CC, 16–21	26.42	26.420	4H-CC, 32–37	36.41	36.000	31.42	31.21	4.99	4.79
in M1a	B *Trilobatus trilobus* s.l.	22.88	4H-CC, 32–37	36.36	35.952	5H-CC, 15–20	45.36	45.360	40.86	40.66	4.50	4.70
top O5	T *Paragloborotalia opima*	27.30	8H-CC, 13–18	73.08	73.080	9H-CC, 20–25	83.27	83.270	78.18	78.18	5.09	5.09
top O4	HCO *Chiloguembelina cubensis*	28.30	9H-CC, 20–25	83.22	83.220	10H-CC, 20–25	92.54	92.540	87.88	87.88	4.66	4.66
in O3	T *Subbotina angiporoides*	30.10	11H-CC, 17–22	102.62	102.451	12H-CC, 12–17	110.52	104.500	106.57	103.48	3.95	1.02
in O2	B *Paragloborotalia opima*	30.80	11H-CC, 17–22	102.62	102.451	12H-CC, 12–17	110.52	104.500	106.57	103.48	3.95	1.02

The mudline sample from Hole U1583C contains the extant taxon *Emiliania huxleyi* (indicative of Zone CNPL11), which indicates that the seafloor is younger than 0.29 Ma. From the seafloor to the lowest sample above the dark brown clay unit (Lithostratigraphic Unit II) (Samples 393-U1583C-2H-2, 114–116 cm [11.14 m CSF-B], and 393-U1583E-2H-CC, 11–16 cm [13.47 m CSF-B]), assemblages represent Pliocene and Pleistocene Zones CNPL1–CNPL11. *Pseudoemiliania lacunosa* occurs in the first sediment sample from both holes (Samples 393-U1583C-1H-1, 135 cm, and 393-U1583E-1H-CC, 12–17 cm; 1.35 and 3.95 m CSF-B, respectively), which indicates that the sediment is older than 0.43 Ma (below Zone CNPL10). In Hole U1583C, the base of medium-sized *Gephyrocapsa* spp. (4–5.5 µm; top of Zone CNPL7) is recorded in Sample 393-U1583C-1H-1, 135 cm (1.35 m CSF-B). Three biohorizons are recorded in Sample 1H-4, 83 cm (5.33 m CSF-B): the top of *Discoaster brouweri* (1.93 Ma), the top of *Discoaster pentaradiatus* (2.39 Ma), and the top of *Discoaster surculus* (2.53 Ma). The wide age range likely reflects the slow sedimentation rate in this interval, and the true tops of these datums are likely spread out between samples. Below this, the top of *Discoaster tamalis* (2.76 Ma; top of Zone CNPL4) is identified in Sample 1H-6, 11–13 cm (7.61 m CSF-B). The next useful biohorizons are the top of *Sphenolithus* spp., the top of *Reticulofenestra pseudoumbilicus* (>7 µm; base of Zone CNPL4), and the base common of *Discoaster asymmetricus* (top of Zone CNPL2), which were all observed in Samples 2H-1, 130 cm, and 2H-2, 114–116 cm (9.80–11.14 m CSF-B in Hole U1583C).

Table T10. Integrated calcareous nannofossil and planktic foraminiferal datums, Hole U1583E. B = bottom, T = top, Bc = base common, Tc = top common, HCO = highest common occurrence. Nannofossil zones follow Martini (1971), Backman et al. (2012), and Agnini et al. (2014), and planktic foraminiferal biozonation is based on Wade et al. (2011). **Download table in CSV format.**

Biozone	Datum type/Taxon	Age (Ma)	Core, section, interval above (cm)	Sample above depth CSF-A (m)	Sample above depth CSF-B (m)	Core, section, interval below (cm)	Sample below depth CSF-A (m)	Sample below depth CSF-B (m)	Midpoint depth CSF-A (m)	Midpoint depth CSF-B (m)	Depth error (±) CSF-A (m)	Depth error (±) CSF-B (m)
			393-U1583E-			393-U1583E-						
in CNPL11	B *Emiliania huxleyi*	0.29	1H-1, 0–0	0.00	0.000	1H-CC	4.03	4.000	2.02	2.00	2.02	2.00
top CNPL10	T *Pseudoemiliania lacunosa*	0.41	1H-1, 0–0	0.00	0.000	1H-CC	4.03	4.000	2.02	2.00	2.02	2.00
in CNPL4	T *Sphenolithus* spp.	3.61	2H-CC	13.84	13.453	3H-CC	23.03	23.001	18.44	18.23	4.59	4.77
top CNPL3	T *Reticulofenestra pseudoumbilicus* (>7 µm)	3.82	2H-CC	13.84	13.453	3H-CC	23.03	23.001	18.44	18.23	4.59	4.77
in CNPL1	B *Ceratolithus cristatus*	5.08	2H-CC	13.84	13.453	3H-CC	23.03	23.001	18.44	18.23	4.59	4.77
in CNM9	T *Cyclicargolithus floridanus*	11.85	2H-CC	13.84	13.453	3H-CC	23.03	23.001	18.44	18.23	4.59	4.77
in CNM9	T *Coronocyclus nitescens*	12.45	2H-CC	13.84	13.453	3H-CC	23.03	23.001	18.44	18.23	4.59	4.77
top CNM8	Tc *Calcidiscus premacintyrei*	12.57	2H-CC	13.84	13.453	3H-CC	23.03	23.001	18.44	18.23	4.59	4.77
top CNM7	T *Sphenolithus heteromorphus*	13.66	2H-CC	13.84	13.453	3H-CC	23.03	23.001	18.44	18.23	4.59	4.77
top CNM5	Bc *Sphenolithus heteromorphus*	17.65	3H-CC	22.98	22.951	4H-CC	32.49	32.390	27.74	27.67	4.76	4.72
top CNM2	Tc *Triquetrorhabdulus carinatus*	19.18	4H-CC	32.44	32.440	5H-CC	42.68	42.000	37.56	37.22	5.12	4.78
in CNO6	T *Reticulofenestra bisecta*	23.13	5H-CC	42.63	41.953	6H-CC	50.39	50.390	46.51	46.17	3.88	4.22
top CNO5	T *Sphenolithus ciperoensis*	24.36	6H-CC	50.34	50.340	7H-CC	61.46	61.000	55.90	55.67	5.56	5.33
in CNO5	T *Chiasmolithus altus*	25.44	8H-CC	70.73	70.501	9H-CC	79.14	79.140	74.94	74.82	4.20	4.32
top CNO4	T *Sphenolithus predistentus*	26.93	10H-CC	89.61	89.451	11H-CC	99.02	99.000	94.32	94.23	4.70	4.77
in CNO4	B *Sphenolithus ciperoensis*	27.13	10H-CC	89.61	89.451	11H-CC	99.02	99.000	94.32	94.23	4.70	4.77
top PT1a	T *Globorotalia tosaensis*	0.61	1H-CC, 12–17	3.98	3.950	2H-CC, 11–16	13.89	13.501	8.94	8.73	4.96	4.78
in PT1a	B *Globorotalia hessi*	0.74	1H-CC, 12–17	3.98	3.950	2H-CC, 11–16	13.89	13.501	8.94	8.73	4.96	4.78
in PL6	B *Globorotalia truncatulinoides*	1.92	2H-CC, 11–16	13.84	13.453	3H-CC, 9–14	23.03	23.001	18.44	18.23	4.59	4.77
top M9	T *Fohsella fohsi s.l.*	11.81	2H-CC, 11–16	13.84	13.453	3H-CC, 9–14	23.03	23.001	18.44	18.23	4.59	4.77
base M8	B *Fohsella praefohsi*	13.78	3H-CC, 9–14	22.98	22.951	4H-CC, 14–19	32.49	32.490	27.74	27.72	4.76	4.77
top M3	T *Catapsydrax dissimilis*	17.51	3H-CC, 9–14	22.98	22.951	4H-CC, 14–19	32.49	32.490	27.74	27.72	4.76	4.77
base M1b	B *Globoquadrina dehiscens*	22.50	4H-CC, 14–19	32.44	32.440	5H-CC, 15–20	42.68	42.000	37.56	37.22	5.12	4.78
in M1a	T *Ciperoella ciperoensis*	22.81	4H-CC, 14–19	32.44	32.440	5H-CC, 15–20	42.68	42.000	37.56	37.22	5.12	4.78
in M1a	B *Trilobatus trilobus*	22.88	5H-CC, 15–20	42.63	41.953	6H-CC, 11–16	50.39	50.390	46.51	46.17	3.88	4.22
top O4	HCO *Chiloguembelina cubensis*	28.30	10H-CC, 7–12	89.61	89.451	11H-CC, 15–20	99.02	99.000	94.32	94.23	4.70	4.77
base O4	B *Ciperoella angulisuturalis*	29.50	11H-CC, 15–20	98.97	98.950	12H-CC, 0–1	105.13	105.130	102.05	102.04	3.08	3.09
in O3	T *Subbotina angiporoides*	30.10	11H-CC, 15–20	98.97	98.950	12H-CC, 0–1	105.13	105.130	102.05	102.04	3.08	3.09
top O2	T *Turborotalia ampliapertura*	30.40	11H-CC, 15–20	98.97	98.950	12H-CC, 0–1	105.13	105.130	102.05	102.04	3.08	3.09
in O2	B *Paragloborotalia opima*	30.80	11H-CC, 15–20	98.97	98.950	12H-CC, 0–1	105.13	105.130	102.05	102.04	3.08	3.09

Table T11. Important calcareous nannofossils, Hole U1583C. **Download table in CSV format.**

Table T12. Important calcareous nannofossils, Hole U1583E. **Download table in CSV format.**

Below the dark brown clay (Lithostratigraphic Unit II), Samples 393-U1583C-2H-5, 34–36 cm (14.84 m CSF-B), and 393-U1583E-3H-CC, 9–14 cm (22.95 m CSF-B), are assigned to the Middle Miocene. In Hole U1583C, six bioevents including the base of *Ceratolithus cristatus* (5.08 Ma), the base of *Amaurolithus* spp. (7.45 Ma), the top of *Cyclicargolithus floridanus* (11.85 Ma), the top of *Coronocyclus nitescens* (12.45 Ma), the top common of *Calcidiscus premacintyrei* (12.57 Ma), and the top of *Sphenolithus heteromorphus* (13.66 Ma) are identified in Samples 393-U1583C-2H-2, 114–116 cm, and 2H-5, 34–36 cm (11.14–14.84 m CSF-B). In Hole U1583E, seven biohorizons including the top of *Sphenolithus* spp. (3.61 Ma), the top of *R. pseudoumbilicus* (>7 µm; 3.82 Ma), the base of *Ceratolithus cristatus* (5.08 Ma), the top of *C. floridanus* (11.85 Ma), the top of *C. nitescens* (12.45 Ma), the top common of *C. premacintyrei* (12.57 Ma), and the top of *S. heteromorphus* (13.66 Ma) are identified between Samples 393-U1583E-2H-CC, 11–16 cm, and 3H-CC, 9–14 cm (13.46–22.95 m CSF-B). The lithology of these intervals is mainly clay-rich sediment (Unit III; see **Sedimentology**); thus, we interpret these intervals in both holes (11.14–14.84 m CSF-B in Hole U1583C and 13.46–22.95 m CSF-B in Hole U1583E) to be a condensed interval spanning ~9 My that encompasses nannofossil Zones CNPL1–CNM8 and the Pliocene/Miocene boundary.

The Early–Middle Miocene (Zones CNM7–CNM1) is recognized between 14.84 and 35.97 m CSF-B in Hole U1583C and between 22.95 and 41.96 m CSF-B in Hole U1583E. The base of *Discoaster signus* (top of Zone CNM6) is located in Sample 393-U1583C-2H-CC, 16–21 cm (16.90 m CSF-B), and the base common of *S. heteromorphus* is identified in Samples 393-U1583C-3H-2, 91 cm (19.44 m CSF-B), and 393-U1583E-3H-CC, 9–14 cm (22.95 m CSF-B). Below this biohorizon, the top common of *Triquetrorhabdulus carinatus* is recorded in Samples 393-U1583C-4H-3, 17–19 cm (29.56 m CSF-B), and 393-U1583E-5H-CC, 15–20 cm (41.96 m CSF-B).

The Oligocene/Miocene boundary is constrained by the top of the short-ranging and distinctive sphenolith taxa *Sphenolithus delphix*, identified in Sample 393-U1583C-5H-3, 4–6 cm (39.04 m CSF-B), along with the top of *Sphenolithus capricornutus* in Hole U1583C. These taxa are not identified in Hole U1583E, likely due to sample resolution, and thus the Oligocene/Miocene boundary is approximated based on the top of *Reticulofenestra bisecta* in Sample 6H-CC, 11–16 cm (50.34 m CSF-B). However, in Hole U1583C the top of *R. bisecta* (23.13 Ma) is recorded above the top of *S. delphix* (23.11 Ma), suggesting that the top of *R. bisecta* might be diachronous in the South Atlantic Ocean. The top of *Sphenolithus ciperoensis* (top of Zone CNO5) is identified in Samples 393-U1583C-6H-4, 93–95 cm (50.95 m CSF-B), and 393-U1583E-7H-CC, 7–12 cm (60.96 m CSF-B). Within Zone CNO5, the top of *Chiasmolithus altus* is recorded in Samples 393-U1583C-7H-5, 20–22 cm (61.12 m CSF-B), and 393-U1583E-9H-CC, 9–14 cm (79.09 m CSF-B).

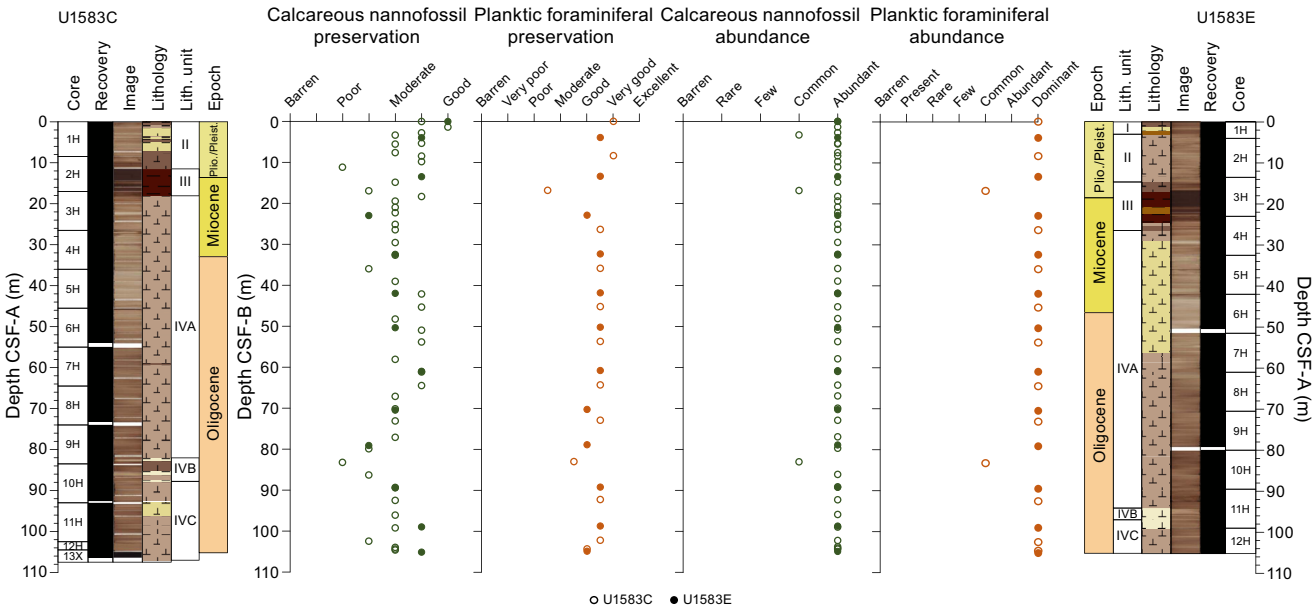

Figure F48. Downhole variations in group abundance and preservation of calcareous nannofossils and planktic foraminifera, Holes U1583C and U1583E.

The top of Zone CNO4 is recognized in Samples 393-U1583C-9H-3, 9–11 cm, and 393-U1583E-11H-CC, 15–20 cm (77.09 and 98.95 m CSF-B, respectively), by the top of *Sphenolithus predistentus*. Below this interval, the base of *S. ciperoensis* is identified in Samples 393-U1583C-9H-3, 9–11 cm (77.09 m CSF-B), and 393-U1583E-10H-CC, 7–12 cm (89.45 m CSF-B), and in Hole U1583C, the top of *Sphenolithus pseudoradians* (within Zone CNO4) is identified in Sample 393-U1583C-11H-5, 29–31 cm (99.19 m CSF-B). The deepest samples examined at Site U1583 contain *Sphenolithus distentus*, which constrains the sediment to younger than 30.0 Ma and corresponds well to both the planktic foraminiferal biostratigraphy and the estimated crustal age for Site U1583 of ~30.6 Ma (see **Background and objectives**).

7.3. Planktic foraminifera

Mudline and core catcher samples from Holes U1583C and U1583E were analyzed for planktic foraminifera. A summary of planktic foraminiferal biostratigraphy is presented in Figure **F47**. Planktic foraminifera are abundant throughout the sedimentary sequence, and preservation is mostly very good to good (Tables **T13**, **T14**). Detailed preservation and abundance data are presented in Figure **F48**. Significant specimens of planktic foraminifera are illustrated in Figure **F50**.

The Hole U1583C mudline sample contains a characteristic modern to Pleistocene planktic foraminiferal assemblage, including the marker species *Globorotalia hirsuta*, which has a lowest

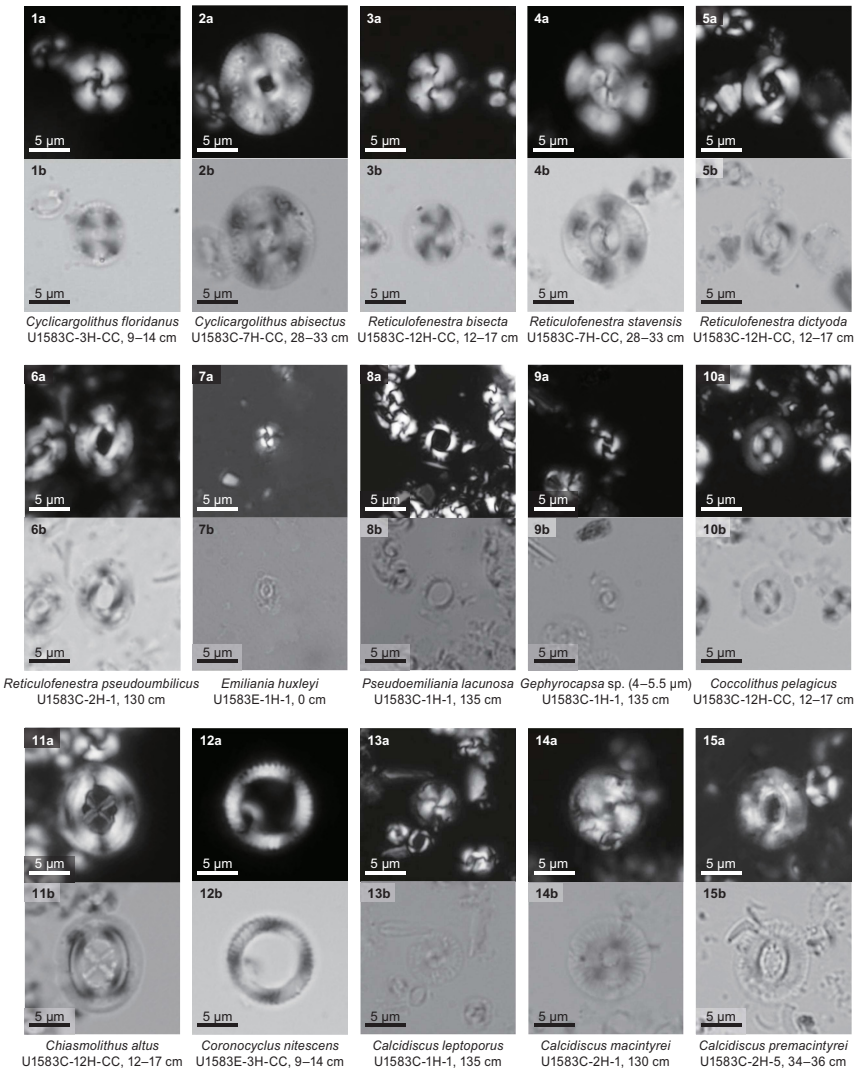

Figure F49. Biostratigraphically important and other notable calcareous nannofossil taxa, Site U1583 ([a] XPL and [b] PPL at 1000× magnification). (Continued on next page.)

occurrence at 0.45 Ma near the base of Zone PT1b. The assemblage in the Hole U1583E mudline sample is characterized by signs of dissolution and increased fragmentation of calcareous microfossils. This assemblage is tentatively interpreted to be modern based on the presence of relatively long ranging but extant taxa such as *Orbulina universa*, *Globoconella inflata*, and *Globigerinoides truncatulinoides*.

Sample 393-U1583E-1H-CC, 12–17 cm (3.95 m CSF-B), contains an Upper Pleistocene assemblage characterized by the presence of *Globorotalia hessi*, which has a base within Zone PT1a (0.74 Ma), and the absence of *G. hirsuta*, which has a base in Zone PT1b (0.45 Ma). Sample 2H-CC, 11–16 cm (13.46 m CSF-B), is assigned to Zones PT1a–PL6 undifferentiated based on the co-occurrence of *Globorotalia tosaensis* and *G. truncatulinoides*.

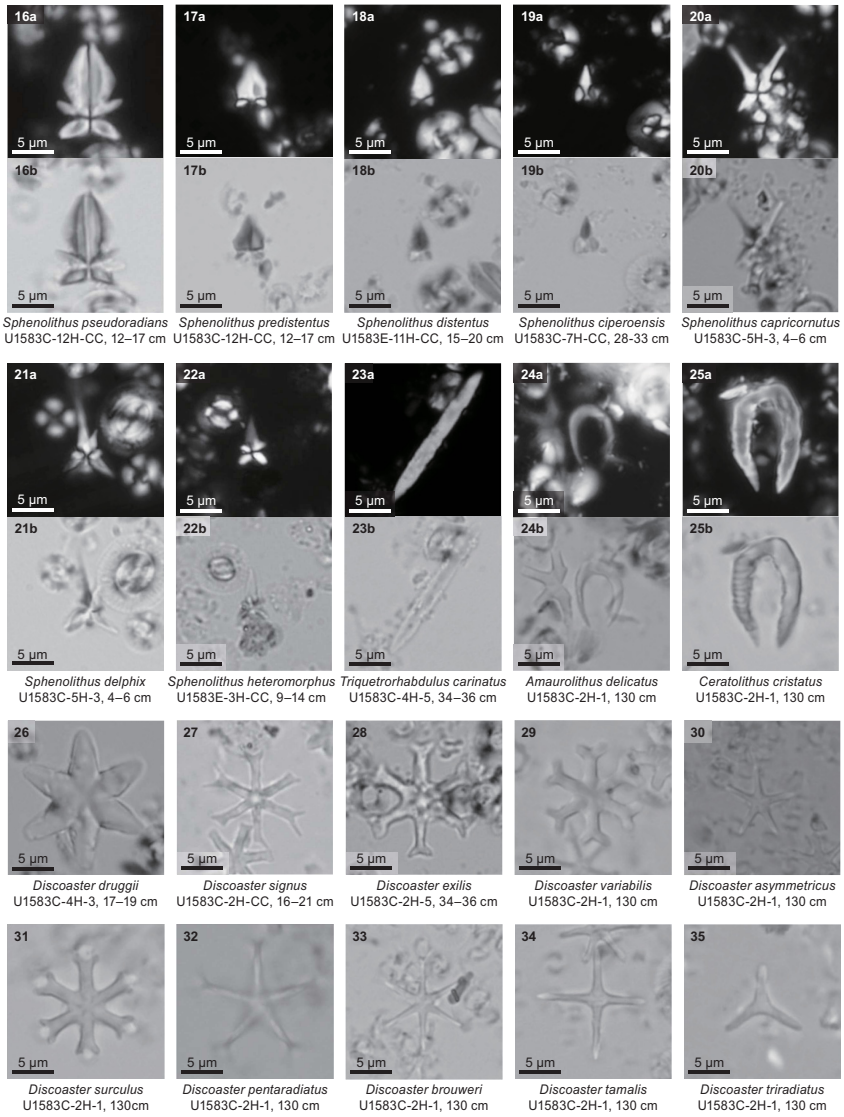

Figure F49 (continued).

Table T13. Important planktic foraminifera, Hole U1583C. **Download table in CSV format.**

Table T14. Important planktic foraminifera, Hole U1583E. **Download table in CSV format.**

The first evidence for Pliocene sediments in Hole U1583C comes from Sample 393-U1583C-1H-CC, 14–19 cm (8.42 m CSF-B), which contains the first occurrences of *Dentoglobigerina altispira* (which marks the top of Zone PL4, 3.0 Ma) and *Globorotalia crassaformis*, and extant species with a lowest occurrence near the base of Zone PL2. In adjacent Hole U1583E, we did not identify any Pliocene-age sediments. The next sample analyzed, Sample 393-U1583E-3H-CC, 9–14 cm (22.95 m CSF-B), contains Middle Miocene taxa, suggesting a condensed interval between 13.50 and 22.95 m CSF-B driven by low sedimentation rates and/or changes in the depth of the CCD.

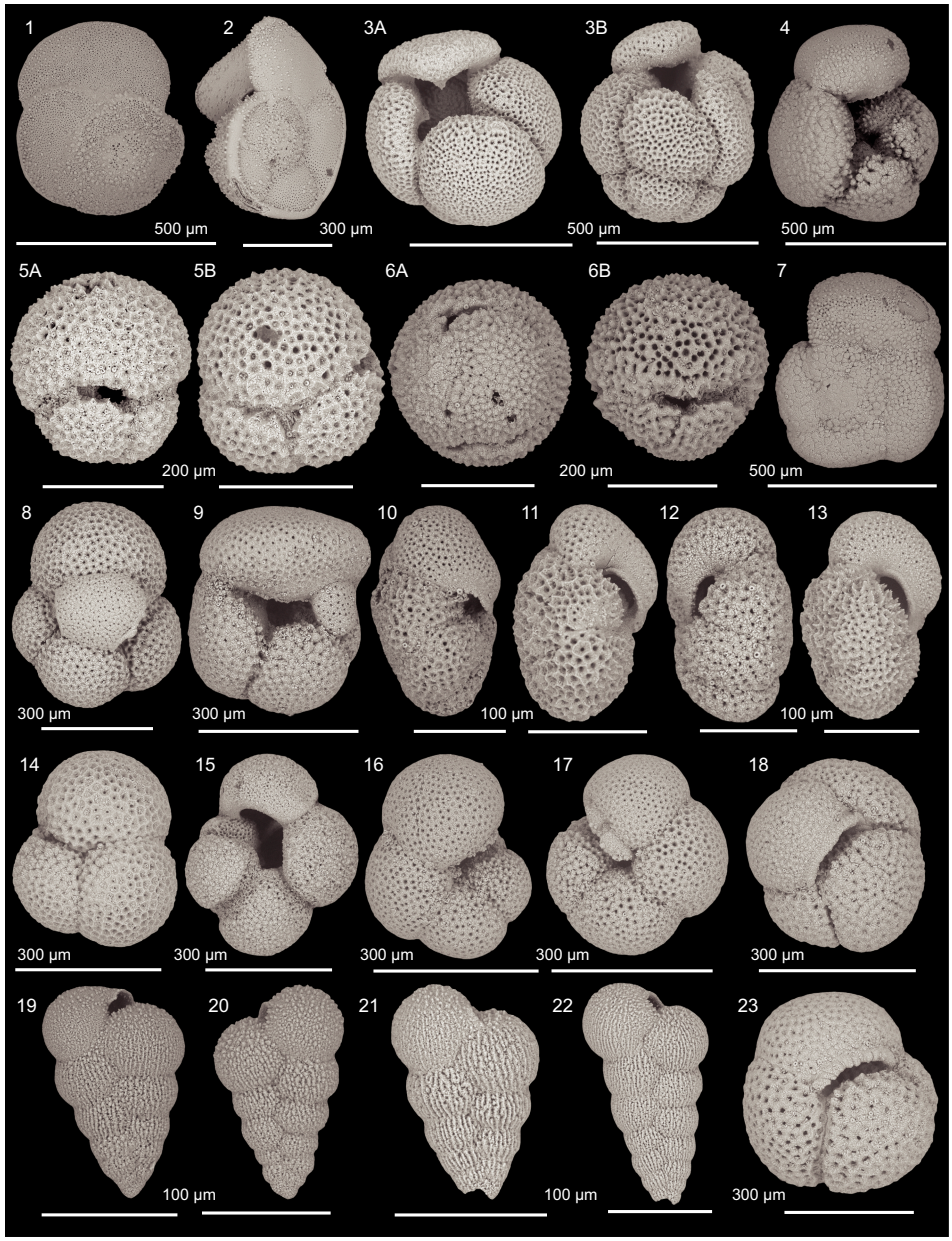

Figure F50. Scanning electron microscope images of biostratigraphically important and other notable planktic foraminiferal taxa, Hole U1583C. Each number represents a specimen; differing views of same specimen are denoted by the addition of letters (except for 4 and 7, which are the same specimen). 1, 2. 1H-1, mudline: (1) *Globorotalia hirsuta;* (2) *Globorotalia truncatulinoides*. 3, 4, 7. 1H-CC, 14–19 cm: (3) *Dentoglobigerina altispira*; (4, 7) *Globorotalia crassaformis*. 5, 6, 8, 9. 2H-CC, 16–21 cm: (5) *Trilobatus sicanus*; (6) *Praeorbulina glomerosa;* (8) *Catapsydrax dissimilis*; (9) *Globoquadrina dehiscens*. 10, 11. *Paragloborotalia kugleri* (10: 3H-CC, 16–21 cm; 11: 4H-CC, 32–37 cm). 12, 13. *Paragloborotalia pseudokugleri* (12: 3H-CC, 16–21 cm; 13: 4H-CC, 32–37 cm). 14, 15. 4H-CC, 32–37 cm: (14) *Trilobus trilobatus;* (15) *Ciperoella ciperoensis*. 16, 17. *Paragloborotalia opima* (9H-CC, 20–25 cm). 18, 23. *Subbotina angiporoides* (12H-CC, 12–17 cm). 19–22. *Chiloguembelina cubensis* (10H-CC, 20–25 cm).

Sample 393-U1583E-3H-CC, 9–14 cm (22.95 m CSF-B), is assigned to Zones M9–M8 undifferentiated based on the occurrence of the distinctive Middle Miocene taxon *Fohsella praefohsi*. In Hole U1583C, Sample 393-U1583C-2H-CC, 16–21 cm (16.90 m CSF-B), contains a population of the similarly distinctive Early to Middle Miocene genus *Praeorbulina* species, including *P. glomerosa, P. circularis*, and *P. curva*. The base of *Praeorbulina circularis*, calibrated at 15.98 Ma, in conjunction with the absence of *Orbulina suturalis* (marker taxa for the base of Zone M6 at 15.12 Ma), allows us to assign this sample to Zone M5b.

Samples 393-U1583C-3H-CC, 16–21 cm (26.42 CSF-B), and 393-U1583E-4H-CC, 14–19 cm (32.44 m CSF-B), are placed in Early Miocene Zones M3–M1b undifferentiated in the sedimentary sequences of both holes. This zonal assignment is based on the co-occurrence of *Catapsydrax dissimilis* and *Globoquadrina dehiscens*. The top of *C. dissimilis* marks the top of Zone M3 at 17.51 Ma, whereas the base of *G. dehiscens* occurs at the base of Zone M1b (22.50 Ma).

Samples 393-U1583C-4H-CC, 32–37 cm (35.97 m CSF-B), and 393-U1583E-5H-CC, 15–20 cm (41.96 m CSF-B), are assigned to Early Miocene Zone M1a based on the co-occurrences of *Ciperoella ciperoensis* and *Trilobatus trilobus*. The top of *C. ciperoensis* (22.81 Ma) and the base of *T. trilobus* (22.88 Ma) both occur within Zone M1a, giving a tight age constraint for these sediments in adjacent holes.

The four consecutive core catcher samples below this in Hole U1583C (Samples 393-U1583C-5H-CC, 15–20 cm, through 8H-CC, 13–18 cm; 45.31–73.08 m CSF-B) and five core catcher samples in Hole U1583E (Samples 393-U1583E-6H-CC, 11–16 cm, through 10H-CC, 7–12 cm; 50.34–89.45 m CSF-B) are dominated by long-ranging taxa (e.g., *Catapsydrax dissimilis* and *Catapsydrax unicavus*) and lack any age-diagnostic species, precluding confident zonal assignments. However, considering that in both holes this interval falls below the base of *T. trilobus*, it is likely late Oligocene.

The planktic foraminiferal assemblage in Sample 393-U1583C-9H-CC, 20–25 cm (83.22 m CSF-B), contains *Paragloborotalia opima,* indicating that these sediments are mid-Oligocene in age. The top of *P. opima* marks the top of Zone O5 at 27.3 Ma and provides an upper age constraint for the sample. The absence of *Chiloguembelina cubensis*, which occurs deeper in the hole, confirms the assignment of this sample to Zone O5 (27.3–28.3 Ma).

The highest common occurrence of *C. cubensis* (28.3 Ma), the marker bioevent for the top of Zone O4, is recorded in large numbers of the nominate taxon in Sample 393-U1583C-10H-CC, 20–25 cm (92.49 m CSF-B). This event, combined with the absence of *Subbotina angiporoides*, which is found farther downhole, allows us to assign this sample to Zones O4–O3 undifferentiated. In Hole U1583E, Sample 393-U1583E-11H-CC, 15–20 cm (98.95 m CSF-B), records the highest common occurrence of *C. cubensis* (28.3 Ma) along with the base of *Ciperoella angulisuturalis* (29.5 Ma), which places this sample firmly within Zone O4. The lowermost sample analyzed, Sample 393-U1583E-12H-CC, 0–1 cm (105.12 m CSF-B), contains rare specimens of *S. angiporoides* and *Turborotalia ampliapertura*. The top of *T. ampliapertura* marks the top of Zone O2, with the zonal assignment for this sample supported by the absence of *Paragloborotalia opima*, the base of which is typically placed within the same zone and calibrated to 30.8 Ma. In Hole U1583C, the lowermost Sample 393-U1583C-12H-CC, 12–17 cm (104.58 m CSF-B), contains common *S. angiporoides* and no *P. opima*. The base of *P. opima* is therefore recognized in the core catcher sample above (Sample 393-U1583C-11H-CC, 17–22 cm; 102.45 m CSF-B). The top of *S. angiporoides* occurs within Zone O3 at 30.1 Ma and, combined with the absence of *P. opima*, allows us to assign Sample 12H-CC, 12–17 cm, to Zones O3–O2 undifferentiated.

7.4. Benthic foraminifera

Benthic foraminifera were not analyzed at Site U1583.

8. Paleomagnetism

8.1. Sediment

Remanent magnetization was measured at 2 cm spacing using the superconducting rock magnetometer (SRM) on the archive halves of the sediment core sections from Holes U1583C and U1583E and the single sediment core from Hole U1583F (Core 393-U1583F-2R). Remanence was measured before and after alternating field (AF) demagnetization at three field strength steps of 5, 10, and 20 mT (see **Paleomagnetism** in the Expedition 390/393 methods chapter [Coggon et al., 2024a]) to isolate the characteristic remanent magnetization (ChRM). Strongly disturbed intervals (~3% of the total core length) were excluded from the measurements to avoid unreliable results. If a section was heavily disturbed for more than 50% of its extent, the entire section was not measured (e.g., Sections 393-U1583E-1H-1, 3H-1, and 11H-2). Two discrete samples (7 cm^3 J-cubes) per core were taken from working halves of Hole U1583C (see **Paleomagnetism** in the Expedition 390/393 methods chapter [Coggon et al., 2024a]), and one sample was also taken from above the sediment/basement interface in Hole U1583F. Remanence before and after AF demagnetization and anisotropy of magnetic susceptibility (AMS) were measured on a total of 25 discrete samples. Acquisition of isothermal remanent magnetization (IRM) was performed on 8 selected samples (at least once per lithostratigraphic unit/subunit). To establish the magnetostratigraphy at Site U1583, magnetic polarities were analyzed using the results from both Holes U1583C and U1583E.

8.1.1. Results

The natural remanent magnetization (NRM) intensities of sediment cores from Holes U1583C and U1583E are generally on the order of 10^{-2} A/m, and 20 mT intensities are mainly between 10^{-4} and 10^{-3} A/m; both holes show similar variations in remanence intensity. Significant differences between NRM and 20 mT remanence intensity are observed in Cores 393-U1583C-2H and 393-U1583E-3H, which are associated with an increase in MS due to the presence of a clay-rich interval (Unit III) (Figures **F51**, **F52**). In Core 393-U1583C-12H, 20 mT remanence values $<10^{-4}$ A/m are recorded, and the remanence intensity decreases from 10^{-3} to 10^{-5} A/m after the 5 mT step; the near-complete loss of the primary remanent magnetization confirms that this core is highly disturbed (see **Operations**). Clear positive and negative polarities in the 20 mT inclination are visible in both Holes U1583C and U1583E that can be dated by magnetostratigraphic correlation to polarity chrons in the geomagnetic polarity timescale (GPTS) (see **Magnetostratigraphy** and **Age model and sedimentation rates**). The 20 mT inclination values have a bimodal distribution in both holes, where values are clustered around +57° and −54° in Hole U1583C and clusters are seen around +59° and −51° in Hole U1583E (Figure **F53**). These angles are slightly steeper than the inclination expected based on the geocentric axial dipole (GAD; ±49.1° at 30°S).

8.1.1.1. Discrete samples

We collected two discrete cubes per core from Hole U1583C, sampling each lithostratigraphic unit/subunit (see **Sedimentology**; Table **T15**). To isolate the ChRM and better constrain the SRM data, samples were subjected to AF demagnetization up to a maximum of 130 mT. The majority of the samples show a single remanent magnetization component after the 5 mT AF demagnetization step with maximum angular deviation angles spanning 2.2°–14.8° (Table **T15**; Figure **F54**). These values are below the maximum cutoff of 15° (Butler, 1992), and consequently the detected ChRM components are considered well defined in the selected samples. Six of the samples displayed noisy orthogonal vector plots, but no lithologic correlation regarding the stability of ChRM could be observed. Data disturbance in those samples is mostly related to the drilling process, in particular for the two samples taken from Core 393-U1583C-12H. Nevertheless, the ChRM inclinations and declinations obtained from discrete measurements coincide with the SRM data (Figure **F51**), supporting the Site U1583 SRM data and the polarity assignments.

Magnetic mineralogy was characterized by performing acquisition of IRM and backfield experiments (Figure **F55A**) on 1 or 2 samples per lithostratigraphic unit/subunit. In both nannofossil ooze and clay-rich units, IRM saturates around 300 mT, revealing the dominance of low-coercivity minerals. The intensity of saturation IRM (SIRM) is significantly higher in Unit III (Table **T16**). The unmixing of the IRM acquisition curves (Figure **F55B**) shows different best-fit models for the

clay-rich Unit III and the nannofossil ooze (Units I, II, and IV). Unit III reveals the presence of two low- to intermediate-coercivity components, with mean remanence coercivity (B_h) of ~1.6 and ~2.3 $\log_{10}$ units, and a low (<5%) contribution of a third high-coercivity fraction. In contrast, nannofossil ooze shows a dominant low-coercivity component of ~1.57 $\log_{10}$ units and a minor to absent content of high-coercivity minerals.

Both the S ratio ($S_{0.3}$) and IRM_{100}/SIRM ratio ($S_{0.1}$) of all measured samples display values close to 1, typical of low-coercivity minerals, with no variations with depth and between lithostratigraphic units/subunits (Table **T16**; Figure **F56**). This implies that each unit/subunit is dominated by low-coercivity magnetic minerals (e.g., magnetite), as supported by coercivity of remanence (B_{cr}) values <50 mT (Table **T16**; Figure **F56**).

AMS measurements show two different trends in the magnetic fabric with either a subvertical or a subhorizontal magnetic foliation (Figure **F57A**). Samples showing subhorizontal magnetic foliation correspond to typical oblate sedimentary fabric (Figure **F57**). In contrast, the presence of samples characterized by a subvertical magnetic foliation might be related to either soft-sediment deformation or upward-arching beds due to drilling disturbance (Yang et al., 2019). No particular correlation of the two different patterns can be related to lithologic changes at this stage. The degree of anisotropy (P) varies between 1.006 and 1.045, and the shape parameter (T) indicates the dominance of oblate fabric throughout the hole (Figures **F57B**, **F58**; Table **T17**). Bulk susceptibility (K_m) generally remains low, <2.5 × 10^{-4} (SI). However, higher values >9 × 10^{-4} (SI) were measured at the top of Unit III because of the high clay content (Figure **F58**; Table **T17**). No clear correlation exists between P and T, though higher values are generally observed in the middle of Subunit IVA between 30 and 50 m CSF-A.

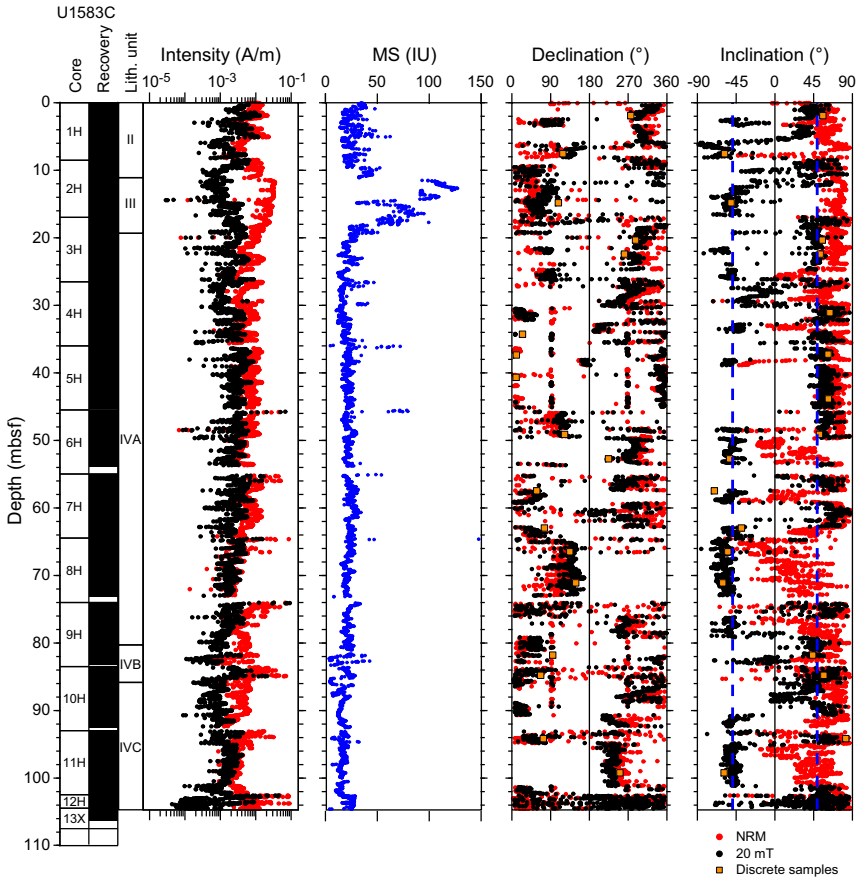

Figure F51. Archive-half MSP (MS; from SHMSL) and SRM measurements in sediments, Hole U1583C. Dashed lines on inclination = inclination (±49.1°) expected based on GAD for this latitude (~30°S).

8.1.1.2. Magnetostratigraphy

Remanence measurements made on sediment archive halves from Holes U1583C and U1583E were used to define the polarity sequence for Site U1583. Our interpretations are based on the remanence inclination sign at the 20 mT demagnetization step, the length of the polarity intervals, and the biostratigraphic datums based on both nannofossils and foraminifera (see **Biostratigraphy**). Where gaps and/or condensed levels were present, our observations were integrated and correlated with physical properties to form the spliced inclination reversal stratigraphy (see **Physical properties and downhole measurements**). Despite the moderate to significant drilling dis-

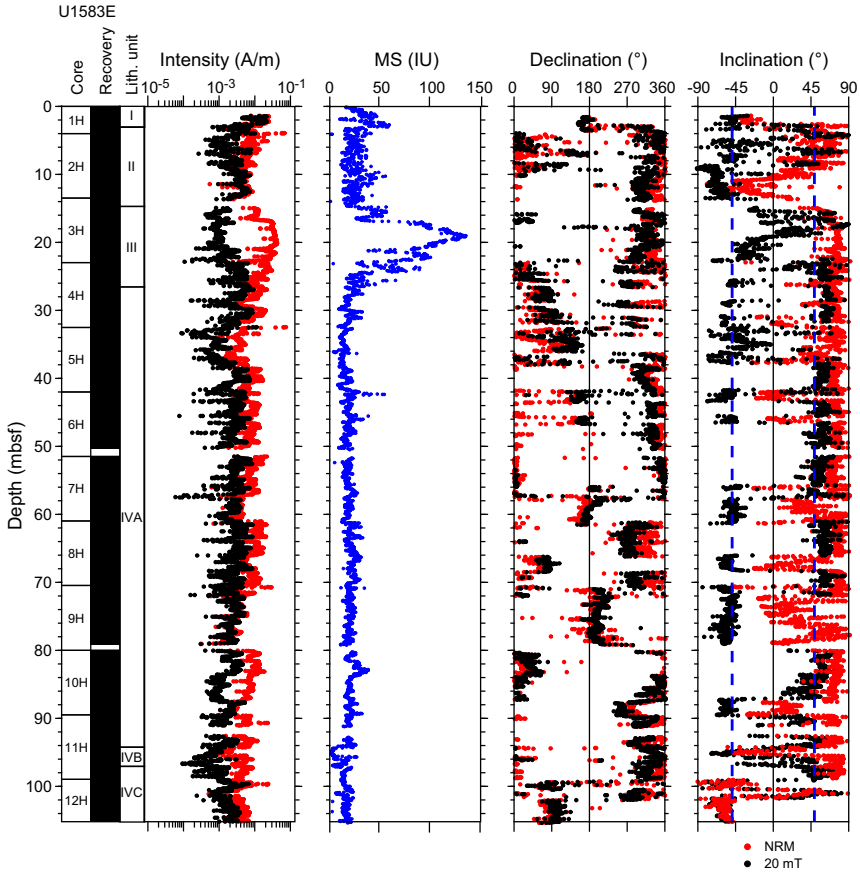

Figure F52. Archive-half MSP (MS; from SHMSL) and SRM measurements in sediments, Hole U1583E. Dashed lines on inclination = inclination (±49.1°) expected based on GAD for this latitude (~30°S).

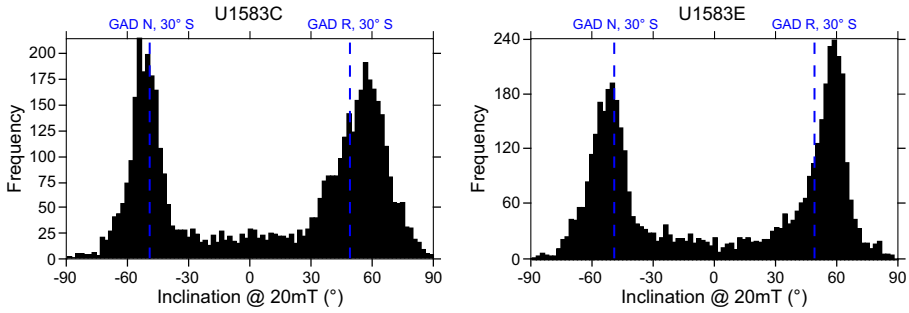

Figure F53. Histogram of inclination data after 20 mT AF demagnetization for sediments, Holes U1583C and U1583E. Dashed lines = inclination (±49.1°) expected based on GAD for this latitude (~30°S) for normal (N) and reversed (R) chrons.

Table T15. NRM, Hole U1583C. **Download table in CSV format.**

turbance in some intervals (e.g., Section 393-U1583C-4H-1, Core 393-U1583E-5H, and Section 393-U1583E-11H-1), the high resolution of the biostratigraphic observations supported a preliminary tie to the GPTS (Gradstein et al., 2020) with high level of confidence (Figure **F59**). The uppermost sediment package in Hole U1583E (to 6 m CSF-A) contains the Brunhes, Matuyama, and Jaramillo Chrons, which are absent from Hole U1583C. Below 6 m CSF-A, the polarity reversals in Hole U1583E show similar patterns to those in Hole U1583C and can be unambiguously correlated. Inclinations from ChRM calculated for discrete samples confirm the values measured from the SRM (Figure **F51**), supporting the polarity interpretations. The interval between ~10 and 20 m CSF-A corresponds to a clay-rich condensed level (Unit III) (see **Biostratigraphy** and **Age model and accumulation rates**), which limits the correlation of the normal and reversed polarity

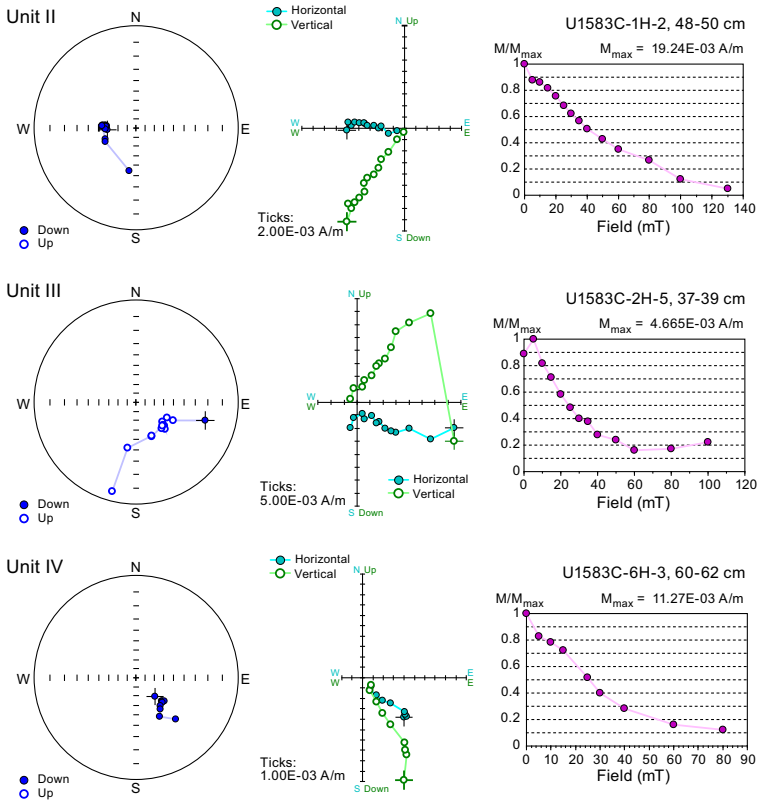

Figure F54. Representative AF demagnetization results for each lithostratigraphic unit, with equal-angle projections, orthogonal vector plots (Zijderveld, 1967), and demagnetization trends of normalized intensity, Hole U1583C.

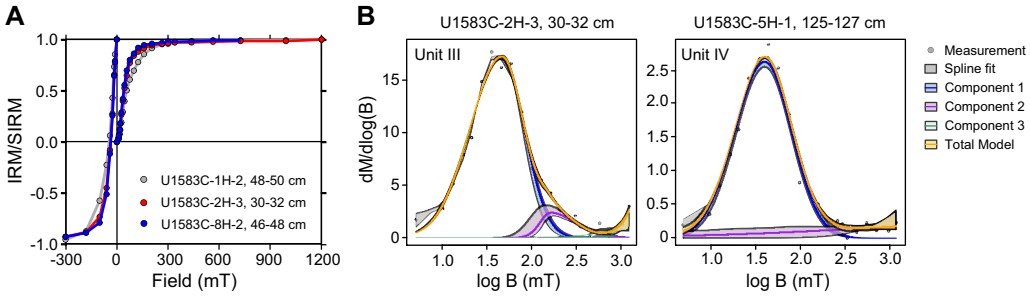

Figure F55. A. SIRM acquisition curves up to 1200 mT and backfield IRM truncated at −300 mT for representative samples from each sediment lithostratigraphic unit, Hole U1583C. B. Coercivity distribution and unmixing of IRM acquisition curves (Maxbauer et al., 2016) for representatives of clay-rich (Unit III) and nannofossil ooze (Unit IV) lithologies.

Table T16. MS, IRM, and MDF, Hole U1583C. **Download table in CSV format.**

patterns at that depth with the GPTS. Based on the biostratigraphic datums, the first reversed interval below the clay-rich unit was observed in Cores 393-U1583C-3H and 393-U1583E-4H and was correlated to Chron C5Br at the base of the Langhian (15.99 Ma) (Gradstein et al., 2020). At Site U1583, the Oligocene/Miocene boundary occurs within Subunit IVA at ~40 m CSF-A in Hole U1583C and at ~45 m CSF-A in Hole U1583E. Paleomagnetic results at the bottom of the sediment package, above the sediment/basement interface (between 100 and 110 m CSF-A), were placed in Chron C11r (29.970–30.591 Ma) (Gradstein et al., 2020) for Hole U1583C and Chron Cr11.2n (29.527–29.970 Ma) (Gradstein et al., 2020) for Hole U1583E. The relative ages of those chrons agree with the estimated basement age of ~30.6 Ma (Kardell et al., 2019).

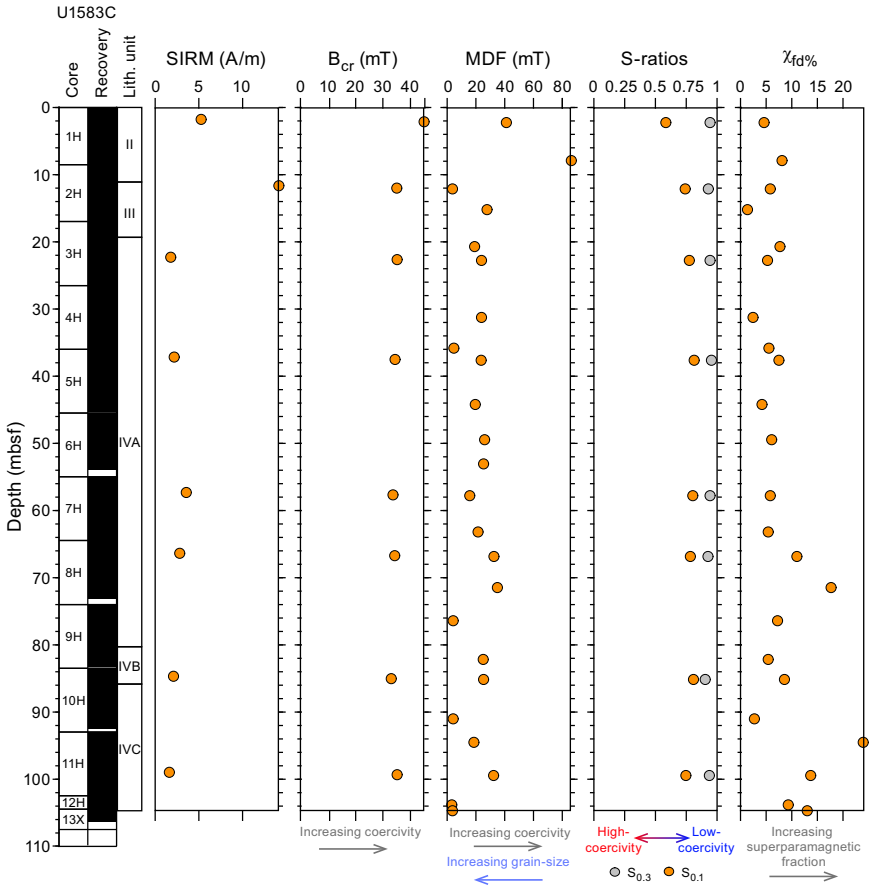

Figure F56. Magnetic mineralogy data, Hole U1583C. $K_{fd\%}$ = frequency-dependent susceptibility.

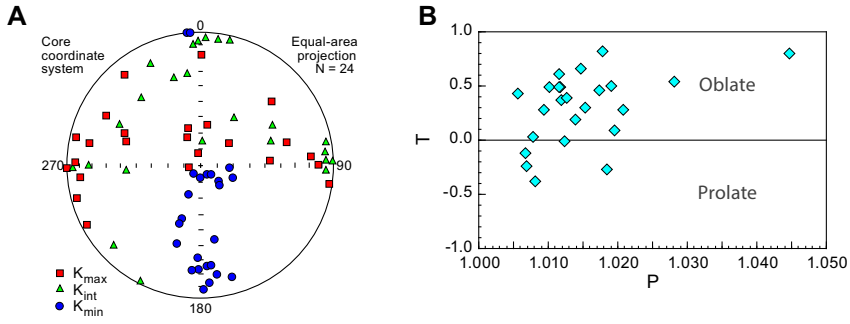

Figure F57. A. Equal-area projection (in core coordinate system) showing orientation of principal magnetic susceptibility axes (K_{max}, K_{int}, and K_{min}) for measured discrete samples of sediments, Site U1583. B. Shape parameter (T) vs. degree of anisotropy (P).

8.2. Basement

Continuous magnetic remanence properties of basement cores from Hole U1583F were measured at 2 cm spacing using the SRM on archive-half pieces longer than 9 cm (see **Paleomagnetism** in the Expedition 390/393 methods chapter [Coggon et al., 2024a]) before and after AF demagnetization at three different steps (5, 10, and 20 mT). The amount of data collected varied depending on the core recovery rate in Hole U1583F (0%–96%). High measurement density was achieved for Cores 393-U1583F-3R through 5R and 12R–14R, where recovery was relatively high. Cores lacking pieces longer than 9 cm, such as Cores 9R, 20R, and 25R–27R, were not measured by the SRM to avoid the collection of spurious data because of edge effects.

About one 8 cm^3 cube per core was sampled from the working halves of Hole U1583F basement cores. A total of 20 cubes were taken predominantly from fresh background basalt pieces, although some samples displayed a range of hydrothermal alteration style and intensity (Table **T18**). Two additional nonoriented samples were taken from sedimentary breccia in Cores 393-U1583F-16R and 23R for magnetic mineralogy experiments. The main goal of paleomagnetic studies on discrete samples was to characterize the magnetic signature of basement rocks and, preliminarily, the magnetic mineralogy. Both AF demagnetization and IRM experiments were performed. In addition, AMS measurements were made to define the magnetic fabric of the different igneous units.

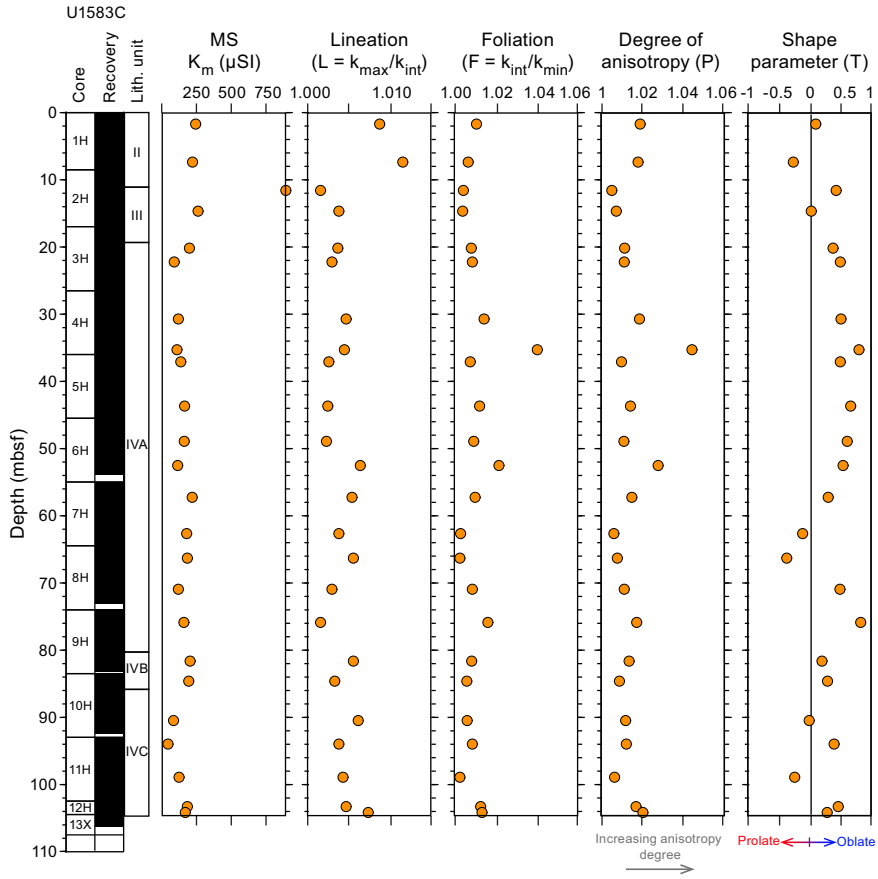

Figure F58. Bulk susceptibility (K_m) and AMS parameters (Jelinek, 1981), Hole U1583C.

Table T17. AMS, Hole U1583C. **Download table in CSV format.**

8.2.1. Results

Measurements of NRM and in-line AF demagnetization of Cores 393-U1583F-2R through 29R characterize the remanent magnetization records of ~30.6 Ma basalts (Kardell et al., 2019). AF demagnetization up to 20 mT removed most of the viscous magnetization, leading to the detection of the primary remanent components. Remanence after the 20 mT AF demagnetization step will be referred to as 20 mT remanence hereafter. The intensities of NRM and 20 mT remanence of the basalts display mean values around 2.7 and 1.4 A/m, respectively (Figure **F60**). Significantly higher NRM intensity was detected in Cores 3R–5R and 13R, which correlates with higher susceptibility values. The 20 mT remanence values predominantly show positive inclinations in measured intervals (Figure **F60**), indicating reversed geomagnetic polarity at this latitude (30°S). Values are clustered around 45° (Figure **F61**) and agree with the calculated GAD (±49.1°). Based on the age of the sediments at the sediment/basement interface (see **Age model and sedimentation rates**), the basement at Site U1583 is placed in reversed Chron C11r with a basal age of 30.59 Ma (Gradstein et al., 2020). However, Sections 3R-1, 4R-3, 16R-2, and 23R-1 show shallow (less than +20°) to negative 20 mT inclination values (Figures **F60**, **F61**). These differences in inclination were mainly detected in breccias or intervals with evidence of high-coercivity minerals (see magnetic mineralogy description in **Discrete samples** below). In those intervals, the 20 mT AF demagnetization step may not be sufficient to reveal the ChRM. Alternatively, those changes in the 20 mT inclina-

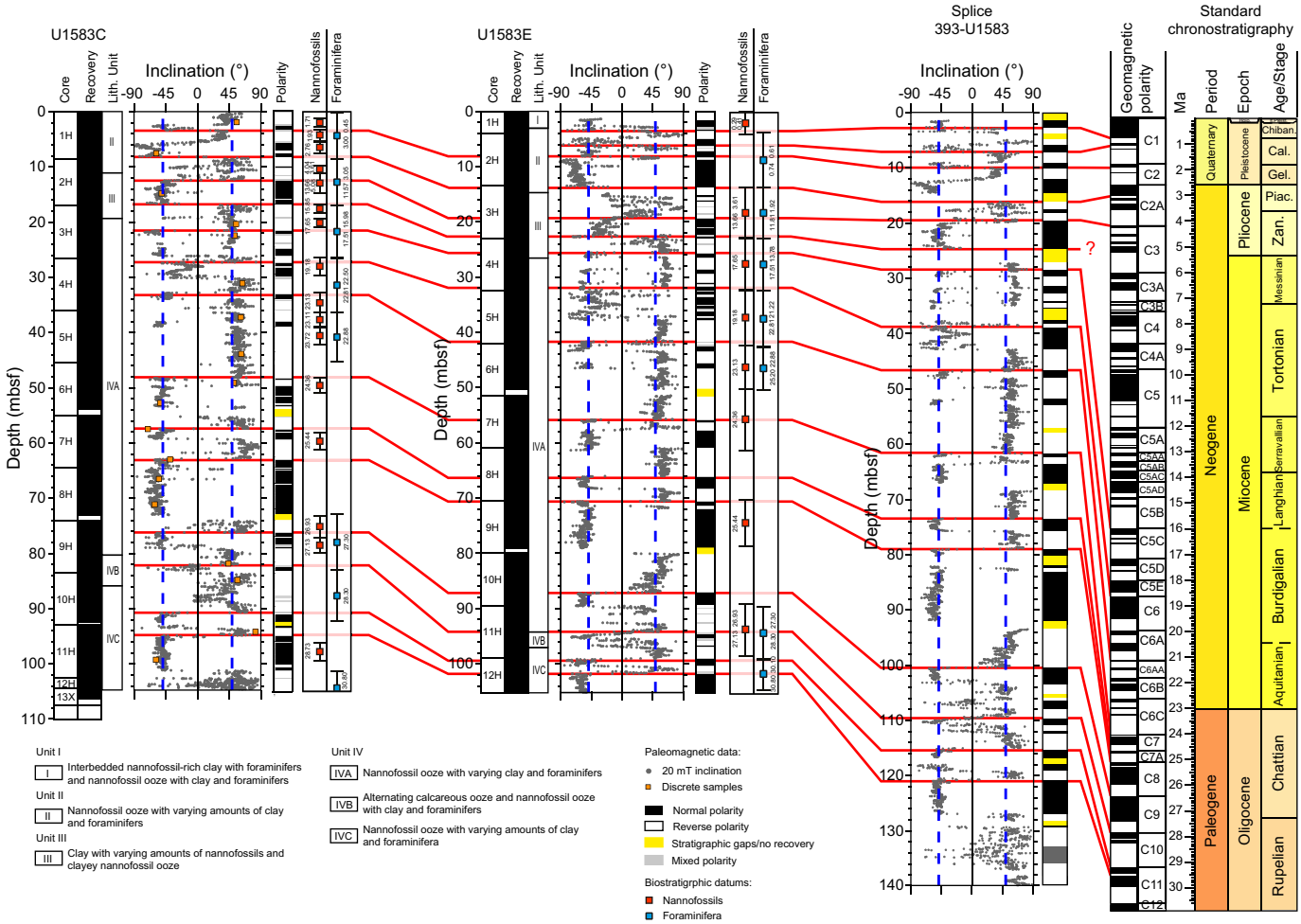

Figure F59. Archive-half SRM inclination measurements after 20 mT demagnetization for Hole U1583C and U1583E sediments, plotted with splice. Red lines = intervals where reversal patterns were associated with GPTS (Gradstein et al., 2020). Biostratigraphic ages based on nannofossils and planktic foraminifera used to constrain magnetic polarity ties are also shown.

Table T18. NRM, Hole U1583F. **Download table in CSV format.**

tion might be related to alteration and overprinting of the primary remanent magnetization by a secondary component.

8.2.1.1. Discrete samples

AF demagnetization up to a maximum of 190 mT was conducted on all of the discrete samples to isolate the ChRM, define the presence of secondary components, and provide constraints on the SRM data. After cleaning the drilling overprint with the 5 mT AF demagnetization step, most samples display a single component converging to the origin of the Zijderveld diagram (Figure **F62A**) that represents the ChRM. However, some samples such as Sample 393-U1583F-20R-1, 8–10 cm (Figure **F62B**), show a more stable secondary component, with the ChRM revealed after the 25 mT step. Those samples also display higher values of the median destructive fields (MDFs), which

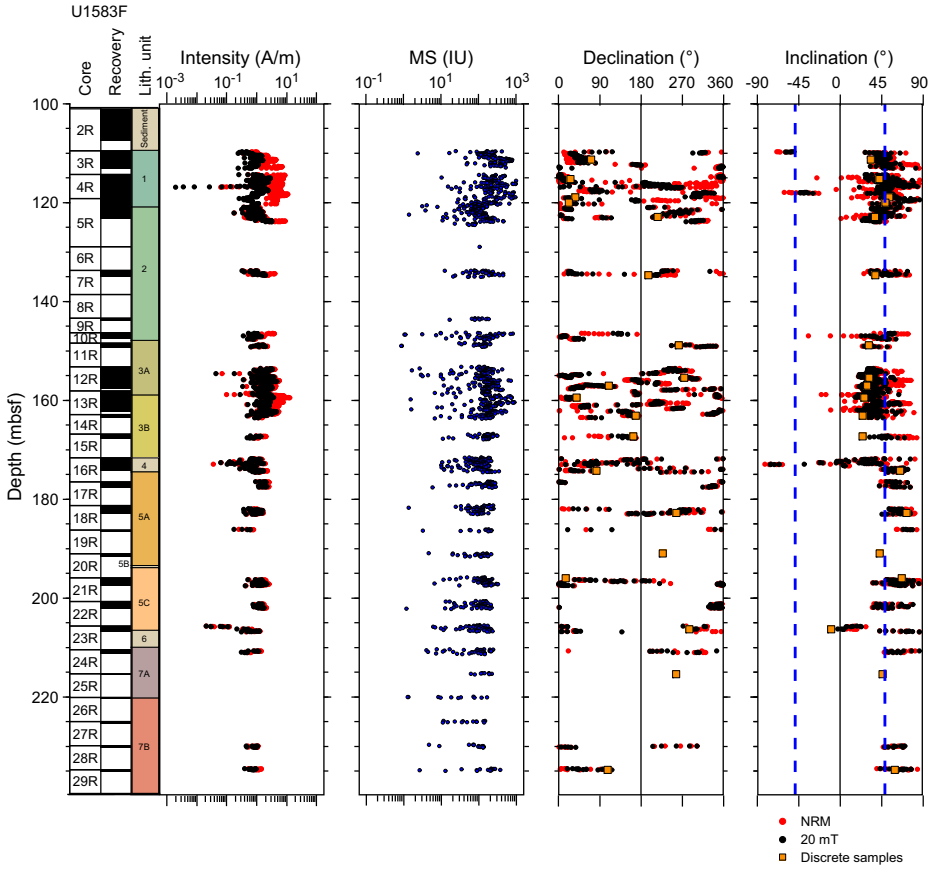

Figure F60. Archive-half MSP (MS; from SHMSL) and SRM measurements from volcanic rocks, Hole U1583F. Dashed lines = inclination (±49.1°) expected based on GAD for this latitude (~30°S).

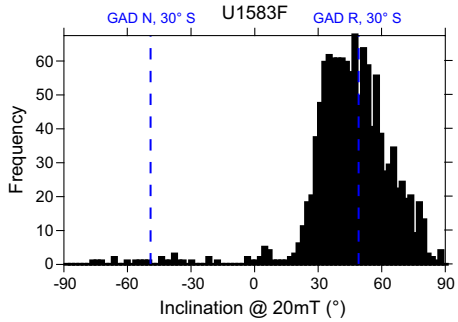

Figure F61. Histogram of inclination data after 20 mT AF demagnetization for volcanic rocks, Hole U1583F. Dashed lines = inclination (±49.1°) expected based on GAD for this latitude (~30°S) for normal (N) and reversed (R) chrons.

indicate decrease of magnetic mineral grain size or a greater contribution of high-coercivity minerals such as hematite or goethite. Overall, the principal components derived from the discrete samples displayed maximum angular deviation angles of 0.3°–14.8°, with most samples showing values less than 3.7°, which indicates that ChRM directions are mostly well defined (Table **T18**) (Butler, 1992). Both inclinations and declinations of the ChRM are consistent with the values measured on the SRM (Figure **F60**).

To further clarify the influence of the magnetic mineralogy on the stability of the ChRM and define the possible relationships with igneous units and alteration types, acquisition of IRM and backfield experiments were conducted on 18 discrete samples. Most of the samples show an IRM acquisition curve that saturated around 100–300 mT (Figure **F63A**), indicating the dominance of low-coercivity minerals such as magnetite or maghemite. A few altered basalts and the breccias (Sample 393-U1583F-16R-2, 53–58 cm) do not reach saturation at the maximum applied field of 1200 mT, suggesting a significant contribution of high-coercivity minerals (e.g., hematite). Deconvolution of the IRM acquisition curves (Figure **F63B**) confirms the presence of different mixtures of high- and low-coercivity minerals within the volcanic rocks at Site U1583. Most of the samples show 2 low-coercivity components characterized by mean remanence coercivity (B_h) < 2 $\log_{10}$ units. In contrast, the samples that do not saturate at 1200 mT show the presence of a high-coercivity component (B_h > 2.5 $\log_{10}$ units) that contributes ~30% of the total SIRM. Those samples are also characterized by high values of coercivity of remanence (B_{cr}) (e.g., samples from Sections 5R-3 and 16R-2; Figure **F63C**). The different contributions from intermediate- to high-coercivity minerals are highlighted by values of the IRM_{100}/SIRM ($S_{0.1}$) ratios of 0–0.50 and S ratio ($S_{0.3}$) of ~0.75 (Figure **F63C**; Table **T19**). In particular, lower values of $S_{0.1}$ and $S_{0.3}$ were detected for breccia samples of Units 4 and 6 and basalts from Subunits 5A–7B, which are more strongly hydrothermally altered. Additionally, discrete samples display a wide range of MDFs (4–77 mT) (Table **T19**; Figure **F63C**), indicating broad and variable ranges in magnetic mineral grain size and coercivity. Two samples collected from Core 4R show significantly lower MDF (<5 mT), implying that the main magnetic carriers in Unit 1 (massive flow) are coarser grained multidomain magnetite (Table **T19**). In contrast, samples from the pillow lava show values consistent with the dominance of finer grained single-domain magnetite. The highest MDF values are associated with the top of Unit 2 and the breccia (Unit 4), where high-coercivity minerals were detected.

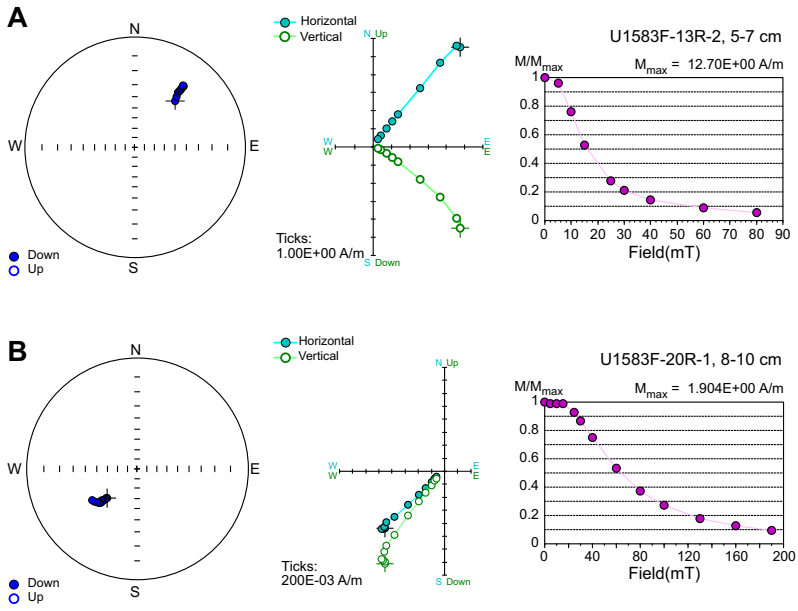

Figure F62. A, B. AF demagnetization results for representative discrete samples, Hole U1583F. Equal-angle projections, orthogonal projection diagrams (Zijderveld, 1967), and demagnetization trends of normalized intensity.

AMS shows high variability in the principal magnetic susceptibility axis (Figure **F64A**). In particular, samples from Unit 1 show prolate magnetic fabric with a well-clustered subhorizontal magnetic lineation (K_{max}) (Figure **F64A**, **F64B**; Table **T20**). Samples from Units 2 and 3 (Cores 393-U1583F-7R through 15R) are characterized by subhorizontal magnetic foliation with slightly prolate susceptibility ellipsoid shape ($-0.5 < T < 0$). Those units also show increased values in the degree of anisotropy (P), with highest values at the top of Subunit 3B, suggesting a preferred orientation of magnetic minerals in the sheet flows.

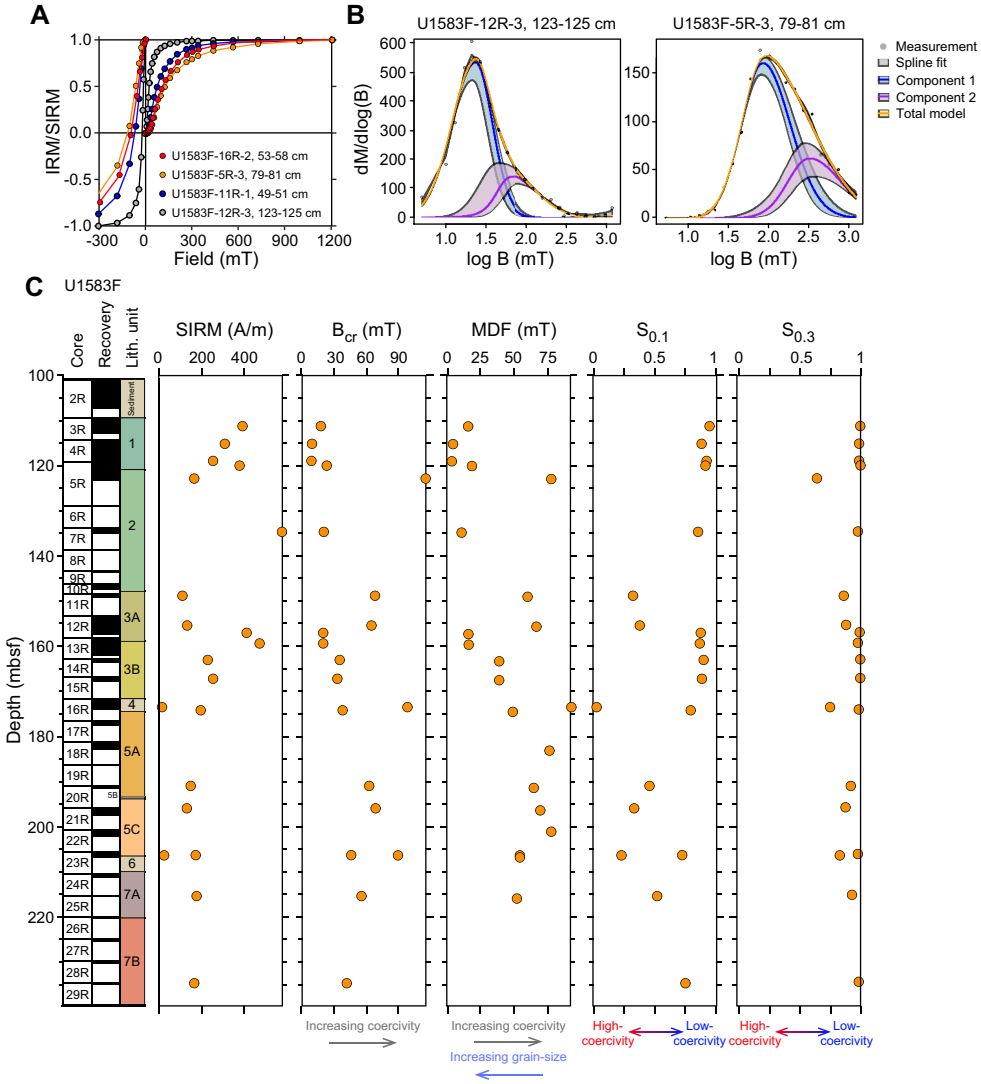

Figure F63. A. SIRM acquisition curves up to 1200 mT and backfield IRM truncated at –300 mT for 4 volcanic rock samples, Hole U1583F. B. Coercivity distribution and unmixing of IRM acquisition curves (Maxbauer et al., 2016). C. Magnetic mineralogy data.

Table T19. IRM and MDF, Hole U1583F. **Download table in CSV format.**

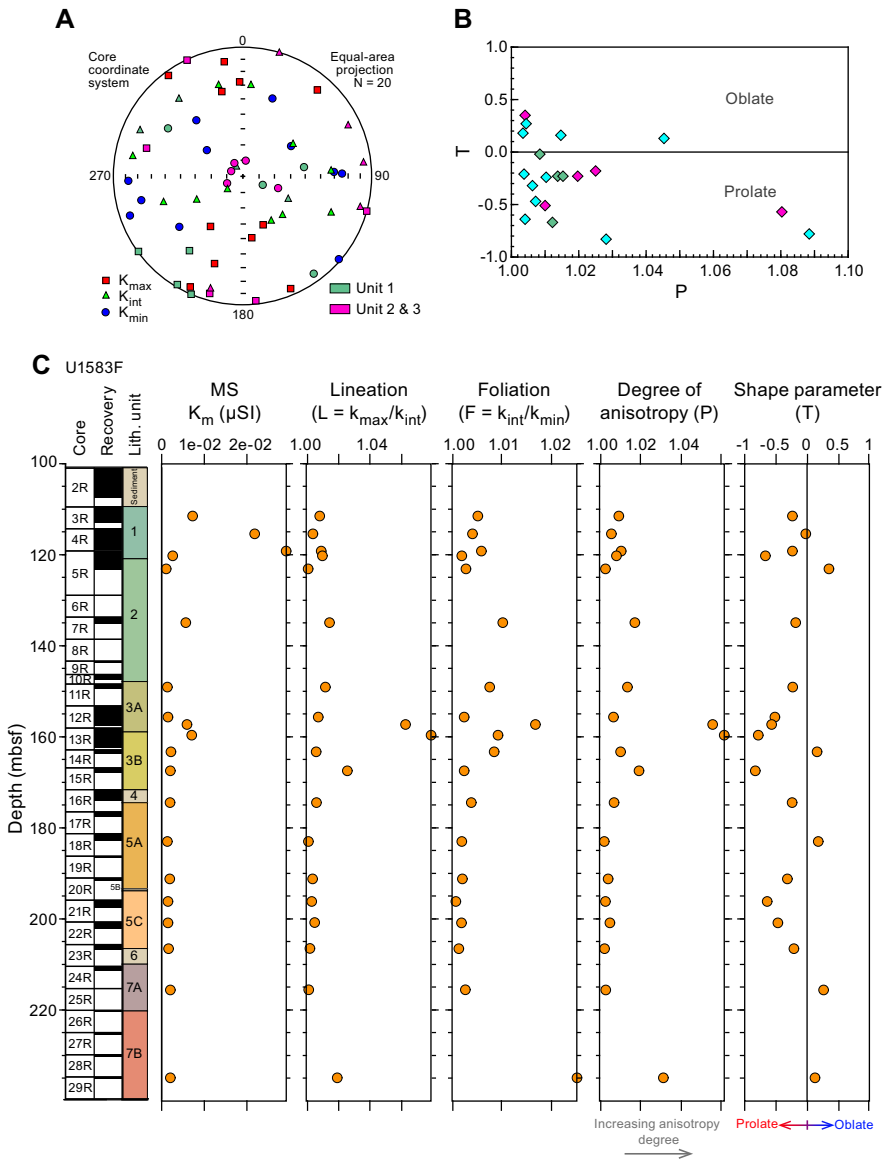

Figure F64. A. Equal-area projection showing orientation of principal magnetic susceptibility axes (K_{max}, K_{int}, and K_{min}), Site U1583. Green = massive flow, violet = pillow lavas. B. Shape parameter (*T*) vs. degree of anisotropy (*P*). C. Bulk susceptibility (K_m) and AMS parameters (Jelinek, 1981).

Table T20. AMS for basalt samples, Hole U1583F. **Download table in CSV format.**

9. Age model and mass accumulation rates

9.1. Age model and linear sedimentation rates

The age model for Site U1583 is based on calcareous nannoplankton and planktic foraminiferal lowest (base) and highest (top) occurrence datums and paleomagnetic reversal datums from Holes U1583C and U1583E (Tables **T21**, **T22**; Figures **F65**, **F66**). Planktic foraminifera and calcareous nannoplankton occur throughout the cored sediments. We identified 11 planktic foraminiferal and 27 calcareous nannoplankton bioevents in Hole U1583C and 22 planktic foraminiferal and 16 calcareous nannoplankton bioevents in Hole U1583E (Figures **F65**, **F66**). We also identified 36 and 34 magnetic reversal boundaries from Holes U1583C and U1583E, respectively.

Table T21. Biostratigraphic and paleomagnetic datums in stratigraphic order, Hole U1583C. * = datums used to plot the age model curve in Figure F65 and calculate LSRs using CSF-A depths. T = top, B = bottom, Tc = top common occurrence, Bc = base common occurrence, HCO = highest common occurrence, B reversal = base of a paleomagnetic reversal event. CN = calcareous nannofossils, PF = planktic foraminifera. Pmag = paleomagnetism. (Continued on next page.) **Download table in CSV format.**

Datum	Taxon/Chron (base)	Age (Ma)	Core, section, interval (cm)	Sample depth CSF-A (m)	Sample depth CSF-B (m)	Sample above/below	Sample above/below depth CSF-A (m)	Sample above/below depth CSF-B (m)	Midpoint depth CSF-A (m)	Midpoint depth CSF-B (m)	Depth error (±) CSF-A (m)	Depth error (±) CSF-B (m)	LSR (cm/ky)
			393-U1583C-			393-U1583C-							
PF	B *Globorotalia hirsuta*	0.450	Mudline	0.00	0.000	1H-CC, 14–19	8.47	8.470	4.235	4.235	4.235	4.235	
PF	B *Globorotalia truncatulinoides*	1.920	Mudline	0.00	0.000	1H-CC, 14–19	8.47	8.470	4.235	4.235	4.235	4.235	
PF	T *Dentoglobigerina altispira*	3.000	Mudline	0.00	0.000	1H-CC, 14–19	8.47	8.470	4.235	4.235	4.235	4.235	
CN	B medium *Gephyrocapsa spp.*	1.710	1H-1, 135–135	1.35	1.350	1H-2, 125–127	2.77	2.770	2.060	2.060	0.710	0.710	
Pmag	B C1r.3r*	1.775	1H-2, 94	2.44	2.440	2H, 96	2.46	2.460	2.450	2.450	0.010	0.010	0.68
Pmag	B C2n (Olduvai)*	1.934	1H-3, 52	3.52	3.520	3H-54	3.54	3.540	3.530	3.530	0.010	0.010	0.27
CN	T *Discoaster brouweri*	1.930	1H-3, 32–32	3.32	3.320	1H-4, 83–83	5.33	5.330	4.325	4.325	1.005	1.005	
CN	T *Discoaster pentaradiatus*	2.390	1H-3, 32–32	3.32	3.320	1H-4, 83–83	5.33	5.330	4.325	4.325	1.005	1.005	
CN	T *Discoaster surculus*	2.530	1H-3, 32–32	3.32	3.320	1H-4, 83–83	5.33	5.330	4.325	4.325	1.005	1.005	
Pmag	B C2r.2r (Matuyama)*	2.595	1H-4, 80	5.30	5.300	1H-4, 82	5.32	5.320	5.310	5.310	0.010	0.010	0.70
CN	T *Discoaster tamalis*	2.760	1H-4, 101–103	5.51	5.510	1H-6, 11–13	7.63	7.630	6.570	6.570	1.060	1.060	
Pmag	B C2An.1n (Gauss)*	3.032	1H-6, 78	8.28	8.280	2H-1, 0	8.50	8.500	8.390	8.390	0.110	0.110	0.52
Pmag	B C2An.2r (Mammoth)*	3.330	2H-1, 144	9.94	9.940	2H-1, 146	9.96	9.960	9.950	9.950	0.010	0.010	0.16
Pmag	B C2An.3n (Gauss)*	3.596	2H-2, 36	10.36	10.360	2H-2, 38	10.38	10.380	10.370	10.370	0.010	0.010	0.35
CN	T *Sphenolithus spp.*	3.610	2H-1, 130–130	9.80	9.800	2H-2, 114–116	11.16	11.160	10.480	10.480	0.680	0.680	
CN	T *Reticulofenestra pseudoumbilicus* (>7 µm)	3.820	2H-1, 130–130	9.80	9.800	2H-2, 114–116	11.16	11.160	10.480	10.480	0.680	0.680	
CN	Bc *Discoaster asymmetricus*	4.040	2H-1, 130–130	9.80	9.800	2H-2, 114–116	11.16	11.160	10.480	10.480	0.680	0.680	
Pmag	B C2Ar (Gilbert)*	4.187	2H-3, 90	12.40	12.400	2H-3, 92	12.42	12.420	12.410	12.410	0.010	0.010	0.24
PF	B *Globorotalia crassaformis**	4.300	1H-CC, 14–19	8.42	8.420	2H-CC, 16–21	16.95	16.950	12.685	12.685	4.265	4.265	0.00
PF	B *Globigerinoides conglobatus*	6.210	1H-CC, 14–19	8.42	8.420	2H-CC, 16–21	16.95	16.950	12.685	12.685	4.265	4.265	
PF	T *Sphaeroidinellopsis seminulina*	3.050	1H-CC, 14–19	8.42	8.420	2H-CC, 16–21	16.95	16.950	12.685	12.685	4.265	4.265	
PF	T *Globigerinoides subquadratus*	11.570	1H-CC, 14–19	8.42	8.420	2H-CC, 16–21	16.95	16.950	12.685	12.685	4.265	4.265	
CN	B *Ceratolithus cristatus*	5.080	2H-2, 114–116	11.14	11.140	2H-5, 34–36	14.86	14.860	13.000	13.000	1.860	1.860	
CN	B *Amaurolithus* spp.	7.450	2H-2, 114–116	11.14	11.140	2H-5, 34–36	14.86	14.860	13.000	13.000	1.860	1.860	
CN	T *Cyclicargolithus floridanus*	11.850	2H-2, 114–116	11.14	11.140	2H-5, 34–36	14.86	14.860	13.000	13.000	1.860	1.860	
CN	T *Coronocyclus nitescens*	12.450	2H-2, 114–116	11.14	11.140	2H-5, 34–36	14.86	14.860	13.000	13.000	1.860	1.860	
CN	Tc *Calcidiscus premacintyrei*	12.570	2H-2, 114–116	11.14	11.140	2H-5, 34–36	14.86	14.860	13.000	13.000	1.860	1.860	
CN	T *Sphenolithus heteromorphus**	13.660	2H-2, 114–116	11.14	11.140	2H-5, 34–36	14.86	14.860	13.000	13.000	1.860	1.860	0.21
CN	B *Discoaster signus**	15.850	2H-CC	16.90	16.900	3H-1, 133–133	18.33	18.330	17.615	17.615	0.715	0.715	1.25
Pmag	B C5Br*	15.974	3H-2, 62	19.15	19.150	3H-2, 64	19.17	19.170	19.160	19.160	0.010	0.010	0.10
Pmag	B C5Cn.1n*	16.268	3H-2, 90	19.43	19.430	3H-2, 92	19.45	19.450	19.440	19.440	0.010	0.010	0.22
CN	Bc *Sphenolithus heteromorphus*	17.650	3H-2, 91–91	19.44	19.440	3H-3, 91–91	20.94	20.940	20.190	20.190	0.750	0.750	
Pmag	B C5Cr*	17.235	3H-3, 150	21.53	21.530	3H-4, 0	21.53	21.530	21.530	21.530	0.000	0.000	0.29
PF	T *Catapsydrax dissimilis*	17.510	2H-CC, 16–21	16.90	16.900	3H-CC, 16–21	26.47	26.470	21.685	21.685	4.785	4.785	
PF	B *Praeorbulina circularis*	15.980	2H-CC, 16–21	16.90	16.900	3H-CC, 16–21	26.47	26.470	21.685	21.685	4.785	4.785	
PF	B *Praeorbulina glomerosa*	16.140	2H-CC, 16–21	16.90	16.900	3H-CC, 16–21	26.47	26.470	21.685	21.685	4.785	4.785	
PF	B *Praeorbulina sicana*	16.390	2H-CC, 16–21	16.90	16.900	3H-CC, 16–21	26.47	26.470	21.685	21.685	4.785	4.785	
Pmag	B C5Dn*	17.533	3H-4, 84	22.37	22.370	3H-4, 86	22.39	22.390	22.380	22.380	0.010	0.010	0.50
Pmag	B C5Dr.2r*	18.007	3H-6, 20	24.73	24.730	3H-6, 22	24.75	24.750	24.740	24.740	0.010	0.010	0.30
Pmag	B C5En*	18.497	3H-7, 66	26.19	26.190	3H-7, 68	26.21	26.210	26.200	26.200	0.010	0.010	0.86
Pmag	B C5Er*	18.636	4H-1, 88	27.38	27.343	4H-1, 90	27.40	27.362	27.390	27.353	0.010	0.009	0.33
CN	Tc *Triquetrorhabdulus carinatus*	19.180	3H-CC	26.42	26.420	4H-3, 17–19	29.70	29.567	28.060	27.994	1.640	1.574	
Pmag	B C6n*	19.535	4H-3, 86	30.37	30.209	4H-3, 88	30.39	30.229	30.380	30.219	0.010	0.010	0.17
PF	T *Ciperoella ciperoensis*	22.810	3H-CC, 16–21	26.42	26.420	4H-CC, 32–37	36.41	36.000	31.415	31.210	4.995	4.790	
PF	B *Globoquadrina dehiscens*	22.500	3H-CC, 16–21	26.42	26.420	4H-CC, 32–37	36.41	36.000	31.415	31.210	4.995	4.790	
Pmag	B C6Ar*	21.130	4H-5, 54	33.06	32.789	4H-5, 56	33.08	32.808	33.070	32.799	0.010	0.009	0.15
Pmag	B C6Bn.1n*	21.985	4H-6, 28	34.30	33.977	4H-6, 30	34.32	33.997	34.310	33.987	0.010	0.010	0.30
CN	T *Reticulofenestra bisecta*	23.130	4H-5, 34–36	32.86	32.597	4H-CC	36.41	36.000	34.635	34.299	1.775	1.702	
CN	T *Sphenolithus delphix*	23.110	4H-CC	36.36	35.952	5H-3, 4–6	39.06	39.060	37.710	37.506	1.350	1.554	
CN	T *Sphenolithus capricornutus*	23.110	4H-CC	36.36	35.952	5H-3, 4–6	39.06	39.060	37.710	37.506	1.350	1.554	
Pmag	B C6Cn.2r*	23.212	5H-2, 54	38.04	38.040	5H-2, 56	38.06	38.060	38.050	38.050	0.010	0.010	1.25
CN	B *Sphenolithus delphix*	23.720	5H-3, 4–6	39.04	39.040	5H-5, 9–11	42.12	42.120	40.580	40.580	1.540	1.540	
Pmag	B C6Cr*	24.025	6H-2, 120	48.21	48.210	6H-2, 122	48.23	48.230	48.220	48.220	0.010	0.010	1.39
Pmag	B C7n.1n*	24.061	6H-3, 20	48.71	48.710	6H-3, 22	48.73	48.730	48.720	48.720	0.010	0.010	1.49
CN	T *Sphenolithus ciperoensis*	24.360	6H-2, 120–122	48.21	48.210	6H-4, 93–95	50.97	50.970	49.590	49.590	1.380	1.380	
Pmag	B C7n.1r*	24.124	6H-3, 114	49.65	49.650	6H-3, 116	49.67	49.670	49.660	49.660	0.010	0.010	1.13
Pmag	B C7n.2n*	24.459	6H-6, 40	53.42	53.420	6H-6, 42	53.44	53.440	53.430	53.430	0.010	0.010	2.07
Pmag	B C7r*	24.654	7H-2, 94	57.45	57.404	7H-2, 946	57.47	57.424	57.460	57.414	0.010	0.010	1.68
Pmag	B C7An*	24.766	7H-3, 132	59.33	59.250	7H-23, 134	59.35	59.269	59.340	59.260	0.010	0.009	1.08
CN	T *Chiasmolithus altus*	25.440	7H-3, 10–12	58.11	58.052	7H-5, 20–22	61.25	61.134	59.680	59.593	1.570	1.541	
Pmag	B C7Ar*	25.099	7H-6, 40	62.93	62.802	7H-6A, 42	62.93	62.782	62.930	62.792	0.000	–0.010	1.04
Pmag	B C8n.1n*	25.264	8H-1, 14	64.64	64.640	8H-1, 16	64.66	64.660	64.650	64.650	0.010	0.010	0.35
Pmag	B C8n.1r*	25.304	8H-1, 28	64.78	64.780	8H-1, 30	64.80	64.800	64.790	64.790	0.010	0.010	1.27
Pmag	B C8n.2n*	25.987	8H-6, 94	72.95	72.950	9H-1, 0	74.00	74.000	73.475	73.475	0.525	0.525	0.62

Table T21 (continued).

Datum	Taxon/Chron (base)	Age (Ma)	Core, section, interval (cm)	Sample depth CSF-A (m)	Sample depth CSF-B (m)	Sample above/below	Sample above/below depth CSF-A (m)	Sample above/below depth CSF-B (m)	Midpoint depth CSF-A (m)	Midpoint depth CSF-B (m)	Depth error (±) CSF-A (m)	Depth error (±) CSF-B (m)	LSR (cm/ky)
CN	T *Sphenolithus predistentus*	26.930	8H-CC	73.08	73.080	9H-3, 9–11	77.11	77.110	75.095	75.095	2.015	2.015	
Pmag	B C8r*	26.420	9H-2, 62	76.13	76.130	9H-2, 64	76.15	76.150	76.140	76.140	0.010	0.010	0.30
PF	T *Paragloborotalia opima*	27.300	8H-CC, 13–18	73.08	73.080	9H-CC, 20–25	83.27	83.270	78.175	78.175	5.095	5.095	
CN	B *Sphenolithus ciperoensis*	27.130	9H-3, 9-11	77.09	77.090	9H-4, 139–141	79.92	79.920	78.505	78.505	1.415	1.415	
Pmag	B C9n*	27.439	9H-4, 64	79.15	79.150	9H-4, 66	79.17	79.170	79.160	79.160	0.010	0.010	0.98
Pmag	B C9r*	27.859	9H-6, 150	83.02	83.020	10H-1, 0	83.50	83.500	83.260	83.260	0.240	0.240	0.56
PF	HCO *Chiloguembelina cubensis*	28.300	9H-CC, 20–25	83.22	83.220	10H-CC, 20–25	92.54	92.540	87.880	87.880	4.660	4.660	
Pmag	B C10r*	29.183	10H-5, 110	90.63	90.630	10H-5, 112	90.65	90.650	90.640	90.640	0.010	0.010	0.98
Pmag	B C11n.1n*	29.477	11H-1, 52	93.52	93.511	11H-1, 54	93.54	92.531	93.530	93.021	0.010	–0.490	2.56
Pmag	B C11n.1r*	29.527	11H-2, 30	94.80	94.769	11H-2, 32	94.82	94.788	94.810	94.779	0.010	0.010	1.46
CN	T *Sphenolithus pseudoradians*	28.730	11H-3, 14–16	96.14	96.085	11H-5, 29–31	99.32	99.209	97.730	97.647	1.590	1.562	
Pmag	B C11n.2n*	29.970	11H-6, 74	101.25	101.105	11H-6, 76	101.27	101.124	101.260	101.115	0.010	0.010	0.64
PF	T *Subbotina angiporoides*	30.100	11H-CC, 17–22	102.62	102.451	12H-CC, 12–17	110.52	104.500	106.570	103.476	3.950	1.025	
PF	B *Paragloborotalia opima**	30.800	11H-CC, 17–22	102.62	102.451	12H-CC, 12–17	110.52	104.500	106.570	103.476	3.950	1.025	

Table T22. Biostratigraphic and paleomagnetic datums in stratigraphic order, Hole U1583E. * = datums used to plot the age model curve in Figure F66 and calculate LSRs using CSF-A depths. T = top, B = base, Tc = top common, Bc = base common, B reversal = base of a paleomagnetic reversal event. CN = calcareous nannofossils, PF = planktic foraminifera. Pmag = paleomagnetism. (Continued on next page.) **Download table in CSV format.**

Datum	Taxon/Chron (base)	Age (Ma)	Core, section, interval (cm)	Sample depth CSF-A (m)	Sample depth CSF-B (m)	Sample above/below	Sample above/below depth CSF-A (m)	Sample above/below depth CSF-B (m)	Midpoint depth CSF-A (m)	Midpoint depth CSF-B (m)	Depth error (±) CSF-A (m)	Depth error (±) CSF-B (m)	LSR (cm/ky)
			393-U1583E-			393-U1583E-							
CN	B *Emiliania huxleyi**	0.290	1H-1, 0	0.00	0.000	1H-CC	4.03	4.000	2.015	2.000	2.015	2.000	0.33
CN	T *Pseudoemiliania lacunosa*	0.410	1H-1, 0	0.00	0.000	1H-CC	4.03	4.000	2.015	2.000	2.015	2.000	
Pmag	B C1n (Brunhes)*	0.773	1H-3, 60	3.60	3.573	1H-3, 62	3.62	3.593	3.610	3.583	0.010	0.010	0.90
Pmag	B C1r.1n (Jaramillo)*	1.070	2H-2, 76	6.26	6.171	2H-2, 78	6.28	6.190	6.270	6.181	0.010	0.010	0.12
Pmag	B C1r.3r*	1.775	2H-1, 74	7.09	6.969	2H-1, 76	7.11	6.988	7.100	6.979	0.010	0.010	0.77
Pmag	B C2n (Olduvai)*	1.934	2H-2, 76	8.31	8.140	2H-2, 78	8.33	8.160	8.320	8.150	0.010	0.010	0.06
Pmag	B C2r.2r (Matuyama)*	2.595	2H-4, 18	8.70	8.515	2H-4, 20	8.72	8.534	8.710	8.525	0.010	0.010	1.29
PF	B *Globorotalia hessi*	0.740	1H-CC, 12–17	3.98	3.950	2H-CC, 11–16	13.89	13.501	8.935	8.726	4.955	4.776	
PF	T *Globorotalia tosaensis*	0.610	1H-CC, 12–17	3.98	3.950	2H-CC, 11–16	13.89	13.501	8.935	8.726	4.955	4.776	
PF	B *Globorotalia truncatulinoides*	1.920	2H-CC, 11–16	13.84	13.453	3H-CC, 9–14	23.03	23.001	18.435	18.227	4.595	4.774	
PF	B *Globorotalia tosaensis**	3.350	2H-CC, 11–16	13.84	13.453	3H-CC, 9–14	23.03	23.001	18.435	18.227	4.595	4.774	Hiatus
PF	B *Globorotalia crassaformis*	4.300	2H-CC, 11–16	13.84	13.453	3H-CC, 9–14	23.03	23.001	18.435	18.227	4.595	4.774	
PF	B *Sphaeroidinella dehiscens*	5.540	2H-CC, 11–16	13.84	13.453	3H-CC, 9–14	23.03	23.001	18.435	18.227	4.595	4.774	
PF	B *Globorotalia tumida*	5.820	2H-CC, 11–16	13.84	13.453	3H-CC, 9–14	23.03	23.001	18.435	18.227	4.595	4.774	
PF	T *Globoquadrina dehiscens*	5.910	2H-CC, 11–16	13.84	13.453	3H-CC, 9–14	23.03	23.001	18.435	18.227	4.595	4.774	
PF	B *Globigerinoides conglobatus*	6.210	2H-CC, 11–16	13.84	13.453	3H-CC, 9–14	23.03	23.001	18.435	18.227	4.595	4.774	
PF	T *Fohsella fohsi s.l.*	11.810	2H-CC, 11–16	13.84	13.453	3H-CC, 9–14	23.03	23.001	18.435	18.227	4.595	4.774	
CN	T *Sphenolithus spp.*	3.610	2H-CC	13.84	13.453	3H-CC	23.03	23.001	18.435	18.227	4.595	4.774	
CN	T *Reticulofenestra pseudoumbilicus* (>7 microns)	3.820	2H-CC	13.84	13.453	3H-CC	23.03	23.001	18.435	18.227	4.595	4.774	
CN	B *Ceratolithus cristatus*	5.080	2H-CC	13.84	13.453	3H-CC	23.03	23.001	18.435	18.227	4.595	4.774	
CN	T *Cyclicalgolithus floridanus*	11.850	2H-CC	13.84	13.453	3H-CC	23.03	23.001	18.435	18.227	4.595	4.774	
CN	T *Coronocyclus nitescens*	12.450	2H-CC	13.84	13.453	3H-CC	23.03	23.001	18.435	18.227	4.595	4.774	
CN	Tc *Calcidiscus premacintyrei*	12.570	2H-CC	13.84	13.453	3H-CC	23.03	23.001	18.435	18.227	4.595	4.774	
CN	T *Sphenolithus heteromorphus**	13.660	2H-CC	13.84	13.453	3H-CC	23.03	23.001	18.435	18.227	4.595	4.774	Hiatus
Pmag	B C5Br*	15.974	4H-2, 110	25.61	25.610	4H-2, 112	25.63	25.630	25.620	25.620	0.010	0.010	0.30
Pmag	B C5Cn.1n*	16.268	4H-3, 46	26.48	26.480	4H-3, 48	26.50	26.500	26.490	26.490	0.010	0.010	0.22
PF	B *Fohsella praefohsi*	13.780	3H-CC, 9–14	22.98	22.951	4H-CC, 14–19	32.49	32.490	27.735	27.721	4.755	4.770	
PF	T *Catapsydrax dissimilis*	17.510	3H-CC, 9–14	22.98	22.951	4H-CC, 14–19	32.49	32.490	27.735	27.721	4.755	4.770	
CN	Bc *Sphenolithus heteromorphus*	17.650	3H-CC	22.98	22.951	4H-CC	32.49	32.390	27.735	27.671	4.755	4.720	
Pmag	B C5Cr*	17.235	4H-4, 110	28.62	28.620	4H-4, 112	28.64	28.640	28.630	28.630	0.010	0.010	0.26
Pmag	B C5Dn*	17.533	4H-5, 38	29.40	29.400	4H-5, 40	29.42	29.420	29.410	29.410	0.010	0.010	0.31
Pmag	B C5Dr.2r*	18.007	4H-6, 36	30.88	30.880	4H-6, 38	30.90	30.900	30.890	30.890	0.010	0.010	0.08
Pmag	B C5En*	18.497	4H-6, 84	31.26	31.260	4H-6, 86	31.28	31.280	31.270	31.270	0.010	0.010	0.32
Pmag	B C5Er*	18.636	4H-7, 8	31.70	31.700	4H-7, 10	31.72	31.720	31.710	31.710	0.010	0.010	0.29
PF	T *Paragloborotalia pseudokugleri*	21.220	4H-CC, 14–19	32.44	32.440	5H-CC, 15–20	42.68	42.000	37.560	37.220	5.120	4.780	
PF	B *Globoquadrina dehiscens*	22.500	4H-CC, 14–19	32.44	32.440	5H-CC, 15–20	42.68	42.000	37.560	37.220	5.120	4.780	
PF	T *Ciperoella ciperoensis*	22.810	4H-CC, 14–19	32.44	32.440	5H-CC, 15–20	42.68	42.000	37.560	37.220	5.120	4.780	
CN	Tc *Triquetrorhabdulus carinatus*	19.180	4H-CC	32.44	32.440	5H-CC	42.68	42.000	37.560	37.220	5.120	4.780	
Pmag	B C6An.2n*	20.765	5H-4, 80	37.82	37.464	5H-4, 82	37.84	37.483	37.830	37.474	0.010	0.009	1.06
Pmag	B C6Ar*	21.130	5H-7, 14	41.69	41.076	5H-7, 16	41.71	41.094	41.700	41.085	0.010	0.009	0.21
Pmag	B C6Bn.1n*	21.985	6H-1, 146	43.46	43.460	6H-1, 148	43.48	43.480	43.470	43.470	0.010	0.010	0.17

There is agreement between fossil datums and paleomagnetic reversal datums in both holes, with a few exceptions. In Hole U1583C, some planktic foraminiferal datums lie ~1.6 to ~1.2 My outside of the calcareous nannofossil and magnetic reversal boundaries in the Oligocene and earliest Miocene. In Hole U1583E, planktic foraminiferal datums lie outside of the calcareous nannofossil and magnetic reversal boundaries by ~1.8 to ~1.6 My in the Pleistocene and 2.8 to ~0.6 My in the Oligocene to Miocene. As with other sites on the SAT (e.g., see **Biostratigraphy** and **Age model and mass accumulation rates** both in the Site U1558 chapter [Teagle et al., 2024a]), such differences may be attributed to species' diachroneity between our midlatitude sites and the tropical/subtropical sites at which these datums were calibrated (Wade et al., 2011; King et al., 2020; Lam et al., 2022). Because planktic foraminifera are relatively well preserved at Site U1583 and some of the asynchronous datums are bases, such age offsets cannot be fully explained by mixing or reworking, and further investigation of this diachroneity will require careful postexpedition work.

A major hiatus that spans from the Middle Miocene to Pliocene (~13–3 Ma) occurs in both holes. Linear sedimentation rates (LSRs) were calculated using microfossil datums as well as paleomagnetic reversal boundaries. Datums used to construct the age model are indicated with asterisks in Tables **T21** and **T22**. Rates are variable in both holes. Average sedimentation rates are low above and below the unconformity, with values in the Pleistocene of 0.22 and 0.28 cm/ky (in Holes U1583C and U1583E, respectively) and in the Lower Miocene of and 0.47 cm/ky in Hole U1583C and 0.29 cm/ky in Hole U1583E. Average sedimentation rates are highest in the Oligocene (0.73 cm/ky in Hole U1583C and 0.89 cm/ky in Hole U1583E).

Table T22 (continued).

Datum	Taxon/Chron (base)	Age (Ma)	Core, section, interval (cm)	Sample depth CSF-A (m)	Sample depth CSF-B (m)	Sample above/below	Sample above/below depth CSF-A (m)	Sample above/below depth CSF-B (m)	Midpoint depth CSF-A (m)	Midpoint depth CSF-B (m)	Depth error (±) CSF-A (m)	Depth error (±) CSF-B (m)	LSR (cm/ky)
Pmag	B C6Cn.2r*	23.212	6H-3, 52	45.53	45.530	6H-3, 54	45.55	45.550	45.540	45.540	0.010	0.010	0.95
PF	B *Trilobatus trilobus*	22.880	5H-CC, 15–20	42.63	41.953	6H-CC, 11–16	50.39	50.390	46.510	46.172	3.880	4.218	
PF	B *Paragloborotalia pseudokugleri*	25.200	5H-CC, 15–20	42.63	41.953	6H-CC, 11–16	50.39	50.390	46.510	46.172	3.880	4.218	
CN	T *Reticulofenestra bisecta*	23.130	5H-CC	42.63	41.953	6H-CC	50.39	50.390	46.510	46.172	3.880	4.218	
Pmag	B C6Cn.3n*	23.318	6H-4, 42	46.54	46.540	6H-4, 4	46.56	46.560	46.550	46.550	0.010	0.010	1.31
Pmag	B C6Cr*	24.025	7H-3, 128	55.79	55.592	7H-3, 130	55.81	55.611	55.800	55.602	0.010	0.009	1.58
CN	T *Sphenolithus ciperoensis*	24.360	6H-CC	50.34	50.340	7H-CC	61.46	61.000	55.900	55.670	5.560	5.330	
Pmag	B C7n.1n*	24.061	7H-4, 34	56.36	56.135	7H-4, 36	56.38	56.154	56.370	56.145	0.010	0.010	1.83
Pmag	B C7n.1r*	24.124	7H-4, 150	57.52	57.241	7H-5, 0	57.53	57.251	57.525	57.246	0.005	0.005	1.14
Pmag	B C7n.2n*	24.459	7H-7, 110	61.34	60.885	8H-1, 0	61.34	61.332	61.340	61.109	0.000	0.224	2.41
Pmag	B C7r*	24.654	8H-4, 52	66.03	65.912	8H-4, 54	66.05	65.931	66.040	65.922	0.010	0.009	2.04
Pmag	B C7An*	24.766	8H-5, 130	68.32	68.148	8H-5, 132	68.34	68.168	68.330	68.158	0.010	0.010	0.67
Pmag	B C7Ar*	25.099	9H-1, 6	70.56	70.560	9H-1, 8	70.58	70.580	70.570	70.570	0.010	0.010	0.55
Pmag	B C8n.1n*	25.264	9H-1, 96	71.46	71.460	9H-1, 98	71.48	71.480	71.470	71.470	0.010	0.010	0.95
Pmag	B C8n.1r*	25.304	9H-1, 134	71.84	71.840	9H-1, 136	71.86	71.860	71.850	71.850	0.010	0.010	1.12
CN	T *Chiasmolithus altus*	25.440	8H-CC	70.73	70.501	9H-CC	79.14	79.140	74.935	74.821	4.205	4.319	
Pmag	B C8n.2n*	25.987	9H-6, 98	79.00	79.000	10H-1, 0	80.00	80.000	79.500	79.500	0.500	0.500	1.74
Pmag	B C8r*	26.420	10H-5, 102	87.04	86.923	10H-5, 104	87.06	86.943	87.050	86.933	0.010	0.010	0.28
Pmag	B C9n*	27.439	11H-1, 38	89.88	89.879	11H-1, 40	89.90	89.899	89.890	89.889	0.010	0.010	1.04
Pmag	B C9r*	27.859	11H-4, 22	94.25	94.240	11H-4, 24	94.27	94.260	94.260	94.250	0.010	0.010	0.69
PF	T *Paragloborotalia opima*	27.300	10H-CC, 7–12	89.61	89.451	11H-CC, 15–20	99.02	99.000	94.315	94.226	4.705	4.775	
PF	HCO *Chiloguembelina cubensis*	28.300	10H-CC, 7–12	89.61	89.451	11H-CC, 15–20	99.02	99.000	94.315	94.226	4.705	4.775	
CN	T *Sphenolithus predistentus*	26.930	10H-CC	89.61	89.451	11H-CC	99.02	99.000	94.315	94.226	4.705	4.775	
CN	B *Sphenolithus ciperoensis*	27.130	10H-CC	89.61	89.451	11H-CC	99.02	99.000	94.315	94.226	4.705	4.775	
Pmag	B C10n.1n*	28.087	11H-5, 30	95.83	95.816	11H-5, 32	95.85	95.836	95.840	95.826	0.010	0.010	0.29
Pmag	B C10r*	29.183	12H-1, 4	99.04	99.040	12H-1, 6	99.06	99.060	99.050	99.050	0.010	0.010	0.48
Pmag	B C11n.1n*	29.477	12H-1, 144	100.44	100.440	12H-1, 146	100.46	100.460	100.450	100.450	0.010	0.010	2.44
Pmag	B C11n.1r*	29.527	12H-2, 116	101.66	101.660	12H-2, 118	101.68	101.680	101.670	101.670	0.010	0.010	0.73
PF	B *Ciperoella angulisuturalis*	29.500	11H-CC, 15–20	98.97	98.950	12H-CC, 0–1	105.13	105.130	102.050	102.040	3.080	3.090	
PF	T *Subbotina angiporoides*	30.100	11H-CC, 15–20	98.97	98.950	12H-CC, 0–1	105.13	105.130	102.050	102.040	3.080	3.090	
PF	T *Turborotalia ampliapertura*	30.400	11H-CC, 15–20	98.97	98.950	12H-CC, 0–1	105.13	105.130	102.050	102.040	3.080	3.090	
PF	B *Paragloborotalia opima*	30.800	11H-CC, 15–20	98.97	98.950	12H-CC, 0–1	105.13	105.130	102.050	102.040	3.080	3.090	

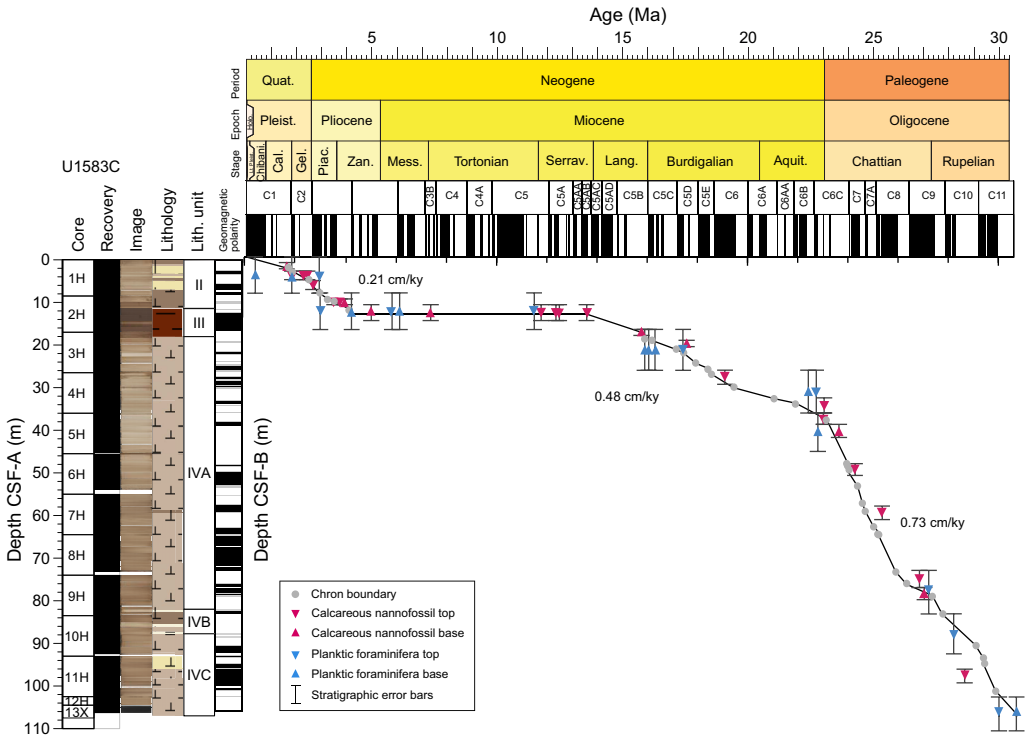

Figure F65. Age-depth model showing biostratigraphic and magnetostratigraphic datums, Hole U1583C. LSRs calculated based on indicated datums in Table T21 and averaged for Pleistocene, Pliocene, Miocene, and Oligocene. See Sedimentology for description of lithology symbols.

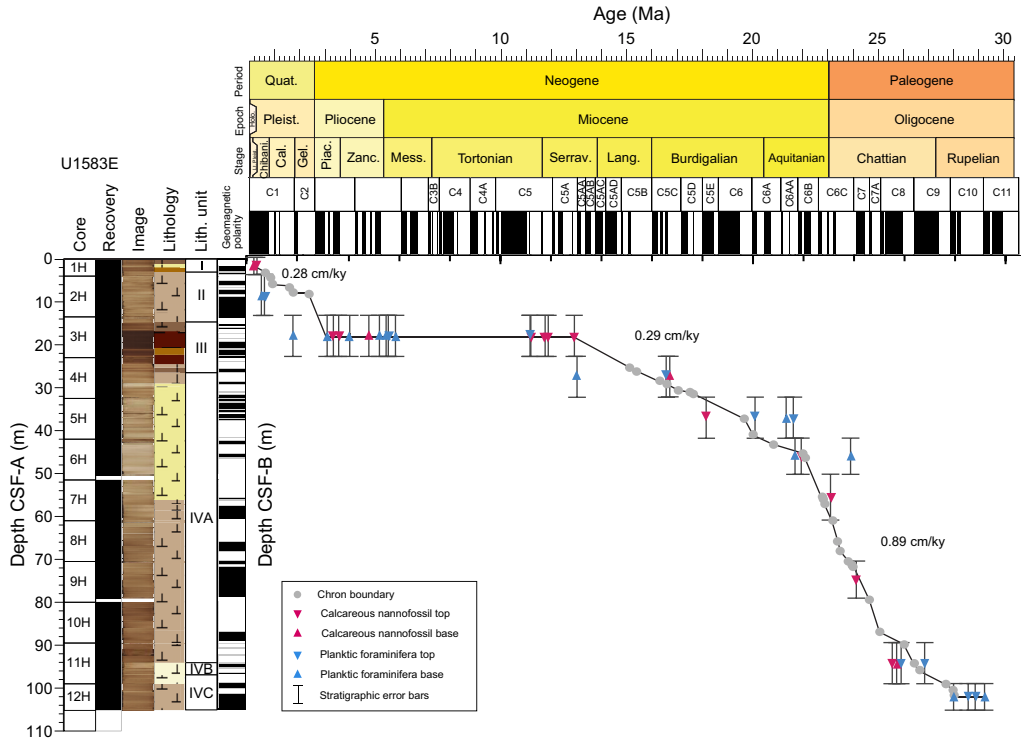

Figure F66. Age-depth model showing biostratigraphic and magnetostratigraphic datums, Hole U1583E. LSRs calculated based on indicated datums in Table T22 and averaged for Pleistocene, Pliocene, Miocene, and Oligocene. See Sedimentology for description of lithology symbols.

9.2. Mass accumulation rates

Mass accumulation rates (MARs), were calculated for Hole U1583C using the LSRs and dry bulk density calculated from gamma ray attenuation (GRA) measurements collected during Whole-Round Multisensor Logger (WRMSL) scans (see **Age model and mass accumulation rates** in the Expedition 390/393 methods chapter [Coggon et al., 2024a]; see also U1583_MAR.xlsx in AGE-MODEL in **Supplementary material**). A hiatus or condensed interval that occurs from the Late Miocene to Pliocene (see **Biostratigraphy**) results in an extended interval of MAR values of zero in Hole U1583C. The data presented in Figure **F67** are binned into 1 My intervals. Carbonate and organic carbon measurements were not taken from Hole U1583E, so MARs were not calculated for this hole.

MARs vary throughout the sedimentary succession in Hole U1583C (Figure **F67A**). MARs are highest in the Oligocene and earliest Miocene, with a peak around 1.7 g/cm^2/ky. Values are much

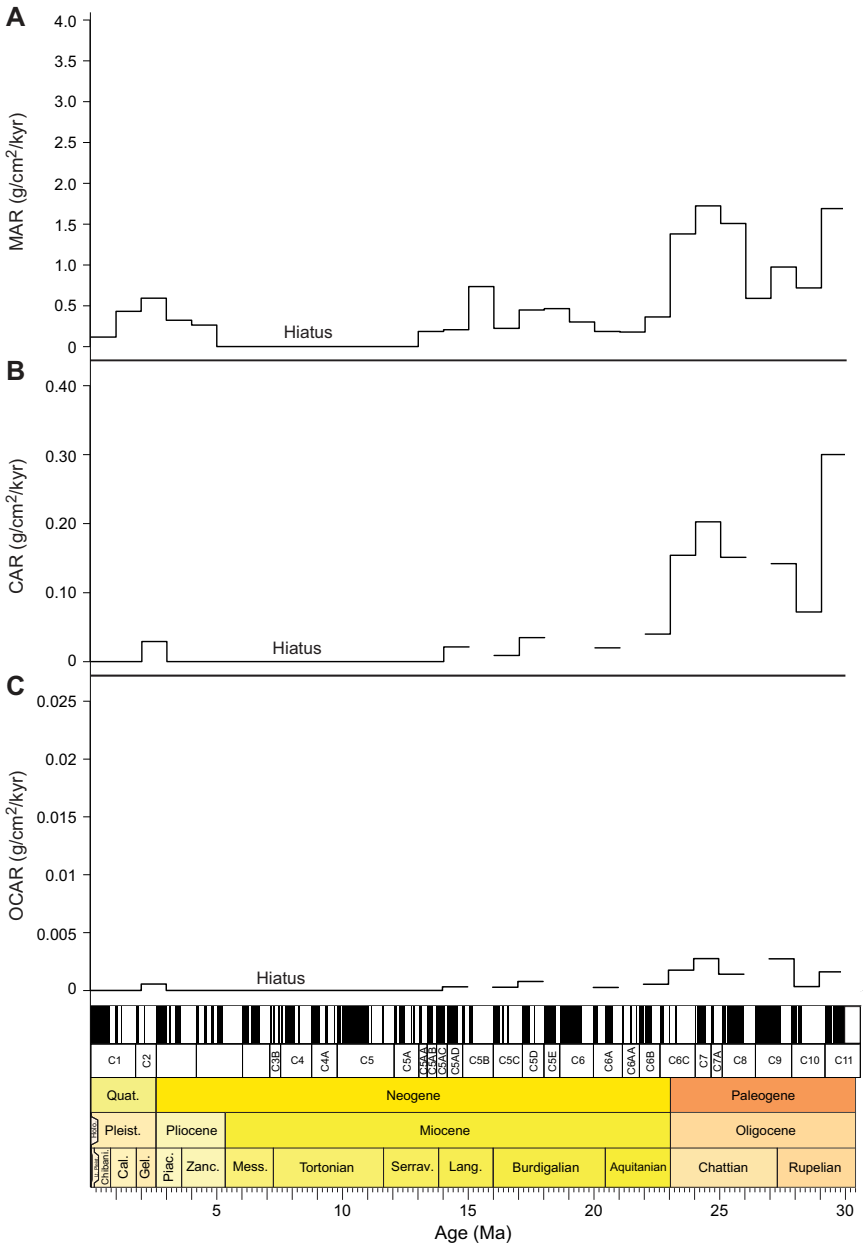

Figure F67. (A) MAR, (B) CAR, and (C) OCAR calculated at 1 My intervals, Hole U1583C. Gaps in CAR and OCAR values = 1 My time intervals with no carbonate or TOC data available.

lower in the rest of the Miocene and Pliocene–Pleistocene. Below the unconformity in the Early Miocene, values range 0.2–0.7 g/cm^2/ky. In the Pliocene–Pleistocene above the unconformity, MAR values range 0.1–0.6 g/cm^2/ky.

9.3. Carbonate and organic carbon accumulation rates

Carbonate accumulation rates (CARs) and organic carbon accumulation rates (OCARs) in Hole U1583C were calculated by multiplying MARs by %$CaCO_3$ and weight percent total organic carbon (TOC). In Hole U1583C, carbonate content and TOC was measured from interstitial water (IW) squeeze cakes, with an additional discrete sample taken from most cores. The data presented in Figure **F67** are binned into 1 My intervals.

CARs broadly follow trends in MARs and are highest for the Oligocene, with values ranging 0.08–0.30 g/cm^2/ky (Figure **F67**). Neogene and Quaternary CARs are lower, with values ranging 0.0001–0.04 g/cm^2/ky. OCARs are extremely low through the sedimentary section at Site U1583, with peak values of 0.003 g/cm^2/ky in the Oligocene (Figure **F67**). OCARs are lowest in the Neogene and Quaternary, with values ranging 0.0003–0.0008 g/cm^2/ky.

10. Physical properties and downhole measurements

10.1. Sediment

Physical properties characterization of the sediment sequence at Site U1583 was primarily based on cores from Holes U1583C and U1583E. Hole U1583E was the only one to recover a clear mudline. Holes U1583A, U1583B, and U1583D were single-core holes abandoned immediately after missing the mudline. Although physical properties measurements were performed on cores from Holes U1583A, U1583B, and U1583D, these results are not discussed here or included in the stratigraphic correlation. Shipboard stratigraphic correlation only later determined that Hole U1583C had also missed the mudline and did not sample the uppermost 5.6 m of Unit I (see **Sedimentology**) at Site U1583 (see **Stratigraphic correlation**), corresponding to Pliocene–Pleistocene (see **Age model and sedimentation rates**). Hole U1583F was drilled without coring through 101 m of sediment before starting RCB coring and encountered basement at 109.5 mbsf. Unfortunately, an intact sediment/volcanic rock interface was not recovered.

Whole-round core section measurements from Hole U1583C, comprising NGR, GRA bulk density, MS (including point magnetic susceptibility [MSP] on the Section Half Multisensor Logger [SHMSL]), and *P*-wave velocity, are shown in Figure **F68**. Split-core section measurements such as *P*-wave velocity, thermal conductivity, and sediment shear and compressional strength are shown in Figure **F69**. A total of 24 discrete sediment samples were taken from the working halves for moisture and density (MAD) analysis (Table **T23**), and select discrete samples were taken for measurements of thermal conductivity, sediment strength, and *P*-wave velocity (Figure **F69**; Table **T24**). Track measurements were made on cores from both holes (Figures **F68**, **F70**), but discrete measurements were only made on cores from Hole U1583C (Figures **F68**, **F69**). The NGR, GRA, MS, and *P*-wave velocity data from both holes display similar features (see **Stratigraphic correlation**), and consequently, the descriptions of Site U1583 sediment physical properties are predominantly based on Hole U1583C. Because Lithostratigraphic Unit I was only recovered in Hole U1583E and not in Hole U1583C, we describe the whole-round track data (NGR, GRA, MS, and *P*-wave velocity) of Unit I in Hole U1583E (Figure **F70**). Unless otherwise specified, we use the uncompressed CSF-A depth scale (mbsf) to show data from each hole. Mean values of all physical properties are represented with ranges of ±1 standard deviation in Table **T25**.

10.1.1. Physical properties

10.1.1.1. Natural gamma radiation

NGR ranges 1–38 counts/s throughout the sedimentary section in Hole U1583C (Figure **F68**). NGR shows a sharp decrease from 57 to 7 counts/s in Unit I in Hole U1583E, reflecting nannofossil-rich clay intervals. NGR is relatively low in Unit II (0–11.3 mbsf in Hole U1583C) and ranges 4–18 counts/s (mean = 8 ± 3 counts/s), but Unit III yields high counts throughout (range =

15–42 counts/s; mean = 27 ± 10 counts/s) (Table **T25**). A similar interval of relatively high NGR values was also detected in Hole U1583E (mean = 23 ± 11 counts/s) and is one of the key tie points for stratigraphic correlation (see **Stratigraphic correlation**). These high NGR values reflect layers of brown clay-rich sediment (see **Sedimentology**). NGR returns to low values and stays relatively stable in Subunits IVA (mean = 6 ± 2 counts/s), IVB (mean = 4 ± 2 counts/s), and IVC (mean = 4 ± 1 counts/s), which are typical values for nannofossil ooze layers at this site (Table **T25**).

NGR total activity can also be expressed in terms of the elemental concentrations of K, U, and Th. Gamma ray total spectrum was deconvolved using a shipboard Matlab routine retrofitted to process the data from Holes U1583C and U1583E (Figures **F71**, **F72**, respectively), where the concentration of potassium is measured in weight percent (wt%) and the other two elements are measured in parts per million (ppm). Elemental concentrations display trends that are all similar to the NGR total counts, with only some minor changes in relative concentrations among the components. There is no indication of independent behavior from any of the individual elemental components.

10.1.1.2. Magnetic susceptibility

MS measured by WRMSL and MSP methods records similar downhole trends and magnitudes in both holes (range = 1–122 instrument units [IU]) (Figures **F68**, **F70**). MS shows a downhole trend similar to the NGR records over the entire hole, with the highest values in Unit III (range = 30–122 IU; mean = 78 ± 34 IU). MS is relatively higher and more variable in Units I and II (mean = 30 ± 10 and 24 ± 9 IU, respectively; Unit I was measured only in Hole U1583E) compared to Subunits IVA

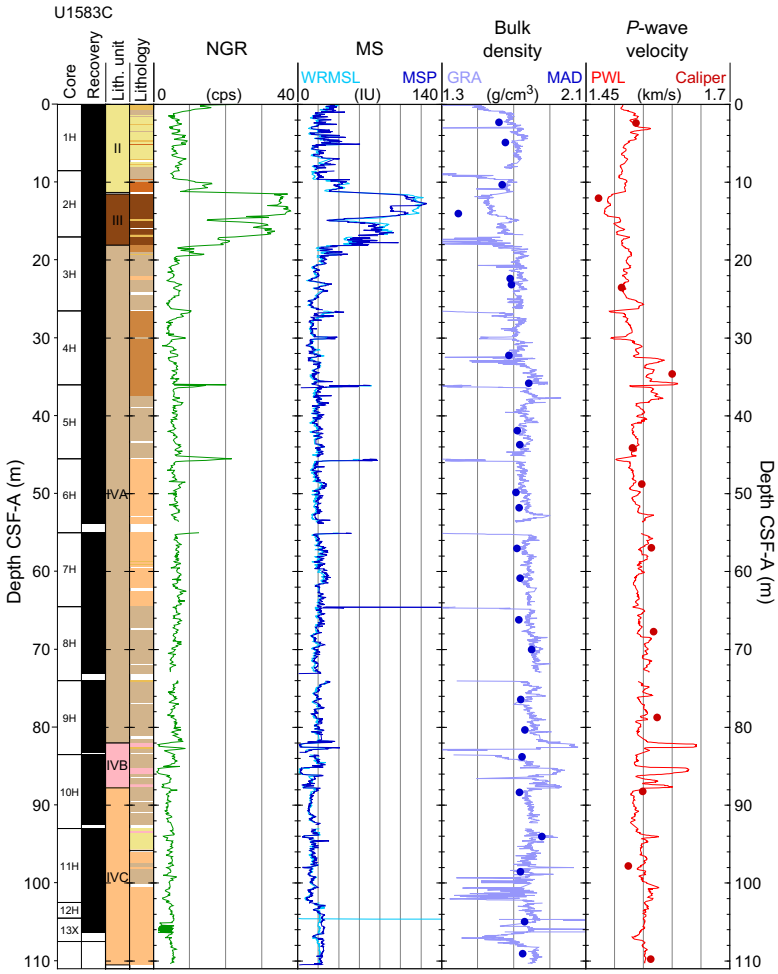

Figure F68. Summary of track physical properties, Hole U1583C. Solid circles = discrete bulk density and *P*-wave velocity measurements. cps = counts per second.

(mean = 19 ± 4 IU), IVB (mean = 12 ± 8 IU), and IVC (mean = 16 ± 4 IU) (Figures **F68**, **F70**; Table **T25**). Several abrupt peaks >40 IU are found at the top of Cores 393-U1583C-5H, 6H, 7H, 8H, and 13X (this one only shown in WRMSL) that are probably due to material falling from the shallower high-susceptibility interval while retrieving the previous core rather than to in-place formation variations. Similar peaks observed at the same depths in the NGR record could have the same origin. These were considered as outliers (as well as any data above the 140 IU cutoff) and therefore removed from statistics calculations. These peaks were not used in stratigraphic correlation. The higher MS values in Unit III correspond to brown clay-rich layers, whereas the relatively low values in Units I, II, and IV reflect the nannofossil ooze sediments.

10.1.1.3. Gamma ray attenuation bulk density

Bulk density from GRA ranges 1.0–2.0 g/cm^3 (Figures **F68**, **F70**); however, we cut off values <1.3 g/cm^3 for Hole U1583C and <1.4 g/cm^3 for Hole U1583E for the purpose of plotting and calculations and because they are all related to edges and cracks in the sediment or incomplete filling of the core liner, where a mixture of sediment and air is measured in both.

GRA density for Hole U1583C shows an overall mean of 1.8 ± 0.1 g/cm^3 and displays consistently lower values in Unit III (1.6 ± 0.1 g/cm^3) (Table **T25**), corresponding to the clay-rich interval. Bulk density shows an overall gradual increase downhole (Figures **F68**, **F70**) because of increasing consolidation of sediments with depth.

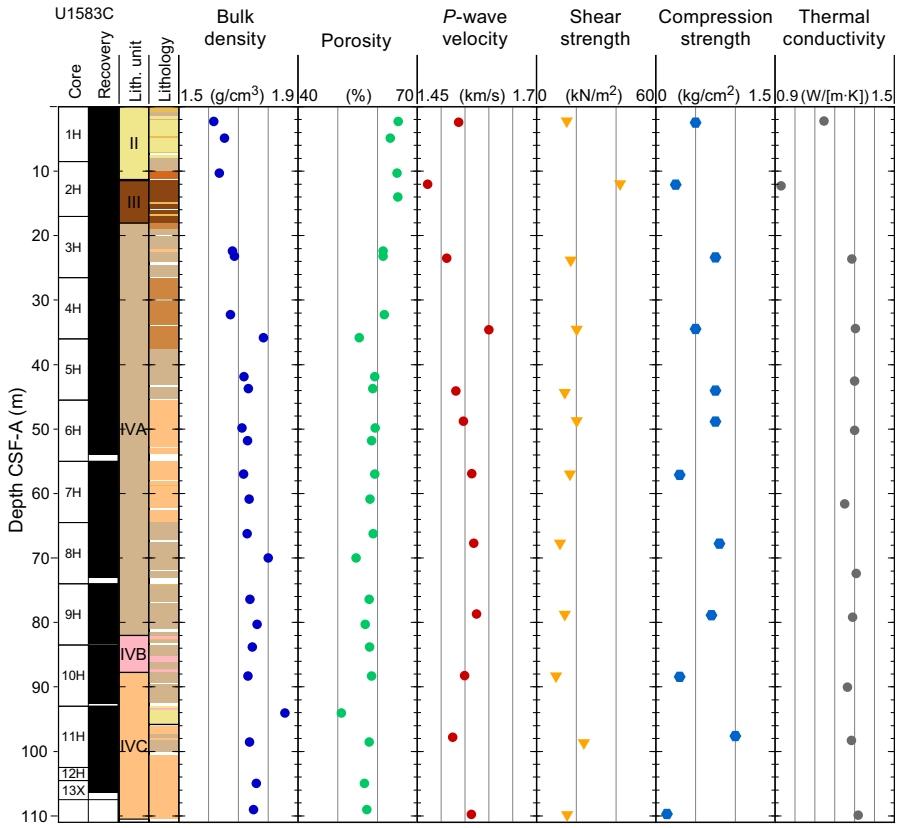

Figure F69. Summary of discrete physical properties, Hole U1583C. *P*-wave velocity data shown is highest value measured for each sample. See Sedimentology for description of lithology symbols.

Table T23. Discrete MAD results, Site U1583. **Download table in CSV format.**

Table T24. Discrete physical properties, Site U1583. **Download table in CSV format.**

10.1.1.4. Moisture and density

MAD analysis investigated 24 discrete samples with generally two samples per core chosen to represent all the lithologies encountered (Figure **F69**; Tables **T23**, **T25**). Porosity of the sedimentary section shows an overall decreasing trend from 65% at the seafloor to 55% at ~40 mbsf in Subunit IVA and stays relatively uniform (50%–60%) from 40 to 110 mbsf near the sediment/basement interface (Figure **F69**). The overall mean for porosity is 59% ± 3% (Table **T25**) with similar values in Units II and III (mean = 64% ± 1% for Unit II; only 1 sample in Unit III at 65%) and somewhat slightly lower values in Unit IV, decreasing with depth because of sediment compaction (Table **T25**). Porosity measurements for Unit I are missing because Unit I was only cored in Hole U1583E, where no discrete samples were taken.

GRA and MAD methods show good agreement between bulk density trends (Figure **F68**), although slightly lower values from the MAD method potentially reflect sediment expansion after splitting and subsequent water loss.

10.1.1.5. *P*-wave velocity

P-wave velocity data are consistent between the WRMSL and caliper methods (Figures **F68**, **F69**) and range 1.45–1.72 km/s (mean = 1.54 ± 0.03 km/s) (Table **T25**). *P*-wave velocity from the WRMSL *P*-wave logger (PWL) is relatively lower in Units I (mean = 1.50 ± 0.01 km/s) and III (mean = 1.50 ± 0.02 km/s) compared to the other two units (means: Unit II = 1.52 ± 0.02 km/s, Subunit IVA = 1.54 ± 0.19 km/s, Subunit IVB = 1.57 ± 0.04 km/s, and Subunit IVC = 1.55 ± 0.02

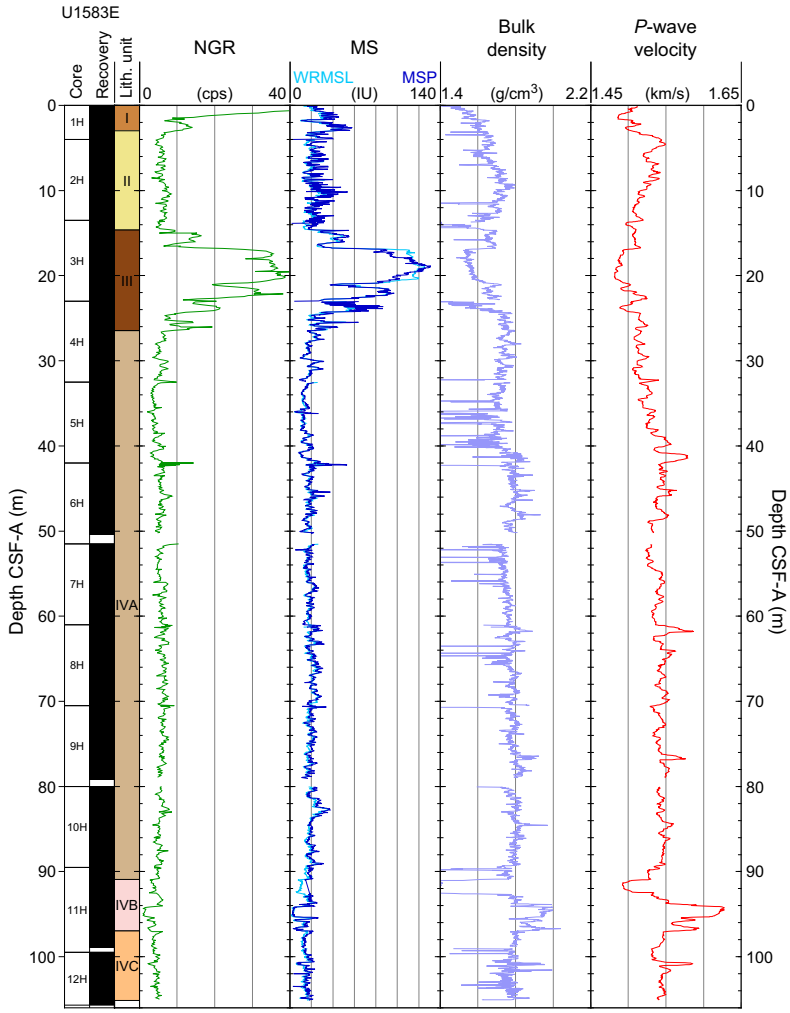

Figure F70. Summary of track physical properties, Hole U1583E. cps = counts per second. See Sedimentology for description of lithology symbols.

km/s) (Table T25). The overall downhole increasing trend imitates the bulk density trend, both of which are likely due to increasing amounts of mechanical and potentially chemical compaction.

10.1.1.6. Sediment strength

Shear strength ranges from 10 to 42 kg/cm^2 in all samples (mean = 18 ± 8 kN/cm^2) (Figure F69; Tables T24, T25). Shear strength is relatively uniform in Unit II and Subunits IVA–IVC (15–16 kN/cm^2); the highest value of 42 kN/cm^2 is in Unit III. Compressional strength scatters from 0.1 to 1.0 kg/cm^2 (mean = 0.6 ± 0.3 kg/cm^2) throughout the sedimentary sections without any apparent downhole trend (Table T25).

10.1.1.7. Thermal conductivity

Twelve discrete thermal conductivity measurements, approximately one per core, were conducted on representative lithologies from Hole U1583C (Figure F69) using the half-space heating puck on split section halves (see **Physical properties and downhole measurements** in the Expedition 390/393 methods chapter [Coggon et al., 2024a]). Thermal conductivity ranges 0.93–1.32 W/(m·K) throughout all sections (Table T24) (mean = 1.25 ± 0.11 W/[m·K]) (Table T25). Thermal conductivity is relatively low in Unit II (1.14 W/[m·K]), with the lowest measurements taken in Unit III (0.93 W/[m·K]), and increases to 1.29 ± 0.02 W/(m·K) throughout the Unit IV subunits (Table T25).

10.1.2. Lithostratigraphic unit comparison

Four physical properties (*P*-wave velocity, GRA bulk density, MS, and NGR) are grouped by lithostratigraphic units (see **Sedimentology**) and compared in Figure F73. *P*-wave velocity (V_P) shows a negative power law correlation with NGR (R^2 = 0.4), with measurements from Unit IV spanning the full range of *P*-wave velocity and the lower range of NGR values (Figure F73A). Data from Subunit IVB stands out in the highest *P*-wave velocity range, whereas samples from Unit III display the widest range of NGR and relatively uniform *P*-wave velocity near ~1.50 km/s. *P*-wave velocity shows a general positive linear correlation with GRA bulk density (R^2 = 0.5), with Unit III falling into the lower bulk density and lower *P*-wave velocity component (Figure F73B). Negative power law correlation is found between GRA bulk density and NGR values (R^2 = 0.4); samples from Unit III are easily distinguished from other units due to higher NGR values and the majority of samples showing GRA mean density of ~1.6 g/cm^3 (Figure F73C). A strong positive linear cor-

Table T25. Physical properties statistics, Site U1583. 1σ = one standard deviation. Groups with only one sample do not have a standard deviation (NA). **Download table in CSV format.**

Group	NGR mean (counts/s)	NGR 1σ (counts/s)	MS WRMSL mean (IU)	MS WRMSL 1σ (IU)	MSP mean (IU)	MSP 1σ (IU)	GRA bulk density mean (g/cm^3)	GRA bulk density 1σ (g/cm^3)	Thermal conductivity mean (W/[m·K])	Thermal conductivity 1σ (W/[m·K])	WRMSL *P*-wave velocity mean (km/s)	WRMSL *P*-wave velocity 1σ (km/s)
Unit I	23	17	30	10	34	11	1.56	0.06	NA	NA	1.50	0.01
Unit II	8	3	24	9	27	9	1.64	0.14	1.14	NA	1.52	0.02
Unit III	27	10	78	34	75	29	1.61	0.09	0.93	NA	1.50	0.02
Unit IVA	6	2	19	4	20	4	1.76	0.08	1.29	0.02	1.54	0.02
Unit IVB	4	2	12	8	13	8	1.83	0.15	NA	NA	1.57	0.04
Unit IVC	5	1	16	4	17	5	1.77	0.08	1.29	0.02	1.55	0.02
Hole U1583C	7	6	23	19	24	18	1.76	0.08	1.25	0.11	1.54	0.03
Hole U1583E	8	8	24	21	25	20	1.72	0.12	NA	NA	1.53	0.03

Group	Caliper *P*-wave velocity mean (km/s)	Caliper *P*-wave velocity 1σ (km/s)	Porosity mean (%)	Porosity 1σ (%)	MAD bulk density mean (g/cm^3)	MAD bulk density 1σ (g/cm^3)	Grain density mean (g/cm^3)	Grain density 1σ (g/cm^3)	Compressional strength mean (kg/cm^2)	Compressional strength 1σ (kg/cm^2)	Vane shear strength mean (KN/m^2)	Vane shear strength 1σ (KN/m^2)
Unit I	NA	NA	NA	NA	NA	NA	NA	NA	NA	NA	NA	NA
Unit II	1.54	NA	64	1	1.64	0.02	2.74	0.02	0.5	NA	15	NA
Unit III	1.47	NA	65	NA	1.39	NA	2.08	NA	0.3	NA	42	NA
Unit IVA	1.56	0.03	59	2	1.73	0.04	2.73	0.01	0.7	0.2	16	3
Unit IVB	NA	NA	58	NA	1.75	NA	2.74	NA	NA	NA	NA	NA
Unit IVC	1.55	0.02	56	3	1.77	0.05	2.72	0.00	0.5	0.5	16	7
Hole U1583C	1.55	0.03	59	3	1.71	0.09	2.70	0.13	0.6	0.3	18	8
Hole U1583E	NA	NA	NA	NA	NA	NA	NA	NA	NA	NA	NA	NA

relation (R^2 = 0.9) is found between NGR and MS (Figure **F73D**), reflecting their similar downhole trends in Figure **F68**. Samples from Unit III fall into the higher MS and higher NGR component, whereas data from the other three units cluster toward lower MS and lower NGR values. Overall in track data, Unit III stands out due to high NGR and MS, likely reflecting the higher clay content intervals.

A similar comparison is shown in Figure **F74**, where the parameters are compared by section-by-section sedimentary classification (see **Sedimentology**) instead of lithostratigraphic unit. The interpretation is the same, with the differences in clay content driving the most significant variations, but it narrows the influence of each type of lithology and illustrates the finer scale variability that can be seen in each unit (Figure **F68**), such as the lower gamma ray in the calcareous ooze layers in Subunit IVB or in layers of clayey nannofossil ooze in Unit III.

10.1.3. X-ray imaging

Sediment cores from Holes U1583C and U1583E were scanned with the X-Ray Logger (XMAN), and images were used to assist core description. For example, in interval 393-U1583C-2H-5, 40–56 cm, several ichnofossils were identified (see **Sedimentology**) from the X-ray images and the core photos (Figure **F75A**). In another example, interval 393-U1583E-12H-1, 5–6 cm, dark spots in the X-ray images were identified as relatively dense carbonate nodules (Figure **F75B**). However, not all features in X-ray images are primary sedimentologic features. For example, the irregular bands and bubble-like shapes seen in interval 393-U1583C-1H-1, 12–22 cm, are drilling disturbance rather than bioturbation (Figure **F75C**). The X-ray images are useful for identifying fall-in at the top of cores, and other drilling-related deformation.

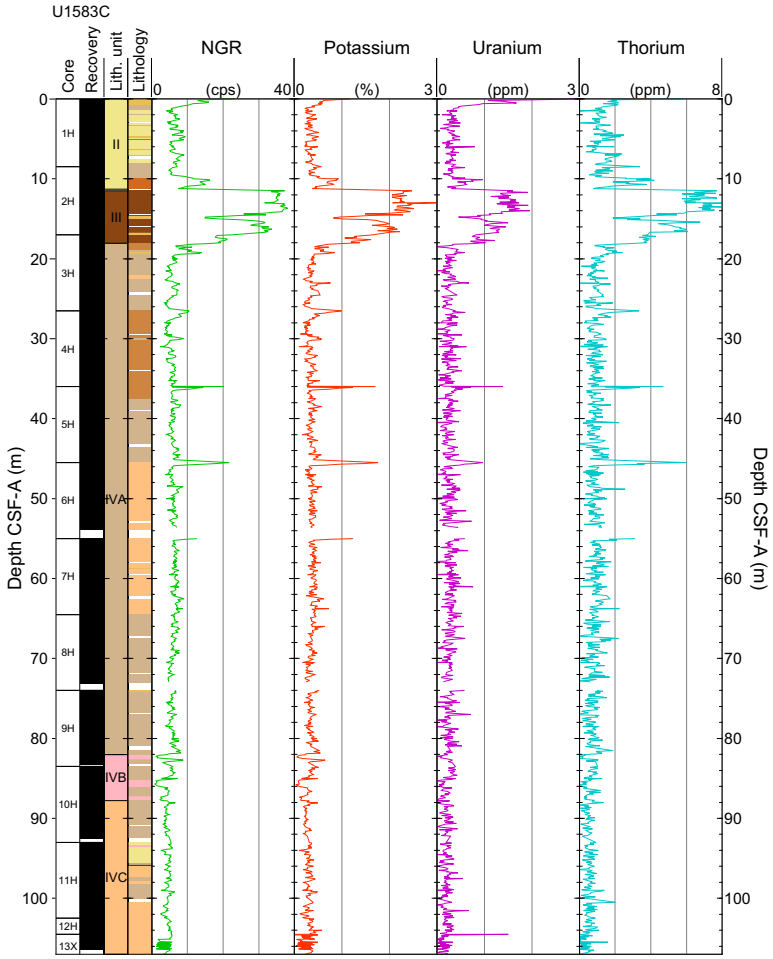

Figure F71. Concentrations of K, U, and Th derived from NGR, Hole U1583C. cps = counts per second. See Sedimentology for description of lithology symbols.

10.1.4. Downhole measurements

10.1.4.1. Downhole temperature

During APC coring in Holes U1583C and U1583E, the advanced piston corer temperature (APCT-3) probe was used to measure in situ formation temperature at selected depths, typically ~30 m apart. The APCT-3 tool was deployed while coring Cores 393-U1583C-4H, 7H, and 10H, as well as Cores 393-U1583E-5H and 8H (Table **T26**). Figure **F76** shows for each deployment the intervals in the temperature records that were used to estimate formation temperature by finding a best fit for a theoretical model to the temperature decay as a function of time as it recovers from the frictional heating generated when entering the formation.

10.1.4.2. Heat flow

Although the temperature records show that most of the temperature stations were stable for only a few minutes (the shallower cores in particular: 393-U1583C-4H and 393-U1583E-5H; Figure **F76**), the resulting temperatures define a steadily increasing temperature profile with a least-squares linear fit gradient of 25°C/km (Figure **F77C**).

A simple estimate of the vertical conductive heat flow can be made from the product of this gradient and the mean thermal conductivity (1.24 W/[m·K]; Figure **F77A**) measured on the cores recovered over this interval: 31 mW/m^2.

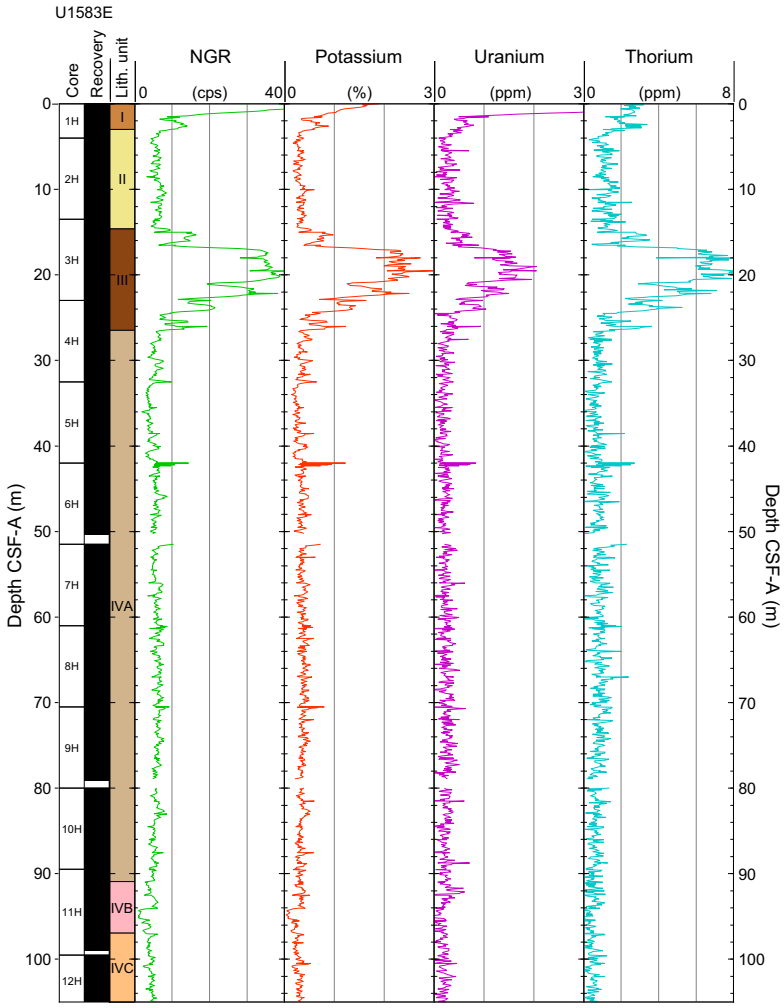

Figure F72. Concentrations of K, U, and Th derived from NGR, Hole U1583E. cps = counts per second. See Sedimentology for description of lithology symbols.

Another measure of the conductive heat flow can be established with a Bullard plot (see **Physical properties and downhole measurements** in the Expedition 390/393 methods chapter [Coggon et al., 2024a]). The heat flow estimate defined by the slope of the least-squares linear fit to the Site U1583 temperature data as a function of thermal resistance is 31 mW/m^2 (Figure **F77D**), identical to the previous estimate.

Table **T27** summarizes these results as well as the results of the same calculation for each hole. It confirms that both holes display very similar temperature gradient and conductive heat flow values, all about half of the 60 mW/m^2 value estimated for 30 Ma Southern Atlantic crust (Sclater et al., 1980) or simple plate cooling models (e.g., Stein and Stein, 1992). However, our results are similar to the geographically nearest heat flow measurement in the global heat flow compilation (29 and 37 mW/m^2; see Fuchs et al., 2021). The significant differences between our measurements of the conductive heat flow in the sediments and the predictions probably result from extensive hydrothermal advection in the crust in this region facilitated by numerous volcanic outcrops and discontinuous sediment blankets (e.g., Kardell et al., 2021).

10.1.5. Stratigraphic correlation

At Site U1583, five holes were cored using the APC system (Holes U1583A–U1583E) (Figure **F8**; see **Operations**) to recover the mudline, which was successfully intercepted only in Hole U1583E. A total of 110.10 and 105.15 m of sediments were recovered from Holes U1583C and U1583E, respectively (Figure **F78**). Cores 393-U1583C-12H and 13X were not considered for correlation and are not shown in the spliced section because Core 12H recovered 8.02 m after only 2 m of drill bit advancement, equal to 401% of core recovery (see **Operations**). This coring artifact is due to suck-in of sediment after hitting basement at the bottom of the hole. Core 13X was 1.8 m of fine-grained basalt recovered by XCB coring.

10.1.5.1. Correlation and splice

Physical properties data such as MS (by Special Task Multisensor Logger [STMSL]), GRA, NGR, and magnetic inclination (after the 20 mT AF demagnetization step, see **Paleomagnetism**) from Holes U1583C and U1583E were correlated to establish a composite depth scale (core composite

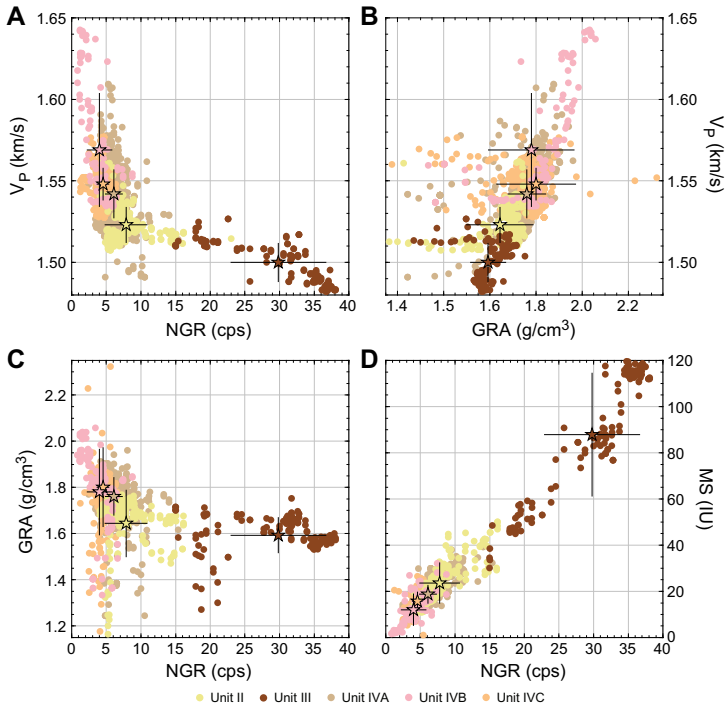

Figure F73. Crossplots of sediment samples by lithostratigraphic units, Hole U1583C. A. NGR vs. V_P. B. GRA bulk density vs. V_P. C. NGR vs. GRA bulk density. D. NGR vs. MS. Mean (stars) and standard deviation (error bars) for each unit are shown. cps = counts per second.

depth below seafloor [CCSF]) for Site U1583 (Figure **F78**; Tables **T28**, **T29**). Correlation from Site U1583 resulted in a spliced record of 129 m CCSF, with a total core gap of ~17 m (Figure **F78**). Correlations allowed us to identify an initial 5.6 m vertical difference between the top of Hole U1583E (i.e., mudline) and the top of Hole U1583C, which is missing the uppermost Unit I (see **Sedimentology**) (Figure **F78**).

Generally, paleomagnetic inclination provided a useful data set for stratigraphic correlation because the positive/negative inclination patterns are less ambiguous to correlate compared to physical properties track data, especially as the latter show no distinctive MS or NGR pattern from ~30 CCSF to the bottom of the hole, because Subunits IVA–IVC are similar lithologies (light-colored nannofossil ooze with clay; see **Sedimentology**) (Figures **F68**, **F70**). In both holes, numerous intervals are affected by severe drilling disturbance or fall-in effects that often occur at the top of the first section of the cores (e.g., 393-U1583E-2H, 3H, 4H, 6H, 9H, and 11H) and/or within the core sections (393-U1583C-4H-3 and 393-U1583E-5H-3, 11H-2). Disturbed layers were also identified by means of X-ray images and sedimentologic description coupled with linescan images (Figure **F75**) and eventually excluded from the splice.

Only in a few cases it was possible to overlap the stratigraphic records between the two holes and establish a continuous splice (e.g., 38–57 and 95–117 m CCSF; Figure **F78**). In the case of aligned core gaps between holes, cores below the gap are no longer tied to the anchor core, but they produce floating sections on the CCSF. Such floating ties were denoted in the affine table as "SET," assuming a constant growth rate of the difference between mbsf and CCSF (Table **T29**). Despite that, some distinctive stratigraphic layers were found to be thicker in Hole U1583E, on the order of 0.3 to 2 m difference with respect to their equivalent in Hole U1583C. We also chose to add 1 m between floating cores to include the unknown missing thickness due to incomplete recovery and the ~10% of expansion mainly due to decompression of the sediments as they are brought to atmo-

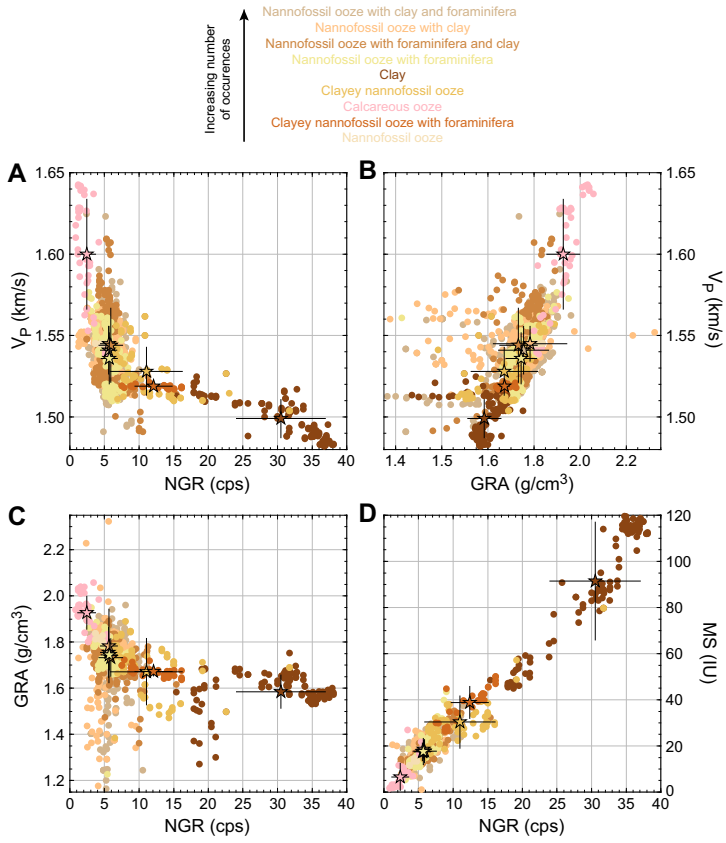

Figure F74. Crossplots of sediment samples by lithology, Hole U1583C. A. NGR vs. V_P. B. GRA bulk density vs. V_P. C. NGR vs. GRA bulk density. D. NGR vs. MS. Mean (stars) and standard deviation (error bars) for each lithology are shown. cps = counts per second.

spheric pressure or stretching that occurs as part of the coring process (see **Physical properties and downhole measurements** in the Expedition 390/393 methods chapter [Coggon et al., 2024a]).

Figure **F78** also shows the splice of paleomagnetic inclination (see **Paleomagnetism**), which can be interpreted as a synthetic polarity scale and integrated with bioevents to create the age model at Site U1583 (see **Age model and sedimentation rates**).

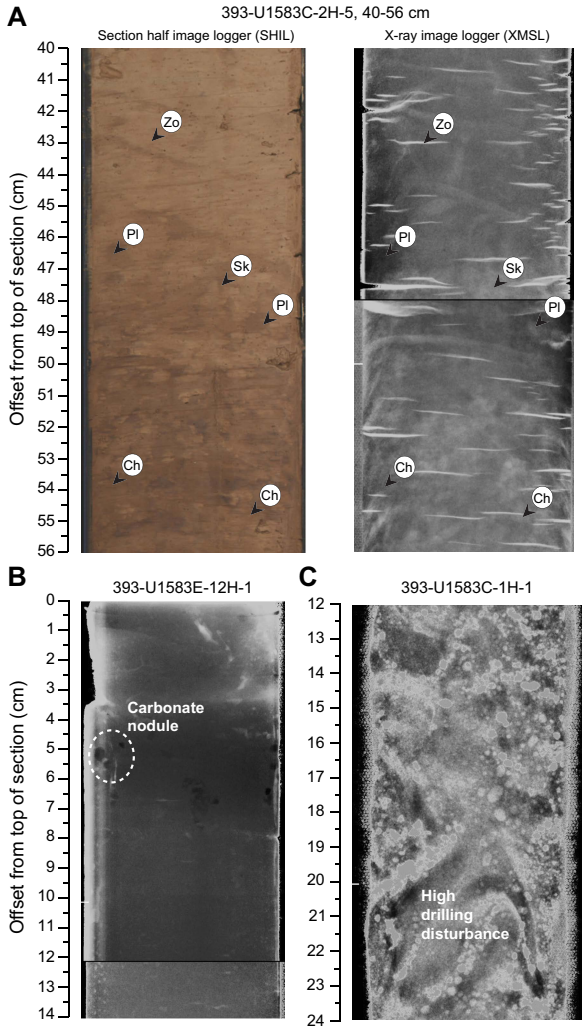

Figure F75. A. SHIL core image compared to XMAN X-ray image to identify trace fossils, Hole U1583C. Interval shows heavy bioturbation. Zo = *Zoophycos*, Pl = *Planolites*, Sk = *Skolithos*, Ch = *Chondrites*. B. Black spots in X-ray images identified as carbonate nodules, Hole U1583E. C. Bands and bubble-like features identified as drilling disturbance instead of real sedimentological features, Hole U1583C.

Table T26. Formation temperature measurements, Site U1583. **Download table in CSV format.**

Core, section	Measurement depth (mbsf)	Equilibrium temperature (°C)
393-U1583C-		
4H	36.0	3.04
7H	64.5	3.42
10H	93.0	4.29
393-U1583E-		
5H	42.0	2.64
8H	70.5	3.38

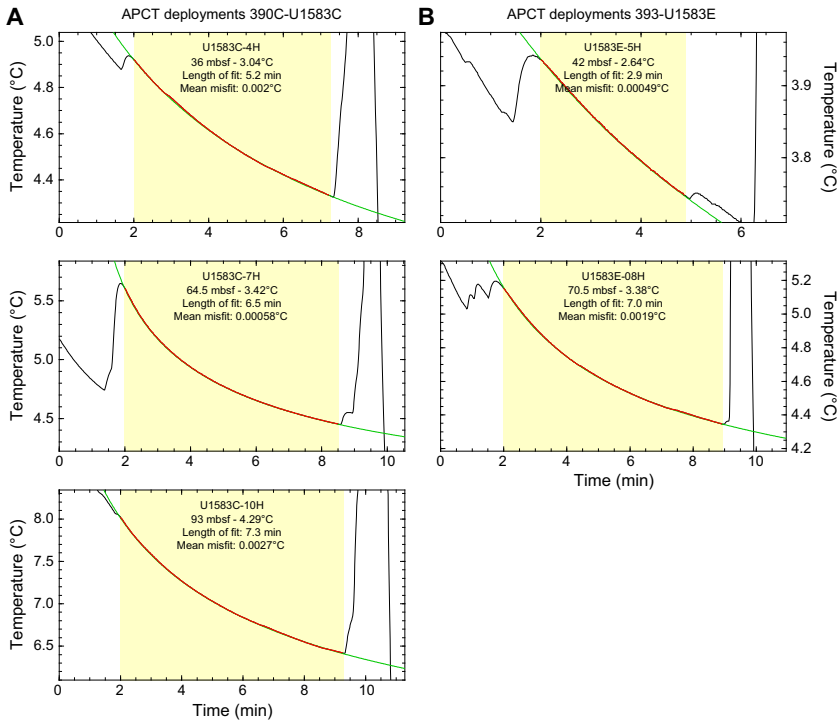

Figure F76. APCT-3 temperature records. A. Hole U1583C. B. Hole U1583E. Highlighted time intervals show where best-fit temperature decay model (green curve) was calculated to derive equilibrium temperature for each deployment. In situ formation temperature value for each record is extrapolated from best-fit model.

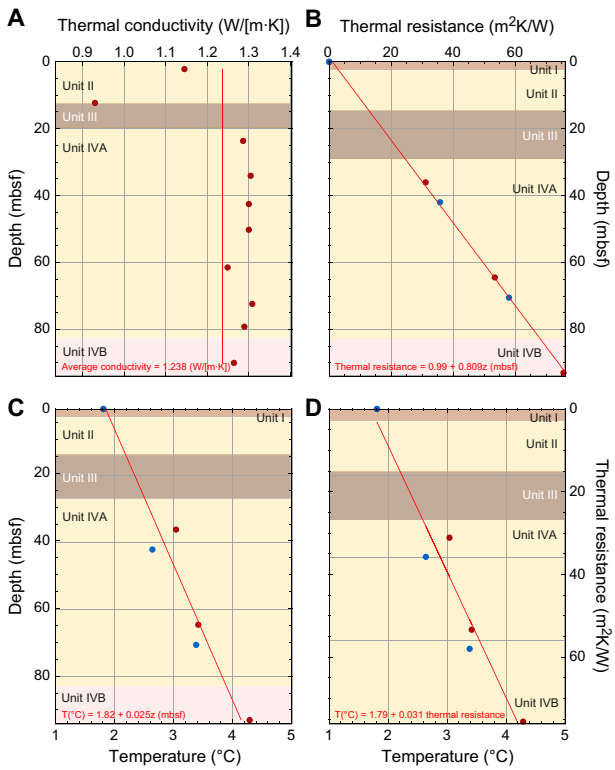

Figure F77. Estimation of conductive heat flow, Site U1583. A. Thermal conductivity measured on cores, Hole U1583C. Mean thermal conductivity for interval above deepest temperature is shown. B. Calculated thermal resistance for Holes U1583C (red) and U1583E (blue) and linear regression for the site. C. Temperature for Holes U1583C and U1583E and linear regression for all measurements. D. Bullard plot of measured temperature vs. calculated thermal resistance, Holes U1583C and U1583E. Slope of regression line is conductive heat flow for Site U1583.

Table T27. Derived temperature gradient and heat flow, Holes U1583C and U1583E. **Download table in CSV format.**

Site/hole	Gradient (°C/km)	Correlation coefficient	Average thermal conductivity (W/[m·K])	Heat flow from gradient (mW/m²)	Heat flow from Bullard plot (mW/m²)	Correlation coefficient
U1583	25	0.97	1.24	31	31	0.97
U1583C	26	0.99	1.24	32	32	0.99
U1583E	22	1.00	1.24	27	27	1.00

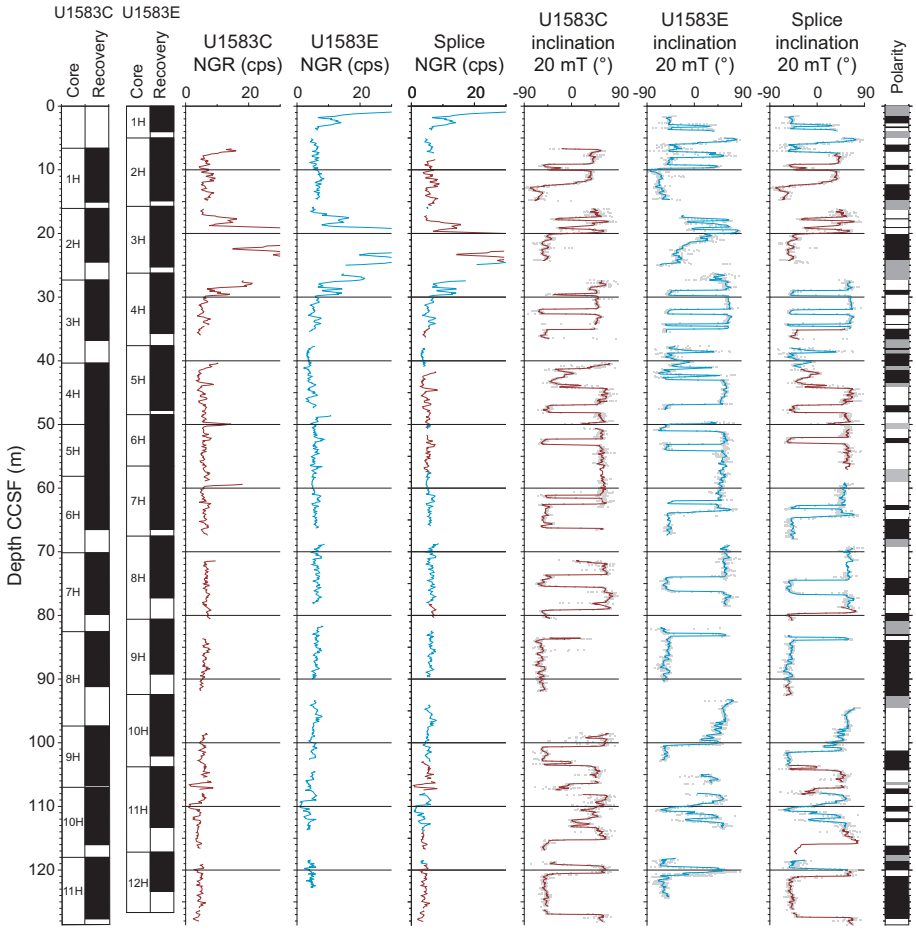

Figure F78. Construction of Site U1583 composite depth scale (CCSF) and splice, using NGR and paleomagnetic inclination. Polarity: black = negative inclination (normal polarity for sites in Southern Hemisphere), white = positive inclination (reversed polarity), gray= no data or magnetic polarity is uncertain. cps = counts per second.

Table T28. Affine table, Holes U1583C and U1583F. **Download table in CSV format.**

Table T29. Splice table, Site U1583. **Download table in CSV format.**

10.2. Basement

Petrophysical characterization of the ocean crustal section at Site U1583 is primarily based on cores from Hole U1583F that were recovered during Expedition 393. A total of 1.89 m of basalt was also recovered from the bottom of Hole U1583C (Core 13X). A clear sediment/basement interface was not recovered in either hole. Wireline logging in Hole U1583F was also completed after finishing basement coring.

10.2.1. Physical properties

Whole-round core section measurements included NGR, GRA bulk density, and MS. Archive halves of all split-core sections were measured for MSP. X-ray imaging was performed on selected sections with breccia to better characterize their structure. A total of 23 discrete sample cubes were taken for compressional wave (*P*-wave) velocity and MAD measurements, including two samples of breccia (Table **T30**). All discrete samples were also used for paleomagnetic measurements (see **Basement** in Paleomagnetism). Thermal conductivity measurements were made on 26 individual pieces from working halves of split cores. Full-circumference, true color images of whole-round core exteriors were recorded with the DMT CoreScan3 system. Approximately 77% of the basement material recovered from Site U1583 could be scanned on the DMT system, including 91% of the basement material from Hole U1583C and 76% of the material from Hole U1583F. An additional ~0.85 m (total) of cylindrical, oriented pieces was used for microbiological sampling in Holes U1583C and U1583F and removed from the cores before scanning took place (see **Microbiology**). A summary of core section and discrete physical properties data from Hole U1583F is shown in Figure **F79** and Tables **T30** and **T31**. All depths in the tables and figures are in meters below seafloor (mbsf; equivalent to CSF-A depth scale; see **Introduction** in the Expedition

Table T30. Discrete physical properties, Site U1583. **Download table in CSV format.**

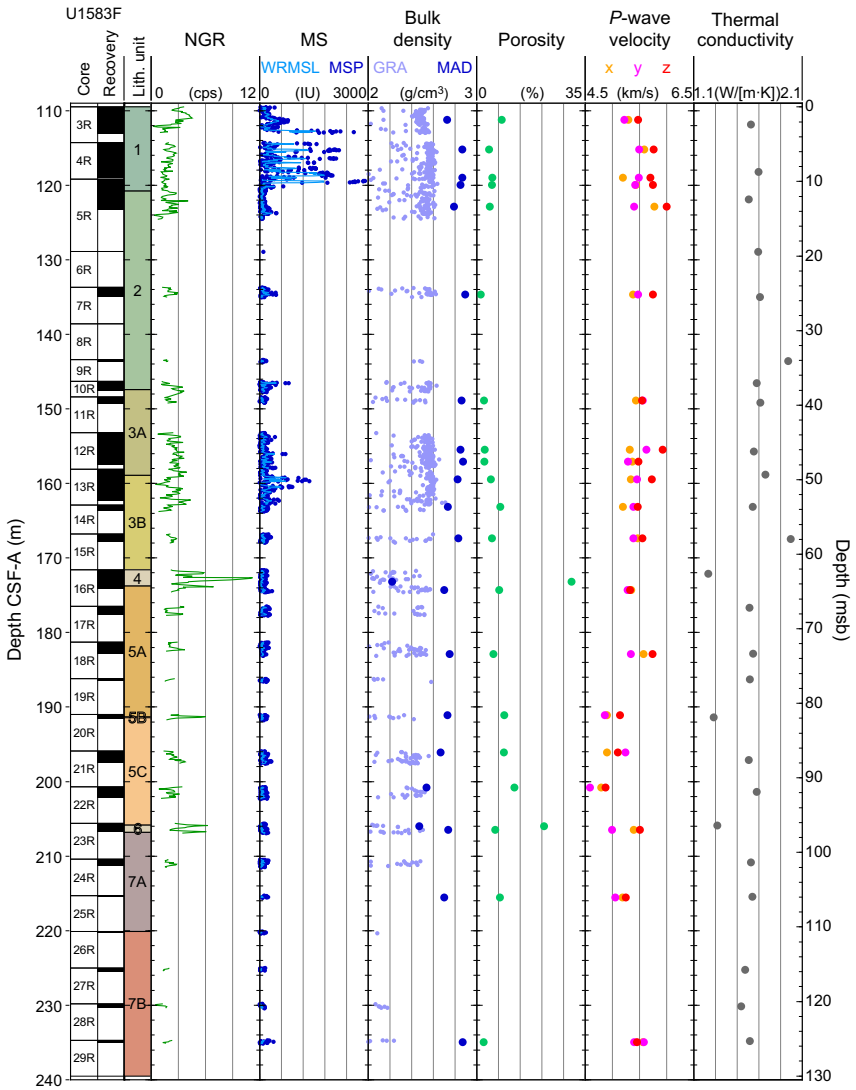

Figure F79. Summary of physical properties, Hole U1583F. cps = counts per second.

390/393 methods chapter [Coggon et al., 2024a]), and the means of all physical properties are arithmetic means represented with uncertainty of ±1 standard deviation (1σ).

10.2.1.1. Natural gamma radiation

In Hole U1583F, mean NGR is 2.4 ± 1.2 counts/s (range = 0.2–11.2 counts/s) (Figure **F79**; Table **T31**). The highest NGR is associated with sedimentary breccias in Units 4 and 6 (mean = 5.1 ± 2.7 and 4 ± 1.5 counts/s, respectively). In Unit 1 (109.5–120.81 mbsf), NGR values are highest in the uppermost ~3 m (~4 counts/s) compared to ~2 counts/s in the lower ~7 m of the unit. Basaltic Units 2, 3, 5, and 7 all show relatively low NGR (mean = 1.9 ± 0.7, 2.4 ± 0.7, 2.6 ± 1.0, and 1.8 ± 0.6 counts/s, respectively). Lithostratigraphic units that are characterized as primarily massive flows, sheet flows, or pillow flows all have a similar mean NGR of ~2.2 counts/s and overlap within ±1 standard deviation, suggesting that emplacement style does not have a strong influence on this property (Table **T31**).

10.2.1.2. Magnetic susceptibility

MS measured using both WRMSL and MSP methods show similar downhole trends; however, the amplitude of these changes varies between the two methods (WRMSL range = 0–1782 IU; MSP range = 1–2910 IU). The lower WRMSL values generally result from core gaps and irregular shaped/small core pieces (heavily influencing the continuous measurements), and potentially from the differences in frequency and resolution between the two magnetic susceptibility systems (see **Physical properties and downhole measurements** in the Expedition 390/393 methods chapter [Coggon et al., 2024a]). MS is highest in the single massive flow making up Unit 1 (MSP mean = 610 ± 686 IU), and the values are highly variable within the unit (Table **T31**). There is

Table T31. Physical properties statistical results, Site U1583. 1σ = one standard deviation. Emplacement style, groundmass grain size, and alteration level for discrete measurements follow Table T30. Emplacement styles for the continuous track measurements are based on the typical emplacement style for each lithostratigraphic unit or subunit (see Igneous petrology). Alteration level and groundmass grain size were not assigned for the track measurements. Groups with only one sample do not have a standard deviation (NA) and empty cells indicate no measurements. (Continued on next page.) **Download table in CSV format.**

	Track measurements							
Group/subgroup	GRA bulk density mean (g/cm^3)	GRA bulk density 1σ (g/cm^3)	NGR mean (counts/s)	NGR 1σ (counts/s)	MS WRMSL mean (IU)	MS WRMSL 1σ (IU)	MSP mean (IU)	MSP 1σ (IU)
Igneous unit								
1	2.49	0.12	2.14	0.95	463	464	610	686
2	2.46	0.14	1.93	0.72	91	69	132	111
3	2.48	0.14	2.44	0.72	139	117	196	178
4	2.21	0.13	5.14	2.68	58	29	98	53
5	2.35	0.15	2.59	0.97	76	38	127	66
6	2.22	0.16	4.00	1.46	56	19	95	61
7	2.24	0.15	1.77	0.60	56	30	105	75
Emplacement style								
Single massive flow	2.49	0.12	2.14	0.95	463	464	610	686
Pillow lavas	2.42	0.16	2.31	0.83	87	57	132	88
Sheet flows	2.48	0.16	2.28	0.79	170	151	247	229
Lava flow								
Breccia	2.21	0.14	4.81	2.37	58	26	97	55
Groundmass grain size								
Cryptocrystalline								
Microcrystalline								
Fine grained								
Medium grained								
Alteration level								
1: gray background								
2: background w/vesicles filled with clay (white-green)								
3: background w/higher clay (yellow-brown), vesicles and groundmass								
4: patchy background								
5: background w/dark gray halo (dark bluish gray halo)								
6: background w/reddish brown halo								
7: background w/brown halo								
8: brown halo								
Site U1583	2.44	0.16	2.44	1.23	179	275	261	407

another smaller peak in MS in Unit 3, and this unit has the second highest mean magnetic susceptibility (MSP mean = 196 ± 178 IU). MS values are generally similar (less than ~110 IU) in other units and show smaller variations (Table **T31**). Sheet flows show the second highest MS after the massive flow (MSP mean = 247 ± 229 IU). MS is relatively low in pillow lavas (MSP mean = 132 ± 88 IU) and lowest in the sedimentary breccias (MSP mean = 97± 55 IU).

10.2.1.3. Gamma ray attenuation bulk density

GRA bulk density ranges 2.00–2.71 g/cm^3 (mean = 2.44 ± 0.16 g/cm^3) and shows a slight decrease downhole (Figure **F79**; Table **T31**). Bulk density values <2 g/cm^3 were culled from figures and interpretations, as these likely represent gaps due to incomplete filling of the core liner and are not representative of the recovered material. The highest bulk density values measured from GRA are consistently ~0.2 g/cm^3 lower than those measured from MAD, largely due to these gap effects. Given the mineral constituents and the low porosity of basalts, a mean GRA density of 2.44 g/cm^3 is unrealistically low, but the general trends of the upper envelope of GRA values may be interpretable, so far as the discontinuous recovery allows. MAD samples may also be biased toward higher density lithologies, as they are selected from cohesive pieces that can withstand being cut into cubes (see **Physical properties and downhole measurements** in the Expedition 390/393 methods chapter [Coggon et al., 2024a]). GRA bulk density is slightly higher in Units 1–3 (~2.7 g/cm^3) compared to Units 4–7 (~2.5 g/cm^3), though this may be influenced by the lower core recovery in the lower part of Hole U1583F (Figure **F79**; Table **T31**).

10.2.1.4. *P*-wave velocity

P-wave velocity ranges 4.03–5.77 km/s along the *x*-axis, 4.59–5.62 km/s along the *y*-axis, and 4.87–6.00 km/s along the *z*-axis. All three velocities measured for each sample are shown in Figure

Table T31 (continued).

	Discrete samples									
Group/subgroup	Thermal conductivity mean (W/[m·K])	Thermal conductivity 1σ (W/[m·K])	Max *P*-wave velocity mean (km/s)	Max *P*-wave velocity 1σ (km/s)	Porosity mean (%)	Porosity 1σ (%)	Bulk density mean (g/cm^3)	Bulk density 1σ (g/cm^3)	Grain density mean (g/cm^3)	Grain density 1σ (g/cm^3)
Igneous unit										
1	1.66	0.05	5.62	0.17	5.5	1.79	2.82	0.06	2.93	0.04
2	1.73	0.14	5.87	0.18	2.75	2.05	2.84	0.07	2.89	0.04
3	1.74	0.16	5.62	0.18	4.08	2.06	2.83	0.05	2.91	0.02
4	1.23	NA	4.08	NA	30.6	NA	2.22	NA	2.75	NA
5	1.57	0.15	5.24	0.33	8.46	2.47	2.68	0.08	2.83	0.05
6	1.32	NA	4.77	1.04	13.85	11.10	2.60	0.19	2.86	0.02
7	1.60	0.04	5.41	0.23	4.85	3.75	2.78	0.12	2.87	0.06
Emplacement style										
Single massive flow	1.66	0.05	5.62	0.17	5.44	1.56	2.82	0.06	2.92	0.04
Pillow lavas	1.68	0.14	5.52	0.40	6.44	3.19	2.73	0.11	2.85	0.06
Sheet flows	1.71	0.00	5.60	0.13	3.66	2.51	2.84	0.06	2.91	0.02
Lava flow	1.63	0.01	5.37	0.21	6.15	2.89	2.76	0.08	2.87	0.04
Breccia	1.28	0.04	4.06	0.03	26.15	6.29	2.35	0.18	2.81	0.09
Groundmass grain size										
Cryptocrystalline			5.70	0.30	4.40	2.14	2.79	0.07	2.87	0.03
Microcrystalline			5.37	0.26	6.01	3.60	2.76	0.12	2.86	0.06
Fine-grained			5.62	0.14	5.68	1.72	2.81	0.06	2.91	0.03
Medium-grained			5.70	NA	5.00	NA	2.87	NA	2.97	NA
Alteration level										
1: gray background			5.73	0.03	3.73	1.67	2.86	0.03	2.93	0.03
2: background w/vesicles filled with clay (white-green)			5.44	0.05	6.65	2.05	2.76	0.04	2.88	0.01
3: background w/higher clay (yellow-brown), vesicles and groundmass			5.51	0.04	6.17	1.36	2.77	0.06	2.88	0.04
4: patchy background			5.84	0.13	3.75	1.63	2.85	0.00	2.92	0.03
5: background w/dark gray halo (dark bluish gray halo)			5.63	0.33	4.57	2.47	2.78	0.08	2.87	0.04
6: background w/reddish brown halo			5.47	0.02	3.75	1.77	2.87	0.00	2.94	0.03
7: background w/brown halo			5.31	0.29	7.63	1.61	2.71	0.04	2.85	0.03
8: brown halo			4.87	NA	12.10	NA	2.54	NA	2.75	NA
Site U1583	1.63	0.17	5.18	1.21	7.28	6.62	2.74	0.16	2.88	0.06

F79 and Table T30; however, only the highest value measured for each sample is used to calculate mean velocities (Table T31) because these are considered most representative of the true formation velocity (see **Physical properties and downhole measurements** in the Expedition 390/393 methods chapter [Coggon et al., 2024a]).

Maximum *P*-wave velocity is relatively high through Unit 1 (5.62 ± 0.17 km/s), Unit 2 (5.87 ± 0.18 km/s), and Unit 3 (5.62 ± 0.18 km/s) compared to those in Unit 5 (5.24 ± 0.33 km/s), Unit 6 (4.77 ± 1.04 km/s, or 5.5 km/s for the single basalt sample in this unit), and Unit 7 (5.41 ± 0.23 km/s) (Figures F79, F80; Table T31). The lowest *P*-wave velocities are seen in sedimentary breccia (4.06 ± 0.03 km/s), whereas massive, sheet, and pillow flow basalts all have a mean *P*-wave velocity within the range of 5.37–5.62 km/s (Figure F81; Table T31). Of the basaltic samples, the highest and lowest *P*-wave velocities were measured in pillow basalts (mean = 5.52 ± 0.40 km/s) (Figure F81; Tables T30, T31). The massive flow has the highest mean *P*-wave velocity (5.62 ± 0.17 km/s), followed by sheet flows (5.60 ± 0.13 km/s), pillow flows, and then lava flows with uncertain emplacement styles (5.37 ± 0.21 km/s) (Figure F81).

P-wave velocity does not show a clear trend with increasing groundmass grain size (Figure F82). The highest *P*-wave velocity is seen in cryptocrystalline basalts, which have a mean velocity (5.70 ± 0.30 km/s) equivalent to the sole medium grained basalt sample (393-U1583F-4R-4, 85 cm). The velocities of fine-grained basalts cluster close to this group, whereas microcrystalline basalts show a lower mean *P*-wave velocity (5.37 ± 0.26 km/s) and are spread over a wide range of values (4.87–5.75 km/s) (Figure F82; Table T30).

10.2.1.5. Moisture and density

The bulk density of discrete samples from MAD analysis ranges 2.22–2.90 g/cm^3 (mean = 2.74 ± 0.16 g/cm^3). Lithostratigraphic Units 1–3 have similar mean MAD bulk densities of ~2.83 g/cm^3 (Figure F80; Table T31). Unit 4 has the lowest overall bulk density (2.22 g/cm^3), though this is represented by only a single breccia sample (Table T30). Unit 6 has a relatively low mean bulk density of 2.60 ± 0.19 g/cm^3, reflecting the mixture of basalt and breccia in this unit, but the MAD

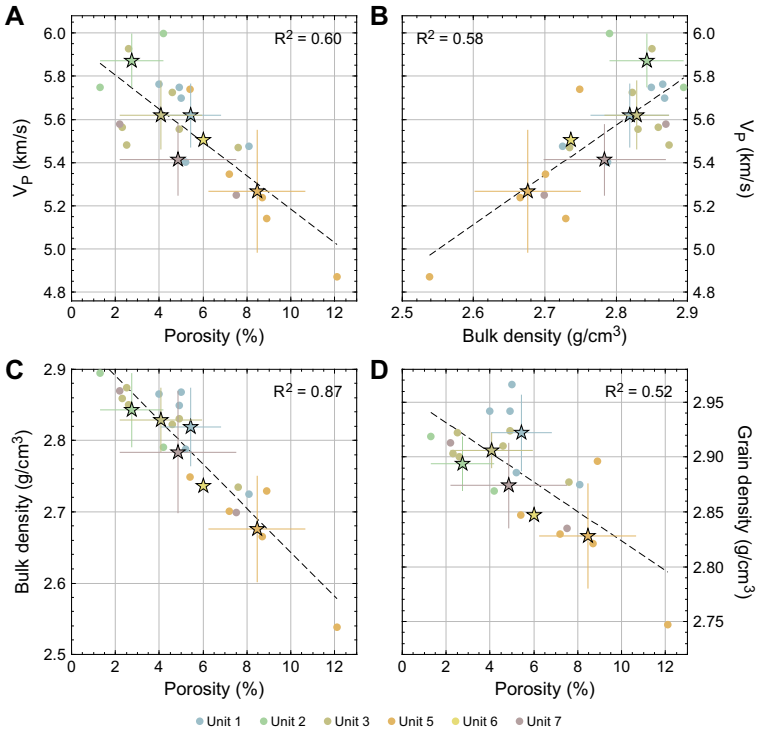

Figure F80. Site U1583 discrete basalt sample physical properties by lithostratigraphic unit (see Igneous petrology). A. V_P vs. porosity. B. V_P vs. bulk density. C. Bulk density vs. porosity. D. Grain density vs. porosity. V_P shown is maximum velocity measured for each sample. Mean (stars) and standard deviation (error bars) for each unit are shown. Breccia samples are not shown or included in means, standard deviations, or regressions.

bulk density of the single basalt sample in the unit (2.74 g/cm^3) is between the mean values of surrounding Units 5 and 7 (Figure **F80**; Table **T31**). Massive flows and sheet flows have the highest bulk and grain densities of the different emplacement styles, although sheet flows have a slightly higher mean bulk density, whereas massive flows have a slightly higher mean grain density (Figure **F81**; Table **T31**). Similar to *P*-wave velocity, changes in density do not change consistently with increasing groundmass grain size (Figure **F82**). Mean bulk and grain densities decrease with decreasing grain size, from medium grained to fine grained to cryptocrystalline and down to microcrystalline basalt (Figure **F82**; Table **T31**).

Porosity values show a wide range of 1.3%–30.6% throughout the Hole U1583F volcanic section. Porosity is the highest in a fragment of a matrix-supported breccia sample in Unit 4 (1 sample; 30.6%) and in Unit 6 (mean = 13.8% ± 11.1%), which is also predominantly represented by sedimentary breccias, and much lower (generally < 10%) in the other five basaltic units (Tables **T30**, **T31**). Considering only basalts, the highest porosities are measured in pillow flows (2.6%–12.1%; mean = 6.44% ± 3.19%) (Figure **F81**). Lava flows with an uncertain emplacement style have a similar mean porosity (6.15% ± 2.89%), followed by massive flows (5.44% ± 1.56%), and the lowest mean porosity is seen in sheet flows (3.66% ± 2.51%) (Figure **F81**; Table **T31**). In terms of grain size, microcrystalline basalts have the highest mean porosity but also span the full range of porosities measured, while cryptocrystalline basalts have the lowest mean porosity. Despite the wide range of observed porosities, the mean values for the different groundmass grain size categories all cluster at ~4%–6% (Figure **F82**).

10.2.1.6. Thermal conductivity

Thermal conductivity ranges 1.20–2.00 W/(m·K) (mean = 1.63 ± 0.17 W/[m·K]) (Figure **F79**; Table **T31**). Thermal conductivity values are lowest in the sedimentary breccias of Unit 4 (one sample; 1.23 W/[m·K]) and Unit 6 (one sample; 1.32 W/[m·K]) and show higher mean values (1.6–1.7 W/[m·K]) in units identified as basalts (Table **T30**). Thermal conductivity does not vary signifi-

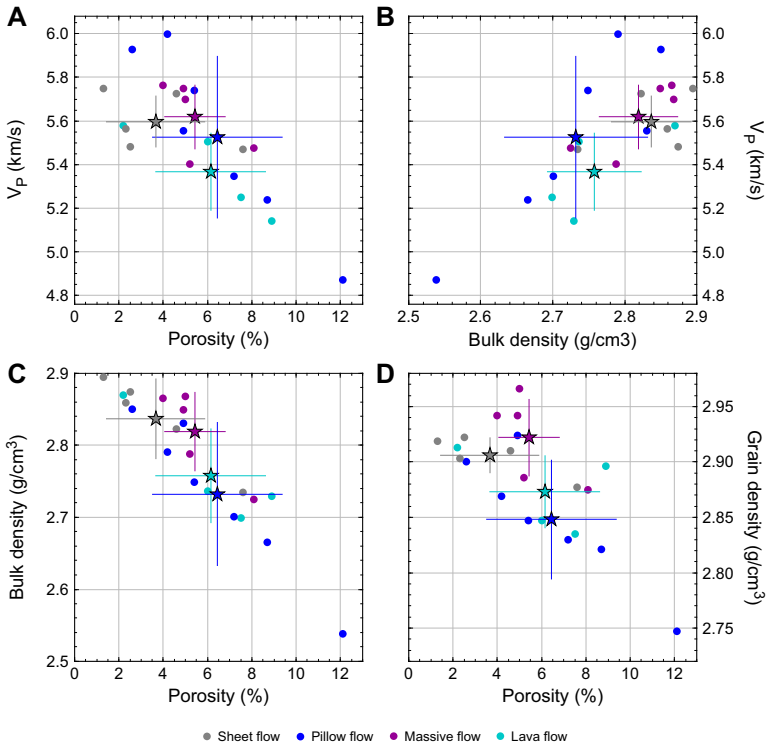

Figure F81. Site U1583 discrete basalt sample physical properties by emplacement style (see Igneous petrology). A. V_P vs. porosity. B. V_P vs. bulk density. C. Bulk density vs. porosity. D. Grain density vs. porosity. V_P shown is maximum velocity measured for each sample. Mean (stars) and standard deviation (error bars) for each emplacement style are shown. Breccia samples are not shown or included in means or standard deviations.

cantly with emplacement style; massive flows, sheet flows, pillow flows, and lava flows with uncertain emplacement all show mean conductivities ~1.67 W/(m·K) (Figure **F79**; Table **T31**).

10.2.2. Data integration

Several clear relationships between the discrete physical properties (*P*-wave velocity, porosity, bulk density, and grain density) become apparent when considering Figures **F80**, **F81**, and **F82**. Considering only basalts, we find inverse relationships between *P*-wave velocity and porosity (R^2 = 0.60), bulk density and porosity (R^2 = 0.87), and grain density and porosity (R^2 = 0.52) and a positive correlation between bulk density and *P*-wave velocity (R^2 = 0.58). Despite showing some variation with respect to different basalt emplacement styles and groundmass grain sizes, these properties alone do not account for the wide range of observed density, porosity, and *P*-wave velocity seen in the samples.

Discrete samples used for MAD and *P*-wave analyses were grouped by alteration level as a way to evaluate the role alteration plays in driving the observed variation in physical properties. This classification was based on color, texture, and presence of alteration halos, following the scheme used in macroscopic core descriptions (see **Igneous petrology** and **Alteration petrology**). Eight levels of alteration, from freshest to most altered, are sequenced as follows: (1) gray background; (2) background with vesicles filled by clay (white-green); (3) background with higher clay (yellow-brown), vesicles, and groundmass; (4) patchy background; (5) background with dark gray halo or dark bluish gray halo; (6) background with reddish brown halo; (7) background with brown halo; and (8) brown halo. Breccias were not included in this classification.

P-wave velocity, porosity, and density all show a consistent relationship with basalt alteration level, where increased alteration level generally corresponds to higher porosity and lower *P*-wave velocity, bulk density, and grain density, though there is some scatter around each trend (Figure **F83**). Samples with gray background, patchy background, and background with reddish brown halo all

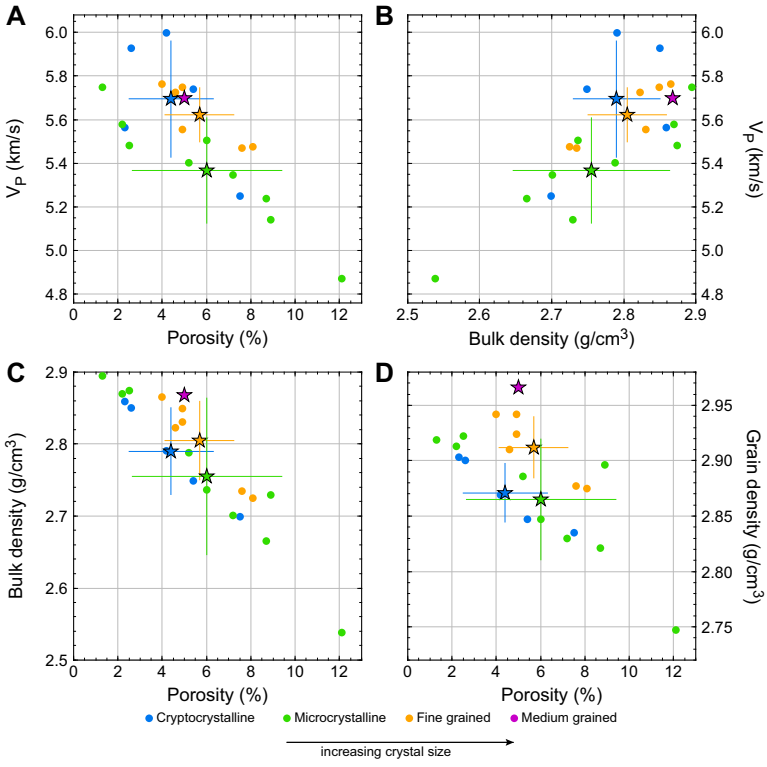

Figure F82. Site U1583 discrete basalt sample physical properties by groundmass grain size (see Igneous petrology). A. V_P vs. porosity. B. V_P vs. bulk density. C. Bulk density vs. porosity. D. Grain density vs. porosity. V_P shown is maximum velocity measured for each sample. Mean (stars) and standard deviation (error bars) for each groundmass grain size are shown. Breccia samples are not shown or included in means or standard deviations.

tend to cluster close together in terms of their bulk and grain densities and porosity but show different *P*-wave velocities (Figure **F83**). The sample with the highest alteration level (brown halo) consistently plots far from the main cluster of samples and has the highest porosity and lowest *P*-wave velocity, bulk density, and grain density (Figure **F83**). Sample grain density should decrease in more strongly altered samples because basalt (typical density of ~3.0 g/cm^3) alteration to less dense clay minerals (e.g., saponite; ~2.3 g/cm^3) progressively reduces the grain density. Similarly, porosity is expected to decrease as the alteration level increases because pore space (e.g., cracks or vesicles) is filled with secondary clay minerals or cement. However, results at sites across the SAT show an opposite, thus counterintuitive trend, suggesting the measurements of porous volume in the most altered samples do not reflect the true porosity of the basement rock. Postexpedition work is needed to address this problem.

As a whole, physical properties trends correspond to an increasing alteration level with depth in Hole U1583F, where Subunits 5A–7B tend to show higher levels of alteration compared to Units 1–3 (Figure **F84**).

10.2.3. Comparison to ODP Hole 896A

Physical properties from discrete samples at Site U1583 were compared to data from Ocean Drilling Program (ODP) Hole 896A (~7 Ma; Shipboard Scientific Party, 1993), which was used as a reference site that allows us to compare results across the SAT to young oceanic crust produced at an intermediate spreading rate ridge. Physical properties data from Hole 896A encompass the range of basalt alteration levels that were sampled from these Site U1583 cores (see **Physical**

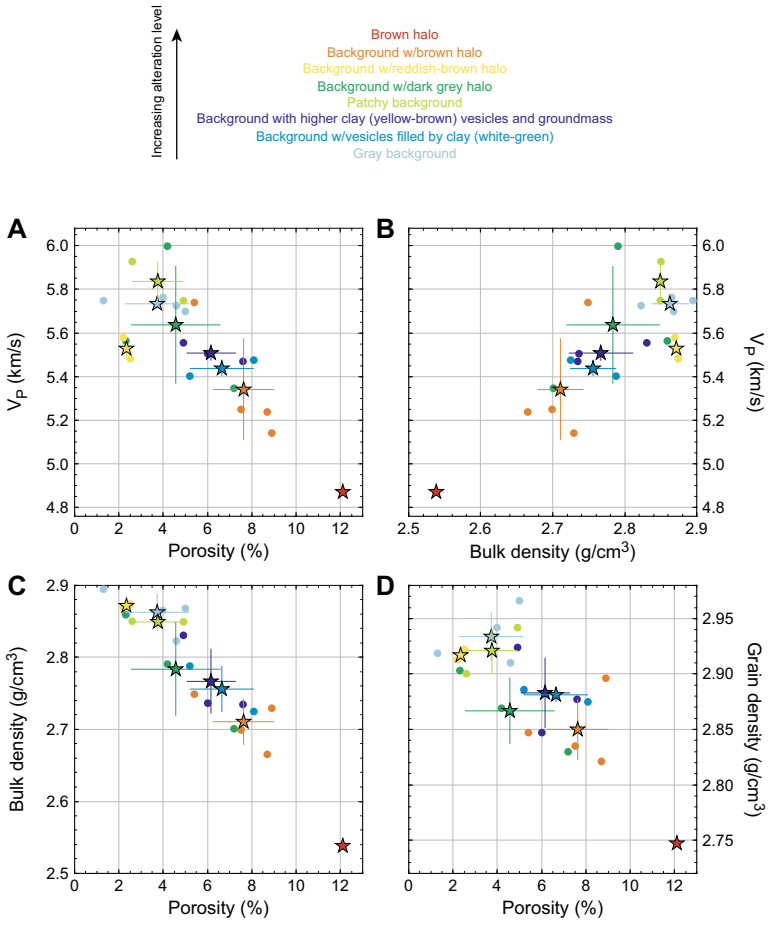

Figure F83. Site U1583 basalt discrete sample physical properties by alteration level (see Alteration petrology). A. V_P vs. porosity. B. V_P vs. bulk density. C. Bulk density vs. porosity. D. Grain density vs. porosity. V_P shown is maximum velocity measured for each sample. Mean (stars) and standard deviation (error bars) for each alteration level are shown. Breccia samples are not shown or included in means or standard deviations.

properties and downhole measurements in the Expedition 390/393 methods chapter [Coggon et al., 2024a]) (Figure **F84**). Lithostratigraphic Units 1–3 and Subunit 7B tend to overlap well with the range from Hole 896A in terms of bulk density and grain density. These intervals are also generally associated with fresher basalts in Hole U1583F (Figure **F84**). Most samples in Subunits 3B–7A diverge from the reference values for young basalt from Hole 896A. Hole 896A shows a wide range of *P*-wave velocity, and all velocities from Hole U1583F fall within ±1σ of the mean of Hole 896A. Hole 896A also shows a wide range of porosity that encompasses all but the most altered basalt sample from Hole U1583F (Figure **F84**). The mean thermal conductivity in Hole U1583F (1.63 ± 0.17 W/[m·K]) is lower by ~0.1–0.2 W/(m·K) than the mean thermal conductivity in Hole 896A (1.8 ± 0.11 W/[m·K]) and significantly lower (by ~0.5 W/[m·K]) in the sedimentary breccias from Unit 4, Subunit 5B, and Unit 6.

10.2.4. Wireline logging

After completion of basement coring in Hole U1583F, three logging runs were considered. A first run with the triple combo tool string would record the most basic measurements (resistivity, gamma ray spectroscopy, neutron log) and evaluate hole conditions. If the conditions for logging (hole size and sea state) were favorable, it would be followed by the FMS-sonic tool string (sonic velocity and electrical images) and the Ultrasonic Borehole Imager (UBI; acoustic images of the borehole wall). As part of the triple combo, the Hostile Environment Litho-Density Sonde (HLDS) was run only for caliper and without a source because of concerns about hole stability; while coring, it was noted that cuttings did not seem to get properly flushed, and there were a few questionable intervals, making the use of the source an unnecessary risk.

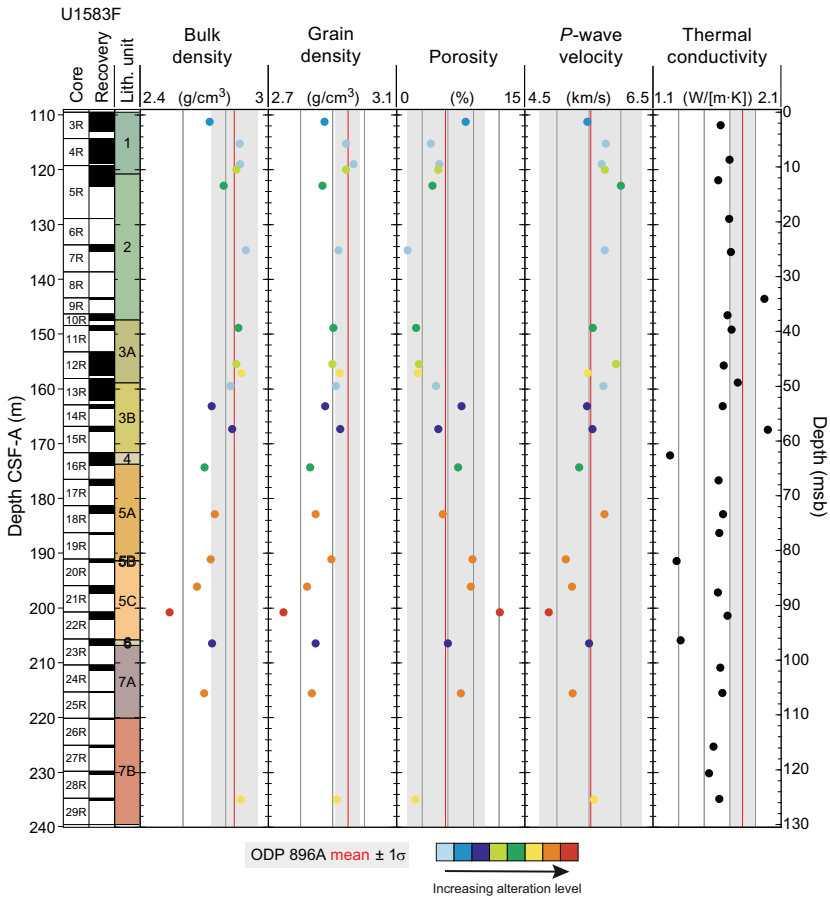

Figure F84. Comparison of discrete physical properties measurements, Hole U1583F and ODP Hole 896A. Hole U1583F data are colored by alteration level (see Alteration petrology). See Figure F83 for color legend. Mean values for Hole 896A, calculated from entire data set for each parameter, are shown (red lines = mean value of each data type, shaded boxes = ±1 standard deviation). *P*-wave velocity shown for Hole U1583F is maximum velocity measured for each sample. Thermal conductivity measurements lack alteration level information.

Eventually, only the triple combo reached the bottom of the hole, and the FMS-sonic tool string was able to record images in the upper ~60 m of basement.

10.2.4.1. Wireline operations

Preparation for logging started at 1730 h (local time, UTC – 2 h) on 16 July 2022 after completion of coring and release of the bit at the bottom of the hole.

The triple combo was built and run into the hole (RIH) at 2040 h. After some issues with telemetry, the tools were brought back to the surface for troubleshooting, and RIH resumed at 0130 h on 17 July with a replacement High-Resolution Laterolog Array (HRLA) sonde. Some distance above the seafloor (4221.5 mbrf), the tools started recording a partial set of data (downlog) until reaching ~5 m off the bottom of the hole (4456 mbrf; 234.5 mbsf), and then started a first upward pass at 0410 h. This first pass was briefly interrupted with the bottom of the tool at ~4394 mbrf when the WHC stopped functioning and the caliper was closed while troubleshooting the failure. The WHC failed to restart, but heave was moderate and the caliper was reopened until completion of the pass at 4365 mbrf. When trying to return to the bottom of the hole for a second pass, we failed to go deeper than 4400 mbrf (~177 mbsf). The second pass started from that depth at 0555 h and was complete after identifying the seafloor with the gamma ray log at 4222.5 mbrf. The tools were back on the rig floor at 0915 h.

Because hole conditions above 170 mbsf seemed satisfactory and the ~60 m open interval encompassed several volcanic units with poor recovery, it was decided to attempt a run with the FMS-sonic tool string. Operations were delayed by a simultaneous vibration isolated television camera survey; the completed tool string was RIH at 1205 h, and a downlog for gamma ray and sonic logs started at 1530 h, shortly before crossing the seafloor. The string also failed to go deeper than 4400 mbrf (~177 mbsf), and the uplog started from that depth at 1556 h. Soon after, one of the FMS arms displayed signs of failure, possibly after hitting some hard ledge(s) during the downlog, but the other arms were recording properly. The pass was stopped with the bottom of the tool and the shallowest images at 4330 mbrf (~110 mbsf, close to the top of the basement). But when trying to record a second pass, it proved impossible to return into the basement, or, when that failed, to bring the tool string fully back inside the pipe. After several hours of effort, the string was brought to the surface with one FMS arm missing and the others damaged; no further logging operations were attempted. Logging tools and equipment were stored, and the rig floor resumed normal operations by midnight on 17 July.

10.2.4.2. Data overview

Summaries of the main data recorded during the triple combo and FMS-sonic runs are shown in Figures **F85** and **F86**, respectively. The caliper log in Figure **F85** is a combination of the two upward passes of the triple combo with the caliper open, and it shows that the hole appeared in generally good condition, most notably in the interval above ~170 m wireline log matched depth below seafloor (WMSF) that was targeted for the FMS run. The dramatically asymmetric FMS calipers in Figure **F86** illustrate the failure of one of the arms at the beginning of the image acquisition.

The gamma ray tools are at the top of the string and could not reach the deepest ~30 m of the hole (Figure **F85**). When the downlog stopped, the data that had been measured over the ~40 m length of the tool string were, in error, not recorded by the acquisition system. As a result, the resistivity data recorded at the beginning of the first uplog are the only logging data of any kind from the deepest ~30 m of Hole U1583F.

The main variations in the resistivity log generally correspond to the various volcanic units identified by the shipboard petrologists (see **Igneous petrology**). The sharp increase in resistivity at 108 m WMSF is a clear indication of the top of the basement, and Volcanic Unit 1 seems to coincide with a ~10 m thick interval with the highest resistivity values recorded over the interval logged. Resistivity gradually decreases with depth in Unit 2, then increases and becomes highly variable in Subunit 3A, possibly delineating individual flows. Resistivity decreases with depth through Subunits 3B–5A, is mostly uniform around 100 Ωm in Subunit 5C, and below a drop that may be related to Unit 6, gradually increases with depth through Unit 7.

In several intervals, mostly below 160 m WMSF, the resistivity measurement with the shallower penetration (RLA1) is significantly lower than the deeper (RLA5) or "true" values. In most of these intervals, the caliper shows an enlarged hole, and the decoupling between the resistivity readings mostly indicates the failure of the shallower measurement to capture the formation resistivity. In intervals with apparent good hole conditions (in Unit 1 or at 160–165 m WMSF, possibly through 170 m WMSF without caliper reading), it could indicate predominantly subvertical fractures in the formation that provide more conductive (less resistive) paths for the shallower currents.

Natural gamma ray increases slightly downhole through Units 1 and 2, following a trend mostly controlled by the potassium content (Figure **F85**). However, below 155 m WMSF (in Volcanic Subunit 3A) an apparent increase in uranium content and significant variability in the uranium values seem to dominate the natural radioactivity in the lower half of the interval logged.

In Figure **F86**, compressional velocity displays significant variability along a slightly increasing trend with depth and agrees well with the core sample measurements, but despite high apparent

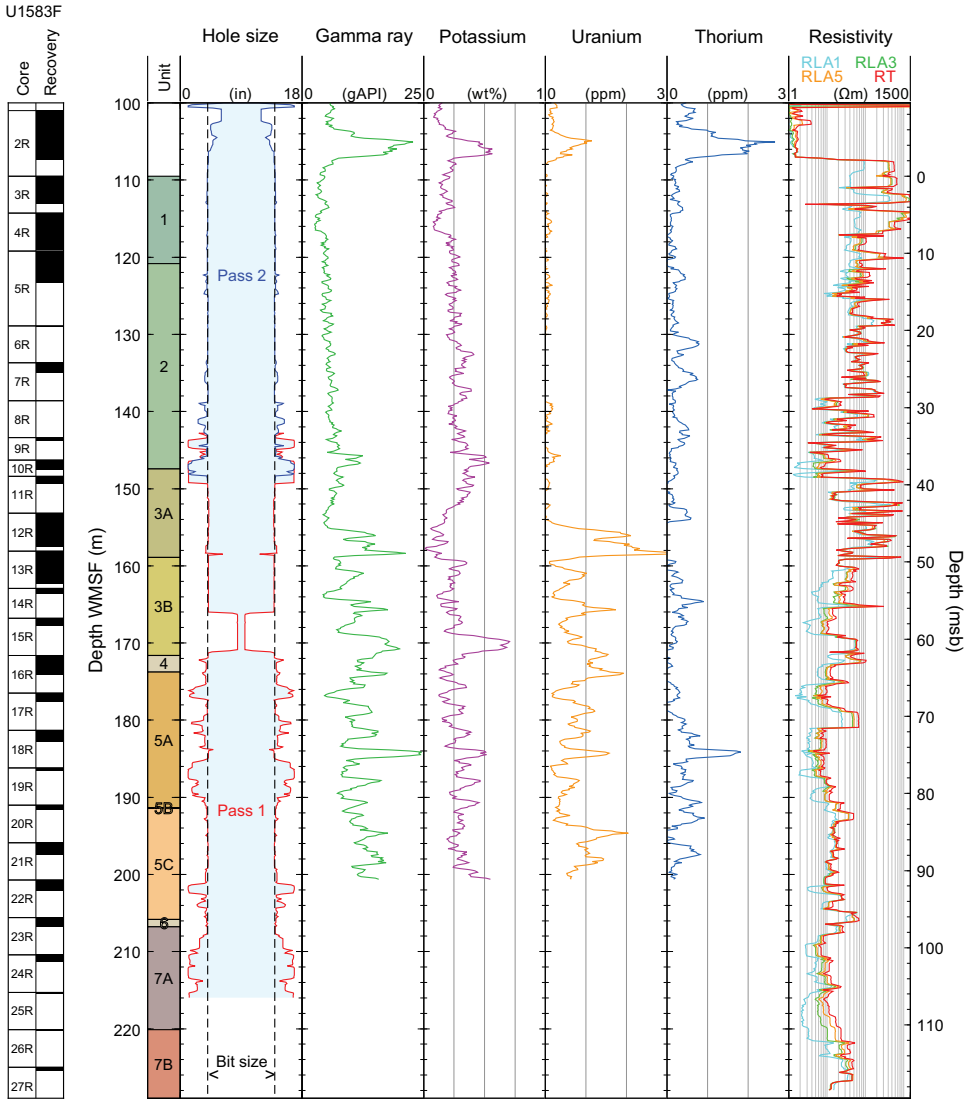

Figure F85. Summary of logging data recorded with triple combo tool string, Hole U1583F. Caliper is combination of the two upward passes. Total and spectral gamma ray data are from Hostile Environment Natural Gamma Ray Sonde downlog. Resistivity data are combination of downlog and first pass. RLA1 = shallow apparent resistivity from computed focusing mode 1, RLA3 = medium apparent resistivity from computed focusing mode 3, RLA5 = deep apparent resistivity from computed focusing mode 5, RT = true resistivity calculated from all modes.

coherence, the sonic acquisition failed to extract reliable shear sonic velocity from either the monopole or dipole waveforms, which will require postexpedition reprocessing.

10.2.4.3. Data quality

Figure F87 shows the data recorded through the pipe by the two gamma ray tools that were part of the two tool strings: the Hostile Environment Natural Gamma Ray Sonde (HNGS) and the Enhanced Digital Telemetry Cartridge (EDTC). One of the main purposes of recording these data is to identify the step in gamma ray at the seafloor and provide a reference depth for the logging data. The triple combo downlog, the very first pass to cross the seafloor, suggested a depth of 4222.5 mbrf, about 1 m deeper than the driller estimate. This depth was confirmed by the following passes, but the gradual increase in gamma ray readings over time in the subsequent passes made identification of the seafloor more difficult. At this point this increase in radiation with time can only be explained by formation material falling in the space between the pipe and the borehole wall.

Although attenuated by the drill pipe, most passes, and most clearly the downlog from the triple combo, captured the high gamma ray values associated with clay-rich Lithostratigraphic Unit III

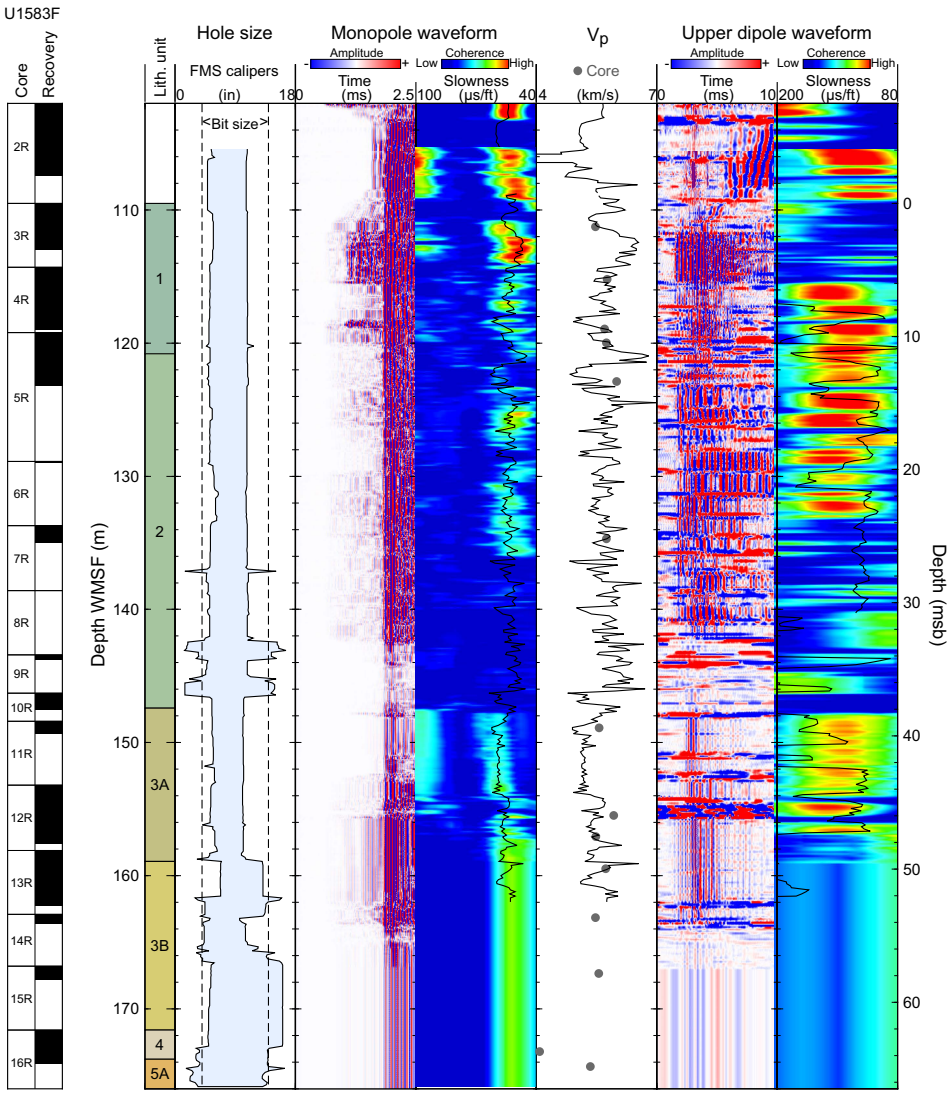

Figure F86. Summary of logging data recorded with FMS-sonic tool string, Hole U1583F. V_P core measurements are maximum velocity for each sample. Black line = V_P from logging data. Coherence calculated from monopole and dipole waveforms provides a measure of velocity measurement reliability. Sonic data shown are combination of downlog and main upward pass.

between ~12 and 22 m WMSF. Figure **F87** illustrates the differences in the depth where this unit was identified in the three holes where it was encountered: this interval sits between the two high gamma ray intervals in NGR core logging values from Holes U1583C and U1583E, between 10–20 m CSF-A and ~15–25 m CSF-A, respectively. These discrepancies come partly from the difficulty to get a clean mudline in deep water and with significant heave, both from logging and coring, but also possibly from local stratigraphic differences at a site with measurable bathymetric variations.

Other factors affecting the logging data and their depth at Site U1583 are illustrated in Figure **F88**. The true resistivity measured during the three passes with the triple combo are displayed alongside the tension measured at the top of the tool string during each pass. Comparison between the different resistivity logs shows similar general trends but significant differences in the depth or thickness of features that could represent separate flows or distinct lithologies. Without acceleration measurements, tension is the only indication of the tool motion, and the figure shows at least two places where the data may have been affected by unexpected changes. During the downlog, the tool appears to have stopped momentarily at ~146 m WMSF, likely resulting in some squeezing and stretching of apparent features above and below this depth. A more consequential event was the WHC failure during the first pass. It forced us to close the caliper at ~170 m WMSF but also forced the tool string to stop and, when it restarted, to merely smear the logs in the interval between 182 and ~170 mbsf. The WHC failure also likely affected the depth tie that was established on the rig floor before the tools started going down. While these two instances are the most

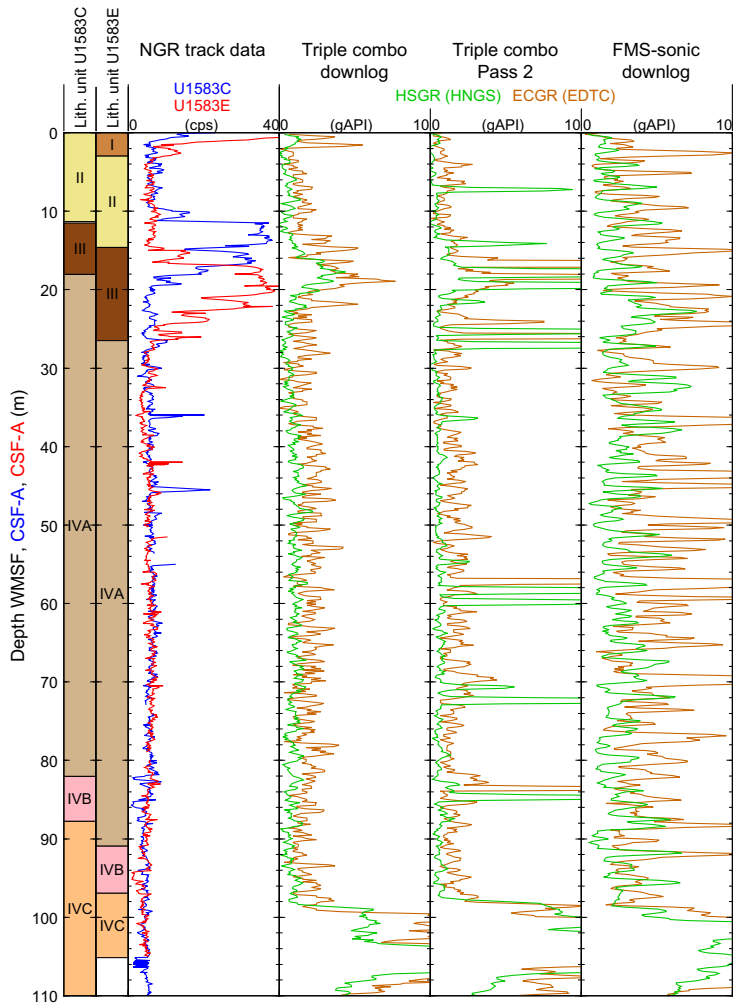

Figure F87. Gamma ray logs recorded through pipe (in sediment section) during two logging runs in Hole U1583F (WMSF) compared with NGR track data (CSF-A) from Holes U1583C and U1583E. HSGR = total spectral gamma ray, HNGS = Hostile Environment Natural Gamma Ray Sonde, ECGR = environmentally corrected gamma ray, EDTC = Enhanced Digital Telemetry Cartridge.

apparent, the motion of both tool strings seems to have been affected by the irregular hole size and probably some hard ledges, and one should afford some flexibility while trying to match features between passes or between log and core data.

10.2.4.4. Data integration

Despite the difficulties and some reservations, the hole quality was good in many places, and the logs should provide insight into the petrophysical properties of the basement at Site U1583 and help constrain the interpretation and position or orientation of features observed in the recovered cores.

Figure **F89** shows what could be the signature in the FMS electrical images of a vein observed in one of the shallowest basement cores. The subvertical dark (conductive) feature in the pad oriented to the north, most visible in the dynamically enhanced image, could be created by a vein observed in Sections 393-U1583F-3R-1 and 3R-2 in Volcanic Unit 1. The different vertical extent between the vein in the core and the pattern in the images is the manifestation of the difference in diameter between the core (2.31 inches) and the borehole (10 inches). The FMS image needed to be shifted upward by ~1.7 m to create a visual match, and there is a possibility that the image may

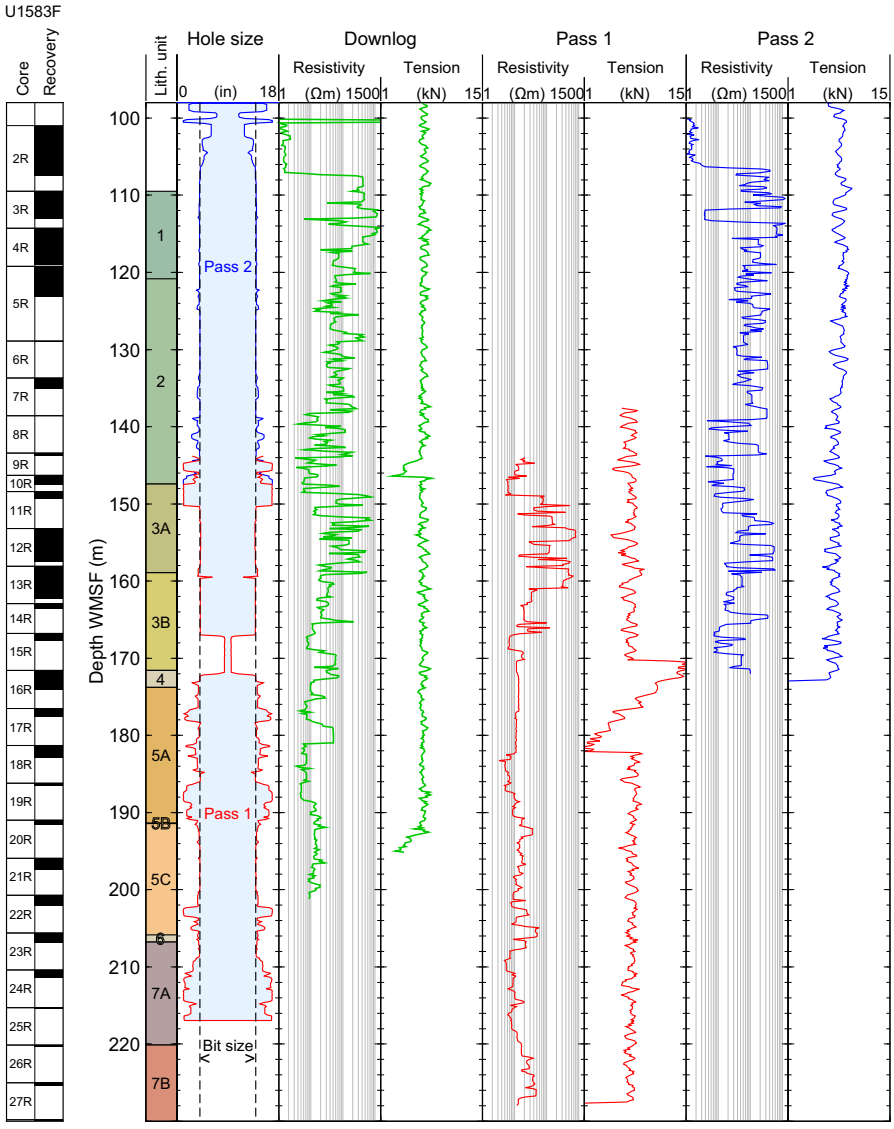

Figure F88. Comparison of resistivity logs and cable tension records during three passes of triple combo tool string with caliper logs from the two upward passes, Hole U1583F. Resistivity is true resistivity (RT). Tension is Calibrated Downhole Force (CDF) recorded at top of tool string.

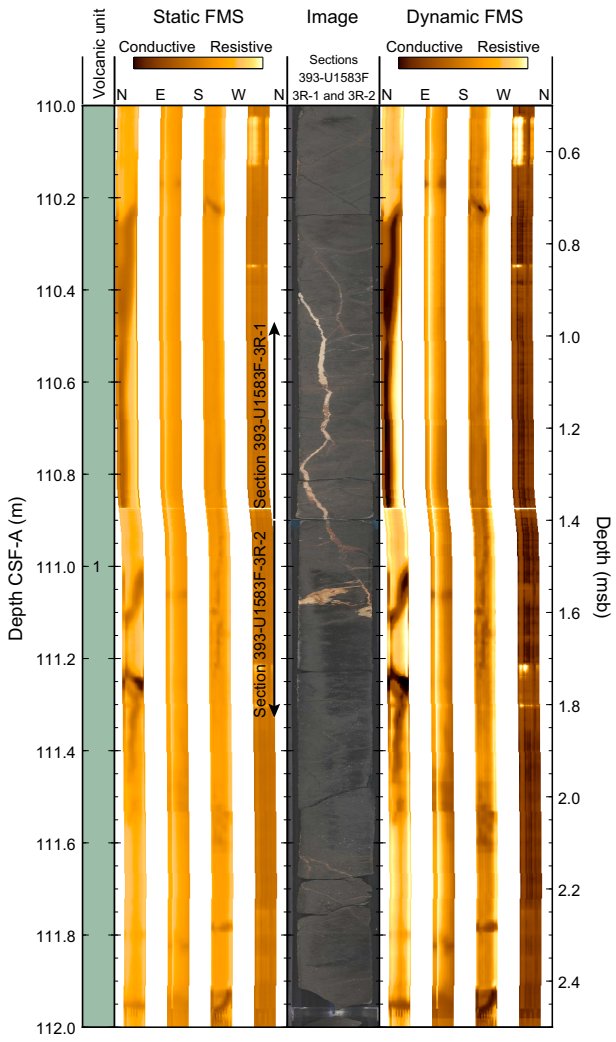

Figure F89. Comparison of FMS electrical images from shallowest part of interval logged with SHIL core images (393-U1583F-3R-1 and 3R-2). FMS images were moved up 1.7 m to achieve best visual match.

be of a different vein, but such an offset could be explained by the incomplete recovery of Core 3R and can be expected in the conditions the data were recorded. If it is not the same vein, the FMS image could suggest the existence in that interval of a network of similarly oriented veins to those recovered in the core.

11. Geochemistry

11.1. Sediment

11.1.1. Interstitial water and mudline sampling

During sediment coring in Hole U1583C, IW was extracted by squeezing whole-round sediment cores under laboratory atmosphere and by in situ Rhizon sampling (see **Geochemistry** in the Expedition 390/393 methods chapter [Coggon et al., 2024a]). Sampling frequency for squeezed IW was twice per core from Cores 393-U1583C-1H through 12H, for a total of 24 samples. Rhizon sampling was performed in Cores 1H–12H at a frequency of one sample per section for Sections 1 through 6 (72 samples total). A mudline water sample was collected in Hole U1583E, and an additional IW sample was collected in Hole U1583F near the sediment/basement interface (105.37 m CSF-A) (Table **T32**). Splits of Rhizon-sampled and squeezed IW fluids and IW solid residues (squeeze cakes) were saved for shipboard analyses and postexpedition research. For Hole U1583C,

oxygen was measured in situ after the cores were run through the STMSL, roughly within 30 min of the core arriving on the catwalk (see **Geochemistry** in the Expedition 390/393 methods chapter [Coggon et al., 2024a]). Sampling frequency was 2–6 measurements per core in Cores 1H–12H.

Both squeezed and Rhizon-sampled IW, along with the mudline, were analyzed for major cations (Na, Mg, K, and Ca) and anions (Cl, Br, and SO_4) by ion chromatography (IC). Only squeezed IW samples and the mudline were analyzed for minor elements (by ICP-AES) and nutrients (by spectrophotometry). Tables **T32**, **T33**, and **T34** present all shipboard analyses for pore water and sediment samples from Site U1583. Selected concentration profiles are illustrated in Figures **F90**, **F91**, **F92**, **F93**, **F94**, and **F95**. Pore fluid concentration trends discussed in the following sections are based on squeezed IW data, unless otherwise noted, and lithostratigraphic units include Units II and III and Subunits IVA–IVC (Unit I was not recovered in Hole U1583C). Moving averages (3–5 points) are provided for those elements that show considerable offset in concentration trends between squeezed IW and Rhizon-sampled fluids. Seawater reference values are based on Ríos et al. (2015) for pH, Sarmiento et al. (2007) for Si, and the International Association for the Physical Sciences of the Oceans (IAPSO) standard for alkalinity, salinity, Na, Cl, Br, Ca, Mg, Sr, Sr/Ca, B, Li, K, and SO_4.

11.1.2. Interstitial water geochemistry

11.1.2.1. Salinity, sodium, chloride, and bromide

Although mudline (i.e., bottom seawater, 0 m CSF-A) and pore water salinities in Hole U1583C are uniform at the seawater value (35) (Table **T32**), downhole concentrations of Na, Cl, and Br change relative to the mudline (Figure **F90**). From 0 to 29.41 m CSF-A (Units II and III and the top of Subunit IVA), pore water concentrations increase beyond analytical uncertainty for Na (479–489 mM), Cl (557–567 mM), and Br (0.85–0.87). Following a slight decrease at 29.41–33.62 m CSF-A, all concentrations remain above the seawater value throughout Subunits IVA (nannofossil ooze with clay and foraminifera) and IVB (calcareous and nannofossil ooze with clay and foraminifera) (Na = 485 ± 4 mM, Cl = 564 ± 5 mM, and Br = 0.86 ± 0.01, 2σ, n = 12).

Table T32. IW geochemical analyses, Site U1583. **Download table in CSV format.**

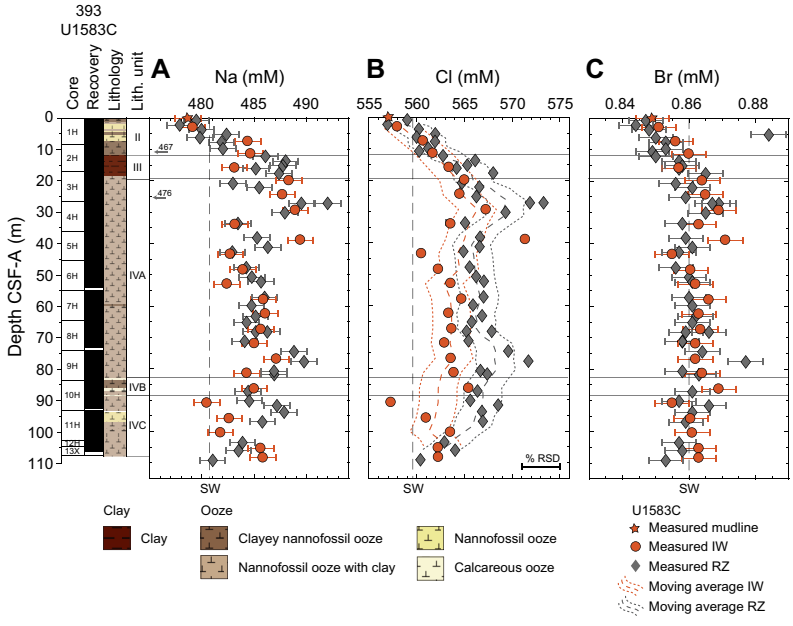

Figure F90. IW profiles of (A) sodium, (B) chloride, and (C) bromide concentrations, Hole U1583C. Moving averages (3–5 points) highlight concentration offsets between squeezed IW and Rhizon-sampled fluids. Seawater (SW) reference values correspond to IAPSO standard composition. Shaded gray lines = unit boundaries. RZ = Rhizon sampler.

A gradual "freshening" is observed in Subunit IVC (nannofossil ooze with clay and foraminifera), with pore fluid concentrations returning to seawater values at the bottom of the hole. This freshening trend is most apparent in the Rhizon Cl concentrations but is not present in the Br data from either sampling technique. This may result from differences in analytical precision (0.5%, 0.7%, and 1.2% relative standard deviation [RSD] for Na, Cl, and Br, respectively), and/or from disturbances associated with XCB sampling.

Na/Cl and Br/Cl ratios remain similar to those in seawater (0.86 and 1.5×10^{-3}, respectively), suggesting that the absolute changes in the concentration of these elements are likely a result of small shifts in local salinity. Finally, agreement between Rhizon-sampled and squeezed IW is best for Na and Br, whereas there are significant differences in measured Cl concentrations in fluids sampled from deeper than 29.41 m CSF-A. This contrasts our results from Hole U1558F, where both sampling techniques showed excellent concentration match.

11.1.2.2. pH and alkalinity

Hole U1583C pore fluid pH is overall uniform over the interval between 2.95 and 57.91 m CSF-A, with an average value (7.5 ± 0.1, 2σ, n = 13) slightly lower than the range for local bottom seawater (7.6–7.7; Ríos et al., 2015) (Figure **F91A**). Below this interval, measured pH increases gradually and reaches values as high as 7.8 at ~100 m CSF-A (Subunit IVC). The two deepest IW samples stand out from this increasing trend and have pH values (7.7) within the seawater range. This offset coincides with drilling disturbances observed below Section 393-U1583C-12H-2 (see **Sedimentology**).

Alkalinity is highly variable throughout Hole U1583C (Figure **F91B**). Values decrease between the mudline (2.3 mM) and 2.95 m CSF-A (2.0 mM) and then increase to 2.5 mM between Units II (nannofossil ooze with clay and foraminifera) and III (clay with nannofossils and clayey nannofossil ooze). In Subunit IVA (nannofossil ooze with clay and foraminifera), alkalinity shows an overall decrease with the exception of a short interval at 43.41–57.91 m CSF-A (2.3–2.4 mM). At the boundary between Subunits IVA and IVB (calcareous and nannofossil oozes with clays and foraminifera), alkalinity increases from 2.2 mM at 76.85 m CSF-A to 2.5 mM at 86.36 m CSF-A. Values drop within the first 10 m of Subunit IVC (2.2–2.3 mM) and, as in the case of pH, the two deepest samples are offset from the overlying fluids and have alkalinity values closer to that of seawater (2.3 mM). Some degree of covariance is observed between pore fluid Ca concentrations and alkalinity in Hole U1583C (R^2 = 0.44). This relationship is likely a result of biogenic carbonate dissolution and reprecipitation of inorganic calcite, which act as source and sink, respectively, of

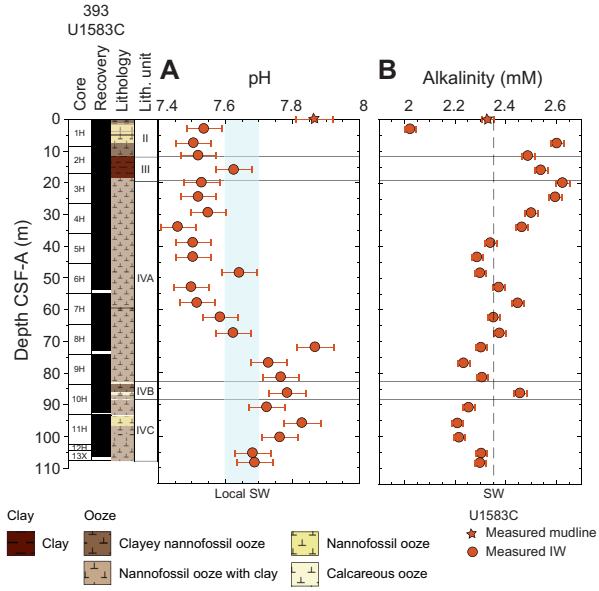

Figure F91. IW profiles of (A) pH and (B) alkalinity, Hole U1583C. Reference values for bottom seawater (SW) pH are based on Ríos et al. (2015) for pH and IAPSO seawater standard composition for alkalinity. Shaded gray lines = unit boundaries.

both Ca and alkalinity in marine sediments (e.g., Hein et al., 1979; Schrag et al., 2013; Turchyn et al., 2021).

11.1.2.3. Calcium, magnesium, strontium, and Sr/Ca

Relative to the mudline, the first squeezed IW measured in Hole U1583C (2.95 m CSF-A) has lower Ca (10.2 mM) and Mg (53.1 mM) concentrations and higher Sr (93.7 µM) and Sr/Ca ratio (9.2 µM/mM) (Figure **F92**). Following this initial drop in Ca concentrations, values increase to 10.8 mM (24.43 m CSF-A) throughout Units II (nannofossil ooze with clay and foraminifera), III (clay with nannofossils and clayey nannofossil ooze), and the first ~6 m of Subunit IVA (nannofossil ooze with clay and foraminifera) (Figure **F92A**). In Subunit IVA, Ca concentrations decrease again between 24.43 and 33.92 m CSF-A (10.8–10.2 mM) and become relatively uniform between ~34 and 100 m CSF-A (10.3 ± 0.3, 2σ, n = 14). The clear exceptions to this concentration uniformity are observed in Subunit IVB (calcareous and nannofossil oozes with clays and foraminifera), where the one measured pore fluid shows considerably higher Ca content (10.7 mM at 86.36 m CSF-A), and in the two deepest pore fluid samples, which approach seawater Ca concentration (10.6 ± 0.4 mM, 2σ, n = 55). Moving averages for squeezed IW and Rhizon-sampled fluids show offsets of up to ~0.5 mM in Ca concentrations, with Rhizon values persistently lower than those obtained from squeezed samples. However, trends overall are similar between the two data sets with the exception of the interval ~20–25 m CSF-A (top of Subunit IVA) and below 100 m CSF-A.

Measured Mg concentrations in Hole U1583C decrease from near-seawater mudline values throughout Units II and III (53.1–52.1 mM at 2.95–15.90 m CSF-A) before increasing to 54.1 mM over the uppermost ~10 m of Subunit IVA (Figure **F92B**). Similar to what is observed in the Ca profile, Mg concentrations become overall uniform from ~34 to 100 m CSF-A (53.5 ± 0.8 mM, 2σ, n = 14). Again, Subunit IVB stands out, with a measured Mg concentration (54.0 mM at 86.36 m CSF-A; squeezed IW) similar to seawater value (53.9 mM ± 0.7, 2σ, n = 55) and much higher than the fluids directly above and below. Squeezed IW fluids in Subunit IVC are relatively uniform (53.1 ± 0.5 mM, 2σ, n = 5). Similar to the Ca profile, Rhizon-sampled pore fluids show persistently lower Mg concentrations compared to squeezed samples. For example, the Mg decrease in Unit III is more pronounced in the Rhizon data set, yielding a moving average as low as 51.2 mM at ~14 m CSF-A. Concentration trends in Subunit IVA are similar between the data sets, and Rhizon-sampled fluids remain largely uniform between Subunits IVA and IVB. Below 100 m CSF-A, Rhizon fluids decrease in concentration (52.0 ± 0.6 mM, 2σ, n = 3).

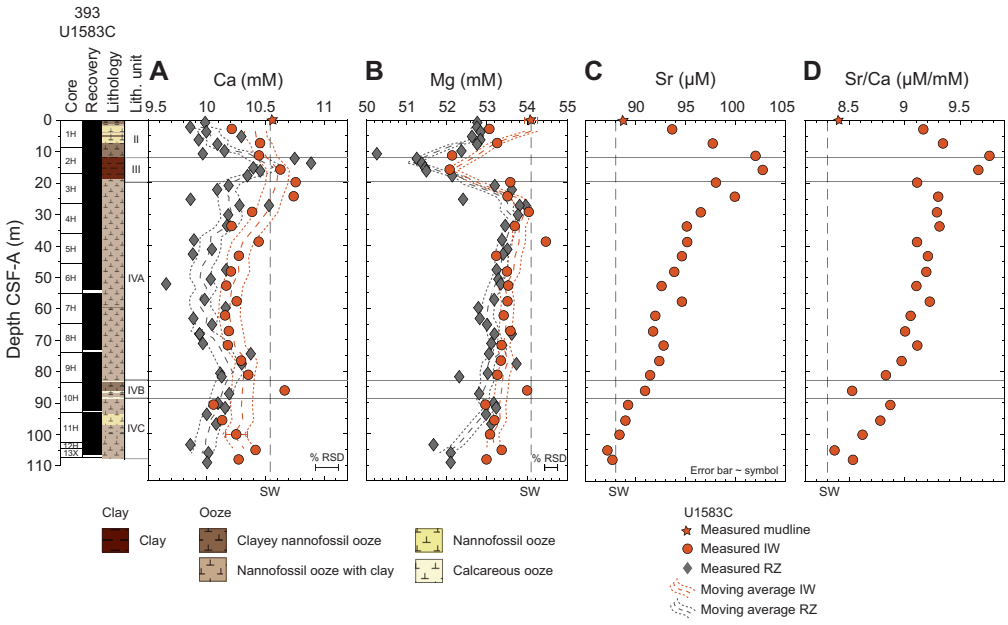

Figure F92. IW profiles of (A) calcium, (B) magnesium, (C) strontium, and (D) Sr/Ca ratios, Hole U1583C. Seawater (SW) reference values are based on IAPSO standard. Shaded gray lines = unit boundaries. RZ = Rhizon sampler.

Sr concentrations and Sr/Ca ratios follow very similar depth profiles. Both Sr (93.7–102.8 µM) and Sr/Ca (9.2–9.7 µM/mM) increase throughout Units II and III and show a broad decrease throughout Unit IV (Sr: 102.8–88.4 mM, Sr/Ca: 9.7–8.6 µM/mM) to the bottom of the hole (Figure **F92C, F92D**). As in the case of Ca and Mg, pore-fluid Sr/Ca ratio in Subunit IVB is significantly offset from surrounding fluids (8.5 µM/mM).

The correlation between Ca and alkalinity observed in Hole U1583C (see **pH and alkalinity**) provides strong evidence for the influence of carbonate diagenesis on the chemistry of these pore fluids. Sr/Ca ratios that are above the seawater value are consistent with biogenic carbonate dissolution, which appears to be most pronounced in Unit III. This observation is in line with the high detrital clay content reported for this unit and calcium carbonate abundances <1 wt% at ~12 m CSF-A (Table **T33**). In Unit II and Subunit IVA, the persistently high Sr/Ca ratios, along with Ca and Mg concentrations that are uniformly below the seawater values, provide evidence for recrystallization from low-Mg biogenic carbonate typical of nannofossil ooze to higher-Mg diagenetic calcite (e.g., Baker et al., 1982; Higgins and Schrag, 2012). Subunit IVC marks a gradual shift toward seawater values of Sr and Sr/Ca ratios, suggesting the potential influence of seawater-like fluids at this interval.

11.1.2.4. Boron, lithium, silica, and potassium

High to moderate concentration increases (relative to the mudline) are observed for B (67%), Li (10%), Si (78%), and K (17%) in Hole U1583C Units II (nannofossil ooze with clay and foraminifera) and III (clay with nannofossils and clayey nannofossil ooze) (Figure **F93**). Following this initial increase, pore fluid concentrations of these elements continue to change as a function of depth and sediment composition.

Between 15.9 m and 48.41 m CSF-A, corresponding to the upper section of Subunit IVA (nannofossil ooze with clay and foraminifera), concentration decreases are observed for B (700.9–520.4 µM), Li (27.0–24.7 µM), Si (149.4–108.5 µM), and K (12.3–11.8 mM). Whereas measured K values continue to decrease throughout Subunit IVA (52.92–81.37 m CSF-A), concentrations increase for B (538–560 µM), Li (25.1–25.5 µM), and Si (115.1–126.8 µM). In Subunit IVB (calcareous and nannofossil oozes with clay and foraminifera), B, Li, and K show measurable decreases in concen-

Table T33. Oxygen concentrations, Hole U1583C. **Download table in CSV format.**

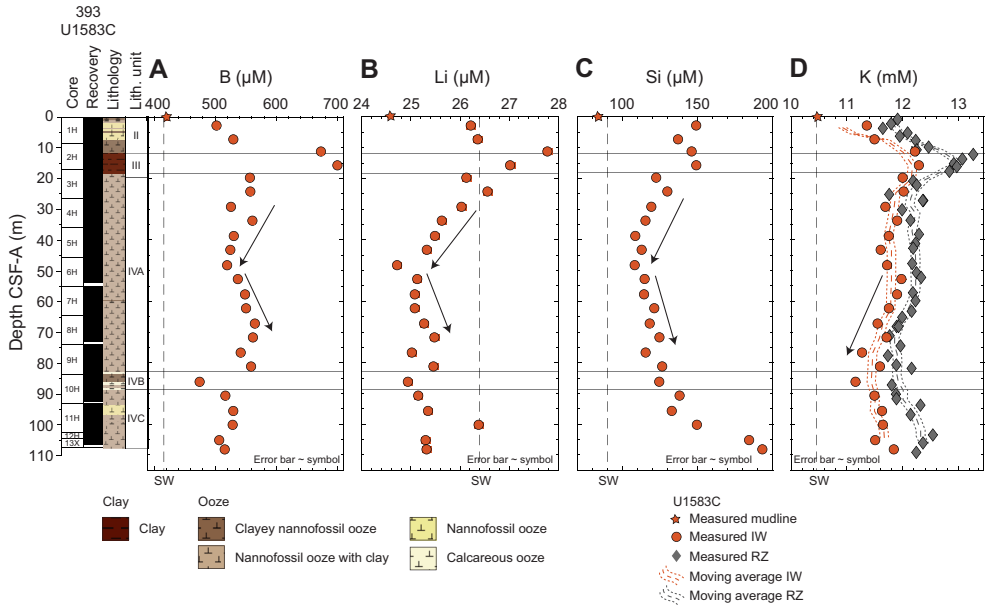

Figure F93. IW profiles of (A) boron, (B) lithium, (C) silicon, and (D) potassium concentrations, Hole U1583C. Seawater (SW) reference values for B, Li, and K correspond to IAPSO standard composition; local Si concentration is from Sarmiento et al. (2007). Shaded gray lines = unit boundaries. RZ = Rhizon sampler.

trations, whereas Si remains similar to concentrations in Subunit IVA. In the lowermost Subunit IVC (nannofossil ooze with clay and foraminifera), pore fluid concentrations of all elements increase. The two deepest pore fluid samples are again distinct in their chemical composition compared to overlying fluids and seawater, which cannot be explained by contamination due to drilling disturbance. Moving averages for K concentrations in squeezed IW and Rhizon-sampled fluids show similar trends, although Rhizon values are persistently higher than squeezed IW samples (up to 0.6 mM offset in Unit III and Subunit IVC).

The most noticeable changes in the concentrations of B, Li, Si, and K in Hole U1583C coincide with unit boundaries and are likely controlled by variations in lithology. For example, Unit III is marked by a significant decrease in calcium carbonate content (<1 wt% at 12.12 m CSF-A; Table **T34**) and a spike in natural gamma ray (>40 counts/s; Figure **F8**), consistent with the presence of detrital silicate phases such as quartz, feldspars, and clays detected by XRD (see **Sedimentology**). Diagenetic reactions involving these silicate components, in addition to biogenic silica, are likely responsible for the large increases observed in B, Li, Si, and K values across this interval. In addition, the concentration changes observed within Subunit IVA (48.41–52.92 m CSF-A) coincide with a transition in the composition of clayey nannofossil oozes, which vary from light brown at 18.07–45.57 m CSF-A to brown and strong brown below ~64.5 m CSF-A (see **Sedimentology**). Si concentrations, in particular, show an inflection point at ~50 m CSF-A, and the increase in Si observed between ~50 and 110 m CSF-A points to Si-sourcing reactions within the sediments.

11.1.2.5. Sulfate, ammonium, and manganese

Sulfate (SO_4) concentrations decrease between the mudline (28.7 mM) and the first measured pore fluid (27.3 mM) at 2.95 m CSF-A in Unit II (nannofossil ooze with clay and foraminifera) but then increase with depth to 28.1 mM at 19.93 m CSF-A in Unit III (clay with nannofossils and clayey nannofossil ooze) and into Subunit IVA (nannofossil ooze with clay and foraminifera) (Figure **F94A**). Concentrations show a broad decrease (28.1–27.7 mM) in Subunit IVA before a change is observed (27.7–28.2 mM) at the transition from Subunit IVA to IVB (calcareous and nannofossil oozes with clays and foraminifera). Pore fluid SO_4 values decrease to 27.5 mM at the top of Subunit IVC (90.87 m CSF-A) and reach 27.8 mM toward the bottom of the hole (108.36 m

Table T34. Sediment geochemical analyses, Site U1583. **Download table in CSV format.**

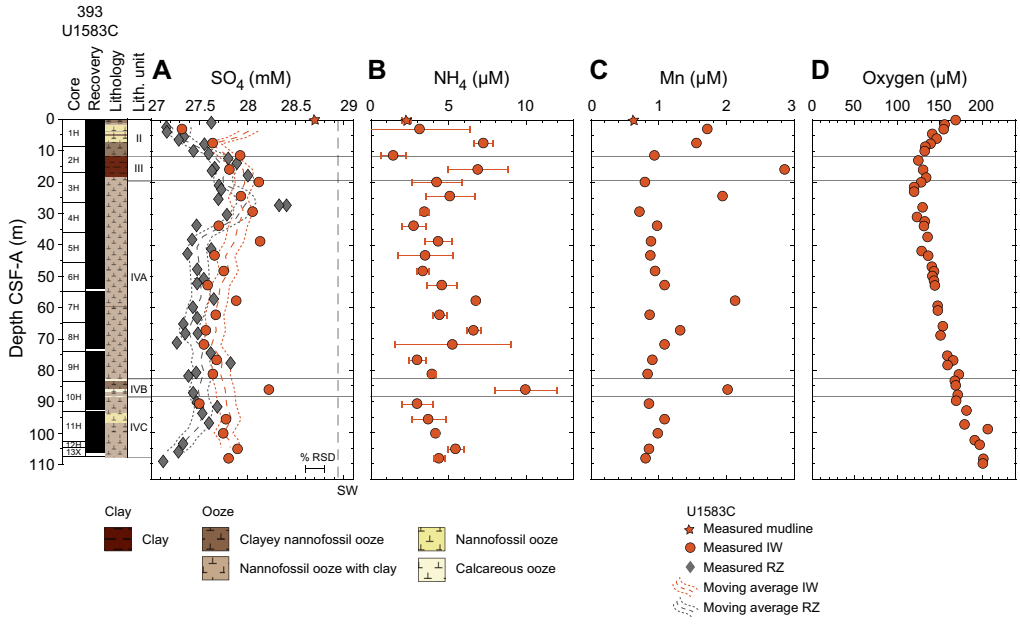

Figure F94. IW profiles of (A) sulfate, (B) ammonium, and (C) manganese and (D) in situ oxygen, Hole U1583C. Seawater (SW) reference value sulfate is based on IAPSO standard composition. Shaded gray lines = unit boundaries. RZ = Rhizon sampler.

CSF-A). Although sulfate-reducing bacteria are obligate anaerobes and pore fluids in Hole U1583C remain oxic throughout (see **Oxygen**; Figure **F94D**), sulfate reduction taking place in reduced microniches within the sediment column (Jørgensen, 1977) might explain the subtle changes in SO_4 concentrations observed here. Despite some overlap between the moving averages from squeezed IW and Rhizon-sampled fluids, SO_4 concentrations in the Rhizon sample set are overall lower than those measured in squeezed IW from similar depths.

Ammonium (NH_4; 3–17 µM) and Mn (0.63–2.86 µM) concentrations remain overall similar to the mudline values in Hole U1583C except for a few intervals (Figure **F94B, F94C**). Specifically, both NH_4 and Mn peak in Unit III, at concentrations up to 7 and 2.86 µM, respectively. Similarly, concentrations rise above background levels in Subunit IVB (NH_4 = 10 µM and Mn = 2.02 µM), where sedimentary organic matter contents are highest (up to ~0.35 wt%; Figure **F95**).

11.1.2.6. Oxygen

Oxygen is the pore water constituent measured with the highest reduction potential and is the first molecule reduced during microbial degradation of organic matter. Its profile provides insight into subseafloor biogeochemical and microbial processes. Oxygen concentrations in Hole U1583C decrease from a mudline concentration of ~170 µM to ~125 µM at the base of Unit II (nannofossil ooze with clay and foraminifera) at ~11 m CSF-A (Table **T33**; Figure **F94D**). There is a slight increase through Unit III (clay with nannofossils and clayey nannofossil ooze) to ~136 µM before O_2 concentrations decrease again to ~120 µM in the uppermost sediments of Subunit IVA (nannofossil ooze with clay and foraminifera). Between ~23 m CSF-A and the bottom of the hole, there is a tight, near-monotonic increase in oxygen concentrations up to ~202 µM in the lowermost sample at ~108 m CSF-A (Figure **F94D**), albeit with greater scatter in measurements taken in Subunit IVC (88–110 m CSF-A; nannofossil ooze with clay and foraminifera).

11.1.3. Sediment sampling

During Expedition 393, sediment samples from Hole U1583C were selected by the sedimentologists from core working halves for measurement of carbon and nitrogen contents (see **Geochemistry** in the Expedition 390/393 methods chapter [Coggon et al., 2024a]). One sample per core was analyzed in Cores 393-U1583C-5H, 6H, 8H, 10H, and 12H; two samples per core were analyzed in Cores 1H–4H, 7H, 11H; and three samples were analyzed in Core 9H. In total, 20 samples were taken at Site U1583, all from Hole U1583C (Table **T34**). In addition, sediment was sampled from whole-round cores on the catwalk for headspace hydrocarbon gas analyses (see **Geochemistry** in

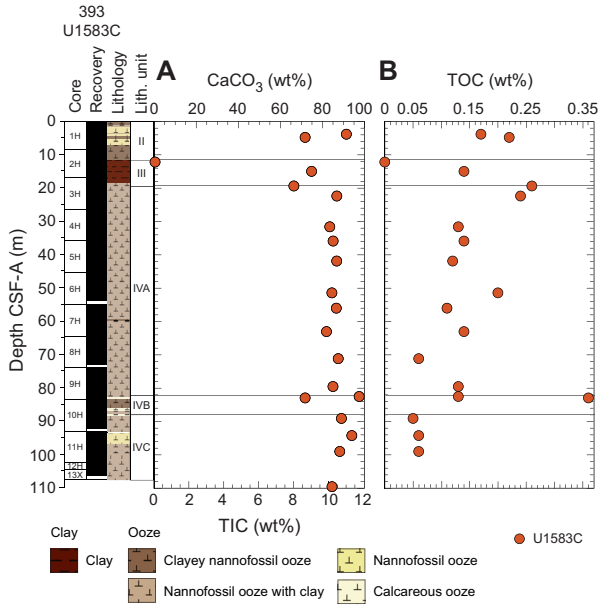

Figure F95. Sediment (A) calcium carbonate and total inorganic carbon (TIC) and (B) TOC, Hole U1583C. Shaded gray lines = unit boundaries.

the Expedition 390/393 methods chapter [Coggon et al., 2024a]). These samples were taken at the top of Section 3 in Cores 1H–12H. In total, 12 samples were analyzed for hydrocarbons at Site U1583, all from Hole U1583C (Table **T34**). Concentrations of all hydrocarbons were near or below detection limit (1 ppmv for methane and 0 for all other hydrocarbons; 1.23 ± 1.74 ppmv, 2σ, n = 12) and will not be discussed further.

11.1.4. Sediment bulk geochemistry

11.1.4.1. Calcium carbonate

The calcium carbonate content of sediments is high throughout Hole U1583C (84 ± 39 wt%, 2σ, n = 20) with the exception of a single sediment sample in Unit III (12.12 m CSF-A; clay with nannofossils and clayey nannofossil ooze) that contains <1 wt% carbonate. In Unit II (nannofossil ooze with clay and foraminifera), two samples yield carbonate contents of 91 and 72 wt%. In contrast, Unit III (clay with nannofossils and clayey nannofossil ooze; ~11.5–18 m CSF-A) contains roughly no calcium carbonate in the uppermost sediment sampled (12.12 m CSF-A), consistent with the predominantly dark brown clay lithology that dominates the unit, although a deeper sample in this unit has ~75 wt% $CaCO_3$. The brown to light brown interbedded clayey nannofossil ooze of Unit III sampled in the middle of the unit (75 wt%, n = 1) resembles near-average values for Hole U1583C. Subunit IVA (nannofossil ooze with clay and foraminifera) has the lowest average $CaCO_3$ values within Unit IV (~18–82 m CSF-A; 83 ± 12 wt%, 2σ, n = 10). The transition to Subunit IVB (calcareous and nannofossil oozes with clay and foraminifera) is marked by a peak in calcium carbonate (97 wt%) for a sample collected from a white calcareous ooze layer, although a neighboring sample from a clayey nannofossil ooze layer in the same subunit has ~72 wt%. Calcium carbonate values in Subunit IVB range 72–97 wt% (~82–88 m CSF-A; n = 2). Subunit IVC (nannofossil ooze with clay and foraminifera; deeper than 88 m CSF-A) has the highest average carbonate values within Unit IV (89 ± 7 wt%, 2σ, n = 4).

11.1.4.2. Total organic carbon and nitrogen

TOC was calculated for all samples measured for $CaCO_3$ (n = 20) as the difference between total carbon (TC) and total inorganic carbon (see **Geochemistry** in the Expedition 390/393 methods chapter [Coggon et al., 2024a]). TOC concentrations (Figure **F95**) in Hole U1583C average 0.15 ± 0.15 wt% (2σ, n = 20). In Unit II (nannofossil ooze with clay and foraminifera), the two measured samples are fairly uniform (0.17–0.22 wt%). TOC concentrations decrease into Unit III (clay with nannofossils and clayey nannofossil ooze), which is marked by a data point at the top of the unit that is below detection limit (due to a very low TC content of 0.06 wt%). A second sample was taken from the brown to light brown clayey nannofossil ooze interbed in Unit III (0.14 wt%), which resembles near-average values for the entire Hole U1583C (~0.15 wt%). Unit IV has the greatest variability in average TOC concentrations (0.14 ± 0.16 wt%, 2σ, n = 16) in comparison to each unit and relative to the entire hole. The sampled sediment at the top of Subunit IVA (nannofossil ooze with clay and foraminifera) has the highest TOC (0.26 wt%), and values gradually decrease to as low as 0.06 wt% toward the bottom of the subunit (unit average = 0.15 ± 0.10 wt%, 2σ, n = 10). The overall decrease in TOC in Subunit IVA is also observed in the SO_4 profile and is consistent with organic matter remineralization through sulfate reduction. The two samples from Subunit IVB (calcareous and nannofossil oozes with clay and foraminifera) show considerable variability. The calcareous ooze sample (82.32 m CSF-A) has TOC content (0.13 wt%) similar to the average value for Hole U1583C, whereas the clayey nannofossil ooze sample (82.75 m CSF-A) shows a higher TOC value of 0.36 wt%. Subunit IVC (nannofossil ooze with clay and foraminifera) has the lowest average TOC concentration (0.07 ± 0.03 wt%, ±2σ, n = 4) in Unit IV.

Total nitrogen concentrations were measured in all samples analyzed for $CaCO_3$ (n = 20). TN concentrations in Hole U1583C are below detection limits (Table **T34**; see Table **T9** in the Expedition 390/393 methods chapter [Coggon et al., 2024a]), and are not discussed further. Total sulfur and total hydrogen were not measured.

11.2. Basement

During Expedition 393, ~134 m of slightly to moderately altered ~30.6 Ma basalts were recovered from Hole U1583F, representing seven distinguishable volcanostratigraphic units (see **Igneous petrology**). A total of 17 volcanic rock samples were selected for shipboard geochemical analyses:

16 basalts, and Unit 4 breccia fill Sample 393-U1583F-16R-2, 73–83 cm (Figure **F7**). Analytical studies included solution analysis by ICP-AES, loss on ignition (LOI) measurements, and direct analyses of sample powders by pXRF (Tables **T35**, **T36**).

11.2.1. Basement rock sampling and geochemical analysis

The geochemical samples selected represented typical material from each of the igneous/volcanostratigraphic units identified (Table **T4**). Geochemical samples were taken adjacent to other sampling (thin sections, PMAG, XRD, etc.) to generate integrated data on these materials. A ~2 g split of each freshly made sample powder was placed in a powder mount for pXRF analysis, and each sample was measured in triplicate with that instrument (see **Geochemistry** in the Expedition 390/393 methods chapter [Coggon et al., 2024a]). ICP-AES measurements were completed on oxidized samples after the completion of LOI determinations, so ICP-AES data are reported on a volatile-free basis.

11.2.2. Bulk chemical compositions and trace element abundances

Table **T35** lists the shipboard geochemical data collected on Site U1583 samples by ICP-AES analysis (including LOI determinations), and Table **T36** presents pXRF data collected for these samples from powder mounts. Supplementary pXRF analyses performed directly on the core cut surfaces are in Table **T6**. In Figure **F96**, the Site U1583 data are plotted on the total alkali versus silica classification diagram of Le Bas et al. (1986). As with the samples from other SAT sites, Site U1583 samples fall in the basalt field. By the Yoder and Tilley (1962) basalt classification scheme, the Site U1583 basalts are all tholeiites or olivine tholeiites. Increases in alkalies and/or losses of Mg related to alteration do not appear to have impacted their normative compositions (Table **T35**).

Table T35. Hard rock geochemical analysis, Site U1583. **Download table in CSV format.**

Table T36. Powder pXRF elemental data, Site U1583. **Download table in CSV format.**

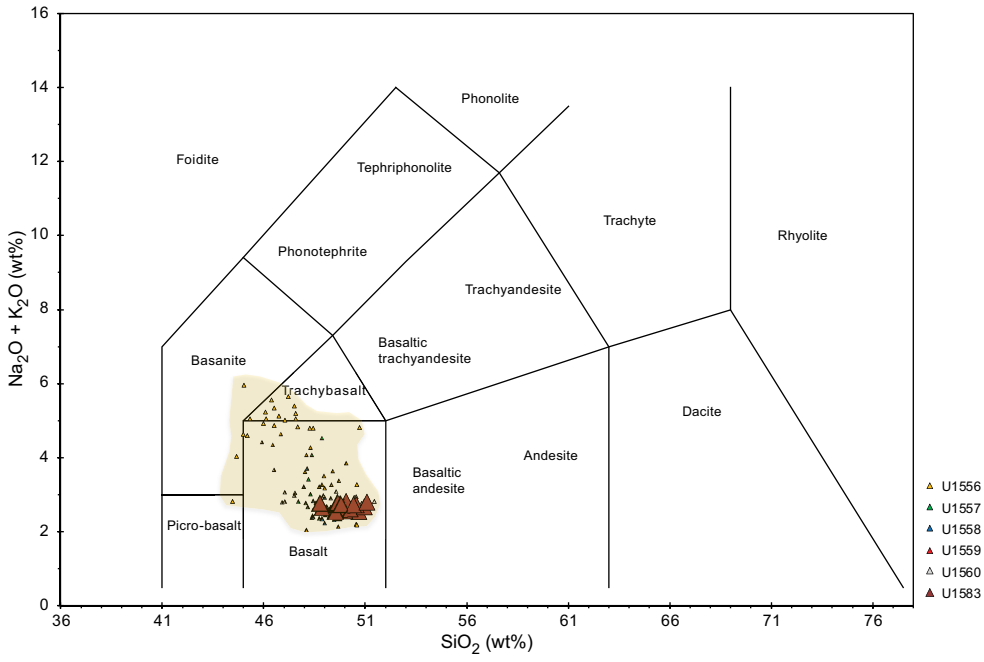

Figure F96. Total alkalis vs. silica diagram (Le Bas et al., 1986) showing ICP-AES data from Site U1583 compared to other SAT sites.

In Figure **F97**, Sr versus TiO_2, the Site U1583 samples cluster near the center of the range for published South Atlantic MORB data, as compiled from the EarthChem Portal. The U1583 basalts range to higher Sr and Ti concentrations than the MORB-like basalts from the older SAT sites (Sites U1558, U1557, and Stratigraphic Sequence C from Site U1556) and the younger basalts recovered at Site U1559.

Figure **F98** presents downhole plots for Site U1583 basalts. Although the Site U1583 samples appear relatively uniform in terms of CaO, trace elements like Sr and especially TiO_2 record variability that maps to many of the lithologic boundaries identified (see **Igneous petrology**). TiO_2 appears particularly sensitive to lithologic changes at a fine scale; pXRF data from U1583 samples suggest regions with different TiO_2 concentrations in Units 1 and 2, and overall these data document a marked dropoff in the TiO_2 content of the basalts in Unit 3. These changes likely relate to changes in the parental magma composition, suggesting the occurrence of more compositionally diverse eruptions on shorter timescales than have been seen in other SAT sites. Also observable in the TiO_2 data are narrow low-abundance horizons proximal to unit boundaries, which may indicate transitions into volcanic-sedimentary breccias, such as in Units 4 and 6, and zones of interpillow sediment or volcanic-sedimentary breccias, such as between Subunits 3A and 3B.

11.2.3. Alteration and differentiation effects

In Figure **F99**, the downhole variations in K_2O and MgO give insights into alteration effects at Site U1583. Although K_2O contents are overall lower than seen in Site U1558 basalts, concentrations are still generally higher than those of fresh MORB. A broad pattern of K_2O increase downhole is evident in measurements on both sample surfaces and rock powders, punctuated by narrow zones of high K_2O in the volcanic-sedimentary breccia zones. MgO contents show marked changes downhole at Site U1583, with the uppermost basalt cores (down to Unit 4, at ~170 mbsf) showing generally higher MgO contents, whereas below Unit 4, MgO contents become highly variable and are in some samples strongly depleted relative to fresh Atlantic MORBs. These differences correlate with lithologic changes downhole. The section above the Unit 4 breccias includes abundant basaltic sheet flows, including a thick (>11 m), fine- to medium-grained massive flow at the top of the sequence. In contrast, below Unit 4 microcrystalline pillow lavas dominate (see **Igneous petrology**). The lowest MgO values we measured are in close proximity to the lower boundaries of sedimentary breccias in Units 4 and 6. In both cases, MgO contents increase (and K_2O contents decrease) in the basaltic rocks immediately below these intervals. This pattern suggests a relation-

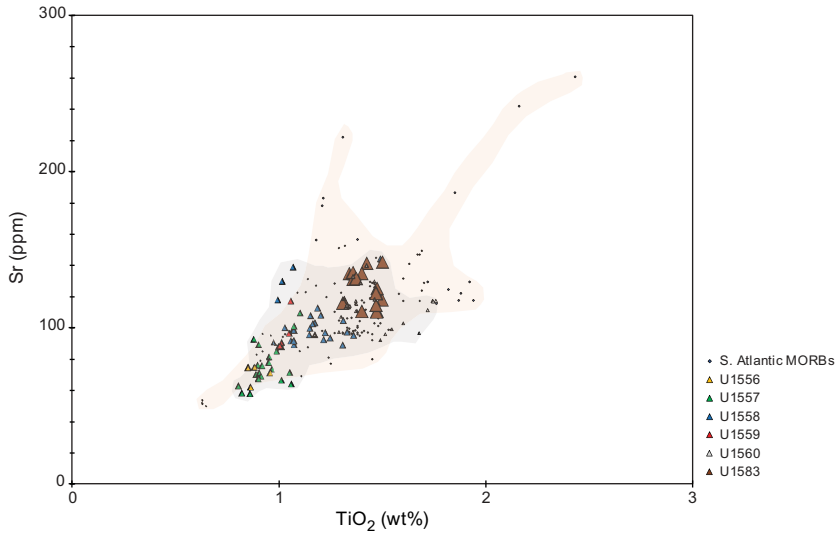

Figure F97. Sr vs. TiO_2 contents comparing Site U1583 basalts to other SAT basalts and South Atlantic basaltic glass compositions compiled from EarthChem Portal (**http://portal.earthchem.org/**) on 10 July 2022 via map polygon function for MORB basalt glasses <100,000 y old from South Atlantic Ocean (specific sources: Kelley et al., 2013; Kendrick et al., 2017; Le Roux, 2000; Michael and Graham, 2015; Paulick et al., 2010; Reekie et al., 2019; van der Zwan et al., 2017; Yang et al., 2018).

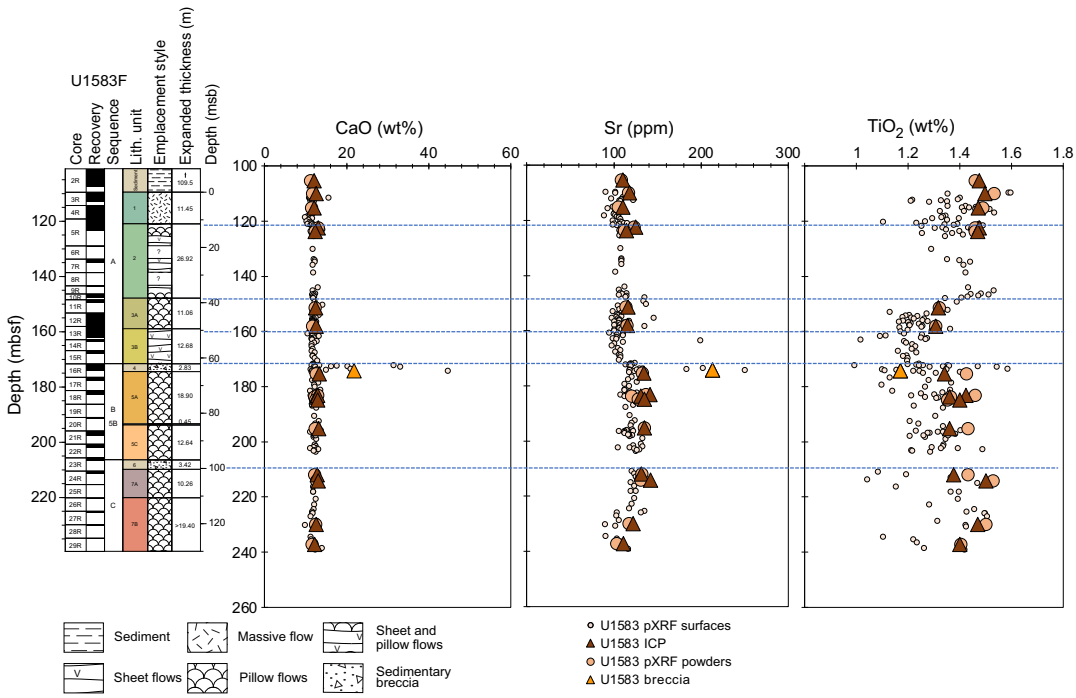

Figure F98. Major elements analyzed on sample powders by ICP-AES and pXRF, as well as on sample surfaces via pXRF, Site U1583. Two volcanic sedimentary breccia samples are from Unit 4. Dotted lines = lithostratigraphic boundaries identifiable in downhole chemical variations.

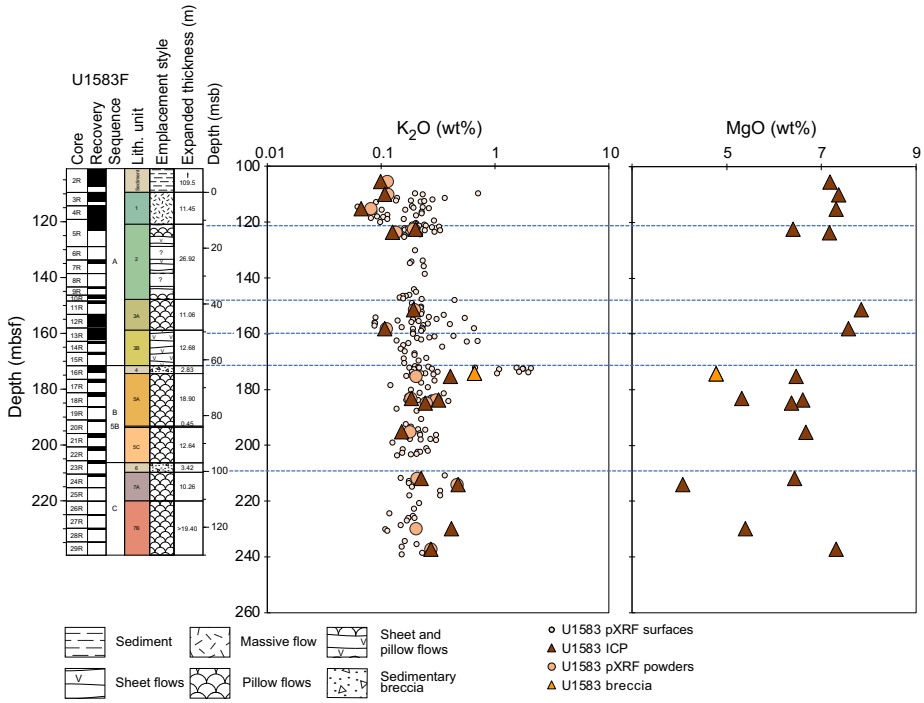

Figure F99. K_2O and MgO contents, Site U1583. Dotted lines = lithostratigraphic boundaries identifiable in downhole chemical variations.

ship between MgO (and to a lesser extent, K_2O) concentrations and proximity to the breccias, which may represent ancient exposed seafloor or possibly permeable zones where seawater-basalt exchanges are enhanced.

In terms of measures of overall K enrichment, the Site U1583 samples span a range in K/Zr ratios that fall between those seen in the older SAT basalts to values like those encountered in the younger Site U1559 lavas (Figure **F100**). The Site U1583 suite spans a range in Cr/TiO_2 ratios consistent with the downhole variability observed in Figure **F98**. Lower Cr/TiO_2 ratios in the Site U1583 basalts are consistent with these lavas being more differentiated, (i.e., they are lower in Cr at MORB-like TiO_2 contents) as opposed to indicating any kind of change in the compositions of their mantle sources.

11.2.4. Immobile trace element systematics and MORB magmatic processes

Figures **F101** and **F102** plot the Site U1583 data on the Zr/Y versus Zr tectonic discrimination diagram of Pearce and Norry (1979) and the V versus Ti/1000 discrimination diagram of Shervais (1982). Although these diagrams are more commonly used to assay the likely tectonic origins of continental mafic rocks, they can also be used as a means for discerning among MORB magmatic suites in terms of parameters such as their mean extents of crystallization or comparative extents of melting. On Figure **F101**, the Site U1583 basalts have, on average, higher Zr contents and higher Zr/Y than do the basalts in either the Site U1558 or Site U1559 sample suites. As noted above, this is consistent with the Site U1583 lavas being somewhat more differentiated than basalts from these other sites, which may be related to differences in their extents of fractional crystallization before eruption. Figure **F102** provides some additional detail on the likely magmatic evolution of Site U1583 basalts. Looking specifically at our higher precision ICP-AES data, the Site U1583 lavas form a positively sloped linear trend, consistent with fractional crystallization effects, which would proportionally increase (or in the case of oxide phases, decrease) magmatic Ti and V abundances. The data from Sites U1558 and U1559 also fall along quasilinear arrays, most likely reflecting crystallization effects. However, the Site U1583 data trend reflects a higher Ti/V ratio than do the trends for the Site U1558 or Site U1559 samples. This difference is probably not crystallization related, given the strong linear correlation of the data. A possible origin for these differences are variations in the mean extent of partial melting involved in generating the parental magmas for each of these suites because differences in the bulk partition coefficients for vanadium and tita-

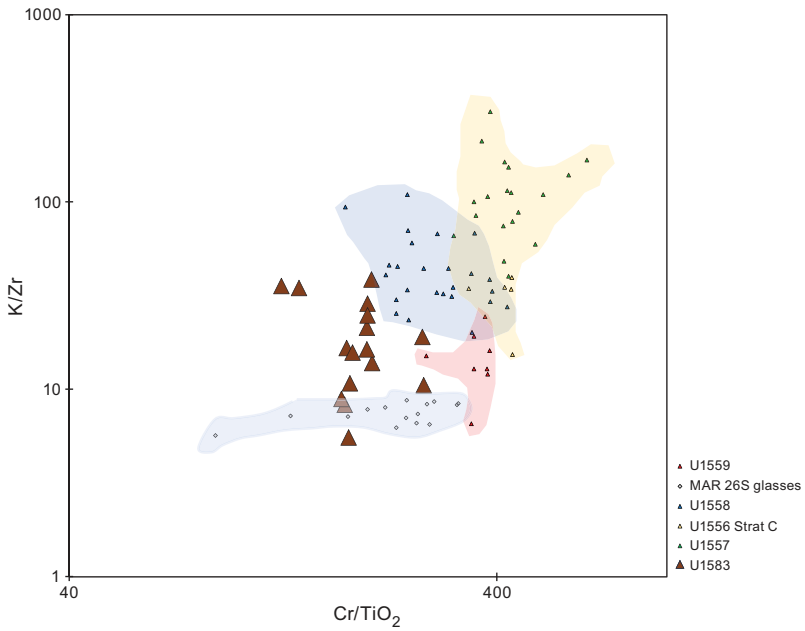

Figure F100. K/Zr vs. Cr/TiO_2 for Site U1583 contrasted with other SAT sites (yellow area = Site U1557 and Stratigraphic Sequence 3 from Site U1556), blue area = Site U1558, red area = Site U1559) and data for zero-age Mid-Atlantic Ridge (MAR) 26°S basalt glasses (Marschall et al., 2017; gray area).

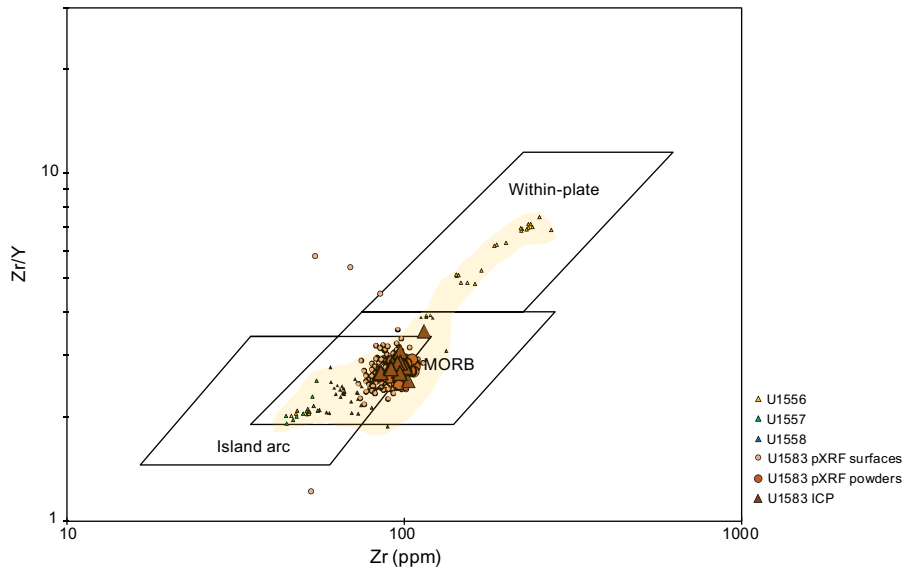

Figure F101. Zr/Y vs. Zr tectonic discrimination diagram of Pearce and Norry (1979) for Site U1583 by ICP-AES and pXRF powders compared to other SAT sites (shaded field).

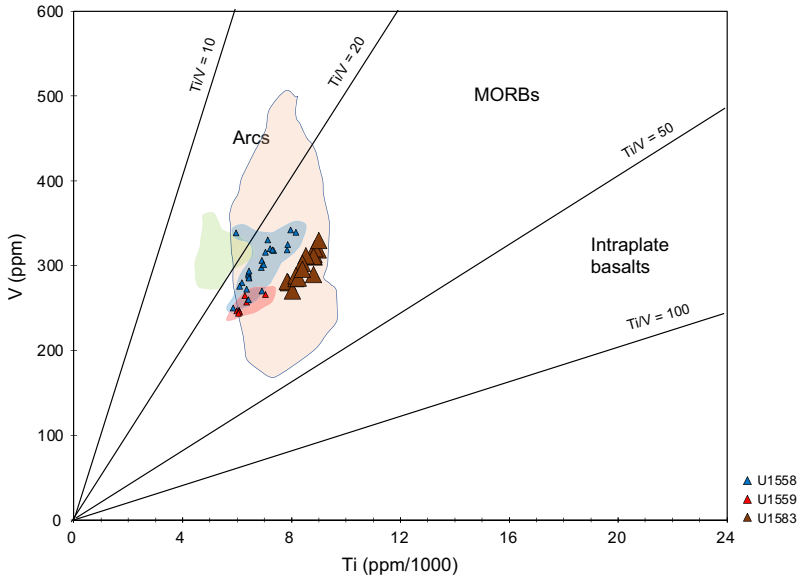

Figure F102. V vs. Ti/1000 discrimination diagram of Shervais (1982) for Site U1583 by ICP-AES and pXRF compared to other SAT sites (yellow area = Site U1556, green area = Site U1557, blue area = Site U1558, red area = Site U1559. Shaded field encompasses all SAT sites.

nium mean these elements can fractionate relative to one another during mantle melting processes. An additional possibility to consider is variation in mantle source composition, although Ti/V ratios normally show only limited variations in MORB systems (e.g., Shervais, 1982, 2022).

12. Microbiology

12.1. Sediment

Microbiology sampling from sediments in Hole U1583C during Expedition 393 focused on exploring evidence for life in the sediments and at the sediment/basement interface using culture-

based and culture-independent approaches. One standard microbiology whole-round sample (5–10 cm long) was collected from each 9.5 m core. These whole-round samples were subsampled for various microbiological analyses to be performed by different shipboard and shore-based scientists, as described below (Table **T37**). Additional personal whole-round cores for specialized shore-based analyses were also taken (Table **T37**). An additional whole-round sample that included both standard and personal microbiology samples was taken in the sediment of Hole U1583F prior to basement drilling at the sediment/basement interface (Table **T37**). In summary, 13 standard microbiology whole rounds were sampled for shipboard analysis and an additional 33 whole rounds were taken for personal shore-based analyses.

12.1.1. Microbiological sample processing and experiments

12.1.1.1. Cell and viral counts

Subsamples for cell counts were taken in duplicate from every standard microbiology whole round except for Sample 393-U1583C-12H-4. An additional cell count subsample was taken in each of the seven cores that were sampled for viral metagenomic analysis to perform viral counts on those core sections. Performing shipboard cell and viral counts is difficult because of the time required for sample processing; therefore, shipboard cell counts were not attempted during the SAT expeditions; instead, samples were preserved for postexpedition analyses by diluting 1 cm^3 in 4 mL of 4% paraformaldehyde in 100 mM phosphate-buffered saline (PBS). Samples were taken in replicates to enable cross-calibration of cell counts between different laboratories. A third sample was collected from samples where samples for viral metagenomics were also collected.

12.1.1.2. Microbial community structure

From the standard microbiology whole rounds, 24 samples were preserved for shore-based polymerase chain reaction [PCR] amplicon-based analysis (from DNA and RNA), 13 samples were preserved for single-cell genomics, 11 samples for viral production experiments, and 11 samples for high-throughput culturing. Additional personal whole rounds (5–10 cm long) were taken and preserved: seven samples for viral metagenomics, seven samples for metagenomics, six samples for stable isotope probing experiments, seven samples for lipid analysis, and six samples for characterization of Archaea (Table **T37**). All samples were preserved as described in **Microbiology** in the Expedition 390/393 methods chapter (Coggon et al., 2024a).

12.1.1.3. Microbial incubation experiments

To determine the extent of viral activity, virus-induced microbial mortality and prophage induction experiments were performed (see **Microbiology** in the Expedition 390/393 methods chapter [Coggon et al., 2024a]) using 10 cm^3 from the standard microbiology samples from Cores 393-U1583C-1H, 5H, and 11H (see Table **T37** for specific sections and depths) to initiate experiments. These samples were chosen to represent a range of oxygen and nutrient concentrations throughout the hole. Duplicate samples were incubated at room temperature (~18°C), and 1 mL duplicate subsamples were collected after 0, 3, 6, 12, 24, and 48 h and then 7 and 14 days. The seawater that was used to dilute 1 cm^3 sediment consisted of 0.22 µm filtered and autoclaved deep seawater collected using a Niskin bottle attached to the subsea camera system frame on 28 June 2022 at a depth of 4333 m. The pH of the deep water upon collection was 7.54.

12.1.2. Microbiological contamination monitoring

To determine the number of microorganisms present in drilling mud fluid and also generate a database of potential contaminants, 25 mL of drilling fluid was collected from the standpipe on the rig floor at the beginning of coring operations in Hole U1583C. This drilling fluid was frozen at −80°C for shore-based molecular biology analysis to determine the microorganisms present in drilling fluid.

12.2. Basement

Microbiology sampling in basement of Hole U1583F during Expedition 393 focused on exploring evidence for life in volcanic basement and at the sediment/basement interface using culture-based

Table T37. Microbiology whole-round samples, Hole U1583C. **Download table in CSV format.**

and culture-independent approaches. For Hole U1583F, sampling efforts aimed to collect one ~10 to 15 cm whole-round core sample from each ~9.5 m advance. To maintain acceptable levels of core recovery, drilling generally proceeded with 4.8 or 4.9 m RCB half-core advances. In practice, this meant taking microbiological samples from alternating cores, although this varied depending on adequate recovery and core characteristics as well as the geologic characteristics of interest. The whole-round cores selected were photographed immediately in the splitting room from overhead, in context with adjacent core pieces. They were then processed and subsampled for different microbiological analyses, with the goal of generating a suite of subsamples that were representative of the different rock and alteration types that comprise the volcanic basement stratigraphy at Site U1583 (see **Igneous petrology** and **Alteration petrology**). Preference was given to core pieces with evidence of alteration or fracturing because the presence of these features indicates past fluid flow and potential avenues for current fluid ingress, which is a prerequisite for delivery of microorganisms to subseafloor basement. In total, 10 whole-round samples (11–17 cm long) were collected for microbiological analyses (Figure **F103**). The rock types sampled were moderately plagioclase-olivine phyric, subtly variolitic massive basalt (2 whole rounds); moderately plagioclase-olivine-clinopyroxene phyric, fine-grained basalt with glassy margin (1 whole round); sparsely plagioclase-olivine-clinopyroxene phyric, microcrystalline basalt with glassy margin (1 whole round); aphyric fine-grained basalt (2 whole rounds); basaltic breccia with limestone matrix (1 whole round); moderately plagioclase-olivine phyric, microcrystalline basalt (1 whole round); moderately plagioclase-olivine-augite phyric, microcrystalline basalt (1 whole round); and sparsely olivine-plagioclase phyric, fine-grained basalt with glassy margin (1 whole round) (Figure **F103**; see **Igneous petrology**). In addition, one whole-round sample was obtained from Core 393-U1583C-13X of aphyric basalt close to the boundary with the lowermost overlying sediments.

After the exteriors of whole-round pieces were removed to avoid material contaminated during coring (see **Microbiology** in the Expedition 390/393 methods chapter [Coggon et al., 2024a]), the remaining material was split into subsamples that were prepared for different microbiological analyses. The number of subsamples depended on the amount of material available from each "parent" whole-round sample (Table **T38**).

12.2.1. Microbiological sample processing and experiments

12.2.1.1. Cell and viral counts

A total of 10 samples were processed for cell and/or viral counts. Performing shipboard cell counts on rock samples is difficult because of the time required to separate cells from rock material in addition to the time required for sample processing of other shipboard tests. Therefore, shipboard cell counts were not attempted during the SAT expeditions. Cell count samples were instead broken into small chips and/or powder and preserved for postexpedition analyses (1 cm^3 sample in 4 mL of 4% paraformaldehyde in 100 mM PBS). Duplicate cell count samples were prepared for all samples so that the measurements could be performed independently in two different laboratories. When samples were taken for viral metagenomics, a third replicate was added to allow for viral counts.

12.2.1.2. Microbial community structure

A total of 10 samples were processed for shore-based DNA (PCR amplicon based and metagenomes) and/or RNA (PCR amplicon based and/or metatranscriptomes) analysis, 10 samples were preserved for single cell genomics, and 10 samples were collected for lipid analysis (Table **T38**). Material for DNA, RNA, and lipid-based analyses of microbial community composition, which will be performed as postexpedition research, was collected and preserved following the procedures described in **Microbiology** in the Expedition 390/393 methods chapter [Coggon et al., 2024a].

12.2.1.3. Microbial incubation experiments

To study nitrogen cycling at the sediment/basement interface, basement samples from Sections 393-U1583C-13X-1 and 393-U1583F-3R-2 from the inner core were used in an ammonium enrichment incubation experiment (see **Microbiology** in the Expedition 390/393 methods chapter [Coggon et al., 2024a]). Briefly, ~9 g of rock crushed with a sterile Diamonite mortar and pestle was diluted in 50 mL vials with deep seawater that had been filtered through a 0.22 µm pore size

Sample	Top depth (mbsf)	Lithology	Alteration	Veins	Foldio turntable photo
393-U1583C-13X-1 0-15 cm	104.5	Moderately plagioclase-olivine phyric, subtly variolitic massive basalt	Overall moderately altered; moderate gray background alteration, locally more brownish; halos are dark gray, light brownish gray, or reddish brown	Veins up to 1.5 mm composed of carbonate, clay, and FeOH	
393-U1583F-3R-2 111-128 cm	112.01	Moderately plagioclase-olivine phyric, subtly variolitic massive basalt	Overall moderately altered; moderate gray background alteration, locally more brownish; halos are dark gray, light brownish gray, or reddish brown	Veins up to 1.5 mm composed of carbonate, clay, and FeOH	
393-U1583F-5R-4 48-63 cm	123.94	Moderately plagioclase-olivine-clinopyroxene phyric, fine-grained basalt with glassy margin	Very dark gray background with a patchy brown appearance (and limited halos) suggesting higher alteration intensity	Veins up to 1.5 mm composed of carbonate, clay, and FeOH	
393-U1583F-10R-1 36-46 cm	146.66	Sparsely plagioclase-olivine-clinopyroxene phyric, micro-crystalline basalt with glassy margin	Typical gray background; brown, reddish brown, and dark bluish gray halos around veins	Veins up to 1.5 mm composed of smectite, carbonate, and FeOH	
393-U1583F-12R-1 15-29 cm	153.35	Aphyric fine-grained basalt	Gray mottled variolitic texture that is dark gray-brown; halos include reddish brown, light yellowish brown, dark gray, and light brownish gray	Veins up to 2 mm composed of carbonate, sediment, FeOH, and clay	
393-U1583F-13R-2 59-75 cm	160.02	Aphyric fine-grained basalt	Gray background alteration with slight greenish tinge due to abundance of green clay-filled vesicles; complex set of halos, particularly toward end of section	Veins up to 1.5 mm composed of smectite, carbonate, and FeOH	
393-U1583F-16R-2 73-84 cm	173.40	Basaltic breccia with limestone matrix; clasts of microcrystalline basalt and glassy pillow margin			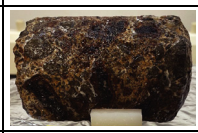
393-U1583F-18R-1 122-139 cm	182.52	Moderately plagioclase-olivine phyric, microcrystalline basalt	Gray background of varying intensity; irregular brown halos related to chilled margins and around veins	Veins up to 1.5 mm composed of smectite, carbonate, and FeOH	
393-U1583F-22R-1 25-36 cm	200.95	Moderately plagioclase-olivine-augite phyric, microcrystalline basalt	Gray background alteration with multiple halo types; extensive brown to dark gray halos	Veins up to 1 mm composed of smectite and carbonate	
393-U1583F-28R-1 14-29 cm	229.94	Sparsely olivine-plagioclase phyric, fine-grained basalt with glassy margin	Gray background; most of interval is low-intensity reddish yellow halos related to chilled margins	Veins up 0.5 mm composed of smectite and carbonate	

Figure F103. Samples collected for shore-based microbiology research, Hole U1583F.

Table T38. Microbiology whole-round samples and subsamples, Hole U1583F. **Download table in CSV format.**

filter to achieve a final volume of 40 mL. The seawater was a mixture of seawater collected from Hole U1583F on 17 July 2022 (~4200 mbsl) and from Hole U1560B on 23 July (~3700 mbsl) using a Niskin bottle attached to the subsea camera system frame. The goal of this setup is to investigate if ammonium addition increases cell abundance and to identify the microorganisms that are translationally active. These vials will be incubated at 4°C for 6 months before shore-based analysis at Texas A&M University (USA).

12.2.2. Microbiological contamination monitoring

Circulation of drilling fluid and mud is a potential source of contamination of cores collected for microbiology analysis (Sylvan et al., 2021). To determine the extent of contamination of microbiology samples, the perfluorocarbon tracer PFMD was injected into drilling fluid at a rate of 0.5 mL/min during circulation in Hole U1583F until the supply of PFMD solution was exhausted, which occurred after drilling Core 393-U1583F-12R. Samples were collected from both the exterior (section directly in contact with drilling fluids; removed during processing) and interior (the part subsampled for postexpedition analyses) of core intervals selected for microbiology analysis to quantify the presence of PFMD. Ideally, PFMD is detected on the exterior, indicating successful delivery down the drill string to the core as it is collected, but not in the interior portions of whole rounds from where the microbiological samples are subsampled. Detection of PFMD in the whole-round interior would indicate intrusion of drilling fluid and hence potential contamination.

When possible, small (<2 cm) exterior samples for PFMD analysis were collected from rubble and core fragments in intervals from which a microbiology sample was collected (Tables **T38**, **T39**). These samples were chosen after the core was laid out in the splitting room, targeting rubble and small pieces in the core catcher that were most likely in contact with drilling fluid but not of high interest for further scientific analysis because of their small size. When no small rubble was available, a piece of the exterior of the microbiological sample was taken after the rock was rinsed and cleaned with ethanol, which may remove or dilute the PFMD and lead to lower detected concentrations but also validates the cleaning process. PFMD was detected from a majority of the exterior samples (rubble and cleaned exterior pieces), with an average concentration of 38.6 ppb PFMD/g core and a median concentration of 27.4 ppb PFMD/g rock (Figure **F104**).

No tracer was detected in the interior microbiology samples, suggesting no to minimal contamination of the samples from drilling fluid.

To determine the number of microorganisms present in drilling fluid and also generate a database of potential contaminants, we collected one sample of drilling fluid from a drill pipe on the rig floor at the end of coring operations in Hole U1583F. Samples were collected for cell counts (1 mL of drilling fluid in 4 mL of 4% paraformaldehyde in 100 mM PBS), and 500 mL of drilling fluid was filtered onto one 0.22 µm pore size 47 mm diameter filter and frozen at −80°C for shore-based molecular biology analysis to determine the microorganisms present in drilling fluid.

Table T39. PFMD tracer contamination comparison, Hole U1583F. **Download table in CSV format.**

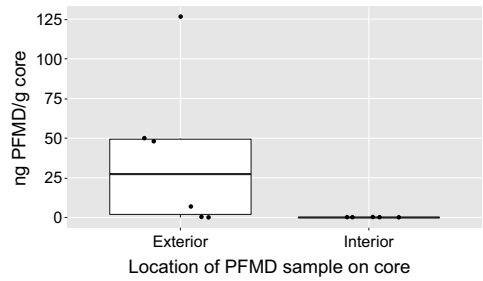

Figure F104. PFMD tracer concentrations measured by gas chromatography comparing concentrations on core exterior surfaces with whole-round interiors for microbiological analyses, Hole U1583F.

References

Agnini, C., Fornaciari, E., Raffi, I., Catanzariti, R., Pälike, H., Backman, J., and Rio, D., 2014. Biozonation and biochronology of Paleogene calcareous nannofossils from low and middle latitudes. Newsletters on Stratigraphy, 47(2):131–181. **https://doi.org/10.1127/0078-0421/2014/0042**

Backman, J., Raffi, I., Rio, D., Fornaciari, E., and Pälike, H., 2012. Biozonation and biochronology of Miocene through Pleistocene calcareous nannofossils from low and middle latitudes. Newsletters on Stratigraphy, 45(3):221–244. **https://doi.org/10.1127/0078-0421/2012/0022**

Baker, P.A., Gieskes, J.M., and Elderfield, H., 1982. Diagenesis of carbonates in deep-sea sediments; evidence from Sr/Ca ratios and interstitial dissolved Sr^{2+} data. Journal of Sedimentary Research, 52(1):71–82. **https://doi.org/10.1306/212F7EE1-2B24-11D7-8648000102C1865D**

Butler, R.F., 1992. Paleomagnetism: Magnetic Domains and Geologic Terranes: Oxford, England (Blackwell).

Christeson, G., and Reece, R., 2020. Bathymetric site survey gridded data in support of IODP Expeditions 390 and 393, South Atlantic Transect (MGL1601, CREST). Interdisciplinary Earth Data Alliance (IEDA). **https://doi.org/10.26022/IEDA/327528**

Christeson, G.L., Goff, J.A., and Reece, R.S., 2019. Synthesis of oceanic crustal structure from two-dimensional seismic profiles. Reviews of Geophysics, 57(2):504–529. **https://doi.org/10.1029/2019RG000641**

Christeson, G.L., Reece, R.S., Kardell, D.A., Estep, J.D., Fedotova, A., and Goff, J.A., 2020. South Atlantic transect: variations in oceanic crustal structure at 31°S. Geochemistry, Geophysics, Geosystems, 21(7):e2020GC009017. **https://doi.org/10.1029/2020GC009017**

Coggon, R.M., Christeson, G.L., Sylvan, J.B., Teagle, D.A.H., Estes, E., Williams, T., and Alvarez Zarikian, C.A., 2020. Expedition 390/393 Scientific Prospectus: The South Atlantic Transect. International Ocean Discovery Program. **https://doi.org/10.14379/iodp.sp.390393.2020**

Coggon, R.M., Teagle, D.A.H., Sylvan, J.B., Reece, J., Estes, E.R., Williams, T.J., Christeson, G.L., Aizawa, M., Albers, E., Amadori, C., Belgrano, T.M., Borrelli, C., Bridges, J.D., Carter, E.J., D'Angelo, T., Dinarès-Turell, J., Doi, N., Estep, J.D., Evans, A., Gilhooly, W.P., III, Grant, L.J.C., Guérin, G.M., Harris, M., Hojnacki, V.M., Hong, G., Jin, X., Jonnalagadda, M., Kaplan, M.R., Kempton, P.D., Kuwano, D., Labonte, J.M., Lam, A.R., Latas, M., Lowery, C.M., Lu, W., McIntyre, A., Moal-Darrigade, P., Pekar, S.F., Robustelli Test, C., Routledge, C.M., Ryan, J.G., Santiago Ramos, D., Shchepetkina, A., Slagle, A.L., Takada, M., Tamborrino, L., Villa, A., Wang, Y., Wee, S.Y., Widlansky, S.J., Yang, K., Kurz, W., Prakasam, M., Tian, L., Yu, T., and Zhang, G., 2024a. Expedition 390/393 methods. In Coggon, R.M., Teagle, D.A.H., Sylvan, J.B., Reece, J., Estes, E.R., Williams, T.J., Christeson, G.L., and the Expedition 390/393 Scientists, South Atlantic Transect. Proceedings of the International Ocean Discovery Program, 390/393: College Station, TX (International Ocean Discovery Program). **https://doi.org/10.14379/iodp.proc.390393.102.2024**

Coggon, R.M., Teagle, D.A.H., Sylvan, J.B., Reece, J., Estes, E.R., Williams, T.J., Christeson, G.L., Aizawa, M., Albers, E., Amadori, C., Belgrano, T.M., Borrelli, C., Bridges, J.D., Carter, E.J., D'Angelo, T., Dinarès-Turell, J., Doi, N., Estep, J.D., Evans, A., Gilhooly, W.P., III, Grant, L.J.C., Guérin, G.M., Harris, M., Hojnacki, V.M., Hong, G., Jin, X., Jonnalagadda, M., Kaplan, M.R., Kempton, P.D., Kuwano, D., Labonte, J.M., Lam, A.R., Latas, M., Lowery, C.M., Lu, W., McIntyre, A., Moal-Darrigade, P., Pekar, S.F., Robustelli Test, C., Routledge, C.M., Ryan, J.G., Santiago Ramos, D., Shchepetkina, A., Slagle, A.L., Takada, M., Tamborrino, L., Villa, A., Wang, Y., Wee, S.Y., Widlansky, S.J., Yang, K., Kurz, W., Prakasam, M., Tian, L., Yu, T., and Zhang, G., 2024b. Expedition 390/393 summary. In Coggon, R.M., Teagle, D.A.H., Sylvan, J.B., Reece, J., Estes, E.R., Williams, T.J., Christeson, G.L., and the Expedition 390/393 Scientists, South Atlantic Transect. Proceedings of the International Ocean Discovery Program, 390/393: College Station, TX (International Ocean Discovery Program). **https://doi.org/10.14379/iodp.proc.390393.101.2024**

Coggon, R.M., Teagle, D.A.H., Sylvan, J.B., Reece, J., Estes, E.R., Williams, T.J., Christeson, G.L., and the Expedition 390/393 Scientists, 2024c. Supplementary material, **https://doi.org/10.14379/iodp.proc.390393supp.2024.** In Coggon, R.M., Teagle, D.A.H., Sylvan, J.B., Reece, J., Estes, E.R., Williams, T.J., Christeson, G.L., and the Expedition 390/393 Scientists, South Atlantic Transect. Proceedings of the International Ocean Discovery Program, 390/393: College Station, TX (International Ocean Discovery Program).

Estep, J., Reece, R., Kardell, D.A., Christeson, G.L., and Carlson, R.L., 2019. Seismic Layer 2A: evolution and thickness from 0- to 70-Ma crust in the slow-intermediate spreading South Atlantic. Journal of Geophysical Research: Solid Earth, 124(8):7633–7651. **https://doi.org/10.1029/2019JB017302**

Fuchs, S., Norden, B., and the International Heat Flow Commission, 2021. The Global Heat Flow Database. GFZ Data Services. **https://doi.org/10.5880/fidgeo.2021.014**

Gale, A., Dalton, C.A., Langmuir, C.H., Su, Y., and Schilling, J.-G., 2013. The mean composition of ocean ridge basalts. Geochemistry, Geophysics, Geosystems, 14(3):489–518. **https://doi.org/10.1029/2012GC004334**

Gradstein, F.M., Ogg, J.G., Schmitz, M.D., and Ogg, G.M. (Eds.), 2020. The Geologic Time Scale 2020: Amsterdam (Elsevier BV). **https://doi.org/10.1016/C2020-1-02369-3**

Hein, J.R., O'Neil, J.R., and Jones, M.G., 1979. Origin of authigenic carbonates in sediment from the deep Bering Sea. Sedimentology, 26(5):681–705. **https://doi.org/10.1111/j.1365-3091.1979.tb00937.x**

Higgins, J.A., and Schrag, D.P., 2012. Records of Neogene seawater chemistry and diagenesis in deep-sea carbonate sediments and pore fluids. Earth and Planetary Science Letters, 357–358:386–396. **https://doi.org/10.1016/j.epsl.2012.08.030**

Jelinek, V., 1981. Characterization of the magnetic fabric of rocks. Tectonophysics, 79(3–4):T63–T67. **https://doi.org/10.1016/0040-1951(81)90110-4**

Jørgensen, B.B., 1977. Bacterial sulfate reduction within reduced microniches of oxidized marine sediments. Marine Biology, 41(1):7–17. **https://doi.org/10.1007/BF00390576**

Kardell, D.A., Christeson, G.L., Estep, J.D., Reece, R.S., and Carlson, R.L., 2019. Long-lasting evolution of Layer 2A in the western South Atlantic: evidence for low-temperature hydrothermal circulation in old oceanic crust. Journal of Geophysical Research: Solid Earth, 124(3):2252–2273. **https://doi.org/10.1029/2018JB016925**

Kardell, D.A., Zhao, Z., Ramos, E.J., Estep, J., Christeson, G.L., Reece, R.S., and Hesse, M.A., 2021. Hydrothermal models constrained by fine-scale seismic velocities confirm hydrothermal cooling of 7–63 Ma South Atlantic crust. Journal of Geophysical Research: Solid Earth, 126(6):e2020JB021612. **https://doi.org/10.1029/2020JB021612**

Kelley, K.A., Kingsley, R., and Schilling, J.-G., 2013. Composition of plume-influenced mid-ocean ridge lavas and glasses from the Mid-Atlantic Ridge, East Pacific Rise, Galápagos spreading center, and Gulf of Aden. Geochemistry, Geophysics, Geosystems, 14(1):223–242. **https://doi.org/10.1002/ggge.20049**

Kendrick, M.A., Hémond, C., Kamenetsky, V.S., Danyushevsky, L., Devey, C.W., Rodemann, T., Jackson, M.G., and Perfit, M.R., 2017. Seawater cycled throughout Earth's mantle in partially serpentinized lithosphere. Nature Geoscience, 10(3):222–228. **https://doi.org/10.1038/ngeo2902**

King, D.J., Wade, B.S., Liska, R.D., and Miller, C.G., 2020. A review of the importance of the Caribbean region in Oligo-Miocene low latitude planktonic foraminiferal biostratigraphy and the implications for modern biogeochronological schemes. Earth-Science Reviews, 202:102968. **https://doi.org/10.1016/j.earscirev.2019.102968**

Korenaga, T., and Korenaga, J., 2008. Subsidence of normal oceanic lithosphere, apparent thermal expansivity, and seafloor flattening. Earth and Planetary Science Letters, 268(1):41–51. **https://doi.org/10.1016/j.epsl.2007.12.022**

Lam, A.R., Crundwell, M.P., Leckie, R.M., Albanese, J., and Uzel, J.P., 2022. Diachroneity rules the mid-latitudes: a test case using Late Neogene planktic foraminifera across the Western Pacific. Geosciences, 12(5):190. **https://doi.org/10.3390/geosciences12050190**

Le Bas, M.J., Le Maitre, R. W., Streickeisen, A., Zanettin, B., the IUGS Subcommission on the Systematics of Igneous Rocks, 1986. A chemical classification of volcanic rocks based on the total alkali-silica diagram. Journal of Petrology, 27(3):745–750. **https://doi.org/10.1093/petrology/27.3.745**

Le Roux, P.J., 2000. The geochemistry of selected mid-ocean ridge basalts from the Southern mid-Atlantic ridge (40°–55°S) [PhD dissertation]. University of Cape Town, Cape Town, South Africa. **http://hdl.handle.net/11427/4207**

Marschall, H.R., Wanless, V.D., Shimizu, N., Pogge von Strandmann, P.A.E., Elliott, T., and Monteleone, B.D., 2017. The boron and lithium isotopic composition of mid-ocean ridge basalts and the mantle. Geochimica et Cosmochimica Acta, 207:102–138. **https://doi.org/10.1016/j.gca.2017.03.028**

Martini, E., 1971. Standard Tertiary and Quaternary calcareous nannoplankton zonation. Proceedings of the Second Planktonic Conference, Roma, 1970:739–785.

Marty, J.C., and Cazenave, A., 1989. Regional variations in subsidence rate of oceanic plates: a global analysis. Earth and Planetary Science Letters, 94(3):301–315. **https://doi.org/10.1016/0012-821X(89)90148-9**

Maxbauer, D.P., Feinberg, J.M., and Fox, D.L., 2016. MAX UnMix: a web application for unmixing magnetic coercivity distributions. Computers & Geosciences, 95:140–145. **https://doi.org/10.1016/j.cageo.2016.07.009**

Michael, P.J., and Graham, D.W., 2015. The behavior and concentration of CO_2 in the suboceanic mantle: inferences from undegassed ocean ridge and ocean island basalts. Lithos, 236–237:338–351. **https://doi.org/10.1016/j.lithos.2015.08.020**

Olson, P., Reynolds, E., Hinnov, L., and Goswami, A., 2016. Variation of ocean sediment thickness with crustal age. Geochemistry, Geophysics, Geosystems, 17(4):1349–1369. **https://doi.org/10.1002/2015GC006143**

Parsons, B., and Sclater, J.G., 1977. An analysis of the variation of ocean floor bathymetry and heat flow with age. Journal of Geophysical Research (1896-1977), 82(5):803–827. **https://doi.org/10.1029/JB082i005p00803**

Paulick, H., Münker, C., and Schuth, S., 2010. The influence of small-scale mantle heterogeneities on Mid-Ocean Ridge volcanism: evidence from the southern Mid-Atlantic Ridge (7°30′S to 11°30′S) and Ascension Island. Earth and Planetary Science Letters, 296(3–4):299–310. **https://doi.org/10.1016/j.epsl.2010.05.009**

Pearce, J.A., and Norry, M.J., 1979. Petrogenetic implications of Ti, Zr, Y, and Nb variations in volcanic rocks. Contributions to Mineralogy and Petrology, 69(1):33–47. **https://doi.org/10.1007/BF00375192**

Reece, R., Christeson, G., Amara, A., Estep, J., Greene, J., Koch, C., Henning, L., Worman, W., and Wright, A., 2016. CREST: Crustal Reflectivity Experiment southern transect South Atlantic multichannel seismic and ocean bottom seismometer experiment, 4 Jan–25 Feb 2016 Cruise Report. **http://www.iris.washington.edu/data/reports/2016/16-003/CREST_2016-01-04-2016-02-25_MGL1601_CruiseReport.pdf**

Reece, R., and Estep, J., 2019. Processed MCS (PSTM) data from the Mid-Atlantic Ridge (MAR) to the Rio Grande Rise, South Atlantic Ocean, acquired by the R/V Marcus G. Langseth in 2016 (MGL1601) **https://doi.org/10.1594/IEDA/500255**

Reekie, C.D.J., Jenner, F.E., Smythe, D.J., Hauri, E.H., Bullock, E.S., and Williams, H.M., 2019. Sulfide resorption during crustal ascent and degassing of oceanic plateau basalts. Nature Communications, 10(1):82. **https://doi.org/10.1038/s41467-018-08001-3**

Ríos, A.F., Resplandy, L., García-Ibáñez, M.I., Fajar, N.M., Velo, A., Padin, X.A., Wanninkhof, R., Steinfeldt, R., Rosón, G., and Pérez, F.F., 2015. Decadal acidification in the water masses of the Atlantic Ocean. Proceedings of the National Academy of Sciences, 112(32):9950–9955. **https://doi.org/10.1073/pnas.1504613112**

Sarmiento, J.L., Simeon, J., Gnanadesikan, A., Gruber, N., Key, R.M., and Schlitzer, R., 2007. Deep ocean biogeochemistry of silicic acid and nitrate. Global Biogeochemical Cycles, 21(1). **https://doi.org/10.1029/2006GB002720**

Schrag, D.P., Higgins, J.A., Macdonald, F.A., and Johnston, D.T., 2013. Authigenic carbonate and the history of the global carbon cycle. Science, 339(6119):540–543. **https://doi.org/10.1126/science.1229578**

Sclater, J.G., Jaupart, C., and Galson, D., 1980. The heat flow through oceanic and continental crust and the heat loss of the Earth. Reviews of Geophysics, 18(1):269-311. **https://doi.org/10.1029/RG018i001p00269**

Shervais, J.W., 1982. Ti-V plots and the petrogenesis of modern and ophiolitic lavas. Earth and Planetary Science Letters, 59(1):101–118. **https://doi.org/10.1016/0012-821X(82)90120-0**

Shervais, J.W., 2022. The petrogenesis of modern and ophiolitic lavas reconsidered: Ti-V and Nb-Th. Geoscience Frontiers, 13(2):101319. **https://doi.org/10.1016/j.gsf.2021.101319**

Shipboard Scientific Party, 1993. Site 896. In Alt, J.C., Kinoshita, H., Stokking, L.B., et al., Proceedings of the Ocean Drilling Program, Initial Reports, 148. College Station, TX (Ocean Drilling Program), 123–192. **https://doi.org/10.2973/odp.proc.ir.148.103.1993**

Smith, D.K., and Cann, J.R., 1990. Hundreds of small volcanoes on the median valley floor of the Mid-Atlantic Ridge at 24–30° N. Nature, 348(6297):152–155. **https://doi.org/10.1038/348152a0**

Spinelli, G.A., Giambalvo, E.R., and Fisher, A.T., 2004. Sediment permeability, distribution, and influence on fluxes in oceanic basement. In Davis, E.E., and Elderfield, H. (Eds.), Hydrogeology of the Oceanic Lithosphere. Cambridge, UK (Cambridge University Press), 151–188.

Stein, C.A., and Stein, S., 1992. A model for the global variation in oceanic depth and heat flow with lithospheric age. Nature, 359(6391):123–129. **https://doi.org/10.1038/359123a0**

Straume, E.O., Gaina, C., Medvedev, S., Hochmuth, K., Gohl, K., Whittaker, J.M., Abdul Fattah, R., Doornenbal, J.C., and Hopper, J.R., 2019. GlobSed: updated total sediment thickness in the world's oceans. Geochemistry, Geophysics, Geosystems, 20(4):1756–1772. **https://doi.org/10.1029/2018GC008115**

Sylvan, J.B., Estes, E.R., Bogus, K., Colwell, F.S., Orcutt, B.N., and Smith, D.C, 2021. Technical Note 4: Recommendations for microbiological sampling and contamination tracer use aboard the JOIDES Resolution following 20 years of IODP deep biosphere research. International Ocean Discovery Program. **https://doi.org/10.14379/iodp.tn.4.2021**

Teagle, D.A.H., Reece, J., Williams, T.J., Coggon, R.M., Sylvan, J.B., Estes, E.R., Christeson, G.L., Albers, E., Amadori, C., Belgrano, T.M., D'Angelo, T., Doi, N., Evans, A., Guérin, G.M., Harris, M., Hojnacki, V.M., Hong, G., Jin, X., Jonnalagadda, M., Kuwano, D., Labonte, J.M., Lam, A.R., Latas, M., Lu, W., Moal-Darrigade, P., Pekar, S.F., Robustelli Test, C., Ryan, J.G., Santiago Ramos, D., Shchepetkina, A., Villa, A., Wee, S.Y., Widlansky, S.J., Aizawa, M., Borrelli, C., Bridges, J.D., Carter, E.J., Dinarès-Turell, J., Estep, J.D., Gilhooly, W.P., III, Grant, L.J.C., Kaplan, M.R., Kempton, P.D., Lowery, C.M., McIntyre, A., Routledge, C.M., Slagle, A.L., Takada, M., Tamborrino, L., Wang, Y., Yang, K., Kurz, W., Prakasam, M., Tian, L., Yu, T., and Zhang, G., 2024a. Site U1558. In Coggon, R.M., Teagle, D.A.H., Sylvan, J.B., Reece, J., Estes, E.R., Williams, T.J., Christeson, G.L., and the Expedition 390/393 Scientists, South Atlantic Transect. Proceedings of the International Ocean Discovery Program, 390/393: College Station, TX (International Ocean Discovery Program). **https://doi.org/10.14379/iodp.proc.390393.106.2024**

Teagle, D.A.H., Reece, J., Williams, T.J., Coggon, R.M., Sylvan, J.B., Estes, E.R., Christeson, G.L., Albers, E., Amadori, C., Belgrano, T.M., D'Angelo, T., Doi, N., Evans, A., Guérin, G.M., Harris, M., Hojnacki, V.M., Hong, G., Jin, X., Jonnalagadda, M., Kuwano, D., Labonte, J.M., Lam, A.R., Latas, M., Lu, W., Moal-Darrigade, P., Pekar, S.F., Robustelli Test, C., Ryan, J.G., Santiago Ramos, D., Shchepetkina, A., Villa, A., Wee, S.Y., Widlansky, S.J., Aizawa, M., Borrelli, C., Bridges, J.D., Carter, E.J., Dinarès-Turell, J., Estep, J.D., Gilhooly, W.P., III, Grant, L.J.C., Kaplan, M.R., Kempton, P.D., Lowery, C.M., McIntyre, A., Routledge, C.M., Slagle, A.L., Takada, M., Tamborrino, L., Wang, Y., Yang, K., Kurz, W., Prakasam, M., Tian, L., Yu, T., and Zhang, G., 2024b. Site U1560. In Coggon, R.M., Teagle, D.A.H., Sylvan, J.B., Reece, J., Estes, E.R., Williams, T.J., Christeson, G.L., and the Expedition 390/393 Scientists, South Atlantic Transect. Proceedings of the International Ocean Discovery Program, 390/393: College Station, TX (International Ocean Discovery Program). **https://doi.org/10.14379/iodp.proc.390393.108.2024**

Turchyn, A.V., Bradbury, H.J., Walker, K., and Sun, X., 2021. Controls on the precipitation of carbonate minerals within marine sediments. Frontiers in Earth Science, 9:618311. **https://doi.org/10.3389/feart.2021.618311**

van der Zwan, F.M., Devey, C.W., Hansteen, T.H., Almeev, R.R., Augustin, N., Frische, M., Haase, K.M., Basaham, A., and Snow, J.E., 2017. Lower crustal hydrothermal circulation at slow-spreading ridges: evidence from chlorine in Arctic and South Atlantic basalt glasses and melt inclusions. Contributions to Mineralogy and Petrology, 172(11):97. **https://doi.org/10.1007/s00410-017-1418-1**

Wade, B.S., Pearson, P.N., Berggren, W.A., and Pälike, H., 2011. Review and revision of Cenozoic tropical planktonic foraminiferal biostratigraphy and calibration to the geomagnetic polarity and astronomical time scale. Earth-Science Reviews, 104(1–3):111–142. **https://doi.org/10.1016/j.earscirev.2010.09.003**

Yang, S., Humayun, M., and Salters, V.J.M., 2018. Elemental systematics in MORB glasses from the Mid-Atlantic Ridge. Geochemistry, Geophysics, Geosystems, 19(11):4236–4259. **https://doi.org/10.1029/2018GC007593**

Yang, T., Zhao, X., Petronotis, K., Dekkers, M.J., and Xu, H., 2019. Anisotropy of magnetic susceptibility (AMS) of sediments from Holes U1480E and U1480H, IODP Expedition 362: sedimentary or artificial origin and implications for paleomagnetic studies. Geochemistry, Geophysics, Geosystems, 20(11):5192–5215. **https://doi.org/10.1029/2019GC008721**

Yeo, I., Searle, R.C., Achenbach, K.L., Le Bas, T.P., and Murton, B.J., 2012. Eruptive hummocks: building blocks of the upper ocean crust. Geology, 40(1):91–94. **https://doi.org/10.1130/G31892.1**

Yoder, H.S., Jr., and Tilley, C.E., 1962. Origin of basalt magmas: an experimental study of natural and synthetic rock xystems. Journal of Petrology, 3(3):342–532. **https://doi.org/10.1093/petrology/3.3.342**

Zijderveld, J.D.A., 1967. AC demagnetization of rocks: analysis of results. In Runcorn, S.K.C., Creer, K.M., and Collinson, D.W. (Eds.), Methods in Palaeomagnetism. Developments in Solid Earth Geophysics, 3: 254–286. **https://doi.org/10.1016/B978-1-4832-2894-5.50049-5**